T.C.
MANİSA CELAL BAYAR ÜNİVERSİTESİ
FEN BİLİMLERİ ENSTİTÜSÜ

MANİSA CELAL BAYAR UNIVERSITY
INSTITUTE OF NATURAL&APPLIED SCIENCE

CİLT:16 SAYI:1 YIL:2020 ISSN: 1305-130X
VOLUME:16 ISSUE:1 YEAR:2020 e-ISSN: 1305-1385

CELAL BAYAR ÜNİVERSİTESİ FEN BİLİMLERİ DERGİSİ

CELAL BAYAR UNIVERSITY JOURNAL OF SCIENCE

CELAL BAYAR
ÜNİVERSİTESİ

Journal of Science

Volume: 16, Issue: 1, Year: 2020

Contact

Manisa Celal Bayar University

Institute of Natural and Applied Sciences

Campus of Şehit Prof Dr İlhan Varank 45140 Yunus Emre – MANİSA, TURKEY

Tel: (00 90) 236 201 27 00

Fax: (00 90) 236 241 21 49

e-mail: cbujos@gmail.com

Web: http://dergipark.gov.tr/cbayarfbe

"CBU Journal of Science is indexed by ULAKBIM-TUBITAK TR-DIZIN"

ISSN 1305-130X E-ISSN 1305-1385

CBUJOS is published quarterly at Manisa Celal Bayar University Printing House

"CBU Journal of Science is a refereed scientific journal"

Celal Bayar University Journal of Science

Celal Bayar University Journal of Science
Volume 16, Issue 1, 2020, p 1-1

CBU Journal of Science

Celal Bayar University Journal of Science (CBUJOS) covers scientific studies in the fields of Engineering and Science and publishes accounts of original research articles concerned with all aspects of experimental and theoretical studies. CBU Journal of Science is a refereed scientific journal published four times annually (March, June, September and December) by Institute of Natural and Applied Sciences of Manisa Celal Bayar University. CBU Journal of Science considers the original research articles written in English for evaluation.

CBU Journal of Science is indexed by TUBİTAK ULAKBIM TR-DIZIN, and also is included in DOAJ, Cite Factor, Journal TOCS, Advanced Science Index and OAJI databases. Digital Object Identifier (DOI) number will be assigned for all the articles being published in CBU Journal of Science.

Instructions for Authors and Article Template can be found on the main page of MCBU Institute of Natural and Applied Sciences (http://fbe.cbu.edu.tr)

Celal Bayar University Journal of Science
Volume 16, Issue 1, 2020, p 1-1

Vol: 16, Issue: 1, Year: 2020

Contents

Celal Bayar University Journal of Science
Volume 16, Issue 1, 2020, p 1-1

Celal Bayar University Journal of Science

Measuring of Core Split Line Defect on Pillar Type Vented Brake Disc and Investigation of Crack Occurrence Potential on the Disc Caused by Its Geometric Deviation

Recep Akyüz[1]*, Eren Kulalı[1], Ramadan Soncu[1], Cem Öztürk[1], Mehmet Karaca[1]

[1] TOFAŞ Turk Automobile Company, R&D Center.
*recep.akyuz@tofas.com.tr

Received: 15 October 2019
Accepted: 17 March 2020
DOI: 10.18466/cbayarfbe.633164

Abstract

In this study, a measuring method was defined to convert the level of defects on the pillar type vented brake disc to numeric data where the defects were formed due to missing material in the structure of the disc. Subsequently, the geometric defects which are existing in the core on the droplets were examined with the defined method in only pillar type vented brake disc. Finally, some thermal performance tests (brake disc thermal fatigue test on bench in accordance with Society of Automotive Engineers Brake Rotor Thermal Cracking Procedure for Vehicles (SAE J2928) [1] and brake disc crack test on vehicle; special test procedure of an original equipment manufacturer, which is performed for inspecting structural strength) and thermal fatigue test with thermal shock (test procedure formed by authors) were performed with defected brake discs to evaluate the risk of defected brake disc usage on the vehicle in terms of safety. The main open point is to determine whether the defect can transform to crack by influencing with notch effect during the worst usage conditions. In the conducted tests; it was investigated that the worst core split line defects which are specified by the defined measuring flow may cause a crack formation by proceeding notch effect under the worst usage condition. In order to simulate the worst usage condition; test laboratories, equipment and test track were used in this period for performing brake disc thermal fatigue test, crack test with thermal shock and crack test on vehicle.

Keywords: Brake disc, casting defect, core, crack analysis, thermal fatigue

1. Introduction

In conventional vented brake discs, different types of ventilation geometries such as pillar, straight or curved are used in order to achieve expected thermal performance on the vehicle. To provide homogeneous heat dissipation, the pillar type vents are generally preferred by original equipment manufacturers. T.J. Mackin et.al. studied that brake rotors are subjected to high thermal stresses during routine braking conditions and can reach temperatures as high as 900 °C during hard braking. These thermal stresses reduce fatigue life of the brake rotor by developing macroscopic cracks on the rotor. These large temperature excursions have two possible outcomes: thermal shock that generates surface cracks; and/or large amounts of plastic deformation in the brake rotor [2, 3]. To create the ventilation geometry, sand core is used into the casting molds and the final pillar geometry is always negative of the sand core geometry [3]. Therefore, if there is a geometric deviation on the core surface, its negative form of the deviation would be observed on the opposite side after casting. It means that, if 1 mm burr is existing on the core split line, this defect will appear on the casting part as 1 mm missing material. This defect, which has not a specific geometry and dimension, is defined in literature as “joint burr” or “core trace” when caused excess material on split line [4]. Core split line defect can be cleaned by grinding when it is formed as excess material, but no corrective actions can be made when it forms as a missing material. In case of 1 mm defect existence on the core split line after casting operation, it is possible that total interface area reduction of the pillar halves is about 18% in average. It means that, the strength of the pillar, where stated into the disc, decreases if the defect level increases on the core split line of the part [5]. Therefore, this common irregularity is considered as an important risk factor, since brake disc is a security part. Nowadays, the sand cores are designed uniquely according to ventilation geometry of the disc and printed generally by cold box method [6, 7, 8, 9]. After the cores are pressed in core box, some split

line burrs remain on the cores and normally these burrs must be cleaned by a cleaning equipment to provide the designed disc geometry. But some burrs might remain on the split line and cause a geometric irregularity onto the pillars. In addition to this, it causes missing material like a trace through the whole split line. This defect can be defined as "core split line irregularity".

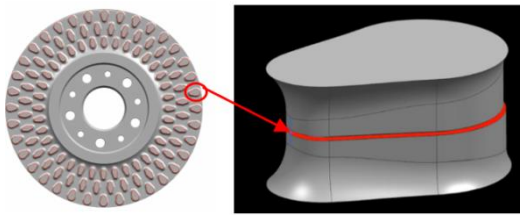

Figure 1. Core split line irregularity illustration on the brake disc pillar.

The defect illustration is shown Figure 1. This type of geometric defect can cause micro or macro cracking on the disc pillars during braking under high temperature and pressure [10, 11]. Goo et.al. investigated the thermal fatigue characteristics of cast iron brake disc under high load pressure. The mechanical and thermal properties of the samples were measured. Thermal fatigue tests were then carried out using equipment developed by the author. It is claimed that the fatigue lifetime of cast iron could be increased by regulating its composition and metallurgical structures [12, 13]. In another study, Gigan et.al. investigated thermo mechanical fatigue of grey cast iron brake discs for heavy vehicles via finite elements method. They claimed that the analysis of stress-strain hysteresis loops showed that the mechanical properties drop substantially at high temperature (above 500 °C) [14, 15]. Maraveas et. al. studied
mechanical properties of structural cast iron at elevated temperatures up to 900 ^{0}C and after cooling down by quenching and air flowing. Their study claims that cast-iron structures can be restored after fire damage, provided there is no visible damage [16, 17]. Brake is the most indispensable safety measure of a vehicle which is quite significant in this context where unexpected noise and vibration from the brake provide information about its status, being faulty or not. Such noise and vibration problems are encountered mainly in highway, railway, airway and off-road vehicles, large-scale work machines, oil drilling rigs and mine lifting systems [18] Due to related studies in literature and feedbacks from manufacturers, noise and accompanying vibration mostly occur as a result of the material of the intermediate parts in the brake, wear over time, or the dimensional errors in the design stage[19].

2. Defect Detection and Measuring Method

Detection and measurement processes of the defect were done according to the flow shown in the Figure 2-3, considering the mold mismatch. One of the important criteria is to consider the saw thickness which was used to cut the disc for defect detection. The thickness of the saw should not be thicker than 2 mm to provide the measurement accuracy. Thicker saws can cause material loss on the defect area.

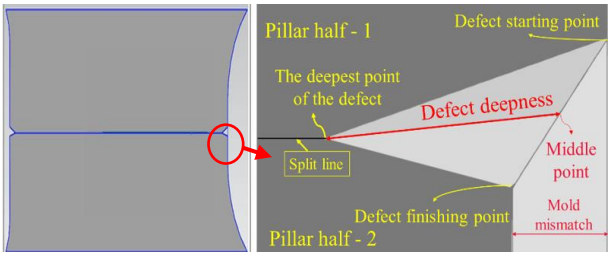

Figure 2. Measuring method of the core split line irregularity under microscope.

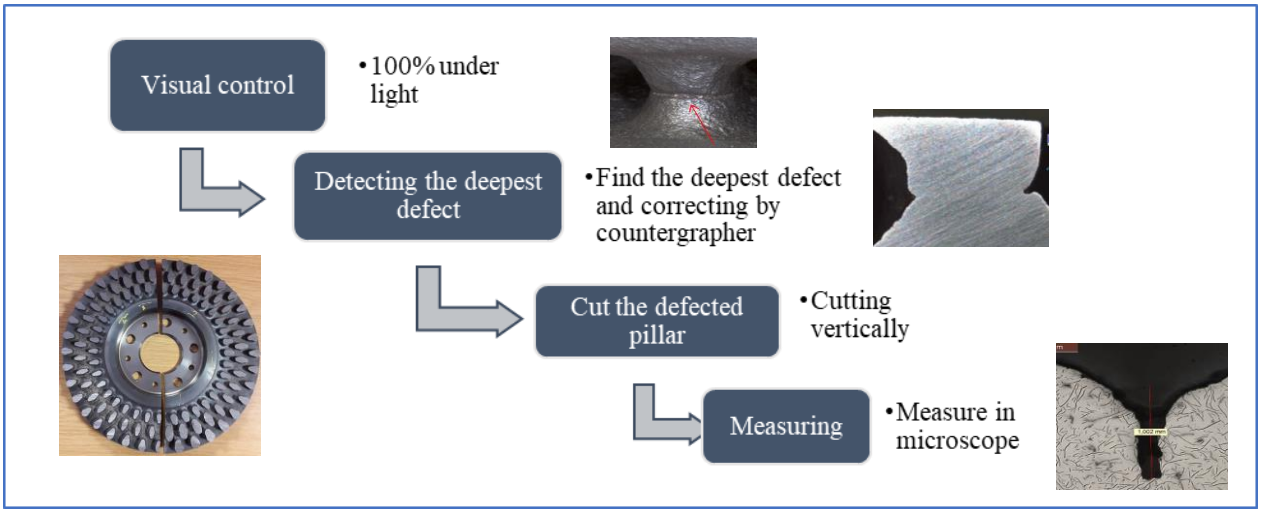

Figure 3. Measuring systematic of the core split line irregularity

Celal Bayar University Journal of Science
Volume 16, Issue 1, 2020, p 1-7
Doi: 10.18466/cbayarfbe.633164

2. Defect Detection and Measuring Method

Before testing, 4 different types of vented brake disc were examined with above specified method in terms of 10 samples which were selected from each type of those brake discs were measured by contour measuring [20] and reported in Figure 4. According to analysis results, the defect characterizations were similar in Type 1 and Type 3. But standard deviation of the defects was bigger in Type 1 (See Figure 5). Also, it is seen that the depth of defects in Type 1 were distributed in a larger range compared to other types. (see Figure 6). After evaluation of the outputs, it was decided to carry out the tests with Type 1.

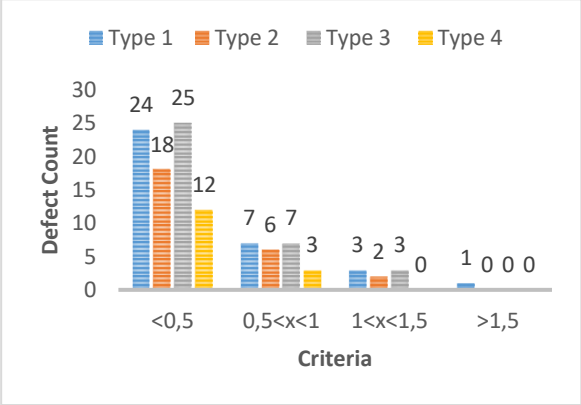

Figure 4. Detected defect amount in inspected 4 type vented brake discs.

The defect depth for each defect was measured non-destructively by contour measuring. The worst discs which had the defect deepness over 1 mm were selected to perform destructive tests. After the tests, samples from these discs were cut and the defects were measured destructively under microscope according to the defined measuring method. In the meantime, occurrence of any crack on the pillars by notch effect was analyzed under microscope.

Table 1. Some characteristics of inspected disc types.

Brake disc	Type 1	Type 2	Type 3	Type 4
Ventilation gap (core thickness) (mm)	10	8	8	12
Pillar Count	108	90	90	93
Total interface area in narrowest section (mm^2)	9270	10753	10753	9970
Casting Method (Moulding)	Vertical	Vertical	Vertical	Horizontal
Core Making Method	Cold box, Painted with water-based paint	Cold box, Painted with water-based paint	Cold box, Painted with water-based paint	Cold box, Painted with water-based paint

defect profile. Each type of brake discs was produced by different foundry. Some defect examples are shown in Figure 7 and comparison table is presented on Table 1.

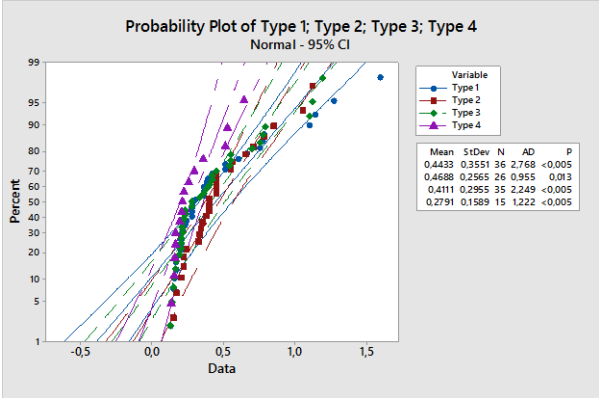

Figure 5. Defect distribution and standard deviation for 4 types.

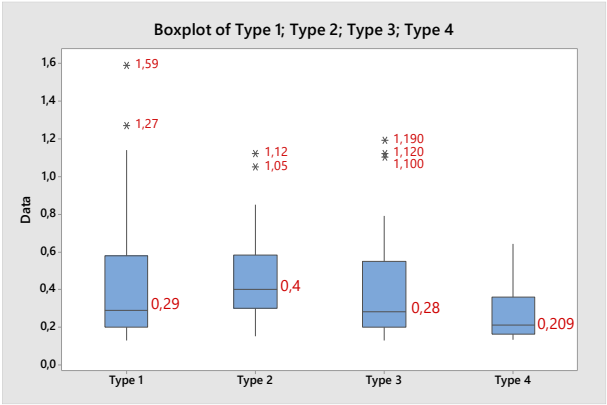

Figure 6. Distribution of the defect for each brake disc type.

Figure 7. Defect sample on the pillars in 4 types vented discs.

2.2. Tests

All tests were carried out in a test facility which is approved by an engineering department of an OEM.

2.2.1. Crack Test (brake disc thermal fatigue test)

The crack test is a structural validation test and generally it is performed according to the regarding standard during the development, design change or material composition change of a part in brake system. The purpose of the test is to assess the capacity of the disc to resist initiation and propagation of cracks on the braking surface and pillars resulting from repeated exposure to thermal stress. Test setup is presented in Figure 8.

Figure 8. Crack test on bench, mounted rotor on dyno.

The brake disc is mounted to the bench together with the components (friction material, caliper, knuckle, hub, bearings) to which it is connected, except the wheel. The rotor speed is increased to 80 km/h then it is decreased to 0 km/h gradually. During this cycle, brake applications are repeated for 100 times after bedding. The same cycle is carried out at least three times and the crack occurrence are investigated on the disc.

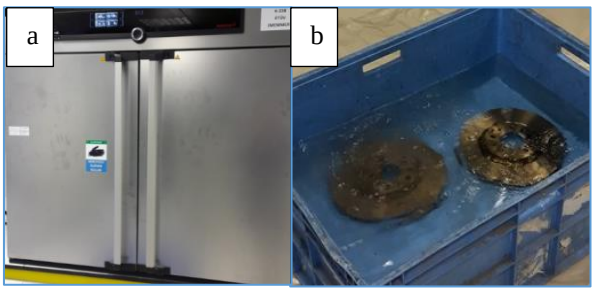

Figure 9. Thermal shocked crack test equipment. **a.** etuv, **b.** water pool.

2.2.2 Thermal Shocked Crack Test

This test is carried out by heating up the disc to 300 ^{0}C, holding it at least 30 minutes in the furnace and then sinking it suddenly to a water pool in room temperature according to regarded standard (see Figure 9 for test equipment). After the rotor and water temperatures are equal, crack formation is investigated on the disc.

2.2.3. Thermal Shocked Crack Test on Vehicle

This test is conducted for simulating the customer usage in the worst environmental conditions. The test is carried out in the performance route by using a pool filled with water which has 10 m length and 30 cm height. The temperature of the water should be between 20-25 ^{0}C. A thermocouple is mounted into the pads for measuring the brake disc temperature during the test. The rotors, which are inspected to have defect levels above 1 mm, are mounted to the vehicle. After the disc surface temperature is increased over 300 ^{0}C, the vehicle is driven in the pool 3 times with 30 km/h in series according to regarded standard. Afterwards, the rotors are dismounted from the vehicle and crack occurrence is investigated on the pillars. Assembled brake disc on vehicle is presented at Figure 10.

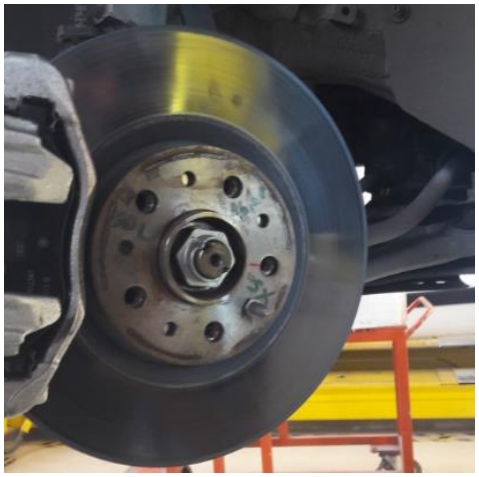

Figure 10. Assembled brake disc on vehicle after thermal shocked crack test on vehicle.

3. Results and Discussions

3.1. Crack Test on Bench & Results

Four rotors that have visually higher defect depth out of 30 rotors which have core split line defect were tested to analyze their crack occurrence. Maximum defect depth and occurrence of cracks on defects' base upon rotors, which cut with fret saw, were analyzed via defined methodology after crack test (Figures 11, 12a, 12b, 13a and 10b) and the results are shown on Table 2.

Table 2. Depth values of core split line after crack test.

Test 1	Def. 1	Def. 2	Def. 3	Def. 4	Def. 5	Def. 6
Rotor 1	0,8	1,11	1,16	1,1	1,2	0,9
Rotor 2	0,75	0,9	1,12	1,59	0,1	0,94
Rotor 3	1,1	0,8	1,15	0,96	0,9	0,85
Rotor 4	1,2	0,7	1,25	0,55	0,9	0,88

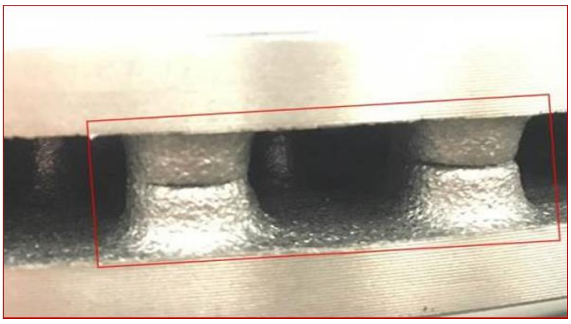

Figure 11. Selected brake disc for the test.

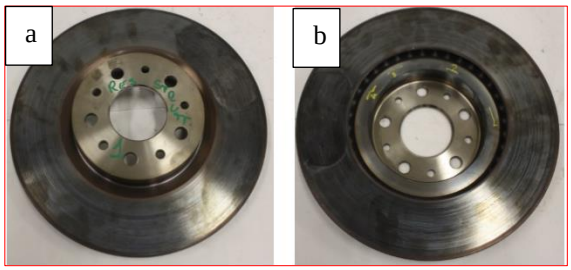

Figure 12. Rotors after crack tests. **a.** left, **b.** right.

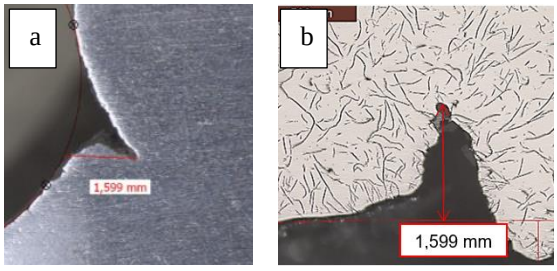

Figure 13. Defect analysis under microscope after crack test. **a.** measurement, **b.** crack analysis.

Before crack test on bench, bedding (burnishing) was implemented for simulating customer usage more realistic results.

3.2. Crack Test with Thermal Shock Results

Defect areas on 4 rotors were analyzed after test (Figure 14, 15a, b, c, d, e). Depth of defects are shown on Table 3. Crack occurrence of 4 pillars that has highest depth was investigated.

Figure 14. Rotors after crack test with thermal shock.

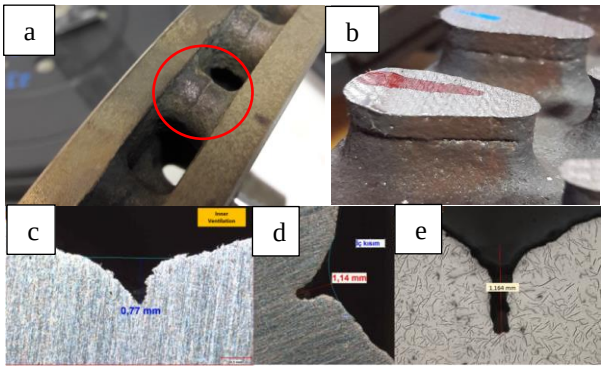

Figure 15. Defects after crack test with thermal shock. **a.** and **b.** defect view, **c, d,** and **e** defect analysis.

Table 3. After thermal shocked crack test, measured maximum defect depths.

Test 2	Def. 1	Def. 2	Def. 3	Def. 4	Def. 5	Def. 6
Rotor 1	0,77	1,1	0,95	0,82	1,14	0,65
Rotor 2	1	0,67	1,12	0,95	0,85	0,88
Rotor 3	0,55	0,94	0,54	1,16	0,65	0,77
Rotor 4	0,85	0,55	1,15	1,1	0,95	0,8

3.3. Results of Thermal Shocked Crack Test on Vehicle

In this test, 2 rotors which were specified as worst according to defined measuring method, were mounted and tested on vehicle. After test, the core split line defects were measured and analyzed crack occurrence under microscope (Figure 16a, b, c). The results are shown in Table 4.

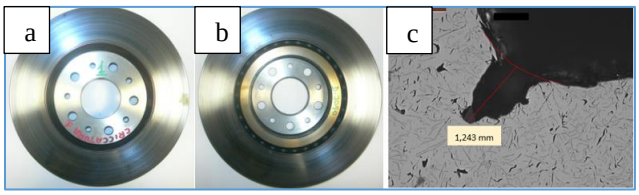

Figure 16. The tested rotors, **a.** left wheel, **b.** right wheel and **c.** analyzing under microscope.

Table 4. The Defect Depths After Test.

Test 3	Def. 1	Def. 2	Def. 3	Def. 4	Def. 5	Def. 6
Rotor 1 (Right)	1,17	0,77	0,9	0,65	1,12	1,14
Rotor 2 (Left)	1,05	0,6	0,85	0,96	1,24	1,18

4. Conclusion

The effect of worst-case core burrs on rotor pillars which has potential risk of crack occurrence on rotor surface was investigated via measurements on depth of those defects which has no regular geometry and dispersion.

- Core burrs with deviation on geometric forms were observed on rotors which were 4 different type of pillar geometry on each. It was also observed that those rotors have 15% of split line defect on their pillars.
- A new methodology was defined to classify the trace on core dimensionally. It is understood that the level of the core split line defect can be determined by contour measuring equipment without any destructive operation.
- Approximately 20% of defects was measured with more than 1 mm depth within all depth distribution. The maximum defect depth was 1,6 mm.
- No cracks on surface of rotors and pillars were observed after crack test (1st test) on bench test. There was any micro crack via checking under microscope. The maximum defect depth was 1,6 mm.
- No cracks – even micro cracks – were observed after thermal shocked crack test (2nd test) on laboratory. The maximum defect depth was 1,16 mm.
- No crack or breakage on pillars were observed after thermal shocked crack test (3rd test) on vehicle. The maximum defect depth was 1,24 mm. Besides, there was no micro-crack on the base of defect.
- It could be evaluated that there is no safety risk (crack and/or breakage) for the Type 1 ventilated rotors which have less than 1.6 mm defect.

This work does not constitute a reference for listed situations below;

- Rotor has min. 15% of its pillars has that kind of defect,
- Rotor which min. 20% of its pillars has more than 1 mm defect
- Brake rotors which have core split line defect on pillars with deeper than 1,6 mm defect.

To verify exact behavior of brake rotors under these circumstances, it is needed to perform a further study based on a proper design of experiment.

Author's Contributions

Recep Akyüz: Drafted and wrote the manuscript, performed the experiment and result analysis.

Eren Kulalı, Ramadan Soncu, Cem Öztürk, Mehmet Karaca: Assisted in analytical analysis on the structure, supervised the experiment's progress, result interpretation and helped in manuscript preparation.

Ethics

There are no ethical issues after the publication of this manuscript.

References

1. Brake Rotor Thermal Cracking Procedure for Vehicles Below 4 540 kg GVWR J2928_201207, https://www.sae.org/standards/content/j2928_201207
2. T.J. Mackin et.al., Thermal cracking in disc brakes, Engineering Failure Analysis 9, 2002, 63 – 76
3. D.M. Stefanescu. ASM handbook Vol.15 Casting, 2002, p 516-523
4. D.M. Stefanescu, ASM handbook Vol.15 Casting, 2002, p 1189, p 1231
5. Amol, A., Ravi, R., FE Prediction of Thermal Performance and Stresses in a Disc Brake System, Journal of SAE, 2572 (2008), 1, pp. 5-8
6. C.W. Meyers and J.T. Berry, The Impact of Robotics on the Foundry Industry, Paper 30, Trans. AFS, 1979, p 107-112
7. J S Campbell, Principles of Manufacturing Materials And Processes, Tata McGraw Hill, 1995.
8. P C Pandey and C K Singh, Production Engineering Sciences, Standard Publishers Ltd., 2003.
9. S Kalpakjian and S R Schmid, Manufacturing Processes for Engineering Materials, Pearson education, 2009. 4. E. Paul Degarmo, J T Black, Ronald A Kohser, Materials and processes in manufacturing, John wiley and sons, 8th edition, 1999
10. Shaniavski, AA. Synergetical models of fatigue-surface appearance in metals: the scale levels of self-organization, the rotation effects, and density of fracture energy. In: Frantsikony PROBAMAT- 21st Century: Probabilities and Materials. Netherlands: Kluwer Academic Publisher; 1998, p.11-44.
11. Maillot V., Fissolo. A. Degallaix. G. and Degallaix S., Thermal fatigue crack networks parameters and stability: an experimental study, In. J. Solids and Structures, 42, 759-769 (2005)
12. Ivanova VS. Synergetics. Strength and failure of metallic materials. Russian, Moscow: Nauka; 1992.
13. B. Goo, and C. Lim, Thermal fatigue of cast iron brake disk materials, Journal of Mechanical Science and Technology 26 (6) (2012) 1719~1724
14. G. Gigan, V. Norman, J. Ahlström and T. Vernersson, Thermomechanical Fatigue of Grey Cast Iron Brake Discs for Heavy Vehicles, projects 2012-03662 and 2012-03625
15. Amol A. Apte and H. Ravi,FE Prediction of Thermal Performance and Stresses in a Disc Brake System, , journal of SAE ,2008.
16. Pevec M, et al. Elevated temperature low cycle fatigue of grey cast iron used for automotivebrake discs. Engineering Failure Analysis 2014; 42: 221-230.

17. C. Maraveas, Y.C. Wang, T. Swailes, G. Sotiriadis, An experimental investigation of mechanical properties of structural cast iron at elevated temperatures and after cooling down, Fire Safety Journal 71 (2015) 340–352

18. Z.Ertekin, N. Özkurt, Noise Analysis of Air Disc Brake Systems Using Wavelet Synchrosqueezed Transform, Celal Bayar University Journal of Science Volume 15, Issue 4, 2019 p 409-414.

19. Beloiu, DM, Ibrahim, RA. 2006. Analytical and experimental investigations of disc brake noise using the frequency-time domain, Structural Control and Health Monitoring. The Official Journal of the International Association for Structural Control and Monitoring and of the European Association for the Control of Structures; 13(1): 277-300.

20. Contour Measuring System, Mitutoyo, CV3200, https://www.mitutoyo.co.jp/eng/support/service/catalog/03/E15010.pdf

Celal Bayar University Journal of Science

A Novel Biosensor Based on Laccase for The Detection of Catechol

Zehra Ölçer[1]*

[1] Department of Chemistry, Gebze Technical University, 41400 Gebze-Kocaeli, Turkey.
* z.olcer@gtu.edu.tr

Received: 18 October 2019
Accepted:17 March 2020
DOI: 10.18466/cbayarfbe.634500

Abstract

Phenolic compounds are broadly used in petrol industrial production processes and thus they are hazardous for ground and surface water and environment. Many of them have harmful effects on plants, animals and human health. Laccases can oxide phenol and phenolic compounds. Biosensors provide ideal sensing systems to determine phenolic compounds. In the present paper, it was developed novel sensor surface with modified laccase on gold electrode which could recognize the phenolic compound catechol. The electrode arrays integrated microfluidics have been fabricated and characterized in order to create a sensor chip which is easy, rapid, and cheaper to produce also have good electrochemical sensing properties. This gold electrode was used to obtain laccase active surface. Laccase was covalently bounded to self-assembled monolayer on gold electrode via glutaraldehyde reactions. Cyclic voltammetry and amperometry activity assays showed that the detection of catechol with laccase modified gold surface. All of the study was carried out using automated biosensor device. Linear range for this biosensor was 0.025 mM to 0.8 mM.

Keywords: Catechol, electrochemical biosensor, laccase immobilization

1. Introduction

Biosensors are of great importance in the bioprocesses, diagnosis, agricultural applications, food industry and environmental imaging. The market share of commercially important biosensors in these areas is expressed in billions of dollars. In this respect, research and development of new sensor devices is of great importance. Electrochemical sensors are the most widely used biosensor group because of their selectivity, rapid analysis, high sensitivity, ease of working with solutions and miniaturization [1-4]. The design of an electrochemical sensor includes many parameters such as electrode design, surface chemistry, recognition element immobilization to the electrode surface and optimum experimental conditions that need to be considered carefully.

Phenolic compounds occupy a large part in nature. They are found in vegetables and fruits and add properties to the products prepared with them; olive-like and they have antioxidant properties. Phenolic compounds are widely used in the production processes of paints, pesticides, surfactants, resins, and plastics in petroleum and pharmaceutical industries. Opposite to their positive properties, phenolic compounds have pollutant properties in nature and water resources that are emerging as by-products of the resin production, pharmaceutical, paint, textile and petrochemical industries. Some phenolic compounds have the ability to mimic endocrine hormones and poses a threat to health [5]. It is possible to identify and quantify phenolic compounds by conventional methods such as spectroscopy and chromatography [6, 7] but these are time-consuming and expensive methods. Recently, biosensor applications have attracted attention for the determination of phenolic compounds.

The laccase enzyme (polyphenoloxidase; EC 1.10.3.2) is a member of the multi-copper-containing family of oxidase enzymes and is capable of oxidizing many organic substrates to reduce molecular oxygen to water. They are produced by a wide variety of organisms such as bacteria, fungi and plants. Laccases can also oxidize both phenolic and non-phenolic compounds and many environmental pollutant compounds. Due to these oxidation ability of laccases, they are preferred in biosensors. Electrochemical sensors are commonly used in the determination of phenolic compounds due to their stability and reproducibility. In order to use the laccase enzyme in the biosensor, immobilization is required for the enzyme to be stable and reusable. Covalent binding

[8-12], physical adsorption [13-16] and entrapmenti in a matrix [17-20] are the immobilization techniques. The method of enzyme binding to the electrode surface is the first step in effective enzyme biosensor due to a critical factor for electron transfer between the enzyme and the electrode surface. The electrode surface modificaiton is carried out with nanomaterials, conductive polymers and self-assembled monolayers (SAM) [21-25].

In this study, a novel biosensor based on laccase enzyme was developed for the detection of phenolic compound catechol. Laccase was covalently bounded to self-assembled monolayer on gold electrode via glutaraldehyde reactions. Modifications and enzyme immobilization on sensor chips integrated into the microfluidic system were carried out quickly and effectively in biosensor device.

2. Materials and Methods

2.1. Materials and Instrumentations

Phosphate buffered saline (PBS, 0.01 M phosphate buffer, 0.0027 M potassium chloride and 0.137 M sodium chloride, pH 7.4) tablets, laccase (EC=1.10.3.2, from *Trametes versicolor*), 2,2′-azinobis-(3-ethylbenzothiazoline-6-sulfonic acid (ABTS) liquid substrate system, 6-amino-1-hexanethiol (AHT), potassium hexacyanoferrate, glutaraldehyde 25%, tris-base, potassium chloride (KCI), ethanol, 1,2-dihydroxybenzene (catechol) were purchased from Sigma-Aldrich. Ultrapure water (18 MΩ cm^{-1}) was obtained from a Milli-Q water system.

MiSens biosensor device was used in electrochemical analysis and assays [26-28]. The biosensor device is an integrated and automated electrochemical biosensor with microfluidic system including tubing connected sample pick up needle and sample/reagent carousel, includes biochip docking station electronic parts and software developed by BILGEM Research Center (BILGEM-TUBITAK, Kocaeli, Turkey). The electrodes were designed on glass plates (10 x 20 mm^2) with a laser-shaped stainless steel thin metal mask. Gold metal coated on glass plates using e-beam evaporator. Biochips includes Au electrode arrays that consist of shared reference/counter electrodes and 8 working electrodes (d =1 mm) has been fabricated and used for the assays (~ 7-10 µL capacity flow cell on the electrode array).

2.2. Modification on The Surface of Electrodes

Before the modification, plasma cleaning was applied on the electrode arrays for a clean sensor surface. A self-assembled monolayer (SAM) was then applied by immersing the sensor chips in ethanolic solution of 2 mM 6-amino-1-hexanethiol (AHT) for overnight (Figure 1). Later they were rinsed with ethanol and water, dryed with nitrogen stream and were vacuum packed. The functionalised biochips were stored at +4°C until used. After the surface modification, the biochip was inserted into the cassette and placed to the device. It was integrated the electronic and fluidic connections and to created a microfluidics system.

2.3. Immobilization of Laccase onto Surface

For the immobilization of enzyme, firstly 6-amino-1-hexanethiol (AHT) functionalised chip surface was activated with 0.5% (w/v) glutaraldehyde (GA) prepared in water. GA (200 µL, 50 µL/min), later laccase solution (100 µg/mL, 200 µL, 25 µL/min) were injected to sensor surfaces (Figure 1). Phosphate buffered saline (PBS, 10 mM, pH 7.4) used for washing buffer and this buffer continuously flowed (100 µL/min) over the sensor surfaces between the injections. Non-reacted aldehyde groups were capped with ethanolamine solution pH 8.5 (1 M, 200 µL, 50 µL/min). Determination of enzyme activity was carried out using substrate solution ABTS (2,2′-azinobis-(3-ethylbenzothiazoline-6-sulfonic acid).

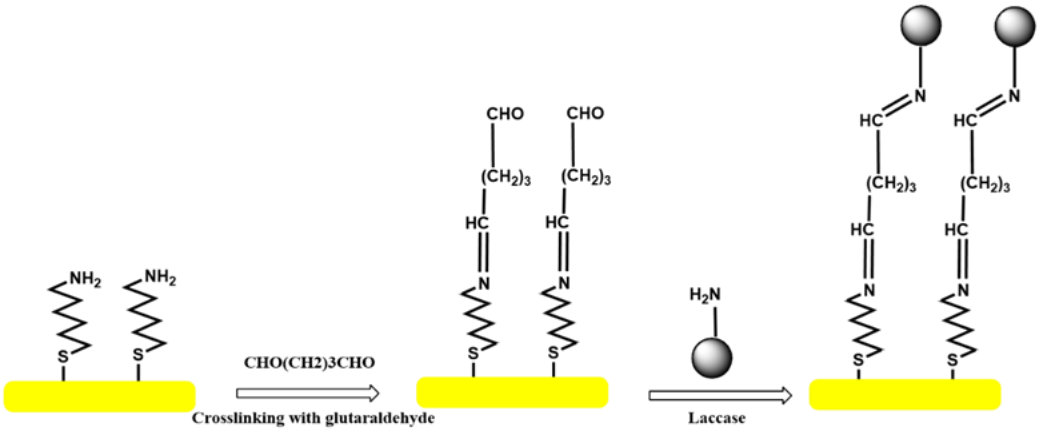

Figure 1. Preparing of the laccase modified biosensor chip

2.4. Detection of catechol and electrochemical measurements

Catechol stock solutions (6 mM) in ethanol were prepared and stored at -20°C until used. Phenolic compound catechol was prepared at varying concentrations (0.025 - 2.0 mM) in PBS buffer solution (10 mM, pH 7.4) and the was measured on laccase immobilized biosensor electrodes.
Cyclic voltammetry (CV) and amperometric measurements were also performed with biosensor device. CV was performed using potassium ferrocyanide solution (1 mM $K_4[Fe(CN)_6]$ / KCI at 100 mV/s scan rate). Amperometric signal was measured using substrate ABTS (2,2′-azinobis-(3-ethylbenzothiazoline-6-sulfonic acid) with a fixed potential of -0.1 V All measurements was carried out during buffer injection and resulted in a real-time amperometric reading.

3. Results and Discussion

3.1. Biosensor Surface Modification

To coating of self-assembled monolayer (SAM) on the gold chip surface, the chips were incubated with 2 mM 6-amino-1-hexanethiol (AHT) solution for overnight. Baregold electrode and AHT coupled electrode were investigated by cyclic voltammetry using potassium ferrocyanide ($K_4[Fe(CN)_6]$) solution as a redox marker in MiSens biosensor device (scan rate: 100 mV/s).

In voltammogram Figure 2, the redox area between the positive and negative potentials of the bare gold electrode, the oxidation and reduction peaks of potassium ferrocyanide are larger than the redox area of the AHT coated chip. After the coating of chip with AHT, a dramatic decrease in redox current was observed.

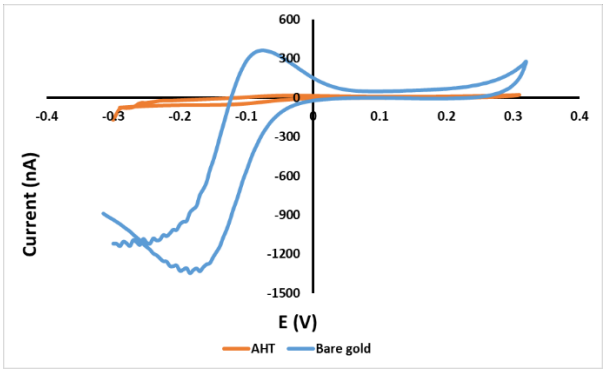

Figure 2. The cyclic voltammetry of bare gold and AHT coated gold electrode arrays (1 mM $K_4[Fe(CN)_6]$/KCI at 100 mV/s scan rate).

It is important that providing high quality packaging in alkanethiol for a good dense and uniform SAM surface. Because the electron tunnel must be formed to enable the transfer of electrons between the electrode and a donor or acceptor [29]. It was observed that a quality packaging achieved using AHT (Fig 1). 6-amino-1-hexanethiol was binded on the gold surface by the strong affinity of a thiol group to gold and thus the amino group ready for enzyme immobilization.

3.2. Activity assay of immobilized laccase

Laccase was immobilized onto AHT coated chips. To binding of laccase on the surface, sensor chip with the SAM of AHT was then placed in the flow cell of the biosensor device, and glutaraldehyde solution was injected (0.5% w/v, 50 µL/min) and then enzyme was injected (100 µg/ml, 200 µL, 25 µL/min). An CHO group binds to NH_2 group of AHT and the other CHO group binds to amino group of enzyme with acetal or semi-acetal formation between amino (NH_2) groups and aldehyde groups (CHO) on the surface. Enzyme activity was determined by amperometric measurement using ABTS (2,2′-azinobis-(3-ethylbenzothiazoline-6-sulfonic acid) substrate solution. In the MiSens biosensor device, Real-time measurement was performed to obtain electrochemical signal by amperometric method, current was measured continuously while applying potential to electrode surface (Real−time Electrochemical Profiling; REP™). A change in catalytic current was observed by injection of ABTS solution (50 µL/min) into the system by reaction of the bound laccase enzyme on the chip surface. While applying potential (-0.1 V) to the electrode surface the current was continuously measured. Initial current measurements during PBS buffer injection were taken and this signal was recorded as a baseline (Figure 3). It was recorded the maximum current value in 170. seconds, average 0.029 ± 0.001 µA current signal.

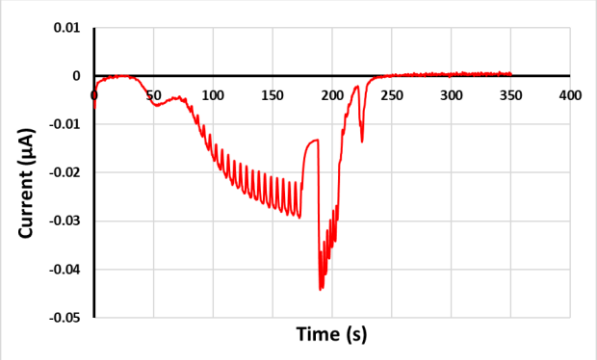

Figure 3. Sensor response of current vs time with respect to ABTS against -0.1V potential.

3.3. Detection of catechol

The determination of catechol on the laccase immobilized sensor surface was performed by cyclic

voltammetry (CV) and amperometric measurement of the catalytic signal formed by the reaction of the enzyme with the catechol. Firstly the laccase immobilized sensor surface was investigated by cyclic voltammetry using catechol solution (400 µM) and also CV measurement was performed for PBS solution. The electrochemical behavior of catechol was characterized by cyclic voltammetry. Comparing the redox peak potentials for laccase immobilized and non-immobilized electrodes, laccase biosensor was the highest current (Figure 4), therefore it was the highest catalytic ability for catechol oxidation. Catechol oxidized to o-quinone on the surface of the biosensor. Amperometric measurement was performed at -0.1V, as shown in CV graphs, with reduction peak.

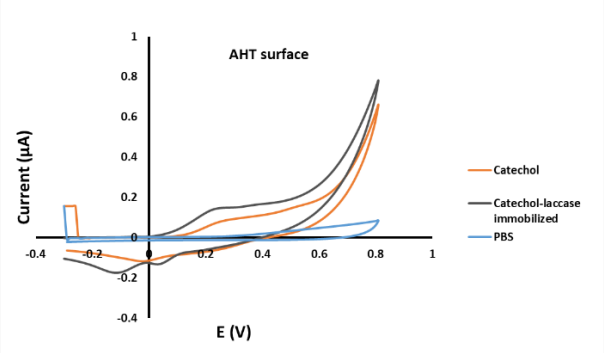

Figure 4. The cyclic voltammetry of laccase immobilized and non-immobilized gold electrode arrays (400 µM catechol solution and PBS at 100 mV/s scan rate).

In the catechol determination study, catechol was prepared in different concentrations (0.025-2.0 mM in PBS buffer solution) and amperometric measurement was performed on the laccase modified chips with the subsequent injection catechol (250 µL) with 50 µL/min fluid flow with a fixed potential of -0.1V. Amperometric signal was measured in real time, an increase in the catalytic current was observed. The initial current is a background measurement taken by injection of PBS solution. Then, as the catechol solution flowed through the sensor, a change in the current was observed by the reaction between the bound enzyme laccase and the catechol on the chip surface (Figure 5) and the subtraction between the current obtained during catechol and buffer was used as sensor response.

The amperometric response of the assay was calculated the maximum current obtained 150 s after the catechol injection was used as the sensor response. The catalytic current proportional increased on increasing the concentration of catechol in the range from 0.025 mM to 0.8 mM with a correlation coefficient of R^2 0.91 and LOD of 0.015 mM (Figure 6).

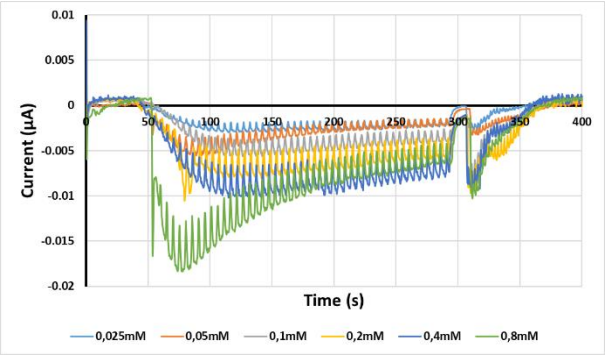

Figure 5. The raw data of the real-time responses of current vs time with respect to catechol concentrations against -0.1V potential.

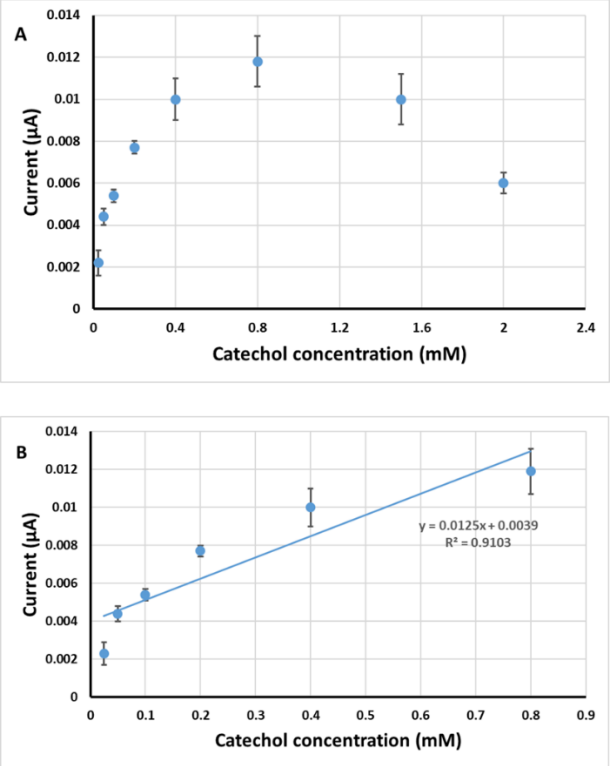

Figure 6. Calibration curve (A) and linear calibration curve (B) for the catechol detection assay.

Phenolic compounds are widely used in the production processes of paints, pesticides, surfactants, resins and plastics in the petroleum and pharmaceutical industries. As a result, they pose a danger to the surrounding water resources. Because these compounds have toxic effects on plants, animals and human health. Catechols (1,2-dihydroxy benzene; catechol), one of these phenolics are used in the industrial synthesis of rubbers, paints, plastics and in the pharmaceutical and cosmetic fields. For these reasons, the determination of catechol is important using biosensors.

In the literature, there is no study on laccase immobilization and catechol detection studies on 6-amino-1-hexanethiol (AHT) surface in microfluidic system, the other studies were carried out in static medium. Protein immobilization step after sensor surface modification with AHT takes approximately 30 minutes on the sensor device however, these steps are carried out in conventional assays times for hours. In the literature, the conventional phenolic detection assays in require long incubation times for the chemicals and protein immobilization [22-25, 30, 31], whereas during microfluidic flow in the biosensor system the mass transfer effects are minimized and a rapid reaction occurs. Another importance of this study is that all experiments are carried out in a microfluidic system. In amperometric biosensors, electron transfer process is a major issue that will occur at the electrode surface and the redox center within the enzyme is provided by the most suitable electron transfer way. Transfer problem occurs when amperometric measurement method is used in static environment [32,33]. The automated electrochemical biosensor with a microfluidic and automatic injection system was useful tools due to their sensitivity and fast response. Laccase immobilization and catechol detection steps were carried out quickly and enabled easy modification of electrode surface with using glutaraldehyde in a short period of time.

4. Conclusion

In this work, it was developed a novel sensor surface modified with 6-amino-1-hexanethiol on gold electrode which could detection of catechol. It was formed self-assembled monolayer on gold electrode via 6-amino-1-hexanethiol and then the laccase was immobilized with glutaraldehyde. All the experiments were carried out first time using automated biosensor device, during microfluidic flow. Cyclic voltammetry and amperometry activity assays showed that the detection of catechol with laccase modified gold surface. This could lead to further studies for developing of high performance biosensors for the specific detection of catechol and other phenolic compounds based on lacccase immobilized surfaces.

Acknowledgement

The author would like to thanks the Gebze Technical University (GTU) for the provided financial support (Grant no: BAP 2018-A105-23). We gratefully acknowledge to Dr. Yıldız Uludag and Dr. Aylin Ersoy from BILGEM-TUBITAK for their contribution to the fabrication of the biochip and the sensing platform.

Ethics

There are no ethical issues after the publication of this manuscript.

References

1. Khan, R, Dey, NC, Hazarika, AK, Saini, KK, Dhayal, M. 2011. Mycotoxin detection on antibody-immobilized conducting polymer-supported electrochemically polymerized acacia gum. *Analytical Biochemistry*; 410: 2,185-190.

2. Cai, H, Cao, X N, Jiang, Y, He, P G, Fang, Y Z. 2003. Carbon nanotube-enhanced electrochemical DNA biosensor for DNA hybridization detection. *Analytical and Bioanalytical Chemistry*; 375: 287-293.

3. Li, Y, Liu, X, Lin, Z. 2012. Recent developments and applications of surface plasmon resonance biosensors for the detection of mycotoxins in foodstuffs. *Food Chemistry*. 132: 1549-1554.

4. Trietsch, SJ, Hankemeier, T, Linden, HJ. 2011. Lab-on-a-chip technologies for massive parallel data generation in the life sciences: A review. *Chemometrics and Intelligent Laboratory Systems*; 108: 64-75.

5. Chang, HS, Choo, KH, Lee, B, Choi, SJ. 2009. The methods of identification analysis, and removal of endocrine disrupting compounds (EDCs) in water. *Journal of Hazardous Materials*; 172: 1–12.

6. Sungur S, Koroglu M, Ozkan A. 2014. Determinatıon of bisphenol A migrating from canned food and beverages in markets. *Food Chemistry*; 142: 87-91.

7. Tepe HD. 2019. Qualitative Analysis of Alfalfa Seed Methanol Extract by GC-MS and Determination of Antioxidant Properties. Celal Bayar University Journal of Science; 15:2, 175-180.

8. Diaconu M, Litescu SC, Radu GL. 2010 Laccase–MWCNT–chitosan biosensor – A new tool for total polyphenolic content evaluation from in vitro cultivated plants. *Sensors and Actuators B Chemical;* 145: 800–806.

9. Roy JJ, Abraham TE, Abhijith KS, Kumar PVS, Thakur MS. 2005. Biosensor for the determination of phenols based on cross-linked enzyme crystals (CLEC) of laccase. *Biosensors Bioelectronics.* 21: 206–211.

10. Chawla S, Rawal R, Kumar D, Pundir CS. 2012. Amperometric determination of total phenolic content in wine by laccase immobilized onto silver nanoparticles/zinc oxide nanoparticles modified gold electrode. *Analytical Biochemistry*; 430:16–23.

11. Chawla S, Rawal R, Pundir CS. 2011 Fabrication of polyphenol biosensor based on laccase immobilized on copper nanoparticles /chitosan/multiwalled carbon nanotubes/polyaniline-modified gold electrode. *Journal of Biotechnology*; 156: 39–45.

12. Quan D, Kim Y, Shin W. 2004 Sensing characteristics of tyrosinase immobilized and tyrosinase, laccase co-immobilized platinum electrodes. *Bulletin Korean Chemical Society*; 25: 1195–1201.

13. Leite OD, Fatibello-filho O, Barbosa ADM. 2003. Determination of catecholamines in pharmaceutical formulations using a biosensor modified with a crude extract of fungi laccase (*Pleurotus ostreatus*). *Journal of Brazilian Chemical Society;* 14: 297–303.

14. Wilkołazka AJ, Ruzgas T, Gorton L. 2005. Amperometric detection of mono and diphenols at Cerrena unicolor laccase-

modified graphite electrode: correlation between sensitivity and substrate structure. *Talanta*; 66: 1219–1224.

15. Haghighi B, Gorton L, Ruzgas T, Jonsson LJ. 2003. Characterization of graphite electrodes modified with laccase from Trametes versicolor and their use for bioelectrochemical monitoring of phenolic compounds in flow injection analysis. *Analytical Chim. Acta*; 487: 3–14.

16. Litescu SC, Eremia SAV, Bertoli A, Pistelli L, Radu GL. 2010. Laccase-nafion based biosensor for the determination of polyphenolic secondary metabolites. *Analytical Letters*; 43: 1089–1099.

17. Timur S, Pazarlıoğlu N, Pilloton R, Telefoncu A. 2004. Thick film sensors based on laccases from different sources immobilized in polyaniline matrix. *Sensors Actuators B Chemical;* 97: 132–136.

18. Escutia IP, Gomez JJ, Calas-Blanchard C, Marty JL, Ramirez-Silva M.T. 2010. Amperometric biosensor based on a high resolution photopolymer deposited onto a screen-printed electrode for phenolic compounds monitoring in tea infusions. *Talanta;* 81:1636–1642.

19. Montereali MR, Della Seta L, Vastarella W, Pilloton R. 2010. A disposable Laccase– Tyrosinase based biosensor for amperometric detection of phenolic compounds in must and wine. *Journal of Molecular Catalysis B Enzymatic*; 64: 189–194.

20. Li D, Luo L, Pang Z, Ding L, Wang Q, Ke H, et al. 2014. Novel phenolic biosensor based on a magnetic polydopamine-laccase-nickel nanoparticle loaded carbon nano fiber composite. *ACS Applied Materials Interfaces*; 6: (7) 5144–5151.

21. Oliveira TMBF, Fatima Barroso M, Morais S, de Lima-Neto P, Correia AN, Oliveira MBPP, et al. 2013. Biosensor based on multi-walled carbon nanotubes paste electrode modified with laccase for pirimicarb pesticide quantification. *Talanta*; 106: 137–143.

22. Rahman A, Noh H, Shim Y. 2008. Direct electrochemistry of laccase immobilized on Au nanoparticles encapsulated-dendrimer bonded conducting polymer: application for a catechin sensor. *Analytical Chemistry*; 80: 8020–8027.

23. Rawal R, Chawla, Devender S, Pundir C.S. 2012. An amperometric biosensor based on laccase immobilized onto Fe3O4NPs/cMWCNT/PANI/Au electrode for determination of phenolic content in tea leaves extract. *Enzyme and Microbial Technology*; 51: 179–185.

24. Vianello F, Cambria A, Ragusa S, Cambria MT, Zennaro L, Rigo A. 2004. A high sensitivity amperometric biosensor using a monomolecular layer of laccase as biorecognition element. *Biosensors and Bioelectronics*; 20: 315–321.

25. Wan J, Si Y, Li C, Zhang K. 2016. Bisphenol A electrochemical sensor based on multiwalled carbon nanotubes/polythiophene/Pt nanocomposites modified electrode. *Analytical Methods*; 8: 3333-3338.

26. Ölçer, Z, Esen, E, Muhammad, T, Ersoy, A, Budak, S, Uludag, Y. 2014. Fast and sensitive detection of mycotoxins in wheat using microfluidics based Real-timeElectrochemical Profiling. *Biosensensors and Bioelectronics*; 62:163–169.

27. Ölcer, Z, Esen, E, Ersoy, A, Budak, S, Kaya, DS, Gök, MY, Barut, S, Üstek, D, Uludag, Y. 2015. Microfluidics and nanoparticles based amperometric biosensor for the detection of cyanobacteria (Planktothrix agardhii NIVA-CYA 116) DNA. *Biosensors and Bioelectronics*; 70: 426-432.

28. Uludag, Y, Olcer, Z, Sagiroglu, MS. 2014. Design and characterisation of thin-film electrode array with shared reference/counter electrodes for electrochemical detection. *Biosensors and Bioelectronics*; 57: 85-90.

29. Chidsey, CED, Loiacono, DN. 1990. Chemical Functionality in Self -Assembled Monolayers: Structural and Electrochemical Properties. *Langmuir;* 6: 682-691.

30. Basmaz, G, Öztürk, N. 2017. Determination of Curcumin in Turmeric Sample Using Edge Plane Pyrolytic Graphite Electrode. Celal Bayar University Journal of Science; 13:3, 689-694.

31. Koçak, ÇC. 2019. Vanillin Determination in Food Products with Pd Nanoparticles Modified Poly(Methylene Blue) Film Electrode. Celal Bayar University Journal of Science; 15:2, 211-215.

32. Bange, A, Halsall, HB, Heineman, WR. 2005. Microfluidic immunosensor systems. Review, *Biosensors & Bioelectronics*; 20: 2488-2503.

33. Habermüller, K, Mosbach, M, Schuhmann, W. 2000. Electron-transfer mechanisms in amperometric biosensors Review. *Fresenius Journal of Analytical Chemistry*; 366: 560-568.

Celal Bayar University Journal of Science

Liquefaction Potential Analysis and Mapping of Alluvium Soil: A Case Study in Nazilli-Aydın (West Turkey)

Hayrullah Yürekli[1], Öznur Karaca[2]*

[1]10. Regional Directorate of State Hydraulic Works, Diyarbakır, Turkey
[2]Canakkale Onsekiz Mart University, Department of Geological Engineering, Canakkale, Turkey
*oznurkaraca@comu.edu.tr

Received: 30 July 2019
Accepted: 17 March 2020
DOI: 10.18466/cbayarfbe.598529

Abstract

The importance of urban planning for sustainable cities is indispensable. For this, the preparation of geotechnical maps, especially, comes to the agenda. Liquefaction susceptibility mapping is important for towns located in first-degree earthquake regions. This study investigated the susceptibility to liquefaction in a possible earthquake in Nazilli (Aydın) county considering geologic and geotechnical studies. In line with this, firstly drilling was completed at 110 points, with experiments performed on location and geotechnical properties determined in soil samples taken during this process. Generally, the county is founded on alluvial soils with groundwater very close to the surface. This situation makes it important to determine the liquefaction status of the town during a possible earthquake. The liquefaction potential (FS) of the study area was determined with the simplified SPT based method and additionally the liquefaction potential index (LPI) was calculated. Using this data and an ArcGIS program, the FS and LPI maps of the study area were prepared. According to the results obtained, the majority of the study area has very high liquefaction potential index.

Keywords: Nazilli, Standard Penetration Test, liquefaction potential, liquefaction potential index.

1. Introduction

For sustainable cities, it is necessary to perform good urban planning and to prepare geotechnical maps. One of the most important geotechnical maps to be prepared for cities located in first-degree earthquake regions, especially, are liquefaction susceptibility maps. Liquefaction events due to earthquakes are recorded in many places around the world [1-10]. Damages during earthquakes and liquefaction also show the importance of structure-soil interaction [11-12].

A sand deposit saturated with loose water displays a tendency to compress and reduce in volume when exposed to ground shaking. If drainage of water is not possible, the reduction in volume causes an increase in cavity hydraulic pressure. If this increase in cavity hydraulic pressure reaches a point equal to vertical stress, effective stress becomes zero and the sand deposit completely loses shear strength. In this situation, liquefaction develops [2].

The first thing required for soil liquefaction analysis is to determine whether the soil profile contains layers that may liquefy. It is long known that clean sands have the potential to liquefy. With the aim of determining soil conditions that may lead to potential liquefaction, the soil conditions are investigated in the field and field and laboratory experiments are performed.

Liquefaction potential analyses and the detailed maps prepared using them have vital importance, especially for regions susceptible to liquefaction. Just as these types of studies may reduce the risks due to liquefaction in these areas, they may reduce or prevent damage that will occur during a possible earthquake. A range of field and laboratory experiments may be performed to determine liquefaction potential. Experiments in the filed include standard penetration test (SPT), seismic refraction, multi analysis surface wave (MASW), (Vs) and conic penetration test (CPT). Laboratory experiments include dynamic simple shear, dynamic three-axis and shaking table. Various liquefaction analyses methods were applied to determine the liquefaction potential of different areas by various researchers [5, 13-17].

Seed and Idriss [1] proposed an analysis method based on SPT data, called as he simplified method, with the aim of determining the liquefaction potential after the

Alaska and Niigata earthquakes in 1964. Additionally, Tokimatsu and Yoshimi [18] recommended a method based on SPT data again. The method of Seed and Idriss [1] was modified several times in the following years [19, 4, 20, 21]. The method was debated for the last time at international earthquake geotechnical engineering symposia and was updated by Youd et al. [8] to reach its final form.

The study area of Nazilli is a county linked to the province of Aydın located in southwest Turkey. Nazilli is located in a first-degree earthquake region. Significant earthquakes have occurred in Nazilli in the historical and instrumental periods.

The main aim of this study is to contribute to organized and sustainable urban planning in light of geologic and geotechnical data. The liquefaction case forms a danger especially for cities located in first-degree earthquake zones. In line with this, within the scope of the study, the liquefaction susceptibility of Nazilli county due to probable earthquakes was investigated.

This study firstly prepared the geological map of the study area based on previous studies. The engineering characteristics of soils in the study area were determined with field and laboratory studies. With the data obtained, the liquefaction potential and liquefaction potential index for Nazilli county were determined and maps were prepared using GIS. The liquefaction susceptibility of Nazilli, located in a first-degree earthquake zone, was not previously determined with these methods. Within the scope of the study, the safety factor against liquefaction (FS) was determined using the simplified approach proposed by Youd et al. [8] using corrected SPT data. Within this framework, the SPT data obtained from drilling in different locations were used. Additionally, with the aim of determining the physical and mechanical features of samples obtained during drilling, laboratory experiments were completed. Groundwater levels were measured in the drilled wells.

2. Materials and Methods

2.1. Liquefaction assessment

The liquefaction assessment for an area can be performed using laboratory tests or in situ tests and empirical methods. The method depending on SPT N value developed by Seed and Idriss [1, 2] and Seed et al. [19, 4] was used in this study to evaluate the liquefaction susceptibility of the Nazilli settlement area. This method developed by Seed and Idriss [1] is based on the relationship between cyclic stress ratio (CSR), necessary for liquefaction to form, and standard penetration test (SPT). CSR is defined as the effective confining pressure ratio of mean earthquake-linked shear stress affecting soil in an earthquake (Equation 1) [1].

$$CSR = 0.65 \frac{a_{max}\sigma_v}{g\sigma'_v} r_d \quad \textbf{(2.1)}$$

Here, r_d is the stress reduction factor calculated in Equation 2 and 3 according to Liao and Whitman [22] and a_{max} is the peak ground acceleration. In first-degree earthquake regions, it is recommended to be taken as 0.4 g by the Disaster and Emergency Management Presidency (AFAD). Within the scope of this study, the a_{max} value was accepted as 0.4 g during liquefaction analyses.

$$r_d = 1\text{-}0{,}00765z \ (z \leq 9.15m) \quad \textbf{(2.2)}$$

$$r_d = 1.174 - 0{,}0267z \ (9.15 \leq z \leq 23\,m) \quad \textbf{(2.3)}$$

Another component of cycle resistance ratio (CRR) is defined as the capacity to resist liquefaction [8]. CRR used in liquefaction potential analyses represents the resistance of a soil to liquefaction (Equation 4). CRR is generally associated with the modified SPT impact number. The CRR of soil also affects the oscillation time and is associated with the magnitude scaling factor (MSF). As a result, for an earthquake with magnitude Mw=7.5, CRR was expressed as follows by Youd et al. [8].

$$\mathrm{CRR}_{7.5} = \frac{1}{34 - (\mathrm{N}_1)_{60}} + \frac{(\mathrm{N}_1)_{60}}{135} + \frac{50}{[10(\mathrm{N}_1)_{60} + 45]^2} - \frac{1}{200} \quad \textbf{(2.4)}$$

Here, σ'_v is effective vertical stress. The $(N_1)_{60}$ expression used in this formula is the SPT-N value obtained in the field and corrected according to some standard systems. These corrections were performed according to Robertson and Wride [5] and are calculated with Equation 2.5.

$$(N_1)_{60} = N_{field} C_N C_R C_B C_E C_S \quad \textbf{(2.5)}$$

N_{field} in the Equation (2.5) is the number of SPT impacts measured in the field. CE, CR and CS are correction coefficients within the scope of the study of the energy correction factor for reliable hammer types CE=0.75 (Donut type of hammer and 2 turns of rope release mechanism was used in this study.), the rod length correction factor (CR) of 0.75, 0.85, 0.95 and 1.00 according to length and the linear correction factor taken as CS =1.0 for standard sampling. The bore-hole diameter correction factor was taken as CB =1.0.

CN, correction factor based on the effective stress is calculated according to Equation 2.6 developed by Liao and Whitman [22].

$$C_N = \sqrt{\frac{P_a}{\sigma'_v}} \quad \textbf{(2.6)}$$

If $(N1)_{60}$ values of silty and sandy soils were greater than 30, they were accepted as non-liquefiable soil by Youd et al. [8] and Seed et al. [9].

Hence, the liquefaction factor of safety (FS) is found by comparing the earthquake loading with the liquefaction resistance (Equation 2.7). If the factor of safety is larger than 1, liquefaction resistance is larger than earthquake loading and liquefaction is not expected in this situation.

$$FS = (CRR_{7.5}/CSR)MSF \quad \textbf{(2.7)}$$

CRR curves state whether liquefaction will occur only in situations with magnitude 7.5, so it is necessary to mention the magnitude scaling factor (MSF). MSF was calculated according to Youd et al. [8] using Equation 2.8. For this study a possible earthquake scenario was considered at a magnitude (Mw) of 6.9.

$$MSF = \frac{10^{2.24}}{M_w^{2.56}} \quad \textbf{(2.8)}$$

If the FS value is larger than 1 at the end of calculations, soil is accepted as not being liquefiable. In situations where FS is smaller than 1, soil is expected to liquefy. However, value of "1" in the limit-balance situation is not a good marker. As a result, in situations with FS between 1 and 1.2, soils are classified as marginally liquefiable and values of FS>1.2 are accepted as not liquefy [1, 25]. However, Seed and Idriss [2] (1982) stated that the acceptable safety factor ranged from 1.25 to 1.5. Considering these types of uncertainties in the safety factor, it can be said this remains a theoretical value. In reality, liquefaction potential is linked to the thickness of the liquefiable soil layers and the depth from the surface. As a result, the liquefaction potential of a region may be determined by finding the liquefaction risk index (Ls) of a soil profile using the factor of safety and soil layer thicknesses. Iwasaki et al. [3] proposed the liquefaction potential index (LPI) to remove this type of limitation from FS. LPI is evaluated in four categories of very low, low, high and very high. However, there are some limitations to this classification. These include the lack of determination of "non-liquefiable" and "moderate" categories in the liquefaction potential index (LPI). As a result, Sonmez [26] made a new proposal by adding these two categories to the classification (Equation 2.9). Here, the FS=1.2 threshold value is determined to be the lowest limit where liquefaction will not occur [2].

$$LPI = \int_0^{20} FS(z)w(z)dz \quad \textbf{(2.9)}$$

Here, FS is the liquefaction factor of safety, z is the depth of the central point of the soil layer investigated and w is the liquefaction potential reduction factor linked to depth from the surface. W is taken from Equation 10-11.

$$z < 20\ m\ \ w(z)=10-0.5z \quad \textbf{(2.10)}$$

$$z \geq 20\ m\ \ w(z)=0 \quad \textbf{(2.11)}$$

$$F_S < 1.0;\ F(z)=1-F_S \quad \textbf{(2.12)}$$

$$F_S \geq 1.0;\ F(z)=0 \quad \textbf{(2.13)}$$

The liquefaction potential index (LPI) with boundary value of LPI modified from Sonmez [26] is tabulated in Table 1 with liquefaction susceptibility descriptions. In this LPI calculation, Sonmez [26] modified F(z) (Equation 14-16).

$$F(z) = 0 \quad \text{for } F_S \geq 1.2 \quad \textbf{(2.14)}$$

$$F(z) = 2\times10^6 e^{-18.427F_S} \quad \text{for } 1.2 > F_S < 0.95 \quad \textbf{(2.15)}$$

$$F(z) = 1 - F_S \quad \text{for } F_S < 0.95 \quad \textbf{(2.16)}$$

Table 1. Modified liquefaction potential index classification [26]

Liquefaction potential index (LPI)	Description
0	Non-liquefiable (based on FS ≥ 1.2)
0<LPI≤2	Low
2< LPI ≤5	Moderate
5≤ LPI ≤15	High
15< LPI	Very high

3. Results and Discussion

3.1. Study area and geological setting

The study area is Nazilli county settlement area in Aydın province, located in southwest Turkey. The study site covers an area of about 644 km^2. The population of Nazilli was 156,748 in 2019.

The basement in the study area is the Plio-Quaternary Asartepe Formation (Tpa) comprising poorly consolidated and low strength conglomerate, sandstone, siltstone, claystone and marl alternations. The formation has fine-medium bedding and occasionally massive appearance. The clasts in the conglomerate have block and coarse clast size and appear to be a debris flow.

Clasts were derived from rocks from the Menderes metamorphics. The Asartepe formation was first mapped by Ercan et al. [27] in the Uşak region. Later it was reported from the north side of the Büyük Menderes Graben by Sözbilir and Emre [28].

Above the Asartepe formation there are Quaternary terrace sediments comprising coarse pebbles, sand and clay units (Qt); Quaternary alluvial fan sediments comprising loose coarse pebbles, sand, silt and clay units (Qaly); and Holocene floodplain-swamp sediments from the Menderes River comprising loose, water-saturated fine sand, silt and clay units (Qtb) (Figure 1) [29].

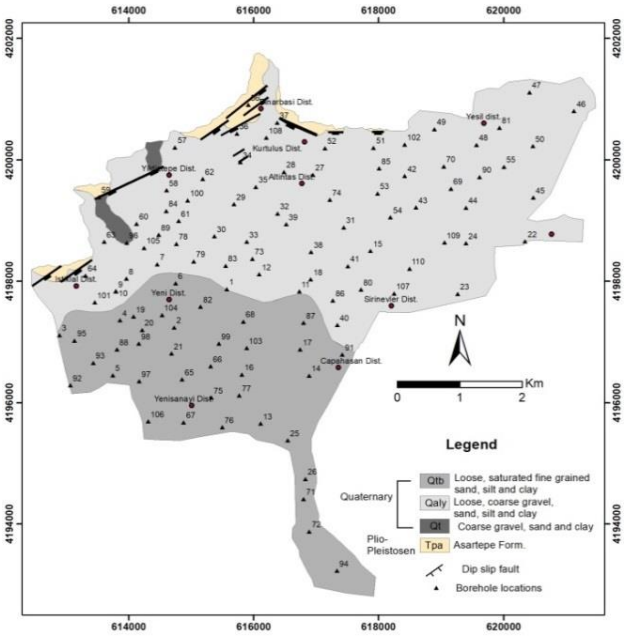

Figure 1. Geological and borehole location map of Nazilli settlement area

3.2. Seismotectonics of the study area

Turkey is located in one of the most seismically active regions on the earth. The study area of Nazilli is located in a first-degree earthquake region according to Turkey's earthquake hazard map.

The Aegean Graben System, encompassing the study area of Nazilli and surroundings, is generally formed by many blocks bounded by E-W striking normal faults [30]. Nazilli is located on the Great Menderes River in Western Anatolia within the Büyük Menderes Graben, an E-W striking depression area between Denizli in the east and Ortaklar in the west [31]. The Büyük Menderes Graben is one of the main active neotectonic structures found in Western Anatolia [32]. In the Büyük Menderes graben, two fault sets with N-S and E-W strike have developed since the Miocene (Figure 2) [33]. The N-S striking faults are found between Nazilli in the north, Kuyucak in the west and Atça-Kılavuzlar. The lengths of these faults observed at the surface vary from 3-5 km. These faults probably continue under alluvium from Nazilli. The second fault set with E-W strike forms steps within the Büyük Menderes graben and are south-dipping normal faults [33] (Figure 2).

According to Ergin et al. [34], the 20 September 1899 earthquake developed between Aydın-Nazilli and was felt throughout the whole of Western Anatolia. The estimated magnitude of the earthquake is IX [34-38]. The 20 September 1899 Menderes earthquake was one of the most destructive events to occur in the Büyük Menderes graben in the last 100 years [32]. Ambraseys and Finkel [37] stated that a 70 km long surface rupture developed between Aydın and Nazilli with a 3-meter offset. Figure 4 shows some photographs taken in Nazilli after the earthquake.

The Aydın-Nazilli fault begins 1 km west of Yılmaz village in the east of Aydın province and continues to 2.5 km west of İmamköy. The fault zone separates alluvium from the Asartepe formation and has 3-5 m fault scarps [33].

Active main fault segments well-defined in Nazilli and surroundings are the Nazilli, Arslanlı, Kuyucak, Yöre, Kurtuluş, Gencelli, Feslek, Çavdardüzü and Ortakçı segments, from west to east. The activity of these faults is not just based on morphotectonic criteria, earthquakes have occurred historically (25 or 26 B·C., 23 February 1653 A.D., and 20 September 1899 A.D. Menderes valley earthquakes with intensity IX) [32, 37, 39, 40, 41] and in recent periods (4 May 1966 Incirliova, 11 October 1986 Çubukdağ earthquakes) due to the main fault segments in the Kuyucak fault zone [41]. Some photos from the 1899 Aydın-Denizli earthquake were shown in Figure 3.

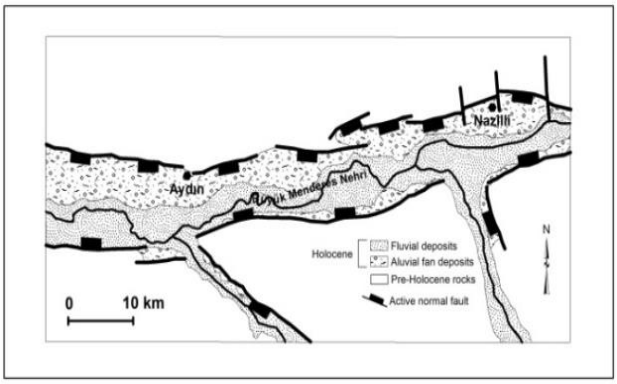

Figure 2. Map showing variation in active fault-controlled facies of sedimentary fill developing in the Holocene in the Büyük Menderes graben [42, 43, 33]

Figure 3. Some images from the 1899 Aydın-Denizli earthquake; a) Nazilli Yahyaoğlu street, b) Nazilli Factory Forbes [44]

3.3. Field studies and geotechnical evaluation

This study chose Nazilli town centre as the research area. Three important parameters are required for liquefaction research. These are soil conditions, water in the environment and seismic characteristics. SPT data have an important place in liquefaction analyses. With the aim of determining changes in the units in the study area in horizontal and vertical directions, engineering properties and geotechnical parameters, 110 boreholes were drilled with depths from 11 m to 25 m. As seen in Figure 2, drillings have very equal distribution within the study area. The horizontal distances of the drillings change from 200 mto 500 m. Bore holes were drilled by Erdem Earth Sciences (Fethiye) with the aim of preparing a geotechnical report for Nazilli town centre. During drilling, groundwater measurements were made. The groundwater level in the study area varied from 1 m to 18 m below the surface (Figure 4). Considering the depth from the surface of groundwater on this map, it is expected that a probable earthquake will cause liquefaction in the majority of Nazilli settlement area.

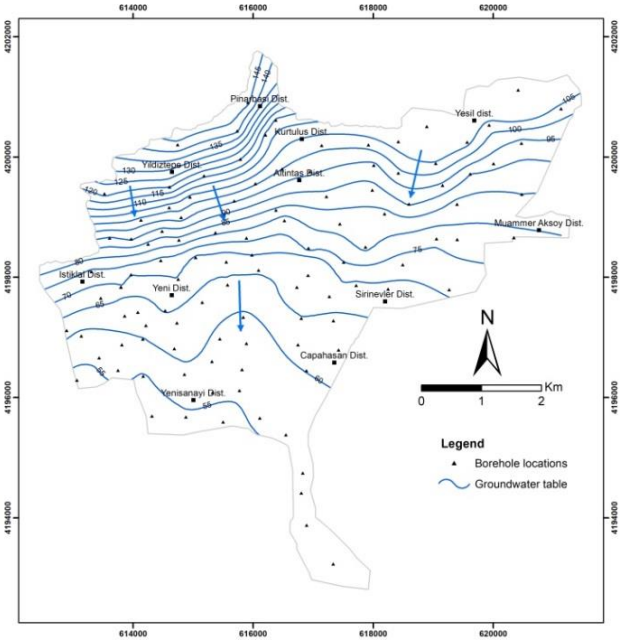

Figure 4. Groundwater table map of the study area

During drilling standard penetration test (SPT) were performed every 1.5 m (ASTM D1586-99). The main rock in the study area is the Asartepe formation comprising dark brown-light yellow mudstone, conglomerate and sandstone intercalations covering small areas in northern sections. In other sections, Quaternary deposits (Qt, Qaly, Qtb) are present (Figure 1). SPTs were performed in all units in the study area (Figure 1). Quaternary alluvial fan sediments and Holocene floodplain-swamp sediments covering large sections of the study area had SPT-N values varying from 2 to 12. The Plio-Quaternary Asartepe Formation found in very limited areas in the north and the Quaternary terrace sediments found along Hamalı stream have values from 12 to 50+. SPT-based zoning map for 9 m were given in Figure 5. Based on this map most part of the city has low SPT-N value (<10) and this supports the results of the liquefaction analysis.
With the aim of determining index properties of the soil samples, disturbed and undisturbed samples were taken from 110 boreholes and laboratory experiments were completed. These were natural moisture content, unit weight, grain size distribution (sieve and hydrometer analysis), and Atterberg limits.

The water content of soils in the study area vary from 11%-28% while unit weight values vary from 18.0-20.0 kN/m^3 but general distribution is 18.0 kN/m^3. The soils taken from boreholes were classified based on “The Unified Soil Classification System (USCS)”. The Quaternary alluvial terrace and fan sediments in the study area were ML, GW, SC-SM, SW and CL group soils, while Holocene flood-swamp sediments were CL, ML and SW group soils. General distribution of the fine contents of the soils in the study area ranges between

13-15%. In Figure 6, depth to groundwater table was given with soil types for 9 m. Therefore, it is easier to see the liquefiable areas for the city. But liquefaction potential (FS) and liquefaction potential index (LPI) maps were prepared considering the depths during 20 m for each boreholes.

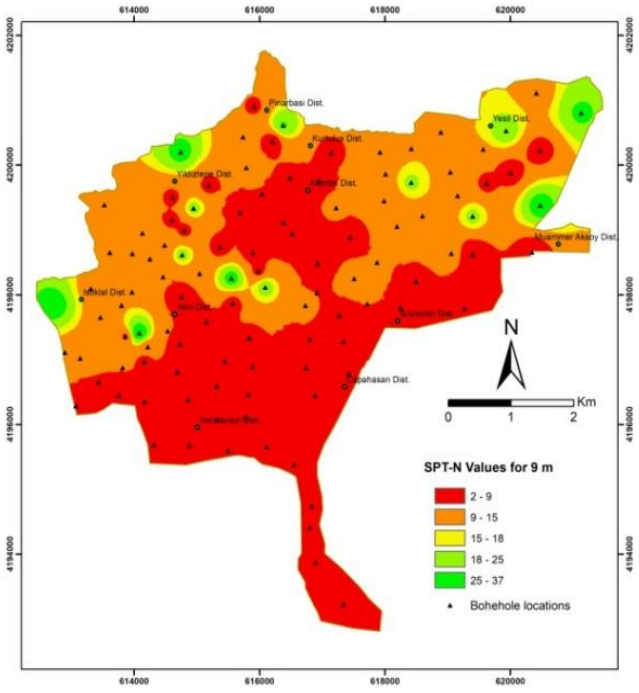

Figure 5. SPT-N zoning map for 9 m

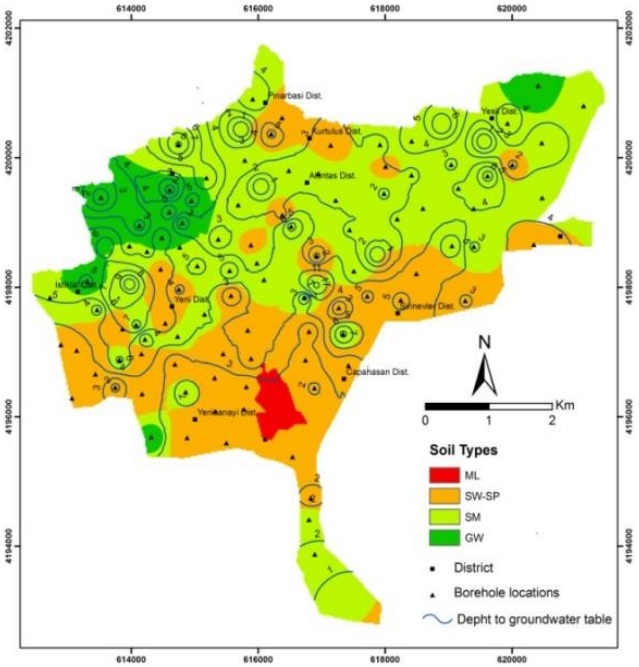

Figure 6. Depth to groundwater and soil type zoning map for 9 m

3.4. Liquefaction potential map of Nazilli settlement area

Assessment of liquefaction potential is one of the critical topics in geotechnical earthquake engineering. At the same time, liquefaction resistance maps are important geotechnical maps and have a very important place in our ability to make good urban planning for sustainable cities. The most susceptible sediments for liquefaction are sediments deposited as a result of Holocene delta, fluvial, floodplain, terrace and coastal sedimentation processes. These types of soils are present in the whole of the study area. Considering the groundwater status in the study area, liquefaction analysis is indispensable in this region.
This study calculated the liquefaction potential of Nazilli settlement area according to Seed and Idriss [1], according to the simplified SPT based method proposed by Seed et al. [4] and based on the liquefaction potential index (LPI) modified by Sönmez [26].

The liquefaction potential indices were calculated for 110 drillholes and liquefaction hazard maps based on LPI were prepared using ArcGIS version 10. Maps prepared according to FS and LPI values are given in Figures 7 and 8, respectively. As seen in both figures, nearly all of Nazilli settlement area has liquefaction potential in a possible earthquake. If the LPI categories in the city are examined, very high liquefaction potential is present for a large area of Nazilli in a probable earthquake. Yesil neighbourhood in the NE of the county has high liquefaction potential index.

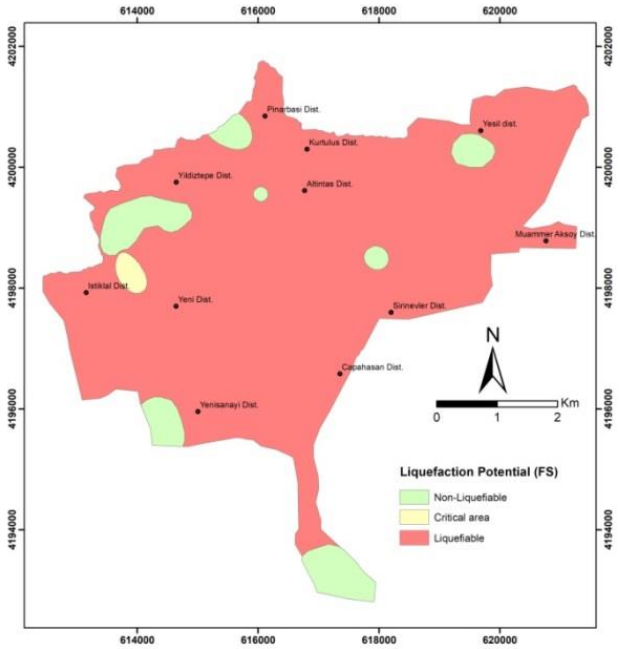

Figure 7. Liquefaction potential (FS) map

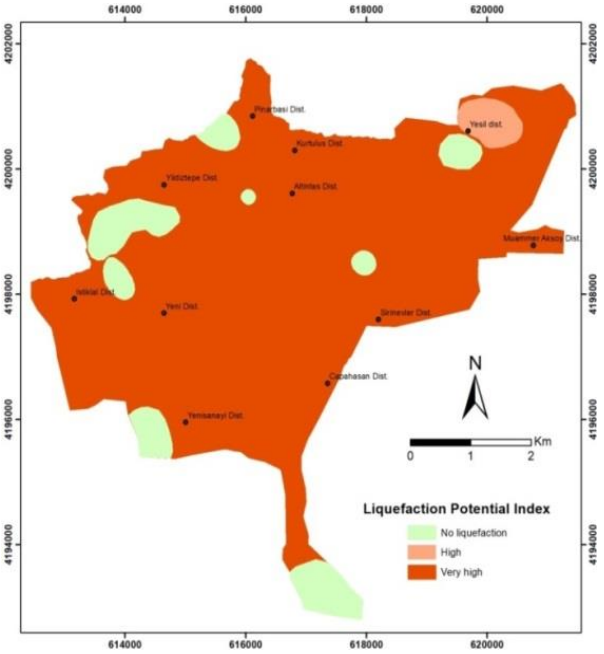

Figure 8. Liquefaction potential index (LPI) map

4. Conclusion

In towns founded on alluvium, especially, the earthquake-soil-building interaction comes to the agenda and these types of areas should be carefully investigated for liquefaction cases. Considering these facts, urban planning should be made carefully and geotechnical maps need to be noted during the planning process.

Nazilli settlement area is located on two different soil types. Both of these are loose and water-saturated soils included in the liquefaction susceptible soil class. The groundwater depth in the study area varied from 1 m to 18 m. As a result, due to the geological, hydrogeological and tectonic properties of Nazilli county, it is at risk of liquefaction during probable strong ground movements. Liquefaction susceptibility maps were prepared for Nazilli settlement area with the scenario magnitude 6.9 (Mw) for subsurface geological materials and horizontal peak ground acceleration of 0.4 g. These were the "liquefaction potential" maps based on results from analyses with the method recommended by Youd et al. [8] and the "liquefaction potential index" map modified by Sonmez [26]. Both maps provide very similar results and it was identified that a large section of Nazilli had conditions susceptible to liquefaction in a possible earthquake.

The results obtained in this study and the liquefaction susceptibility maps comprise very beneficial base maps for urban and regional planning in Nazilli. In this situation, care should be taken of the geotechnical features of liquefiable soils during appropriate foundation design for buildings planned in the study area to prevent loss of life and property during a possible earthquake.

Acknowledgement

This study was produced from a master thesis with the title 'Geological and Geotechnical Investigation of Soil in Nazilli City Center and Near Surroundings', and it was supported by Çanakkale Onsekiz Mart University Scientific Research Coordination Unit with project no. 2010/165. The authors also would like to thank Erdem Earth Sciences (Fethiye) for their supports.

Author's Contributions

Hayrullah Yürekli: Performed the field studies and experiments, prepared the maps.

Öznur Karaca: Drafted and wrote the manuscript, supervised the experiment's progress and preparing the maps, result interpretation and analysis.

Ethics

There are no ethical issues after the publication of this manuscript.

References

1. Seed, HB, Idriss IM. 1971. Simplified procedure for evaluating soil liquefaction potential. *Journal of the Soil Mechanics and Foundations Division ASCE*, 107(SM9) 1249-1274.

2. Seed, HB, Idriss, IM. Ground motions and soil liquefaction during earthquakes. Earthquake Engineering Research Institute, Berkeley, CA, 1982; pp 134.

3. Iwasaki, T, Tokida, K, Tatsuoka, F, Watanabe, S, Yasuda, S, Sato, H. Microzonation for soil liquefaction potential using simplified methods. In: Proceedings of the 3rd International Conference on Microzonation, Seattle 3, 1982, 1319-1330.

4. Seed, HB, Tokimatsu, K, Harder, LF, Chung, RM. 1985. Influence of SPT procedures in soil liquefaction resistance evaluations. *J Geotech Eng*, 111(12), 1425-1445.

5. Robertson, PK, Wride, CE. 1998. Evaluating cyclic liquefaction potential using the cone penetration test. *Can Geotech J*, 35(3):442–459.

6. Ulusay, R, Aydan, O, Kumsar, H, Sonmez, H. 2000. Engineering geological characteristics of the 1998 Adana-Ceyhan earthquake, with particular emphasis on liquefaction phenomena and the role of soil behaviour. *Bull Eng Geol Env*, 59:99-118.

7. Youd, TL, Idriss, IM. 2001. Liquefaction resistance of soils: summary report from the 1996 NCEER and 1998 NCEER/NSF workshops on evaluation of liquefaction resistance of soils. *Journal of Geotechnical and Geoenvironmental Engineering*, Vol. 127, No. 4, April, 2001.

8. Youd, TL, Idriss, IM, Andrus, RD, Arango, I, Castro, G, Christian, JT, Dobry, R, Finn, WDL, Harder, LF, Hynes, ME, Ishihara, K, Koester, JP, Liao, SSC, Marcuson, III WF, Martin, GR, Mitchell, JK, Moriwaki, Y, Power, MS, Robertson PK, Seed, RB, Stokoe, II KH. 2001. Liquefaction resistance of soils: summary report from the 1996 NCEER and 1998 NCEER/NSF

workshops on evaluation of liquefaction resistance of soils. *J Geotech and Geoenviron Eng*, 817–833.

9. Seed, RB, Cetin, KO, Moss, RES, Kammerer, AM, Wu, J, Pestana, JM, Riemer, MF, Sancio, RB, Bray, JD, Kayen, RE, Faris, A. 2003. Recent advances in soil liquefaction engineering: a unified and consistent framework. EERC Report No. 2003-06.

10. Cox, BR, Boulanger, RW, Tokimatsu, K, Wood, CM, Abe, A, Ashford S, Donahue J, Ishihara K, Kayen R, Katsumata K, Kishida, T, Kokusho, T, Mason, H.B, Moss, R, Stewart, JP, Tohyama, K, Zekkos, D. Liquefaction at strong motion stations and in Urayasu City during the 2011 Tohoku-Oki Earthquake. Earthquake Spectra, March 2013, Vol. 29, No. S1, pp S55-S80.

11. Korkmaz, KA, Çarhoğlu AI, Usta, P, Gedik, YH. 2013. Tokat Yağıbasan medrese yapısının deprem riskinin değerlendirilmesi. C.B.U. Journal of Science, 8(2): 43 –51.

12. Gürbüz, A, Tekin, M. 2015. Performans sıralaması yöntemiyle mevcut binaların bölgesel deprem risk dağılımının belirlenmesi. C.B.U. Journal of Science, 11(1): 37-48.

13. Yilmaz, I, Bagci, A. 2006. Soil liquefaction susceptibility and hazard mapping in the residential area of Kütahya (Turkey). *Environ Geol*, 49:708–719.

14. Uyanık O. 2006. An Aproach for cyclic stress ratio of liquefied or unliquefied soils. *DEU Faculty of Engineering, Journal of Science and Engineering*, 8(2), 79-91.

15. Uyanık O and Taktak AG. 2009. A new method for liquefaction analysis from shear wave velocity and predominant resonance period. *Süleyman Demirel University, Journal of Science and Engineering*, 13(1),74-81.

16. Uyanık, O, Ekinci, B, Uyanık, A. 2013. Liquefaction analysis from seismic velocities and determination of lagoon limits Kumluca/Antalya example. *Journal of Applied Geophysics*, 95, 90–103.

17. Tunusluoglu, MC, Karaca, O. 2018. Liquefaction severity mapping based on SPT data: a case study in Canakkale city (NW Turkey). *Environmental Earth Sciences*, 77:422.

18. Tokimatsu, K, Yoshimi, Y. 1983. Empirical correlation of soil liquefaction based on SPT-N Value and Fines Content. *Soil and Foundations*, 23: (4), 56-74.

19. Seed, HB, Idriss, IM, Arango I (1983) Evaluation of liquefaction potential using filed performance data. ASCE *J Geotech Geoenviron Eng*, 109(3):458–482.

20. Seed, HB, De, Alba P. Use of SPT and CPT tests for evaluating the liquefaction resistance of soils. Proceedings of the specialty conference on the use of in situ tests ingeotechnical engineering ASCE, Blacksburg Virginia, 1986, Special Publication No. 6.

21. Seed. HB, Harder, LF. SPT-Based analysis of cyclic pressure generation and undrained residual strength. Proceedings of H. Bolton Seed Memorial Symposium, BiTech Publishers Ltd., 1990, 351–376.

22. Liao, SSC, Whitman, RV. 1986. Overburden correction factors for SPT in sand. *J Geotech Eng Div ASCE*, 112(3):373–377.

23. Tosun, H, Ulusay, R. 1997. Engineering geological characterization and evaluation of liquefaction susceptibility of foundation soils at a dam site, southwest Turkey. *Environ Eng Geosci*, 3(3):389–409.

24. Ulusay, R, Kuru, T. 2004. 1998 Adana-Ceyhan (Turkey) earthquake and a preliminary microzonation based on liquefaction potential for Ceyhan town. *Nat Hazards*, 32:59–88.

25. Duman, ES, İkizler, SB. 2014. Assessment of liquefaction potential of Erzincan Province and its vicinity, Turkey. *Nat Hazards*, 73:1863–1887.

26. Sonmez, H. 2003. Modification of the liquefaction potential index and liquefaction susceptibility mapping for a liquefaction-prone area (Inegol, Turkey). *Environ. Geol.*, 44 (7), 862–871.

27. Ercan, T, Dinçel, A, Metin, M, Türkecan, A, Güney, E. 1978. Geology of Neogene basins in Uşak region. *Geological Society of Turkey Bulletin*, 21, 97–106 (in Turkish with English abstract).

28. Sözbilir, H, Emre, T. 1990. Neogene stratigraphy and structure of the northern rim of the Büyük Menderes Graben. *International Earth Sciences Congress on Aegean Regions, Proceedings*, II, 314–322.

29. Yavuz, MA. 2010. Aydın İli, Nazilli ilçesi yerleşim alanının uygulama imar planına esas jeolojik-jeoteknik etüt raporu. Erdem Yerbilimleri. Fethiye.

30. Demirtaş R. and Yılmaz R., 1996. Türkiye'nin sismotektoniği. T.C. Bayındırlık ve İskân Bakanlığı, Ankara, 91.

31. Şaroğlu F., Emre Ö. and Boray A., 1987. Turkey's active faults and seismicity. MTA Report No: 8174.

32. Altunel E., 1999. Geological and geomorphological observations in relation to the 20 September 1999 Menderes Earthquake, Western Turkey. Journal of the Geological Society, 156: 241-246.

33. Utku, M, Sözbilir, H. 2003. Aydın-Nazilli fayının paleosismolojik ön bulguları, Türkiye Kuvaterneri Çalıştayı-IV, Bildiriler Kitapçığı, Makaleler, s. 120-128, 29-30 Mayıs 2003, İstanbul.

34. Ergin, K, Güçlü U, Uz Z. 1967. Türkiye ve civarının deprem kataloğu (Milattan sonra 11 yılından 1964 sonuna kadar). *İstanbul Teknik Üniversitesi Maden Fakültesi, Arz Fiziği Enstitüsü Yayınları,* No:24.

35. İlhan, E. 1971. Earthquakes in Turkey. In: Campbell, A.S.(ed.) Geology and History of Turkey. Petroleum Exploration Society of Libya, 431-442.

36. Sipahioğlu, S. 1979. Büyük Menderes alçalımı ile Menderes Masifi yükseliminin sınırını oluşturan kuşağa uygulanan bir deprem öncesi çalışma. *Deprem Araştırma Enstitüsü Bülteni;* 25, 5-27.

37. Ambraseys, NN, Finkel, CF. 1987. Seismicity of Turkey and neighbouring regions, 1899-1915. *Annales Geophysicae;* 5B, 701-726.

38. KOERI, http://www.koeri.boun.edu.tr/sismo/Depremler/thistoric.htm (accessed at 10.07.2019).

39. Eyidoğan, H, Utku, Z, Güçlü, U, Değirmenci, E. Türkiye büyük depremleri makro sismik rehberi (1900-1988). İTÜ. Maden Fak., Jeofizik Müh. Bölümü Yayınları, İstanbul, 1991; pp 198.

40. Ocakoğlu, F, Açıkalın, S, Güneş, G, Özkes, S, Dirik, K, Özsayın, E. 2013. Was the 1899 Menderes Valley Earthquake a double earthquake? Historical and paleosismological constraints. *Journal of Asian Earth Sciences;* 67–68, 187–198.

41. Koçyiğit, A. 2015. An overview on the main stratigraphic and structural features of a geothermal area: the case of Nazilli-Buharkent section of the Büyük Menderes Graben, SW Turkey, *Geodinamica Acta;* 27:2-3, 85-109.

42. Paton, S. 1992. Active normal faulting, drainage patterns and sedimentation in southwestern Turkey. *Journal of the Geological Society, London;* 149, 1031-1044.

43. Hakyemez, YH, Erkal, T, Göktaş, F. 1999. Late Quaternary evolution of the Gediz and Büyük Menderes grabens, Western Anatolia, Turkey. *Quaternary Science Reviews;* 18, 549-554.

44. Atar, Z. 2013. The 1899 Earthquake of Aydın-Denizli with photos. *Journal of Modern Turkish History Studies*; XIII/27 (2013- Autumn), 5-32.

Celal Bayar University Journal of Science

Design of an Automatic Item Pick-up System for Unmanned Aerial Vehicles

M. Emin Mumcuoğlu[1], Ilgaz Yüksel[1] and Erdinç Altuğ[1]*

[1] İstanbul Technical University, Department of Mechanical Engineering, İnönü Cad. No:65, Beyoğlu, İstanbul.
*altuger@itu.edu.tr

Received: 21 February 2019
Accepted: 17 March 2020
DOI: 10.18466/cbayarfbe.529996

Abstract

The interest of Unmanned Aerial Vehicles (UAVs) for the purpose of package delivery has increased significantly in recent years. However, the abilities of those vehicles are quite limited since the arms have not being designed considering the UAV geometry and the center of gravity (CG) changes. Usual approach taken by various researchers were to use a regular gripper or a robotic manipulator, which is not quite satisfactory for access. In this paper, a novel arm mechanism has been proposed to access objects near and under the UAV without risking any collision, with little rotor wash on objects and little change of UAV CG while enabling grip of variable shaped objects. The mechanism is based on a double four-bar linkage. Moreover, the gripper and the mechanism enable access to objects from locations below as well as next to UAV. With the help of the onboard controller and camera, the arm acts as an independent entity to identify the position of the part, catch it, and autonomously hold it. It is also possible to carry more than one object within the storage area. A flexible three-finger gripper has been designed to hold several different geometric shaped objects. The proposed arm and gripper designed, manufactured and installed on a UAV. Initial tests verify that it can identify and catch spherical, cylindrical, and box shaped pieces weighting up to 650 grams.

Keywords: Robotics arm design for UAV, Flexible Gripper, Four-bar mechanism.

1. Introduction

Unmanned aerial vehicles (UAVs), also known as drones, are among one of the most interesting research topic in the robotic field since last decade. These are aerial vehicles that can be operated remotely or can work autonomously. Nowadays they are being used for civilian, military and scientifically domains, for aerial photo shootings, agricultural tasks, drone races, commercial tasks, as well as just for fun. Non-military drone sales reach above 3 million in 2017 [1]. Quadrotors UAVs are the most popular subclass of UAVs. Thanks to their relatively simple mechanism and abilities of vertical take-off and landing, as well as agile maneuvering and hovering, it is accepted as an ideal candidate for search and rescue [2], mapping [3] and exploration [4].

Even though they are popular in many applications, they lack interacting with environment and objects. In previous literature, robotic manipulators or grippers are installed on UAVs for manipulation. In [5], a deployable manipulation system with 2 degrees of freedom (DOF) developed for a helicopter and in [6] serial chain manipulator for a commercial quadrotor has been designed. Some research focused on increasing the limit of DOF and payload capacity [7]. Many of the designed manipulation mechanisms are connected to UAV from a single spot, which can easily cause undesired moment on the vehicle. Image-based control for aerial manipulation [8] is also relevant. UAVs are also used for disasters, such as the radiation monitoring in Fukushima, where nuclear leakage occurred in 2011 [9]. Picking and transporting objects could be valuable at these locations.

In the logistics sector, due to rapid urbanization, congestion and pollution increased, and logistics efficiency declined. A study conducted by Swiss Re predicts that the global urban population will increase by between 1.4 billion and 5 billion between 2011 and 2030. This trend will further increase delays in the flow of people and goods. In addition, research by McKinsey shows that e-commerce, has increased at an extraordinary level [10]. With all of this in mind, the widespread use of UAVs in the logistics industry can create great relief, especially within the city by taking a certain portion of the traffic from land to air (Fig. 1).

There are some prototypes of cargo carrying UAV systems of global cargo companies. Generally, objects are loaded to the UAV with a human or automatic system. UAVs with the ability to take parts from one place can only take one piece from the vertical direction. Moreover, if they have an arm, it is a general robotic manipulator designed for general robotic activities. It has not been designed by keeping in mind the UAV center of gravity change and accessibility.

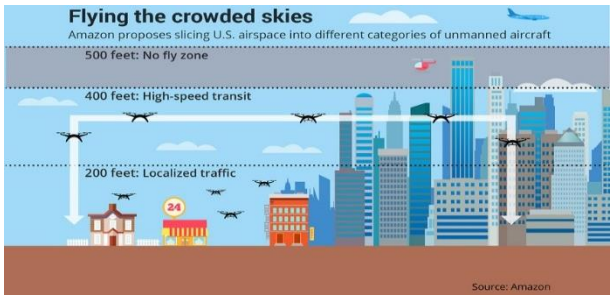

Figure 1. UAVs to be used for the logistics sector [11].

USA based e-commerce company, Amazon, launched a project in 2013 that target delivery of a product within 30 minutes of the customer's order placement [12]. After the ordered product is placed in the box, it will be brought under the storage area under the UAV system with the rail system and the vehicle will be released for delivery. Amazon Prime Air, produced by Amazon, has a maximum weight of 25 kg and a carrying capacity of 2.26 kg. Amazon Prime Air predicts delivery at an average of 80.5 km per hour to destinations within 16 km range. In this context, the first experiment successfully in Cambridge, England on December 7, 2016.

DHL, an international logistics company, aims to deliver cargo with Parcelcopter unmanned aerial vehicle. Cargo loading to Parcelcopter is done manually by an operator [13]. DHL Parcelcopter has a carrying capacity of 1.2 kg. It has a 12 km range and planned speed of 43 km/h.

"Matternet M2" unmanned aerial vehicle, developed by Matternet company in partnership with Mercedes, is planned to be inserted in cargo vehicles. Therefore, when the cargo vehicle goes to the nearest delivery area, the range and charge limitations of the UAV will no longer be limited. In this system, the product to be delivered is placed under the UAV by the automatic shelf system [14]. Matternet M2's box size is 19x11x13 cm with a maximum weight of 2 kg and the maximum weight of the UAV is 11.5 kg. It is able to deliver at a distance of up to 20 km from the place where it is located with a flight speed of 36 km/h.

Another international cargo company, UPS, has built its own unmanned aerial vehicle for product distribution. UAV named, as "UPS HorseFly" will be loaded by the operator into the cage below the UAV. UPS will also use commercial vehicles, such as those on Matternet M2, for cargo distribution [15]. UPS HorseFly's maximum speed is 80 km/h and the flight time is 30 minutes with a carrying capacity of 4.5 kg.

Unmanned aerial vehicle made by American-based Pepsi for commercial purposes has the ability to receive an object vertically [16]. This unmanned aerial vehicle, whose specifications are not shared, has designed to receive a ball.

Another important issue in design is the gripper. The ability to pick up objects other than standard boxes, such as spherical or cylindrical objects could be very useful. In literature, it has been seen that 3-finger holders provide a better grip on spherical objects than 2-finger systems.

The Robotiq Company [17] designed an articulated fingered gripper. The three fingers in Festo's product "Multichoice Gripper" are flexible, and provide a firm grip on different shaped objects [18]. Bosch's product "Apas Assistant" contains a 3-fingered holding system, which provides good grip on the cylindrical and box-shaped parts. In addition, hollow structures like cups or pipes can be hold [19]. In the patent "Gripper device for gripping objects" of FESTO Company in 2013, a spherical piece is held by a three-fingered mechanism [20].

Some researchers focus on vehicle routing side of delivery with drones [21, 22]. Some projects focused on UAV design and landing [23, 24].

In previous studies, UAVs are usually equipped with a simple robotic manipulators and simple grippers. It is quite easy to cause flight instabilities with a manipulator movement. This approach is not quite satisfactory since it changes the center of gravity of the vehicle, moreover does not enable easy access to objects near or under the UAV. In this paper, a novel mechanism for catching and holding variable shaped objects without considerable changing dynamic balance of the UAV, while enabling easy access to objects around it, has been proposed (Fig.2).

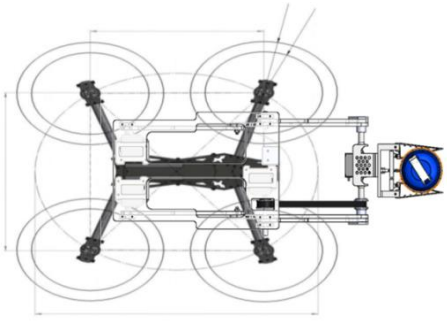

Figure 2. Top view of a robotic gripper and arm mechanism to be used on an UAV.

Since the object pick up and drop tasks require hovering, the type of UAV to be integrated in this paper was considered as a multi-rotor, quadrotor UAV.

The developed mechanism consisting of four-bar linkages mounted on the UAV and work cooperatively to avoid obnoxious moves. It will determine the location of an object by using image-processing techniques and will be capable of autonomously grasping multiple objects with different shapes. With this feature, the system can be easily used as a garbage collector (such as pet bottle, gum box) and keep it in its storage area. In addition, due to its ability to pick up objects it can be used in hard conditions/environments such as in a radiation environment that people cannot enter. The system also has a camera and on board vision processing to distinguish objects using QR or barcodes on them.

The mechanism designed in the project has the ability to receive objects from open shelves, such as the ones in pharmacies. The pick-up mechanism was designed to reach beyond the UAV propellers when it is going to make a horizontal pick up. It can also be used to pick up or deliver products to area under UAV, due to the rotating gripper mechanism.

The paper is organized as follows: Section 2 presents the design of the arm mechanism and adaptive gripper. In section 3, design of the mechanical and electronic of the arm, which can be implemented on a quadrotor, is described with applied computer vision method. Section 4 explains the autonomous grasp operation. In section 5 experiments are exhibited. Finally, in section 6 conclusions and future works are introduced.

2. Design of the Arm and the Adaptive Gripper

2.1. Design of the Arm Mechanism

The goal of the mechanism is to move the gripper to desired location in order to retrieve the object as needed. For indoor operation, a mini UAV is suitable, yet useful payload capacity of a mini UAV is very limited. Any additional weight not only limits useful payload capacity, but also useful flight time as well. Therefore, the arm mechanism has to be low weight, yet strong, and it should not move the center of gravity of the UAV beyond its stabilization limits. The load, which is at a considerable distance from the center of gravity of the drone during gripping, forces the vehicle to tilt, creating an additional torque to be balanced by the UAV. There are balancing systems on the drone against external factors such as wind, etc. However, designing the robotic gripper as physically balanced as possible will help those systems work properly. To limit CG and the torques due to the payload, the mechanism rests initially under the UAV. It moves forward when it needs to grasp an object. When it grasps an object, it carries it its initial position to limit its impact on UAV center of gravity.

For maneuverability and its ease of control, a mechanism consisting of four-bar linkages was selected. This approach is quite useful to extend and grasp the object and retrieve it towards to the center of the vehicle, therefore limit the center of gravity changes. The limits of the motion of the mechanism while it is holding an object is shown in Fig.3.

The other desired specification is the ability to grab the object even if there is some eccentricity in object location with respect to the UAV. To overcome this problem a mechanism consisting of two four-bar linkages was selected. With this design, the mechanism can grab objects with crosswise movements. The mechanism also enables slight yaw motions of the adaptive gripper to be placed at the end. In addition, a basket is put between the four bar linkages, enabling a secure storage area for multiple objects.

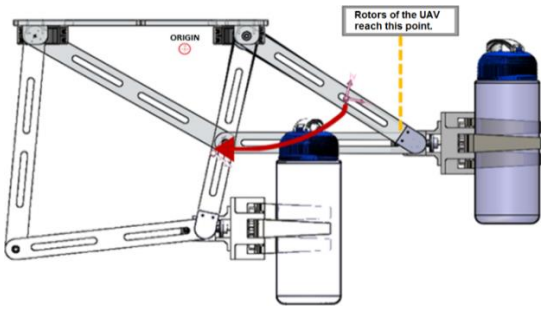

Figure 3. Motion limits of the mechanism

The target UAV's distance from its center to the tip of the rotors are 33 cm. The arm and the gripper should extend at least this far to grip and release any object. The selection of servomotors for the peak torque requirements, reachability analysis of the mechanism and cost were critical factors in design. Under strict torque requirements and weight limits, the size of the four-bar mechanisms were determined (Fig.4).

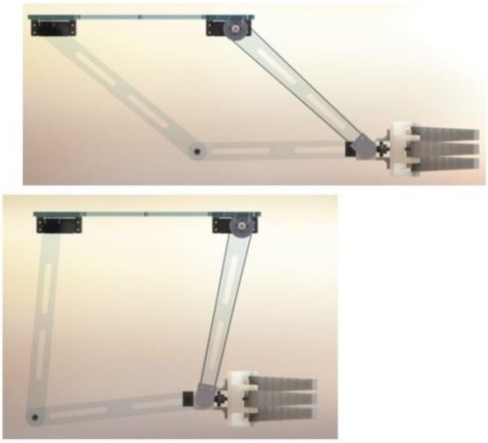

Figure 4. Mechanism at the position of grapping (up). Mechanism is at the position of balance (bottom).

2.2. Design of the Adaptive Gripper

The gripper is the most critical part of the system. It will grab objects horizontally as well as vertically. Various different shapes of objects e.g. spherical, cylindrical or rectangular shapes should be grasped. It should also hold this object safely, without dropping. The shape and size of some potential objects to be carried are listed in Table.1.

Table.1 : Shape and Size of objects to be carried.

Shape	Size
Medication box	5x7,5x10 cm
A small box	7x12,5x12,5 cm
Bottle	Diameter of 8 cm x 28 cm
Water Bottle	Diameter of 5~7,5 cm x10 cm
Apple	Diameter of 5 cm

Taking into the size, weight and reliability criteria into consideration, a three-fingered adaptive retention mechanism was developed. The fingers have a flexible structure that allows the object to take its shape during the gripping movement. A screw mechanism that works with a continuous servo motor gives it the ability to grip and release.

A mechanical force analysis can determine the maximum load capacity of the gripper (Fig.5). The PowerHD AR3606HB servomotor can take 6 volts and a maximum of 1.2 amps. As the servo is squeezing the part, it will apply 0.4151 Nm. The maximum torque (M) applied on the M5 screw of pitch p of 0,8 mm with 0.15 (μ_k) friction can be gripped up to 8 cm.

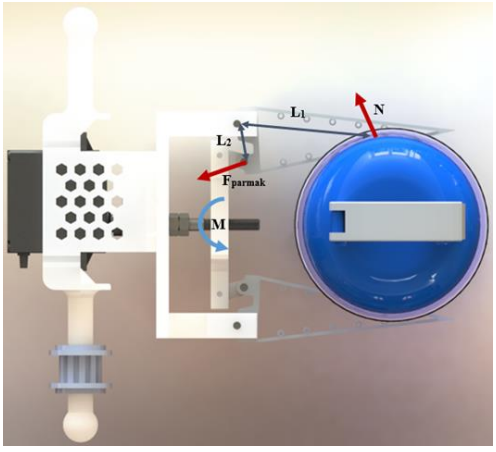

Figure 5. Design of the gripper rotater, and gripper moving systems.

Applied torque the gripper is;

$$T = F_{force}\left(\frac{d_2}{2}\tan(\varphi + p) + \mu_k \frac{d_k}{2}\right) \qquad \textbf{(2.1)}$$

where φ, p and d_k values are given as

$$\varphi = \tan^{-1}\frac{p}{\pi d} = 2.91°$$

$$p = \tan^{-1}\frac{\mu_k}{\cos\frac{\alpha}{2}} = 8.66°$$

$$d_k = 1.4d = 7mm.$$

The gripper force, F_{force}, can be calculated from Eqn.2.1 as 379.7 Newtons. The force per finger (F_{finger}) can be calculated by dividing this number to 3. The finger force determined to be 126,6 Newtons. The gripper's fingers are made of polyurethane (with a coefficient of friction 0.2). The friction force can be calculated with Eqn.2.2, where g is the gravitational acceleration.

$$F_{friction} = mgk \qquad \textbf{(2.2)}$$

In addition, there is a relation between finger force and friction force as

$$L_2 F_{friction} = 3L_1 F_{finger} \qquad \textbf{(2.3)}$$

where L_1 and L_2 are given in Fig.5.

Combining these two equations lead us to calculate the maximum object weight that can be gripped without slipping as 2.97 kg.

$$m = \frac{3L_1 F_{friction}}{L_2 gk} \qquad \textbf{(2.4)}$$

The designed system was produced with a 3D printer and mounted as shown in Fig.6.

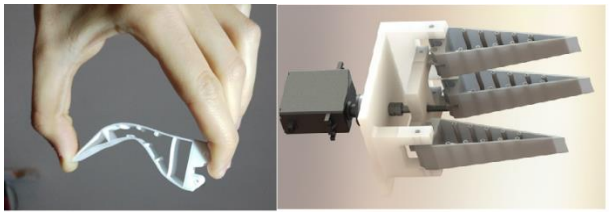

Figure 6. a) Flexible finger, b) Manufactured gripper with three fingers.

2.3. Design of the Belt-Pulley System

A belt-pulley system was developed to rotate and hold the gripper, if needed (see pulley located on lower left side on Figure 5). To determine the torque transferred from the servo to the smaller pulley, gear ratio and belt efficiency are considered. The weight of the object and the gripper should be balanced with the transferred torque (Eqn.2.5).

$$T_{SmallPulley} > m_{gripper} gL_1 + m_{object} gL_2 \qquad \textbf{(2.5)}$$

Under strict torque requirements and weight limits, the capacity of the gripper as well as the belt-pulley system

(to rotate the gripper) were designed (Fig.7). It was determined that for the particular choice of the servo mentioned previously, the upper limit of the weight of the object to be less than 746.63 grams. In addition, length of the belt for suitable operation is calculated.

Figure 7. Belt-pulley system.

One other issue to be investigated is the motion of the center of gravity (CG) as the manipulator grasps any object. Using SolidWorks program, CG location variation with respect to servo shaft angle are calculated (Table.2). It is verified that, for 700 grams of payload, the CG change is acceptable for the UAV.

Table.2: The center of gravity change.

Degree	x (mm.)	y (mm.)
30	203,8	-55,43
40	192,22	-64,29
50	171,19	-71,94
60	146,81	-78,03
70	119,81	-82,32
80	90,99	-84,61
90	61,2	-84,74

The mechanical design was finalized as presented in Fig.8.

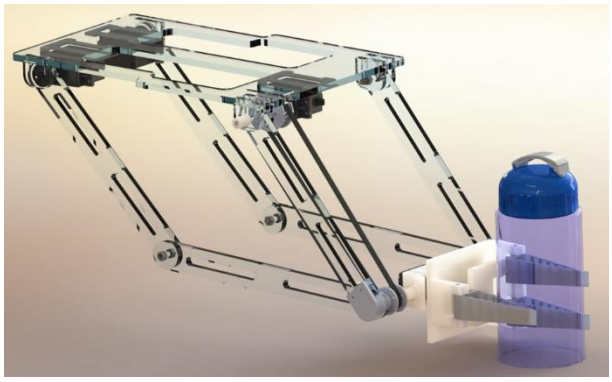

Figure 8. Final design of the mechanism.

Table 3 lists the materials and the weights of each component of the arm. Total designed weight of the arm, gripper and the electronics is 1013 grams. A mini-UAV that has a payload capacity of 2.5 kg can easily lift the mechanism and any object that weight up to 700 grams.

Assuming a 1 kg weight acting on the gripper, various analyses were made on ANSYS program (Fig.9) to determine the size, thickness, weight and strength of the mechanism. The four-bar mechanism and the shaft stress levels are calculated, and found to be low for failure. For the four-bar mechanism, the biggest stress appears at the connection points of the arm to the upper plate, as expected. The maximum stress determined to be 3.26 MPa is less than the stress limit of polycarbonate (63 MPa), which is the material choice for the arm. The safety factor, the ratio of the stress of the material to the calculated maximum stress value, is determined to be 19.2.

Table.3 : The weight of the materials.

Name	Quantity	Weight (g)
Finger	3	28,82
Gripper lower plate	1	61,99
Gripper connector	1	17,63
Shaft	1	41,63
Polycarbonate Bar	6	227.43
Upper plate	1	239,27
Pulley	1	11,21
Shaft-bar connection	2	13,21
Upper late connection	2	8,88
Servo Motor	4	160
Arduino	1	25
Raspberry Pi	1	45
Camera	1	15
Battery	1	88
Other Electronics	-	15
Other mechanical components	-	15
TOTAL		1013,11

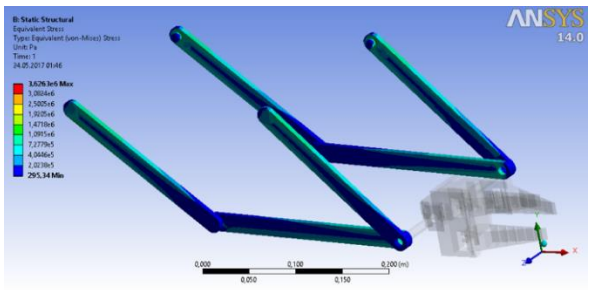

Figure 9. Design of the mechanism in ANSYS.

For the robotic gripper, the most critical part has been found as the gripper shaft. The maximum stress found to

be 12.9 MPa (Fig.10), appearing near the pulley. The shaft is made from ABS-M30, whose limit is 36 MPa. The safety factor was determined to be 2.79.

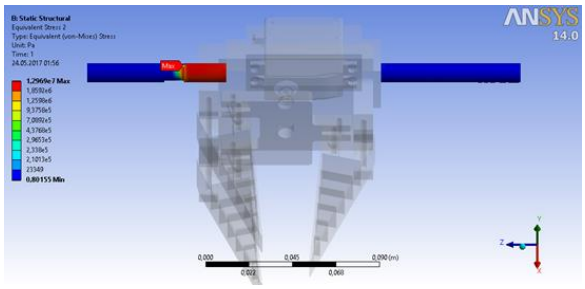

Figure 10. ANSYS analysis of the gripper.

Additional ANSYS analysis were made to verify that the servomotors could supply the required torque values as the arm and gripper are working. For the servomotors, the safety factor determined to be over 3.

2.4. Control of the Manipulator Arms and the Gripper

The manipulator and gripper control intentionally separated from the UAV control to build a self-sufficient system. This enabled an autonomous system that can easily installed to any UAV. The block diagram of the developed system is shown in Fig.11. When there is an object with the desired QR or barcode tag (within reach), the arm will approach to grasp it. The UAV will wait in hover mode during the reaching and grasping operation. The arm actuation is done with four DC servomotors. The position control of these motors were managed by the Arduino Uno card with the help of the data received from the image processing.

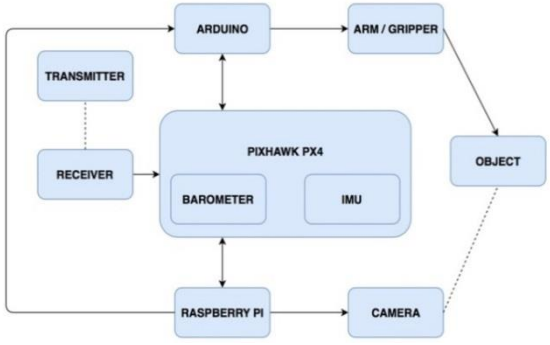

Figure 11. Block diagram of the autonomous grab ability of the robotic gripper system.

The power required by the system is provided by an 1150 mAh Lithium-ion polymer battery running at 11.1V. This type of batteries is preferred in the UAV operations due to the high energy density and efficiency. In addition, to reduce the 11.1 V battery output value to 6V, which is the operating voltage of the servomotors, LM2596 adjustable voltage regulator, which can carry up to 3 amperes, were used. In order to verify that an object was securely kept in the robot gripper, a current meter was used in the circuit. When the servomotor starts to compress object higher currents are observed. The controller monitors the current meter to prevent servomotor and/or object damage during grasping.

2.5. Vision-based Object Detection and Grabbing

The goal of the vision-based detection and grabbing system is to locate a label and then direct the arm to grab it, independent of the UAV system. This requires tag detection in a scene, and estimation of its relative distance to the camera. Object detection and segmentation is the most important and fundamental task of computer vision. Even though it is still an open problem due to the variety and complexity of object classes and backgrounds, there is an easy and in some application acceptable solution for this problem which is using color based methods to detect and segment an object from an image.

For an autonomous grasping of an object, a color based computer vision algorithm has been developed on RaspberryPi by using a fish-eye lens camera and OpenCV library. To simplify the object detection process a label attached to it (Fig.12). This can be a QR code, a barcode or a special colored tag. A camera is positioned on UAV looking towards the arm extension area. The captured image frames by this camera are converted into HSV, since it is easier to work in HSV color space rather than RGB. At last step, we apply threshold with predefined value to discriminate the label from everything else in the environment and apply some morphological operations and Gaussian filter to reduce noise and have smooth output. The edge detection methods are used to calculate the area of the label. With pre-known measures of label, the position and distance of the object can be determined. Eventually the location and distance of the object are obtained in the 3D space.

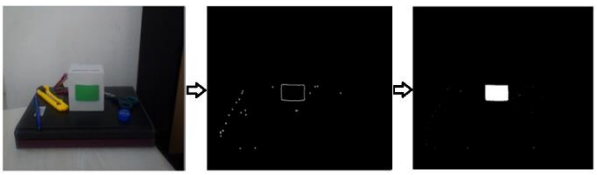

Figure 12. Vision-based object detection algorithm.

The distance (d) of the tag with respect to the camera is calculated from pixel data, and it is used to control the arm. Using this distance data, controller calculates suitable angle (α) of the mechanism to grasp the object (Fig.13), using Eqn.2.6.

$$\alpha = a\cos(1.73d^2 - 0.813) \qquad \textbf{(2.6)}$$

Celal Bayar University Journal of Science
Volume 16, Issue 1, 2020, p 25-33
Doi: 10.18466/cbayarfbe.529996

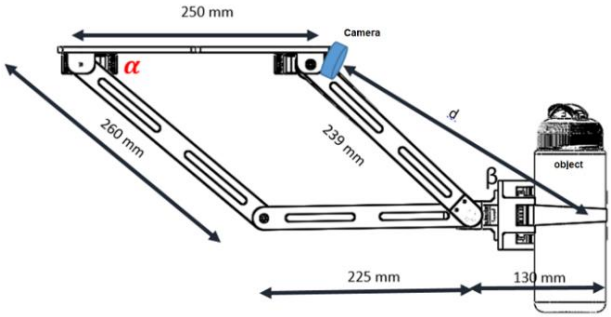

Figure 13. Geometry of the camera and the object on the UAV.

If the tag is at the center, the α angle for both of the four-bar mechanisms will be same. If the object is slightly off the center, α angle for both of the four-bar mechanisms should be different to compensate the offset of the tag, so that it can be grasped.

3. Object Detection and Gripping

The flow-chart of the operation of the system is shown in Fig.14.

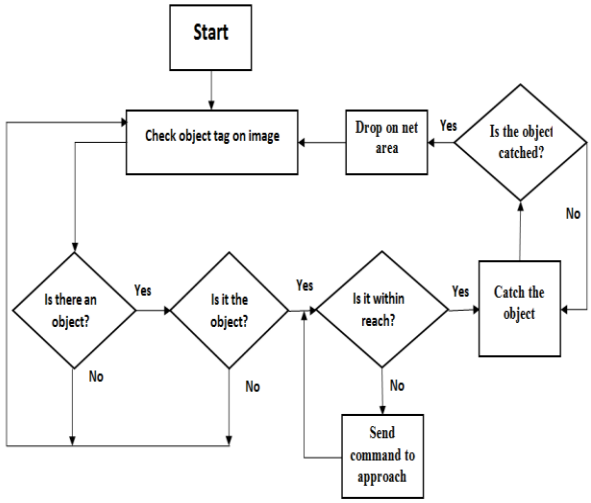

Figure 14. Flowchart of the object grapping approach.

In operation, quadrotor UAV adjusts its position autonomously until the object is within reach of gripping mechanism. The arm is expected to grab the stationary object itself, independent of the UAV system. The system equipped with Pixhawk flight control card which has an internal barometer that measures the aerial pressure and sensors output used by Pixhawk to switch altitude hold mode. RaspberryPi uses the MAVLink protocol over a serial connection to communicate with Pixhawk. The position data is sent to the Pixhawk from RaspberryPi to adjust horizontal alignment of UAV according to object and the distance between vehicle and object is sent to Arduino UNO, which initiates autonomous grasping by operating the arm. Then the four-bar linkage moves with the calculated angle that is directly related to the distance between the object and camera. After that, the adaptive gripper takes its position by belt and pulley mechanism. Gripper compresses the object until the current sensor in the gripper shows the critical current value, which means gripping process, is successful. Finally, the four-bar linkage turns into its initial balance position and release the object to basket. When the object is securely stored, the system is ready for another gripping. All these steps are coded with a locking system that avoids mechanism to skip processes without success.

4. Tests

The first step was to test the gripper's ability to grasp and hold various shaped and weighted objects. With its flexible fingers, the gripper can hold different objects firmly (Fig.15).

Figure 15. Object grasping test.

Table 4 presents grip test results, where it was observed if the UAV has enough payload carrying capacity, then the developed gripper mechanism can successfully grip and hold objects up to 650 grams.

Table 4: Designed gripper test results

Test Object No	Weight (grams)	Result
1	504	Successful
2	650	Successful
3	658	Unsuccessful

Second experiment was performed to test the ability to move the four-bar mechanism effectively to reach and grip objects.

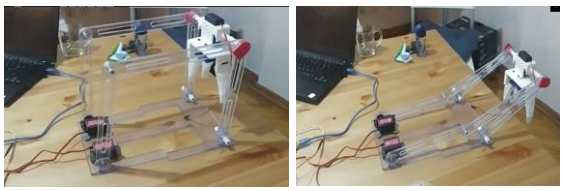

Figure 16. Mechanism motion tests.

Finally, vision algorithm implemented on RaspberryPi was tested. In this test, whole system approached to the stationary test object, and the objects label were identified by the camera. When the distance is within acceptable limit, the mechanism was activated to grip the object by first approaching it with the four bar mechanism, and then grip it until the gripper servo reached a limiting current value.

When all of the subsystems are determined to be functional as desired, the whole system was assembled and mounted on a mini UAV system (Fig.17).

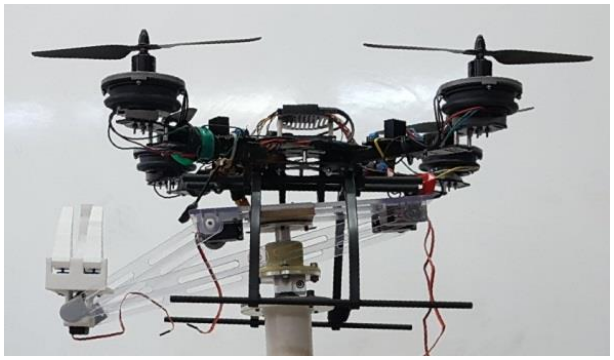

Figure 17. Manufactured mechanism, gripper and the electronic system installed on a UAV.

5. Conclusion

In this study, a self-sufficient, robotic arm with a gripper has been designed for UAV operations. Firstly, an adaptive flexible gripper is designed which can grasp various shaped objects. To improve grasping ability, inner surfaces of the retaining fingers were covered with a material with a higher coefficient of friction. It was seen that the system was quite successful in terms of strength with the analysis and observations made.

3D printer technology has been highly utilized to produce the ideal design. Especially the production of flexible gripper, this method was quite useful and easy. Embedded computer vision algorithm to determine object tag enabled the system to locate the object and grasp it if it is within reach, independent from the UAV controller.

This work assumed that the mechanism control and UAV control are two separate and distinct tasks. Combining the UAV control and arm control can improve grasping of objects considerably. The UAV controller and arm controller can communicate about the location of the target, grip status, as well as other data. Similarly, the arm dynamics can be integrated on the UAV controller, which can lead to a more stable flight.

During the pick-up from horizontal position, the center of gravity should not change too much to disrupt the UAV balance. Another future work could be to develop a platform that has the center of gravity shifting ability. This can be done by extending another arm towards the opposite side of the grasping arm to balance the moment.

Flight tests were outside the scope of this paper. Our future work will include testing the system during flight and gripping items firstly with remote control of the UAV, and then with autonomous operation of the UAV.

Acknowledgement

We would like to thank the Symmetrical Design for its support to the project. We also would like to thank Mr. Snyder, Eyüp Yüksel and Mr. Majid Mohammad Sadeghi for their support.

Author's Contributions

M. Emin Mumcuoğlu and Ilgaz Yüksel: Drafted and wrote the manuscript, performed the experiment and result analysis.

Erdinç Altuğ: Assisted in analytical analysis on the structure, supervised the experiment's progress, result interpretation and helped in manuscript preparation.

Ethics

There are no ethical issues after the publication of this manuscript.

References

1. Gartner Inc., Gartner says almost 3 million personal and commercial drones will be shipped in 2017. http://www.gartner.com/newsroom/id/3602317 (accessed at 3.5.2017).

2. Michael, N, Shen, S, Mohta, K, Mulgaonkar, Y, Kumar, V, Nagatani, K, Tadokoro, S. 2012. Collaborative mapping of an earthquake-damaged building via ground and aerial robots. *Journal of Field Robotics*; 29 (5): 832-841.

3. Ozaslan T, Shen, S. Mulgaonkar, Y, Michael, N, Kumar, V. Inspection of Penstocks and Featureless Tunnel-like Environments Using Micro UAVs. In: Mejias L, Corke P, Roberts J. (eds) Field and Service Robotics, Springer Tracts in Advanced Robotics, vol 105, pp 123-136.

4. Tomic T, Schmid, K, Lutz, P, Domel, A, Kassecker, M, Mair, E, Burschka, D. 2012. Toward a Fully Autonomous UAV: Research

Platform for Indoor and Outdoor Urban Search and Rescue. *IEEE Robotics & Automation Magazine*; 19 (3): 46-56.

5. Kucinski T. et al. Deployable Manipulator Technology with Application for UAVs. In: Sasiadek J (eds) Aerospace Robotics II. GeoPlanet: Earth and Planetary Sciences, Springer, Cham, 2015, pp 93-103.

6. Orsag, M, Korpela, C, Oh, P. 2013. Modeling and Control of MM-UAV: Mobile Manipulating Unmanned Aerial Vehicle. *J Intell Robot Syst*; 69: 227-240.

7. Fanni, M, Khalifa, A. 2017. A New 6-DOF Quadrotor Manipulation System: Design, Kinematics, Dynamics, and Control. IEEE/ASME Transactions on Mechatronics. Institute of Electrical and Electronics Engineers (IEEE). https://doi.org/10.1109/tmech.2017.2681179

8. Mebarki, R., & Lippiello, V. 2014. Image-Based Control for Aerial Manipulation. Asian Journal of Control. Wiley-Blackwell. https://doi.org/10.1002/asjc.887

9. International Atomic Energy. 2014. Monitoring radiation with drones. [Online]. [Accessed: 3 May 2017]. https://www.iaea.org/newscenter/multimedia/podcasts/monitoring-radiation-drones

10. Kuckelhaus, M. 2014. Microdrones in logistics. https://www.microdrones.com/en/applications/growth-markets/quadcopter-for-logistics/. [Online]. [Accessed: 3 May 2017].

11. Amazon Lays Out Plan for Drones to NavigateSkies. https://www.wsj.com/articles/amazon-lays-out-plan-for-drones-to-navigate\-skies-1438106902. [Online]. [Accessed: 9 December 2018].

12. Wikipedia. 2017. Amazon Prime Air. [Online]. [Accessed: 3 May 2017]. https://en.wikipedia.org/wiki/Amazon_Prime_Air

13. DHL. 2014. DHL Parcelcopter. [Online]. [Accessed: 14 February 2019]. https://discover.dhl.com/business/business-ethics/parcelcopter-drone-technology

14. Matternet. 2017. In action for public health:MatternetM2.[Online].[Accessed:3 May 2017].https://www.post.ch/-/media/post/ueber-uns/medienmitteilungen/2017/drohnen/spezifikationen-matternet-m2.pdf?la=en

15. Perez, S. 2017. 'UPS tests show delivery drones still need work'. [Online]. [Accessed: 3 May 2017]. https://techcrunch.com/2017/02/21/ups-tests-show-delivery-drones-still-need-work/

16. Macleod, D. 2015. Pepsi Max Drone Football. [Online]. [Accessed: 3 May 2017]. http://theinspirationroom.com/daily/2015/pepsi-max-drone-football/

17. Robotiq. 2017. Adaptive 2-finger robot gripper. [Online]. [Accessed: 3 May 2017]. http://robotiq.com/products/adaptive-robot-gripper/

18. FESTO, 2014. Multichoicegripper. https://www.festo.com/net/SupportPortal/Files/333986/Festo_MultiChoiceGripper_en.pdf [Online]. [Accessed: 3 May 2017].

19. BOSCH. 2017. APAS Asistant. [Online]. [Accessed: 3 May 2017]. http://www.bosch-apas.com/en/apas/produkte/assistant/apas_assistant_3.html

20. FESTO AG & CO KG. 2014. Gripper device for gripping objects. European Patent, No: EP2735408 (A1), 2014.

21. Dorling, Kevin, Jordan Heinrichs, Geoffrey G Messier, and Sebastian Magierowski. "Vehicle Routing Problems for Drone Delivery." IEEE Transactions on Systems, Man, and Cybernetics: Systems 47, no. 1 (2016): 70-85.

22. Scott, Judy, and Carlton Scott. "Drone Delivery Models for Healthcare." Paper presented at the Proceedings of the 50th Hawaii international conference on system sciences, 2017.

23. Köse O, and Oktay, T. "Non Simultaneous Morphing System Desing for Quadrotors," European Journal of Science and Technology , vol.16, pp.577-588, 2019

24. Ören, A, Koçyiğit, Y. "Unmanned Aerıal Vehicles Landing Sequencing Modelling Via Fuzzy Logic / İnsansız Hava Araçları İniş Sıralamasının Bulanık Mantık Modellemesi". Celal Bayar University Journal of Science, 12, 2016.

Celal Bayar University Journal of Science

Comparative Evaluation for PCA and ICA on Tongue-Machine Interface Using Glossokinetic Potential Responses

Kutlucan Gorur[1,*], M. Recep Bozkurt[2], M. Serdar Bascil[3], Feyzullah Temurtas[1]

[1]Department of Electrical and Electronics Engineering, Bandirma Onyedi Eylul University, 10200 Balikesir, Turkey
[2] Department of Electrical and Electronics Engineering, Sakarya University, 54187 Sakarya, Turkey
[3]Department of Electrical and Electronics Engineering, Yozgat Bozok University, 66200 Yozgat, Turkey
[*]kutlucan.gorur@yobu.edu.tr

Received: 30 May 2019
Accepted: 17 March 2020
DOI: 10.18466/cbayarfbe.571994

Abstract

The tongue-machine interface (TMI) between the paralyzed person and computer makes it possible to manage assistive technologies. Severely disabled individuals caused by traumatic brain and spinal cord injuries need continuous help to carry out everyday routines. The cranial nerve is arisen directly from the brain to connect the tongue that is one of the last affected organs in neuromuscular disorders. Besides, the tongue has highly capable of mobility located in the oral cavity, which also provides cosmetic advantages. These crucial skills make the tongue to be an odd organ employed in the human-machine interfaces. In this study, it was aimed to investigate 1-D extraction and develop a novel tongue-machine interface using the glossokinetic potential responses (GKPs). This rarely used bio-signs are occurred by contacting the buccal walls with the tip of the tongue in the oral cavity. Our study, named as GKP-based TMI measuring the glossokinetic potential responses over the scalp, may serve paralyzed persons an unobtrusive, natural, and reliable communication channel. In this work, 8 males and 2 females, aged between 22-34 naive healthy subjects, have participated. Linear discriminant analysis and support vector machine were implemented with mean-absolute value and power spectral density feature extraction process. Moreover, independent component analysis (ICA) and principal component analysis (PCA) were used to evaluate the reduced dimension of the data set for GKPs in machine learning algorithms. Furthermore, the highest result was obtained at 97.03%.

Keywords: Assistive Technologies, Glossokinetic Potential Responses, Independent Component, Analysis, Principal Component Analysis, Tongue-Machine Interface

1. Introduction

Assistive technologies (AT) are crucial to helping disabled persons with their intentions to evolve the quality of life. Individuals with spinal cord injury (SCI), locked-in syndrome (LIS), and other impairments of the degenerative neuromuscular disorders require self-supported possibilities to be able tasks in performing daily needs without another person's continuous help [1]. There are so many ongoing research on a kind of electroencephalography (EEG)-based brain-computer interfaces (BCI) developed for paralyzed persons. Other systems such as head and eye trackers demand high concentration and visual dependence. Then these systems may result in neck pains. However, tongue-operated methods are convenient because they are almost invisible and manageable. Moreover, the tongue is characterized as a good manipulator for assistive devices, including sophisticated motor control [2]. The hypoglossal cranial nerve is the bridge between the brain and tongue, which has the ability direct communication channel at a relatively low distance from the brain.

Furthermore, the tongue can not be damaged easily and named as the last affected organ in spinal cord injuries. Another advantage of using the tongue in ATs is that this organ has complex muscle groups and is not exhausted due to the less sensed effort [3-5]. Besides, the oral cavity is a very sensitive area compared to other body parts. Oral structures perform a cortex mapping similar to hand size. In contrast, the whole body and lower limbs of the body have a relatively small mapping in the somatic sensory cortex. Otherwise, some mouth structures such as the tongue are more delicate than the fingertip according to the psychophysical papers about the strength of discrimination and sensitivity [6]. For this reason, it appears that tongue can yield encouraging

performances for a human-machine interface (HMI) compared to other body parts, depending on the cortex brain mapping [7-8].

Glossokinetic potentials are electrical responses, which occur when the tongue touches the tissues in the mouth, especially the buccal walls. The tip of the tongue possesses a negative electric charge compared to the tongue root; therefore, when the tongue touches the tissues, it causes decreasing of potential levels near the contact surface. Hence analyzing the spatial pattern of GKP responses can be used to trace the tongue movements inside the mouth. GKPs originate in the noncerebral region, therefore interfering with the alpha/beta frequencies obtained from mental activities is very low. Because delta (1-3 Hz) and theta (4-7 Hz) waves occur in the low bands of frequencies [3-5]. In conventional synchronous brain-computer interfaces, the nonstationary EEG signals have inherent problems. These are the loss of control (LoC) and degrees of freedom (DoF) [9]. Besides, the major disadvantages of synchronous BCIs are shown as high cognitive workload and long training duration [10]. At this point, GKP and tongue might serve to give solutions without so much effort due to voluntary intuitive movements.

Recently, tongue-operated assistive technologies have been proposed in the literature. Few of them are benefited from the glossokinetic potentials. Nam et al. have developed the "Tongue Rudder." In this article, the researchers measured GKPs and electromyography (EMG) electrical signals over the scalp to drive the electric wheelchair for 1-D control. Then the teeth clenching is to calibrate and toggle the wheelchair [4]. The same authors have also attempted the "GOM-Face." In this work, electrooculogram (EOG) biosignals were utilized besides the GKP and EMG to remote the humanoid robot for 2-D control in a real-time application. All the potential variations were recorded from the face. Eigenvalue decomposition of two covariance was determined to discriminate eye and tongue movements due to being called charged organs. Then the SVM was employed to recognize each movement. Also, the review paper of the glossokinetic potential in using the ATs was published by the same researchers [5]. At this point, to the best of our knowledge, this research is also the first attempt using the support vector machine (SVM) and linear discriminant analysis (LDA) with power spectral density (PSD) and mean-absolute value (MV) using GKPs to structure a TMI.

So far, considerable amount of the tongue-driven work on the assistive devices has been dealing with the hardware inside the mouth and around the headset. Primary of them are; Huo et al. realized a series of tongue-driven systems that communicate with wireless transmissions in a state of stroke. Some were connected directly to the computer, and others were forwarded via smartphone for processing. However, they have a similar principle. A small permanent magnet is connected to trace the induced magnetic variations on the scheme of sensors assembled in the oral cavity [1]. Krishnamurthy et al. handled a similar principle to carry out an interface technology [11]. Nevertheless, interfaces operated by such an equipment-based system can irritate paralyzed patients while breathing or speaking, and at the same time are not hygienic and visually appealing. Therefore, GKP-based TMI may offer a natural, fast, attractive, and accurate control approach for stroke individuals.

Another approach of a tongue-based interface is on the airflow pressure variations generated by the tongue movements in the oral cavity. Vaidyanathan et al., have designed several ATs using a microphone attached to the ear canal to detect changes of airflow pressure in the ear canal due to the discrete tongue movements [12]. However, GKP-based TMI may contribute an inherent solution to trace the tongue motion without disturbing the listening performance.

This article is intended to carry out a natural, reliable, fast, and easy-to-use tongue-operated machine for stroke patients. GKP-based TMI is a novel AT utilizing glossokinetic potential responses to extract 1-D motion. The experimental paradigm has been configured in the offline measurement. Linear discriminant analysis and support vector machine and were employed in mean-absolute value (MAV) and power spectral density (PSD) methods. Moreover, principal component analysis (PCA) and independent component analysis (ICA) were implemented to the data to reduce the dimension. And comparison was made by these methods (ICA and PCA) in the article.

2. Materials and Methods

The glossokinetic potential responses were measured over the scalp in terms of the 10-20 international system for the location of electrodes [8]. The left-eyebrow and earlobes of left-right (A1-A2) were assigned as ground and reference, respectively. The monopolar placement of electrodes is represented in Table 1. The sampling frequency was at 1024 Hz and 0.5-100 Hz range was implemented for filtering operation. Also, the notch filter of 50 Hz was applied for elimination the noise of the power line. Then GKP biosignals were filtered using a low-pass filter of 10th order infinite impulse response (IIR) Butterworth in the cutoff frequency of 40 Hz [8]. The low-pass filtering EOG signal processing was also made at the same time because of the general assumption for lower frequency filtering (40 and 100 Hz) of EOG signals.

Celal Bayar University Journal of Science
Volume 16, Issue 1, 2020, p 35-46
Doi: 10.18466/cbayarfbe.571994

Table 1. The Monopolar Placement Electodes.

Number of Channels	Name of Channels
1	Fp2
2	Fp1
3	F7
4	F3
5	Fz
6	F4
7	F8
8	T3
9	C3
10	Cz
11	C4
12	T4
13	T5
14	P3
15	Pz
16	P4
17	T6
18	O1
19	O2

Then filtered data was normalized in the range of (0-1) according to the Eq.2.1 below:

$$X_S^{norm} = \frac{X_S - X_{min}}{X_{max} - X_{min}} \qquad (\mathbf{2.1})$$

X_S defines the *sth* data in the data set, X_{max} (maximum) and X_{min} (minimum) are the least and highest values [8]. The main illustration of the system can be viewed in Fig.1.

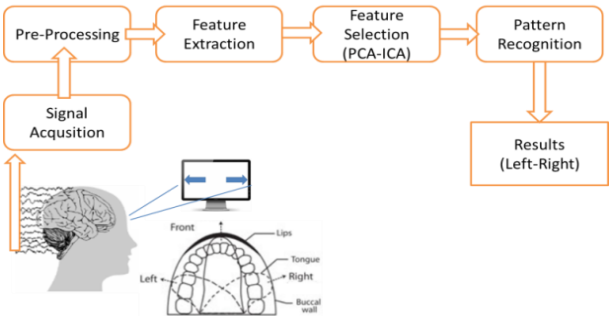

Figure 1. The workflow graph of GKP-based TMI.

2.1. Data Collection

This work consists of naive healthy subjects (8 male and 2 female) who were right-handed without any disorder of the nervous system. Subjects were in a comfortable situation placed in front of the LCD screen half-meter away without any movement except tongue movements during the experimental setup instructions. The statistical information for each participant can be shown in Table 2.

GKPs were measured and recorded by employing the EEG signal acquisition device of Micromed SAM32RFO with 19 channels, and the electrode impedances were held below 10kΩ. The recorded each trial was 98 seconds and initiated after the 10 s delay. Each touching process was 6 s, and the rest period was 5 s between the following instructions for right- left tongue movements. Four right and four left tongue movements were implemented in terms of the experimental sequences represented in Fig.2. For each channel, 6 s tongue movements and toucings to the buccal walls are stored with digitized samples of (6×1024). Participants were directed to touch the tongue and buccal walls during distinct, fast, and rhythmic contacts between 10-15 times for 6 seconds. Then, the resting time of the extended tongue was 5 seconds and no longer motion at this interval.

Table 2. Statistical information for each participant.

	Gender	Age
Subject-1	F	25
Subject-2	M	23
Subject-3	M	22
Subject-4	F	22
Subject-5	M	23
Subject-6	M	32
Subject-7	M	22
Subject-8	M	25
Subject-9	M	23
Subject-10	M	34

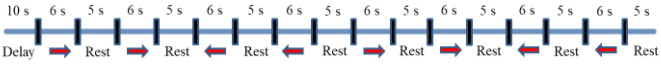

Figure 2. The experimental setup sequence of tongue Movements.

2.2. Feature Extraction

The transformation of the input signal data into a feature vector is named as feature extraction. The stage's purpose is to highlight distinctive properties in the input signal patterns. Mean-absolute value (time-domain) and power spectral density (frequency domain) methods were implemented in this research study. MAV is situated on the signal amplitude and does not need a transformation process between domains [8]. However, PSD has a transformation stage that implies more computational time. Frequency domain properties are calculated, estimating the power spectrum density of the signal and are implemented via parametric methods and periodogram [8]. In Eq.2.2, the mathematical presentation of the mean-absolute value is defined as:

$$MAV = \frac{1}{N}\sum_{i=1}^{N}|x_i| \qquad (\mathbf{2.2})$$

where X_i=1,2,3…N shows time series of samples, and N means the samples' length. Power signal variations of hemispherical scalp in motor tasks including the tongue

have different frequency ranges on the cortex that the PSD exhibits. The PSD is a function that defines the power distribution over a signal frequency. The mathematical expression of PSD is as follows in Eqs.2.3.-2.6.:

$$Px(f) = \frac{1}{N}\left|\sum_{n=0}^{N-1} x(n)e^{-j2\pi fn}\right|^2 = \frac{1}{N}|X(f)|^2 \quad (\mathbf{2.3})$$

where *X(f)* means the Fourier transform of the data sequence of *x(n)* and *N* is length of the sampled signal. The PSD formation is periodogram. Moreover the Welch's method is a special usage of periodogram. The data segments are divided and then overlapped, as shown below:

$$x_i(n) = x(n + iD) \quad n = 0,1,\dots,M-1 \quad i = 0,1,\dots,L-1 \quad \mathbf{(2.4)}$$

where *i* represents the segment of the data, while *n* is the segment length. Moreover, *iD* is the first point of the *ith* order where *D = M*, and then the segments do not overlap. However, *D = M/2*, 50 % overlapping occurs between the consecutive data segments. After that, each data segment was windowed to obtain the overall PSD. The Eq.2.5. represents the modified periodogram:

$$\bar{P}_X^{(i)}(f) = \frac{1}{MU}\left|\sum_{n=0}^{N-1} x(n)w(n)e^{-j2\pi fn}\right|^2 \quad (\mathbf{2.5})$$

where *U* is the normalization factor in the window function of power ''*w(n)*'' as:

$$U = \frac{1}{M}\sum_{n=0}^{N-1} w^2(n) \quad (\mathbf{2.6})$$

The references can be examined for more details of PSD and Welch's method [8]. In our research, eight segments and 50% overlapping with hamming windows were used for data samples.

The collected data set for each subject have (6×8×1024)×19 dimension that 1024 stands for sampling frequency, 8 means total durations for four right and four left tongue motions in a trial, six presents 6 s of contact duration for discrete tongue movements and 19 are the channel numbers. Throughout the feature extraction, 100 ms was applied to form the feature vector due to the covering all EEG frequencies. 1 second data have 1024/100ms=10 parts (approx), therefore (6x8x10) equals 480 data length. However, some of the subjects were not able to start and end the sessions at the exact time during the experiment. For this reason, we have to cut out and equalize the data set for each trial and participant to 400 data lengths. Finally, the raw data set was set to 400x19 for each subject.

2.3. Principal Component Analysis

Principal component analysis (PCA) constructs a set of new orthogonal features by calculating the data variance, called principal components. PCA intends to take away the unnecessary data. Thus, easier computation is obtained for MLs [8]. Calculating the eigenvalues and eigenvectors of the covariance matrix (*C*) are employed in converting higher dimensional vector (X_t) into a lower dimensional one (S_t). The concerned equations of PCA are those:

$$C(X) = \sum_{1}^{N} \frac{(X_i X^T)}{N} \quad (\mathbf{2.7})$$

$$\lambda_i u_i = C u_i, \qquad i = 1,2,3 \dots m \quad (\mathbf{2.8})$$

where λ_i presents the eigenvalues and u_i is named as the corresponding eigenvector of covariance matrix.

$$S_t(i) = u_t^T X_t, \qquad i = 1,2,3 \dots m \quad (\mathbf{2.9})$$

where $S_t(i)$ defines the principal components of the (X_t) [8]. By selection of principal components according to the variance values, In this research, twelve features' vector were created for a 400×12 data set indicating in the range of 98.18%-99.79%. The feature selection process by PCA and ICA was shown in Fig.3.

Figure 3. Feature selection process (PCA and ICA).

2.4. Independent Component Analysis

Independent component analysis (ICA) is a very powerful method for revealing concealed factors called independent components. ICA is a kind of statistical technique aiming to find linear projections of data that maximize mutual independence. Also, the widespread blind source separation (BSS) technique is based on ICA that can be used to select the best EEG channels. The system of assistive technologies with fewer EEG channels is preferred for better portability and convenience. In particular, ICA may serve to understand the functioning of the human brain easier as a finer mapping of brain responses during voluntary tongue movements [13].

$$x_i(t) = a_{i1}s_1(t) + \cdots + a_{in}s_n(t) \quad i = 1,2,\dots,n \quad (\mathbf{2.10})$$

where x_i *(t)* is the linear signal mixture belongs to *n* differently and randomly varying coefficients, and s_n *(t)* is the hidden component [8], as shown in Eqs.2.10-2.12. ICA notation can be presented in matrix form below:

$$\begin{bmatrix} x_1(t) \\ \vdots \\ x_n(t) \end{bmatrix} = A \begin{bmatrix} s_1(t) \\ \vdots \\ s_n(t) \end{bmatrix}, \quad A = [a_{i1}, a_{i2}, \dots, a_{in}] \quad (\mathbf{2.11})$$

$$x = As \quad (\mathbf{2.12})$$

In this article, ICA was employed to reduce the size of the data (400×12) for the (400×19) raw data set, and the results compared to PCA.

3. Machine Learning Algorithms

Applying feature extraction and feature selection (PCA-ICA) operations, the data set is conveyed to classifiers to discriminate glossokinetic potential responses for 1-D movements. Support vector machine and linear discriminant analysis are the common pattern recognition algorithms in biomedical signal processing and called kernel-based methods adapting the problem easier [8].

Accuracy (ACC), specificity (SPEC), sensitivity (SENS), and information transfer rate (ITR) was calculated to evaluate the performance of the GKP-based TMI. All the results were processed using the k-fold cross-validation technique, which is called the hold-out method to take out one part of the k-divided parts and structure the training data set. Moreover, the rest of the (k-1) parts are joined to form the test data set. Then all processes are repeated k-times in the independence of selection for samples [8]. In this study, 10-fold cross-validation was employed on all processed results for more robustness. Mathematical equations for the accuracy of the classification success can be seen in Eqs.3.1.-3.3.:

$$ACC(TS) = \frac{\sum_{i=1}^{|TS|} estimate(n_i)}{|TS|}, \; n_i \in TS \quad (\mathbf{3.1})$$

$$Estimate(n) = \begin{cases} 1, & if\ estimate(n) = cn \\ 0, & otherwise \end{cases} \quad (\mathbf{3.2})$$

$$Class.ACC = \frac{\sum_{i=1}^{|k|} accuracy(TS_i)}{|k|} \quad (\mathbf{3.3})$$

in which *TS* is the test data set, while $n \in TS$, c_n means the class of *n*. Furthermore, *estimate(n)* stands for the classification result of *n*, *k* is the number of k-fold cross validation [8].

Transmitting data of information per trial or time in EEG-based BCI systems is provided by information transfer rate (ITR). The ITR was produced from Shannon and Weaver's study and denoted by *B*. The approach of ITR can be seen in Eq.3.4.:

$$B = \log_2 N + P \log_2 P + (1-P) \log_2 \frac{(1-P)}{(N-1)} \quad (\mathbf{3.4})$$

B defines the bit numbers per trial, *N* is the different type of mental tasks, and *P* means the classification accuracy. The more various mental functions for a BCI system enhance the ITR, and the parameter value is shown in the range of (0-1) [8].

3.1. Support Vector Machine

Support vector machine is included in machine learning algorithm concept [8]. Support vectors are the keys for SVM to define the decision boundary (hyperplane). Margin is called as the distance from the hyperplane to the nearest support vectors for both sides. Then gaining generalization ability is aimed to maximize the margin and to find the optimal hyperplane [8], as depicted in Fig.4. The formulations of SVM is exhibited in Eqs.3.5-3.7.

$$X\{t\} = \begin{cases} r^t = +1, & x^t \in C1 \\ r^t = -1, & x^t \in C2 \end{cases} \quad (\mathbf{3.5})$$

$$g(x) = \begin{cases} w^T x^t + w_0 \geq +1, & x^t \in C1 \\ w^T x^t + w_0 \leq -1, & x^t \in C2 \end{cases} \quad (\mathbf{3.6})$$

$$r^t (w^T x^t + w_0) \geq +1 \quad (\mathbf{3.7})$$

The hyperplane is described by *g(x)*, w_0 situates the hyperplane and the orientation is pointed by *w*. Learning rate, initializations and checking for convergence is not carried out by SVM [8].

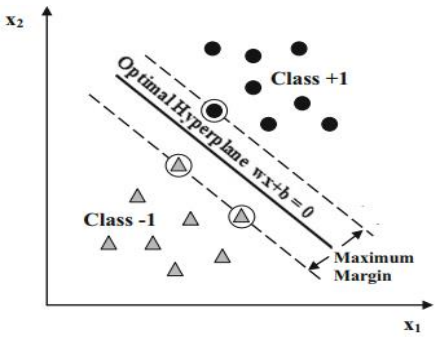

Figure 4. SVM and maximizing margin [8].

3.2. Linear Discriminant Analysis

Linear discriminant analysis is a kind of projection technique classifier reducing the dimension of the data. LDA intends to maximizing the between-class distance and minimizes within-class distance [22]. When *C1* and *C2* are the classes of the samples and LDA finds the projection direction (*w*) to discriminate the spatial pattern for maximum separability as possible. Formulations of LDA can be seen in Eqs.3.8-3.10.

$$z = w^T x \quad (\mathbf{3.8})$$

where, *x* (samples) are projected onto w. Projection technique of LDA is shown in Fig.5 below:

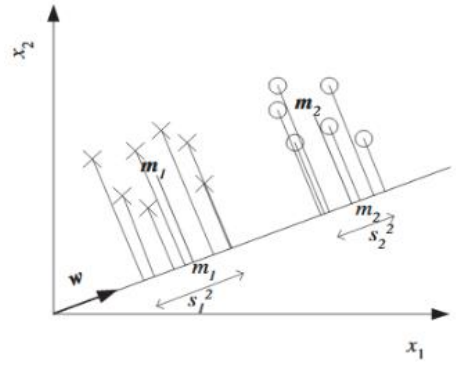

Figure 5. Classification task of LDA via the projection of data [8].

where projection technique implements from $\boldsymbol{m1}$ to $m1$ referring to means of samples in $C1$ before and after respectively. Thus, $\boldsymbol{m1} \in \Re^d$and $m1 \in \Re$. Then $\boldsymbol{m2}$ and $m2$ have the same means. s_1^2 and s_2^2 are scattered samples around the means [8]. If training sample is $X\{x^t, r^t\}$:

$$X\{t\} = \begin{cases} r^t = 1, & x^t \in C1 \\ r^t = 0, & x^t \in C2 \end{cases} \quad (\mathbf{3.9})$$

$$J(w) = \frac{w^T S_B w}{w^T S_W w} = \frac{|w^T(m1 - m2)|^2}{w^T S_W w} \quad (\mathbf{3.10})$$

where in $J(w)$, S_B and S_W are named as between-class scatter matrix and within-class scatter matrix, respectively. Moreover, *x* represents the input, *r* is the output in the training sample pairs.

4. Results

In this research, the discrimination of glossokinetic potential responses generated by the tongue for 1-D extraction has been investigated by implementing the SVM and LDA algorithms.

The mean-absolute value and power spectral density methods have been applied to machine learning methods. The raw data set for each participant was determined as a 400x19 dimension. The data sets to be processed by machine learning algorithms were obtained as:

- The raw data set (400x19)
- The data set reduced by PCA (400x12)
- The data set reduced by ICA (400x12)
- The frontal and temporal lobes' data set (11 channels) (400x11)

The classification performances were arranged according to the data sets above. All results throughout the article were represented in the decimal base and percentage expression (in %) except the outcomes of ITR. Then, the best and worst participants were stated by taking into account of results of the raw data set for distinguishing and comparison in an easy manner. Thus, the statements and implications of findings were stated on these subjects throughout the paper.

Table 3. Performance outcomes in the raw data set (400×19).

Met	..	Sb1	Sb2	Sb3	Sb4	Sb5	Sb6	Sb7	Sb8	Sb9	Sb10	Aver
LDA (MAV)	**Acc**	75.13	96.02	77.21	77.44	91.06	95.01	86.29	72.17	76.02	96.01	84.24
	Sen	76.52	93.50	79.98	73.13	90.80	97.05	84.00	64.19	68.88	97.83	82.59
	Spe	73.63	98.52	73.44	83.84	91.67	92.04	88.93	82.22	85.85	93.51	86.36
	ITR	0.191	0.759	0.226	0.230	0.565	0.714	0.423	0.147	0.205	0.758	0.422
LDA (PSD)	**Acc**	74.04	93.01	76.02	78.01	89.35	95.09	83.03	72.21	73.19	93.14	82.71
	Sen	72.23	88.50	76.98	71.47	91.21	97.46	76.60	63.32	59.73	97.83	79.53
	Spe	76.46	97.52	75.07	87.27	86.97	91.74	90.66	83.52	91.27	87.10	86.76
	ITR	0.174	0.634	0.205	0.240	0.511	0.717	0.343	0.147	0.161	0.640	0.377
SVM (MAV)	**Acc**	77.07	**97.03**	77.14	79.05	91.12	94.23	85.39	74.22	78.00	96.02	**84.93**
	Sen	87.23	97.50	84.55	80.49	93.33	96.20	83.59	69.21	74.02	97.84	86.4
	Spe	63.35	96.52	67.51	76.95	87.79	91.48	87.38	80.73	83.30	93.58	82.86
	ITR	0.223	0.807	0.224	0.259	0.567	0.682	0.400	0.177	0.240	0.758	0.434
SVM (PSD)	**Acc**	77.10	96.02	77.07	79.13	90.07	94.07	85.69	**67.80**	75.17	96.22	83.83
	Sen	86.40	96.00	82.71	73.55	92.45	97.03	80.22	85.77	62.77	99.13	85.6
	Spe	65.31	96.06	69.61	86.78	86.06	90.02	91.89	44.61	92.47	92.20	81.5
	ITR	0.224	0.758	0.223	0.261	0.533	0.675	0.408	0.094	0.191	0.768	0.414

Table 4. Performance outcomes in the PCA data set (400×12).

Met	..	Sb1	Sb2	Sb3	Sb4	Sb5	Sb6	Sb7	Sb8	Sb9	Sb10	Aver
LDA (MAV)	Acc	77.26	95	79.07	75.18	89.16	94.04	84.7	69.02	71	94.04	82.85
	Sen	79.29	91	81.38	73.59	88.64	96.2	81.26	61.05	60.13	95.71	80.82
	Spe	74.41	99.02	76.57	77.33	90.02	91.17	88.65	78.94	86.01	91.48	85.36
	ITR	0.226	0.714	0.26	0.192	0.505	0.674	0.383	0.107	0.131	0.674	0.387
LDA (PSD)	Acc	75.12	91.29	78.1	76.05	87.31	91.15	82.25	66.01	67.02	93.02	80.73
	Sen	71.25	85	80.51	73.19	89.51	93.7	69.94	69.8	48.53	96.96	77.84
	Spe	80.24	97.49	75.03	79.78	84.03	87.82	96.25	61.33	92.44	87.49	84.19
	ITR	0.191	0.573	0.242	0.206	0.451	0.568	0.325	0.075	0.085	0.635	0.335
SVM (MAV)	Acc	77.03	**97.01**	77.16	76.39	91.04	95.24	85.31	**69.05**	72.01	95.07	**83.53**
	Sen	85.85	97.5	82.79	81.43	91.65	96.61	82.71	65.65	61.9	97.83	84.39
	Spe	65.55	96.43	69.89	69.41	89.94	93.13	88.09	73.06	85.74	91.5	82.27
	ITR	0.223	0.806	0.225	0.211	0.565	0.724	0.398	0.107	0.145	0.717	0.412
SVM (PSD)	Acc	79.33	95.02	76.33	77.62	88.16	93.01	84.1	61.13	68.28	95.01	81.8
	Sen	86.78	95	86.26	79.2	90.82	96.56	77.47	87.53	55.43	97.84	85.29
	Spe	70.02	95.09	63.65	75.67	84.59	88.01	91.65	27.41	86.04	91.31	77.34
	ITR	0.265	0.715	0.21	0.233	0.475	0.634	0.368	0.036	0.099	0.714	0.375

The highest accuracy of the classification performance in the raw data set (400x19-Table 3) was obtained as 97.03% in SVM+MAV method. Then the lowest result was achieved with SVM+PSD method as 67.80%. Thus, Subject-2 (the best subject) and Subject-8 (the worst subject) were defined as the highlighted participants in the article. The accuracy results are very close to each other except for LDA+PSD (93.01%) in the best subject. After that, the LDA+MAV and SVM+PSD values were calculated as the same (96.02%). However, the SENS, SPEC, and ITR values are different. For the worst subject, SVM+MAV had the highest score (74.22%), followed by LDA+PSD and LDA+MAV as 72.21% and 72.17% success, respectively. The similarity was observed for the highest average result with SVM+MAV (84.93%).

Reduced data set with PCA (400×12) has relatively successful results represented in Table 4. The SVM+MAV method provided the highest outcomes for the best (97.01%) and worst (69.05%) participants. Then SVM + PSD (95.02%), LDA+MAV (95.00%), and LDA + PSD (91.29%) were achieved in terms of accuracy for the best subject. Meanwhile, the worst subject's results were ranked in decreasing order as LDA+MAV (69.02%), LDA+PSD (66.01%), and SVM+PSD (61.13%). Similar to the highest value of raw data set results, SVM+MAV was characterized by 83.53%. Hence consistent result (1.64% decreasing) was obtained compared to the average highest value of the raw data set (84.93%). The presentation of the covariance matrix for reduced data set was exhibited between the 98.18%-99.79% values. And the average highest presentation was observed as 99.45% with PSD.

According to Table 5, ICA results seem to be better than PCA [8]. Especially, the worst subject has reached 74.03% (in SVM+MAV), an increasing percentage is 6.72 (compared to 69.05%). Moreover, the other MLs also have greater outcomes compared to the PCA for the worst subject. On the other hand, the variations for the best subject is limited, and the results are close to the PCA. The best participant achieved 96.28% accuracy (in SVM+MAV), and the decline is about 0.75% compared to the highest outcome of PCA (97.01%). Moreover, the ultimate mean accuracy is again provided by SVM+MAV method (84.35%), and 0.97% boosting was obtained to the PCA.

The brain is structured by different functional lobes consisting of the cerebral and subcortical regions. Core and crucial functions of the body, such as involuntary breathing and heartbeat, are implemented by subcortical neuronal areas. Then the brain cortex carries out high-level functions such as conscious thinking and planning related to the voluntary movement of body functions, including tongue movement. The frontal lobe is known in charge of attention, planning, conscious motor functions, and behavioral control. Then, the temporal lobe is known in language-speech and face recognition as well as in the responsible of memory [8]. Thus voluntary tongue movement needs focus and planning efforts in fast, rhythmic, and stable motions during GKP-based TMI experimental work. For this reason, the results of frontal and temporal lobes were observed against voluntary tongue movements.

One of the goals of the GKP-based TMI is to explain the effect and contribution of different lobes of the brain

to the tongue-machine interface in terms of the classification accuracy. Therefore, the data set of 400×11 were generated by extracting 11-channels (Frontal + Temporal Lobe) data sets from the raw data set (400×19). T3, T4, T5, and T6 electrodes were used for eleven channels (Frontal + Temporal Lobe) as well as these seven electrodes for the seven channels (Fp1, Fp2, F7, F8, Fz, F3, and F4) (Frontal Lobe), as shown in Table 1.

According to Table 6, the joining effect of the frontal and temporal lobes for GKP-based TMI are encouraging and robustness compared to the raw data set (400×19) results. Not only the individual's success is observed highly acceptable, but also average achievements are in similar conditions. The best subject had provided 97.05% accuracy via SVM+MAV when the worst subject realized 71.06% correctness with the LDA+MAV algorithm. The deviation for the best and worst participant have increasing (0.02%) and decreasing (4.25%) characteristic respectively. Again the greatest outcome of average accuracy is observed in SVM+MAV (83.22%). The boosting impact of the temporal lobe (11-channels) to the frontal lobe (7-channels) was obtained as a 6.37% value. Thus, the performance of eleven channels seems to be more accurate and consistent outcomes than seven channels. It's almost as good as 19-channels of success. During experimental tasks, GKP signal variations for concentrated participants occur in the delta and theta bands [3]. The discriminating power of each tongue movements touching the buccal walls has spatial patterns on the scalp. As shown in Figs.6 and 7, to further analyze the brain mappings of the best subject, the high power alterations can be observed on the frontal and temporal lobe regions and partly pre-motor and motor cortex on delta bands. This vital finding was confirmed by the classification success shown in Table 6. Moreover, in theta and alpha frequency bands, negligible power assessments were obtained to distinguish the certain GKP responses. However, insufficient power signals were occurred at the occipital lobe between the beta frequency bands on the co ntralateral hemispherical side of the brain, depending on the visual stimulus in front of the LCD monitor [8].

The brain mappings for the worst participant (Figs. 8 and 9) showed dissimilar characteristics as against to the best subject. First, there are high-intensity power signal variations in the frontal lobe, but not lying correctly and smoothly in the temporal lobes of the delta and theta frequency. However, the temporal lobe power signal variations of the best subject include the T3, T4, T5, and T6 electrode locations shown in Fig.6 and Fig.7. Another crucial distinction in the worst subject is that the theta frequencies have highly acceptable power signals on the frontal lobe, which includes only Fp1 and Fp2. Furthermore, parietal lobe power signals are higher than the best subject's own. The reason for this may be that the worst subject was to deal with experimental tasks with inadequate target-oriented motivation and disturbing perception [8].

Table 5. Performance outcomes in the ICA data set (400×12).

Met	..	Sb1	Sb2	Sb3	Sb4	Sb5	Sb6	Sb7	Sb8	Sb9	Sb10	Aver
LDA (MAV)	**Acc**	76.13	93.05	78.45	77.42	88.82	94.22	87.01	73.44	75.53	95.51	83.96
	Sen	78.81	89.5	81.88	73.19	89.15	95.4	86.36	67.33	65.89	97.84	82.54
	Spe	72.14	96.64	74.47	83.01	88.34	92.41	87.65	81.19	89	92.42	85.73
	ITR	0.207	0.636	0.248	0.229	0.495	0.681	0.443	0.165	0.197	0.736	0.404
LDA (PSD)	**Acc**	75.15	92.5	76.05	78.65	89.12	93.27	82.38	73.05	73.18	93.19	82.65
	Sen	73.56	88.5	79.9	72.68	92.01	94.51	81.19	64.78	61.03	97.83	80.6
	Spe	76.66	96.52	70.63	86.19	84.74	91.5	83.39	83.52	89.76	86.61	84.95
	ITR	0.191	0.616	0.206	0.252	0.504	0.644	0.328	0.159	0.161	0.641	0.37
SVM (MAV)	**Acc**	77.01	**96.28**	77.29	79.23	90	93.06	85.25	**74.03**	77.33	94.01	**84.35**
	Sen	85.06	96	83.52	80.14	90.8	94.13	82.23	70.04	74.02	95.24	85.12
	Spe	66.41	96.39	68.79	78.65	88.78	91.68	88.53	79.01	82.21	92.19	83.26
	ITR	0.222	0.771	0.227	0.263	0.531	0.636	0.397	0.174	0.228	0.673	0.412
SVM (PSD)	**Acc**	76.89	95.24	77.02	80.24	88.17	94.59	83.15	73.01	76.05	95.77	84.01
	Sen	88.18	96	85.32	78.3	93.7	97.01	80.74	66.92	67.12	97.83	85.11
	Spe	62.21	94.39	66.19	83.4	80.3	91.19	85.97	80.97	88.33	93.17	82.61
	ITR	0.22	0.724	0.222	0.283	0.476	0.696	0.346	0.159	0.206	0.747	0.408

Table 6. Performance outcomes in the 11-channels (Frontal Lobe+Temporal Lobe) data set (400×11).

Met	..	Sb1	Sb2	Sb3	Sb4	Sb5	Sb6	Sb7	Sb8	Sb9	Sb10	Aver
LDA (MAV)	**Acc**	76.08	96.25	76.2	72.06	88.03	94.26	87.16	**71.06**	72.07	94.02	82.72
	Sen	76.17	94	80.45	70.14	89.53	95.76	83.96	62.96	61.01	96.54	81.05
	Spe	76.11	98.55	70.19	74.12	85.64	91.87	90.88	81.66	87.14	90.49	84.66
	ITR	0.206	0.769	0.208	0.145	0.472	0.683	0.447	0.132	0.145	0.673	0.388
LDA (PSD)	**Acc**	76.3	92	77.04	69.12	87.23	92.05	83.04	69.4	68.03	92.08	80.63
	Sen	75.36	87.5	82.67	64.06	89.55	95.76	72.32	71.01	50.69	97.39	78.63
	Spe	77.3	96.37	70.49	76.12	83.59	86.95	95.44	67.38	91.52	84.75	82.99
	ITR	0.21	0.598	0.223	0.108	0.449	0.6	0.343	0.111	0.096	0.6	0.334
SVM (MAV)	**Acc**	79.14	**97.05**	75.27	72.03	88.29	94.29	86.02	70.06	74.07	96.01	**83.22**
	Sen	88.52	97.5	83.14	75.78	90.4	96.21	83.98	70.45	66.65	99.57	85.22
	Spe	67.08	96.54	64.95	66.52	85.14	91.42	88.23	69.65	84.13	91.11	80.48
	ITR	0.261	0.808	0.193	0.145	0.479	0.684	0.416	0.119	0.174	0.758	0.404
SVM (PSD)	**Acc**	79.46	95.02	72.41	71.2	89.06	93.22	84.25	62.2	70.01	94.01	81.08
	Sen	89.33	95	87.61	72.3	92.9	96.2	75.17	91.92	54.09	96.96	85.15
	Spe	66.57	94.94	53.43	70.03	83.08	88.12	94.59	24.19	91.86	89.81	75.66
	ITR	0.267	0.714	0.15	0.134	0.502	0.642	0.372	0.043	0.119	0.673	0.362

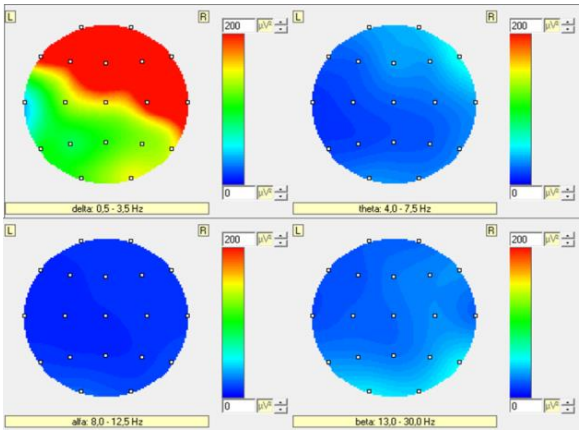

Figure 6. The best participant's brain mapping in touching the right buccal wall (delta, theta, alfa, beta frequencies).

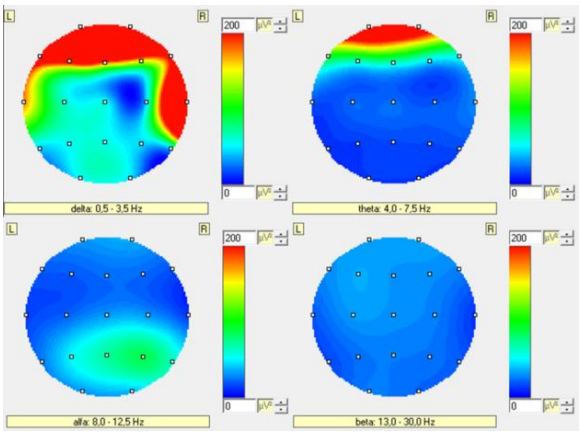

Figure 8. The worst participant's brain mapping in touching the right buccal wall (delta, theta, alfa, beta frequencies).

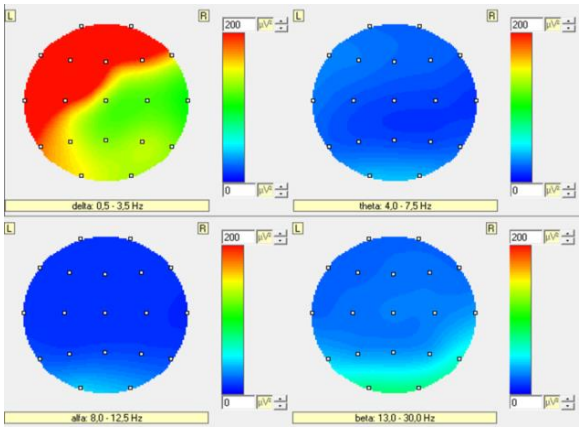

Figure 7. The best participant's brain mapping in touching the left buccal wall (delta, theta, alfa, beta frequencies).

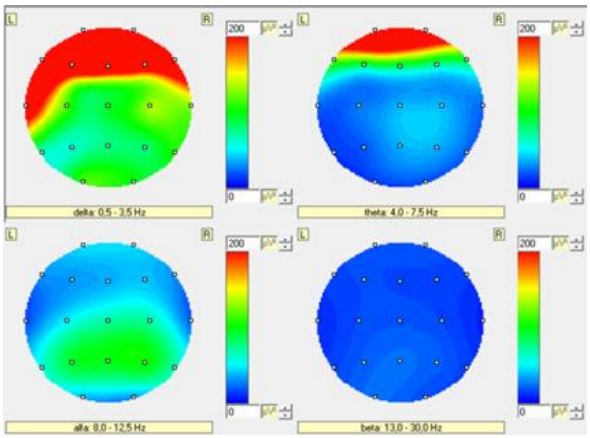

Figure 9. The worst participant's brain mapping in touching the left buccal wall (delta, theta, alfa, beta frequencies).

Table 7. Computation times of the linear discrimant analysis and support vector machine process.

Method	LDA +MAV	LDA +PSD	SVM +MAV	SVM +PSD
F.E.T.+ C.T.	0.0057	0.9222	0.0028	0.8936

F.E.T. (Feature Extraction Time-s), C.T. (Classifying Time-s)

The computation time is a significant metric for TMI's real-time applications [1, 5]. According to Table 7, the SVM+MAV method is shown the least computation time (0.0028 s) among the other methods. Then LDA+MAV (0.0057 s) yielded faster performance than SVM+PSD (0.8936 s) and LDA+PSD (0.9222 s) methods. It can be observed that the mean-absolute value has less computation time than the power spectral density because of not requiring transformation from the time domain to the frequency domain [8]. Similarly, SVM has less processing time than LDA. Computation time results were acquired in 1-fold cross-validation for an average of the test samples in the best participant's raw data set. All reported results in this paper were realized using MATLAB (License No: 834260) on a computer (Intel Core i5-7200 U CPU 2.50 GHz, Windows 10, 64 bit and 8 GB RAM). Finally, it is noteworthy that the SVM+MAV method is the best algorithm concerning the classification accuracy and the speed of execution in real-time usage of the GKP-based TMI research. Furthermore, the MAV feature extraction method provided better outcomes than PSD regarding the average values. Perhaps because of this reason, the MAV feature reflects the proper representation of glossokinetic potential responses better in GKP-based TMI.

5. Discussion

Computational neuroscience information notices the design of feedback control methods to distinguish the area of the motor cortex at different electrode installations on the human-computer interfaces during activated human body parts by measuring the local field potentials (LFPs). Thus, the multidisciplinary investigation aims to design a modern brain-machine interface (BMI) reconciling the statistical signal processing, machine learning, and information theory [15]. It is worth to report that the contribution and effects of the frontal+temporal lobes (11-channel) were observed in Tables 6, respectively. The correlation of frontal and temporal lobes' results are highly promising in terms of the classification accuracy for the tongue motion. Therefore, the results of eleven-channels are very close to the raw data set's (400×19) outcomes. This significant finding was also verified by the brain mappings of the best participant shown in Figs.6 and 7. Moreover, fewer electrodes with 11-channels may provide more degrees of freedom and reliable control to the GKP-based TMI [9-10]. For this reason, fewer electrodes can lead "wearable" and easy-to-use biomedical support technologies and ATs to work in the future for stroke individuals [17]. Moreover, corticomuscular coupling analysis reveals the mutual effect amid ongoing muscular activities (EMG) and the brain regions. However, the brain cortex and GKP coherence in delta and theta bands during the tongue-muscle motor functions were realized by GKP-based TMI research for the first time in the literature as our best knowledge.

The unexpected case of the study of Nam et al. is that the antisymmetric formation of GKP responses has emerged on the power of brain mapping. However, in our research, the power of GKP responses on the brain mappings has arisen in symmetric creation. This may have occurred from this reason; in the case of producing GKP signals, the same team noted that the negatively charged of the tip of the tongue uncover a potentially increased variation on the noncontact surface as it creates a negative potential reduction on the contact surface of the buccal wall [3-5]. On the other hand, Nam et al. have investigated the patterns of GKPs on the scalp related to the language and phonetics research.

The GKP biological responses are constituted of different spatial and temporal patterns on the brain maps during tongue movement. Moreover, in the mentioned paper, pronouncing the retroflex consonants led to a very strong potential increase over the frontal lobe during the tongue bending [14]. For this reason, in our study, an antisymmetric occurrence may have been suppressed due to strong and fast movements while the tongue is bent to touch the buccal walls during experimental tasks. Therefore, our results may have a symmetrical formation on the brain maps, as shown in Figs.7 and 8. The same researchers noted that the electrode location and the reference point, which was intentionally taken different contrary to general manner to occur the antisymmetric state on the brain mappings. Also, the experimental setup is different compared to our work, not just unlike electrode configurations. In their study, the tongue moves in an uninterrupted motion on the right-front-left path to touch the buccal walls [4-5]. However, in our study, multiple discrete contacts were realized in the same duration of 6 s task. Thus, all these points might encourage the assumption of symmetrical outcomes on brain maps in our study.

The results of GKP-based TMI may be considered more reliable and robust, depending on 8 male and 2 female subjects (all naive healthy) who were not previously experienced. Then, Subject_2 (the best subject) and Subject_8 (the worst subject) were chosen to point out and compare the distinct spots. The distinctive distinction of the best participant shows that having motivation, distinct and fast tongue movements provides the basis of achievement. However, the success of the worst participant was acceptable because

of less concentration and not properly doing instructed tasks. Motivation and cognitive effort in the relevant literature have been identified as the critical parameter for the high performance of BCI / HMI [8].

In recent years, ICA has been widely utilized in EEG-based BCI models to reduce the dimension of features or to reveal the source components. However, it has not been used in GKP signals to reveal the sources and reduce the dimension. Therefore, when these two methods are used, both ends of the predictions about the statistical distribution of the data are tried. Not all EEG signals are non-Gaussian (ICA) and uncorrelated (PCA). This basis may be the same for GKP signals. Therefore, according to Tables 4 and 5, PCA and ICA results are so close to each other. However, ICA is relatively better than PCA, especially for the worst and low participants. Because of this reason may be that the data set of the worst subject has more non-Gaussian and highly spatial overlapping of cortical activity [18]. Moreover, finding linear projections of the data by ICA aims is to maximize their mutual independence. Therefore, the selection process of the 12 EEG channels was made to maximize the classification results in the randomly searching algorithm for each iteration [8, 18]. The advantages and disadvantages for ICA and PCA were stated in Table 8:

Table 8. ICA and PCA comparison for data sets.

ICA	PCA
ICA can improve classifier performance as it moves away from the normal distribution (non-Gaussian). Therefore, the insignificant and worst participant data sets are more fitting for ICA	PCA is benefiting from the normal distribution of data. Thus, better participant performances can be improved by PCA
More convenient for highly spatial overlapping of cortical activity. Therefore, EEG channels from different parts of regions can be separated by ICA. However, the selection process can take a long time	New orthogonal features, called principal components, are calculated by PCA. Thus, dimension reduction and selection of high variance features are easy to compute. However, PCA is not enough to resolve complex brain signals
Removal artifact of signals can be made by ICA	Focusing on the reduction of data and decreasing the classification cost time

In BCIs, inter-trial and inter-subject instability are observed an important problem regarding the performance and reliability of the system. Moreover, long sessions of the BCI process present challenges in terms of consistent classification. The concept of these issues is referred to as transfer learning techniques that describe a procedure for using a stored relative data (statistical distribution of trial or session) to improve performance in another task [15]. However, the GKP-based TMI study may offer greater robustness for trial effects due to the voluntary tongue movements and glossokinetic potential responses with high amplitude and low frequencies [3, 4].

Moreover, it has been reported that the flexible and long cognitive planning time experiments can advance to the BCI and HMI research due to goal-oriented results that allow the subject to instinctive considerations [8]. In future work, the GKP-based TMI system can be advanced over this concept.

6. Conclusion

This paper describes GKP-based TMI as a new 1-D tongue machine interface research applying mean-absolute value and power spectral density methods with SVM and LDA over scalp-recorded GKP biosignals. Some of the equipment based tongue-machine interfaces have reached up to the 96-98% accuracy [12]. However, these systems have bulky devices inside the mouth and in the ear canal or around the headset for stroke people.

The rarely used glossokinetic responses have given promising results reaching up to the 97.03 accuracies for the construction of assistive technology that can be natural, reliable, attractive, and high-throughput efficiency for locked-in and ALS conditions. Then frontal and temporal lobe contributions can help neuroscientific understanding of cortical activity and statistical signal processing techniques by measuring local field potentials (LFPs) for tongue-related motor functions [16]. As far as we know, this critical point and glossokinetic potential have been dealt for the first time regarding the classification success of SVM and LDA with mean-absolute value and power spectral density in a tongue-machine interface. Moreover, comparing to our previous articles, SVM and LDA algorithms using mean-absolute value has greater performances compared to the root-mean-square feature extraction method for the best subject. Then this outcome provides very close results to the neural networks in the raw data sets [19-20].

The main challenges and focal point of this article are dedicated to advance the life quality of paralyzed individuals with tongue-based ways to reveal their wishes without traditional neuro-muscular pathways. Furthermore, GKP-based TMI may give a lead of real-time alternative control channels for traditional EEG-

driven BCIs with significant deficiencies resulting from the nature of EEG signals, which are low signal-to-noise ratio, and internally induced stationary mental activities or some external factors.

The future work of this research study can be progressed by real-time applications using wireless, highly accurate data acquisition devices with fewer electrodes for developing more portable systems. Moreover, the real-time system performances should be recorded on the different levels of paralyzed people.

Acknowledgement

The authors would like to thank Bozok University students for their participation in this research.

Author's Contributions

Kutlucan Gorur: Drafted and wrote the manuscript, performed the experiment, and result analysis. He also contributed to the main concept of the experiment.

M.Recep Bozkurt: Assisted in analytical analysis on the structure, supervised the experiment's progress, result interpretation.

M. Serdar Bascil: Helped in manuscript preparation and interpretation of the results.

Feyzullah Temurtas: Contributed to the theory and conceptual ideas.

Ethics

The study was confirmed by the Ethical Committee of Sakarya University (61923333/044). All procedures performed in studies involving human participants were in accordance with the ethical standards of the institutional and / or national research committee. Informed consent was obtained from all individual participants who participated in the study.

References

1. Huo, X, Ghovanloo, M. 2012. Tongue Drive: A wireless tongue-operated means for people with severe disabilities to communicate their intentions. *IEEE Communication Magazine*; 50(10):128-135.

2. Andreasen, Struijk, L.N.S. 2006. An inductive tongue computer interface for control of computers and assistive devices. *IEEE Transactions on Biomedical Engineering*; 53(12):2594-2597.

3. Nam, Y, Koo, B, Cichocki, A, Choi, S. 2016 Glossokinetic Potentials for a tongue–machine interface. *IEEE Systems, Man, & Cybernetics Magazine*; 2(1): 6-13.

4. Nam, Y, Zhao, Q, Cichocki, A, Choi, S. 2012. Tongue-Rudder: A Glossokinetic-Potential-Based tongue–machine interface. *IEEE Transactions on Biomedical Engineering*; 59(1): 290-299.

5. Nam, Y, Koo, B, Cichocki, A, Choi, S. 2014. GOM-Face: GKP, EOG, and EMG-Based multimodal interface with application to humanoid robot control. *IEEE Transactions on Biomedical Engineering*; 61(2):453-462.

6. Tang, H, Beebe, D.J. 2006. An oral tactile interface for blind navigation. *IEEE Transaction On Neural Systems & Rehabilitation Engineering*; 14(1):116-123.

7. Bao, X, Wang, J, Hu, J. Method of individual identification based on electroencephalogram analysis, International Conference on New Trends in Information and Service Science, 2009, pp 390-393.

8. Gorur, K. Makine Öğrenmesi Algoritmaları Kullanılarak Glossokinetik Potansiyel Tabanlı Dil-Makine Arayüzü Tasarımı; Sakarya Üniversitesi Fen Bilimleri Enstitüsü: Doktora Tezi, Sakarya, 2019.

9. Reuderink, B, Poel, M, Nijholt, A. 2011. The impact of loss of control on movement BCIs. *IEEE Transaction On Neural Systems & Rehabilitation Engineering*; 19(6):628-637.

10. Rupp, R, Rohm, M, Schneiders, M, Kreilinger, A, Müller-Putz, G.R. 2015. Functional rehabilitation of the paralyzed upper extremity after spinal cord injury by noninvasive hybrid neuroprostheses. *Proceedings of the IEEE*; 103(6):954-968.

11. Krishnamurthy, G, Ghovanloo, M. Tongue Drive: A tongue operated magnetic sensor based wireless assistive technology for people with severe disabilities, IEEE International Symposium on Circuits and Systems, 2006, pp 5551-5554.

12. Vaidyanathan, R, Chung, B, Gupta, L, Kook, H, Kota, S., West, J.D. 2007. Tongue-movement communication and control concept for hands-free human–machine interfaces. *IEEE Systems, Man, & Cybernetics Magazine*; 37(4):533-546.

13. Vigário, R, Särelä, J, Jousmäki, V, Hämäläinen, M., Oja, E. 2000. Independent component approach to the analysis of EEG and MEG recordings. IEEE Transactions on Biomedical Engineering; 47(5):589-593.

14. Nam, Y, Bonkon, K, Choi, S. Language-related glossokinetic potentials on scalp, IEEE International conference on systems, Man, and Cybernetics, San Diego, USA, 2014, pp 1063-1067.

15. Jayaram, V, Alamgir, M, Altun, Y, Schölkopf, B, Grosse-Wentrup, M. 2016. Transfer learning in brain-computer interfaces. IEEE Computational Intelligence Magazine; 20-31.

16. Kao, J.C, Stavisky, S.D, Sussillo D, Nuyujukian, P, Shenoy K.V. 2014. Information systems opportunities in brain–machine interface decoders. Proceedings of the IEEE; 102(5):666-68.

17. Cerutti, S. 2009. In the Spotlight: Biomedical signal processing. IEEE Reviews In Biomedical Enginering; 2:9-11.

18. Genc, H.M, Cataltepe, Z, Pearson, T. A New PCA/ICA based feature selection method, IEEE Signal Processing and Communations Applications, Eskisehir, Turkey, 2007.

19. Gorur, K, Bozkurt M.R, Bascil M.S, Temurtas F. 2018. Glossokinetic potential based tongue–machine interface for 1-D extraction. Australasian Physical & Engineering Sciences in Medicine; 41(2):379-391.

20. Gorur K, Bozkurt M.R, Bascil M.S, Temurtas F. 2018. Glossokinetic potential based tongue–machine interface for 1-D extraction using neural networks, Biocybernetics and Biomedical Engineering; 38(3):745-759.

Celal Bayar University Journal of Science

Obtaining the Heart Rate Information from the Speckle Images by Fractal Analysis Method

Ayla Burçin Şişli[1], Arman Jalali Pahnvar[2], Mehmet Engin[3], Erkan Zeki Engin[3*]

[1]Ege University, Graduate School of Natural and Applied Science, Department of Biomedical Technologies,
[2]Ege University, Graduate School of Natural and Applied Science, Department of Nuclear Sciences,
[3]Ege University, Faculty of Engineering, Department of Electrical and Electronics Engineering,

*erkan.zeki.engin@ege.edu.tr

Received: 16 January 2019
Accepted: 17 March 2020
DOI: 10.18466/cbayarfbe.513732

Abstract

Heart rate is the main data that shows if the heart is working properly. Therefore, obtaining the heart rate information has a vital importance. There are some methods to measure the heart rate, but the most commonly used one is the Electrocardiography (ECG). However, this method is expensive and non-portable. Therewithal, optical studies have recently been conducted to measure heart rate. Being non-invasive, inexpensive, and safe are the advantages of optical measurements. Laser speckle contrast imaging is an effective and simple technique for imaging heterogeneous environments such as human and animal tissues. By laser speckle contrast analysis, heart rate can be obtained easily. It is the standard technique, but fractal analysis method is also very convenient way to study speckle images because speckle pattern is quite appropriate for studying fractality due to its granular structure. In this paper, we present fractal analysis method for obtaining heart rate information from speckle images. The results of this method for the various in-vivo and in-vitro data were compared with the reference model results of speckle contrast analysis method and it is observed that the proposed analysis method has provided sufficient results.

Keywords: Fractal analysis, box-counting, speckle, heart rate

1. Introduction

The heart circulates oxygen and nutrient-rich blood throughout the body. When it is working improperly, just about everything is affected. Heart rate is central to this process because the function of the heart is directly related to it. A normal heart rate for adults is between 60 to 100 bpm. This parameter gives us vital physiological information. It can help monitor health situation and spot developing health problems. Heart rate is an important point of view in terms of metabolism and development of blood circulation of an organism [1, 2].

To measure the heart rate, Electrocardiography (ECG) is widely used method. In this method, electrical activity of heart is recorded by the probes placed to the body. However, being expensive and non-portable are disadvantages of this method [3, 4]. When normal ECG technique is insufficient, Holter ECG is a great option to monitor the activity of heart. In this method, the cardiac rhythm is monitored and recorded 24 hours by a portable device called 'holter' [5]. In addition, ultrasound based alternative method can be used to measure heart rate via ECG signal [6]. Lastly, laser speckle contrast analysis is another method to measure the heart rate. In this method, contrast analysis is applied to the speckle patterns obtained by the speckle method [4]. In our study, it is aimed to measure heart rate by applying fractal analysis method to speckle patterns.

Speckle pattern is quite appropriate for studying fractality due to its granular structure (speckle). These speckles generally show statistical behavior. The well-known analysis method of active series of speckles is relied on laser speckle contrast. However, fractal statistics is also very convenient way to study speckle images. The behavior of the process at different times can be measured by calculating the fractal statistics of the speckle signal. Evaluation of the fractal dimension of speckle images gives very important information coming from flow process. The fluid is always pulsed at almost the same frequencies with the human heart [7-9].

In this paper, the heart rates that were measured by fractal analysis method from in-vitro and in-vivo speckle images (frames) will be shown. Three different sets of in-vivo and three different sets of in-vitro images were used for this study. Differential box-counting method was performed to measure the change of fractal dimension according to time for speckle images. At the end, all the results were compared with the model results obtained by laser speckle contrast analysis method which we got from another study [4].

2. Materials and Methods

2.1 What is Speckle?

The term speckle refers to a random granular pattern. This pattern is a random intensity distribution produced by the scattered light that is formed when coherent light scatters from a random medium (Figure 1). Because of its randomness, it can only be described statistically. This random interference pattern in the image plane changes because of the phase shifts in the scattered light produced by the motion of scattering particles inside of the medium. The speckle image contains spots of different sizes and intensities. In speckle based techniques, the sample is mostly enlightened by a laser and the scattered light is gathered by a sensor. The collected light gives us significant information about the living medium. By laser speckle contrast imaging method, it is possible to ensure exhaustive information about system dynamics [7-10]. The speckles could be divided in two groups according to their formation geometry. When the laser illuminates a sample and the speckles resulting from the back-scattered radiation is directly collected using a screen or a sensor array in the absence of lens system are known as objective speckles. In contrast, when the speckles are obtained through a lens system, the resulting speckles are known as subjective speckles [11].

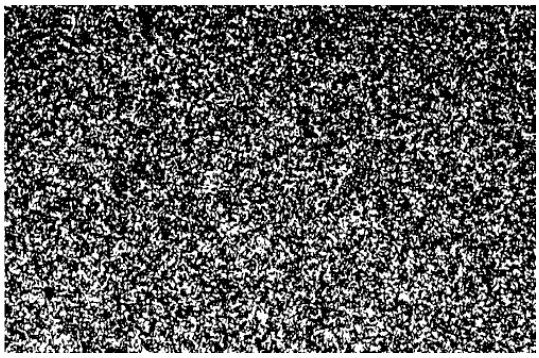

Figure 1. A typical laser speckle contrast pattern [12].

2.2 Fractal Analysis of Speckle Images

A fractal is a geometrical figure used to define and imitate inherently occurring items. Artificially created fractals generally show almost identical patterns at increasingly small scales [13]. A fractal dimension is a ratio that ensures a statistical index of complexity collating how particular in a fractal pattern varies with the scale [14, 15]. Fractal analysis identifies fractal properties of input. It is possible to get lots of information such as heart rate by this method [16]. Fractal analysis is now widely used in all areas of science [17, 18].

Breaking the image into small structures shows the measure of fractality. In scaling law, an image is a combination of 'N', which is the distinct, non-overlapping replicas of itself. The replicas can be reduced by a ratio 'r = M/s'. Here, 'M' is size of the image and 's' is the size of the length scale of the created replicas. N is connected to these parameters by the equation of ' $N_s \cong r^{-D}$ '. Here, 'D' is the fractal dimension (FD) [9]. In order to perform fractal domain analysis of image, there are number of techniques such as variance methods, box-counting methods [19]. It is a great way to measure the distribution of a structure in a surface and could be distinctly connected to the measurement of a spatial distribution in a speckle image. The time advancement of this within the area beneath investigation is exceptionally valuable in the consideration of dynamical systems. In the box-counting method, the speckle image, in which the main features of fractals can be observed, is divided into boxes on a certain scale and the fractal dimension is calculated by using the important boxes, which are determined through this method. When the amount of boxes (N_s) is predicted between the range of s, then the connection between $\log(N_s)$ and $\log(1/s)$ can be seen. The resultant slope shows the fractal dimension. The relation is shown as:

$$FD = \lim_{s \to 0} \frac{\log(N(s))}{\log\left(\frac{1}{s}\right)} \quad \textbf{(2.1)}$$

The differential box-counting can be applied instead of traditional box-counting when an image is considered as a surface where its height is relative to its intensity or its gray value.

In this study, differential box-counting has been applied by considering the image as a 3D surface. Hereby, the speckle images were replaced with the fractal images. The FD of each image was computed and then the time series of it were used to define the matching frequency spectrum for analyzing dynamics [9].

2.2.1 Box-Counting Method

Box-counting method is used to collect data for analyzing complex patterns. This method is performed by splitting the image, object, etc. into smaller box-shaped pieces [20, 21]. This is one of the most often used methods for computing FD of an image [22].

Generally, box-counting technique uses the geometric-step (GS) method. In GS method, the step size is limited to a power of two, hence the potential wasted pixels of the image are prevented [23].

The box-counting method consists of three main steps; generation of a set of box sizes 's' for placing grids on the image, calculation of the number of boxes, N_s , required for complete coverage of the object for each s, and determination of FD by using the slope of points (log(1/s), log(N_s)). In the differential box-counting method, how to calculate N_s is explained below [23].

On each block, (s x s x s') size boxes form a column, where s' refers to the height of any boxes, and G/s'=M/s, where G refers to the amount of gray level. k^{th} and l^{th} boxes represent minimum and maximum gray level in the (i, j)th block, respectively. The boxes covering this block are calculated as:

$$n_s(i,j) = l - k + 1 \quad \textbf{(2.2)}$$

For the case of all blocks, N_s is calculated as:

$$N_s = \sum_{i,j} n_s(i,j) \quad \textbf{(2.3)}$$

Then, from the least squares linear fit of log(N_s) versus log (1/s), the FD can be evaluated for each image.

2.3 Algorithm

In this study, the algorithm seen in Figure 2 was used to obtain the heart rates from the speckle videos. After calculating the heart rates, they were compared with the model results that obtained by laser speckle contrast analysis method [4] and then the errors were computed.

2.4 Setups of the Reference Model Results

The model results were obtained by laser speckle contrast method. The speckle images used in the study were obtained by different setups and conditions. At the end of the processes, three different in-vitro and three different in-vivo speckle videos were observed. After recording the videos, they were divided into 220 frames (Figure 3) and analyzed [4].

2.4.1 In-vitro Setup

In addition to the equipment in the in-vivo system, there is also a speaker in this system (Figure 4). The required system was set up and video recordings were taken at different times from the egg shell. In order to simulate the in-vivo environment, egg shell in different color and roughness was glued to the membrane of the speaker. Artificial heart beats (or the vibrations) were obtained by adjustable voltage amplitude and frequency regulated signal generator. Under this periodic excitation, speckle videos were recorded in order to calculate fundamental vibration frequency corresponding to the actual heart rate in in-vivo conditions. These 10-second speckle videos were then divided into 220 frames. Then, the speckle contrast values were calculated from these frames using the speckle contrast analysis method [4].

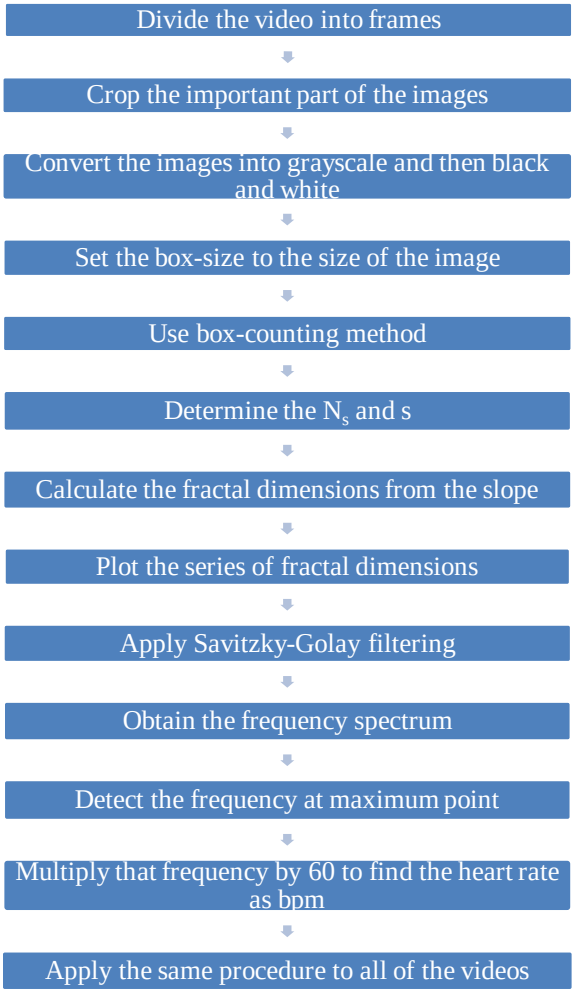

Figure 2. The flowchart of the proposed method

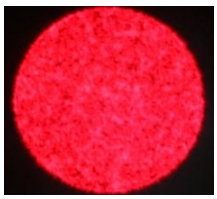

Figure 3. The speckle image obtained from a frame [4].

Two different excitation function types, sinusoidal and ramp were used in this system [4]. In this study, the speckle contrast values calculated from the measurements observed under 1 V – 1 Hz, 1 V – 2 Hz, and 1 V – 3 Hz excitation were used. As an excitation function type, sinusoidal was used in this study.

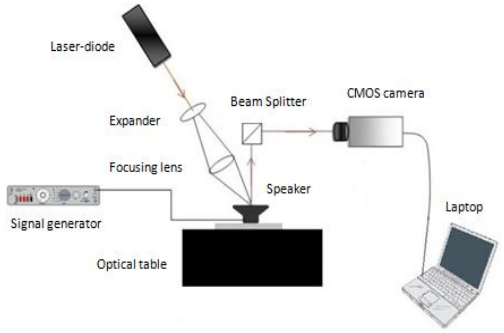

Figure 4. The in-vitro setup [4].

2.4.2 In-vivo Setup

The chicken egg was held in artificial incubator at 37.8±1°C temperature and 50-60% relative humidity for the in-vivo measurements. All procedures were performed in accordance with regulation (2014) of Turkish Ministry of Forest and Water Affairs for experimental animals' ethic board for measuring process. The required system was set up and video recordings were taken at different times from the egg. There were laser-diode source, lens and CMOS camera in this system. These 10-second speckle videos were then divided into 220 frames. Then, the speckle contrast values were calculated from these frames using the speckle contrast method [4].

For the measurement, the egg was taken from the incubator and placed in the measuring hole of the optical setup (Figure 5). To obtain a speckle image, three points on the most pointed part of the egg shell were marked as a triangle, and then a point at the center of the triangle was marked. These marked points were used as targets for each laser light focus. After the speckle contrast analysis, a contrast value was calculated for each image. Finally, at the end of the algorithm, a single heart rate was obtained by taking the average of the heart rates corresponding to the four marked laser targets [4].

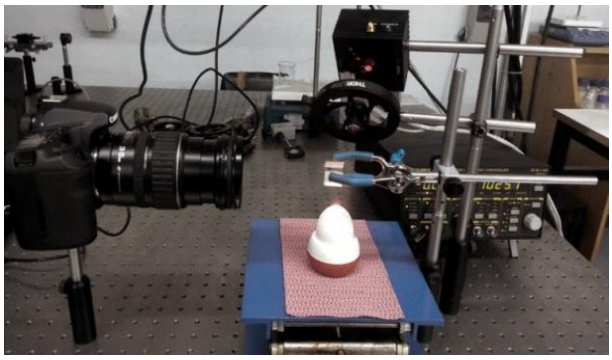

Figure 5. The in-vivo setup [4].

In this study, the speckle contrast values calculated from the measurements observed on 8, 10, and 18 day chicken embryos were used.

3. Results and Discussion

At the end of the process, fractal dimensions and heart rate (in Hz) graphs of chicken embryos were plotted. The heart rates (in Hz) were obtained by applying FFT on the fractal dimensions. After multiplying the X values (Figure 6) in the Heart Rate Graphs by 60, the heart rates were obtained as bpm.

The errors of in-vivo results are less than the errors of in-vitro results. However, according to the all results, the errors are smaller than 10%. Based on this ratio, it can be said that fractal analysis method gives a valid results. So, this method can be used to obtain the heart rate.

3.1 In-vitro Results

Values of the fractal dimensions and the heart rate (in Hz) of 1 Hz data can be seen in Figure 6. By multiplying the X value in Heart Rate Graph by 60, it can be said that the heart rate of 1 Hz data is '54 bpm'. However, according to the contrast analysis method, the heart rate of 1 Hz data is '60 bpm'. As we can see in the Table 1, the error is 10%, here.

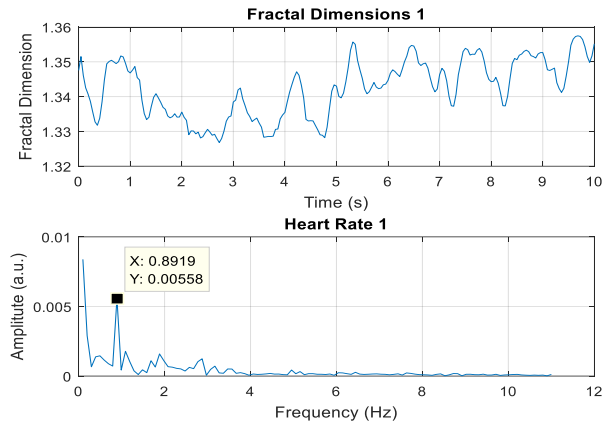

Figure 6. Fractal dimensions and the heart rate for the 1 V – 1 Hz sinusoidal signal.

Values of the fractal dimensions and the heart rate (in Hz) of 2 Hz data can be seen in Figure 7. It can be said that the heart rate of 2 Hz data is '108 bpm'. However, according to the contrast analysis method, the heart rate of 2 Hz data is '120 bpm'. As we can see in the Table 1, the error is 10%, here.

Values of the fractal dimensions and the heart rate (in Hz) of 3 Hz data can be seen in Figure 8. It can be said that the heart rate of 3 Hz data is '162 bpm'. However, according to the contrast analysis method, the heart rate of 3 Hz data is '180 bpm'. As we can see in the Table 1, the error is 10%, here.

Table 1. The comparison of spectral contrast and fractal analysis in-vitro results.

Excitation	Results from speckle contrast analysis		Results from fractal analysis		Error(%)
	Frequency (Hz)	Heart Rate (bpm)	Frequency (Hz)	Heart Rate (bpm)	
1 V – 1 Hz	1	60	0.9	54	10%
1 V – 2 Hz	2	120	1.8	108	10%
1 V – 3 Hz	3	180	2.7	162	10%

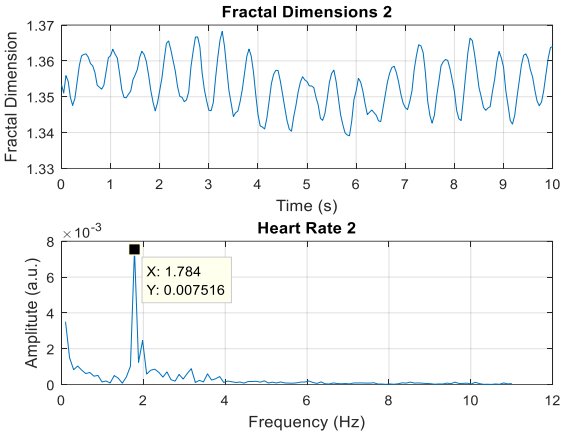

Figure 7. Fractal dimensions and the heart rate for the 1 V – 2 Hz sinusoidal signal.

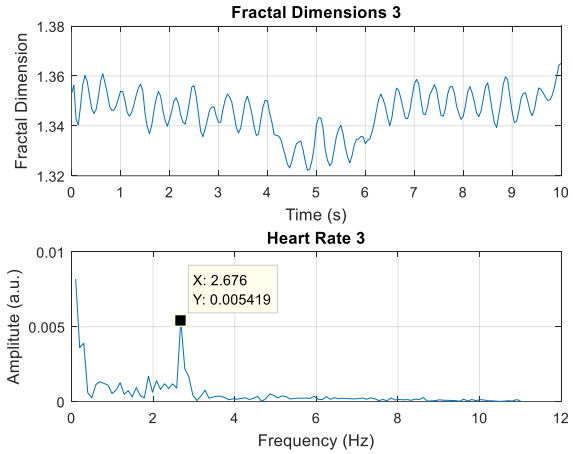

Figure 8. Fractal dimensions and the heart rate for the 1 V – 3 Hz sinusoidal signal.

All the results, comparisons and the errors for the in-vitro study can be seen in Table 1. As seen in Table 1, the speckle contrast method can be used as a reference method, because excitation frequencies can be detected with this method without error. It is thought that the reason of the fixed error (10%) between the two methods is that the excitation wave shape (sinusoidal) and amplitude do not change.

3.2 In-vivo Results

Values of the fractal dimensions and the heart rate (in Hz) of 8 day chicken embryo can be seen in Figure 9. It can be said that the heart rate of 8 day chicken embryo is '143.34 bpm'. However, according to the contrast analysis method, the heart rate of 8 day chicken embryo is '151.86 bpm'. As we can see in the Table 2, the error is 5.6%, here.

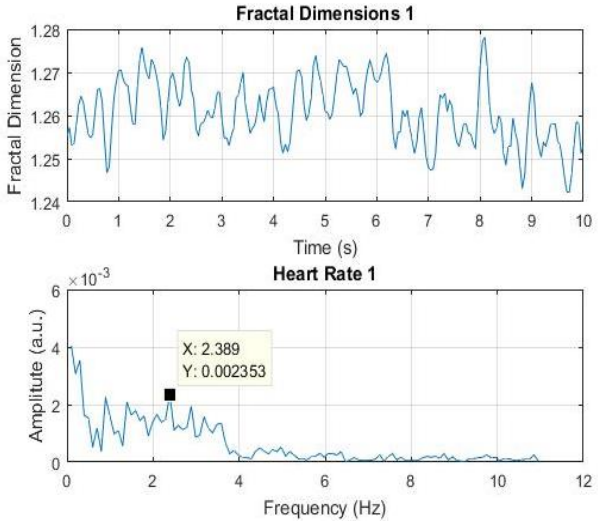

Figure 9. Fractal dimensions and the heart rate of the 8 day chicken embryo.

Values of the fractal dimensions and the heart rate (in Hz) of 10 day chicken embryo can be seen in Figure 10. It can be said that the heart rate of 10 day chicken embryo is '237.84 bpm'. However, according to the contrast analysis method, the heart rate of 10 day chicken embryo is '241.86 bpm'. As we can see in the Table 2, the error is 1.7%, here.

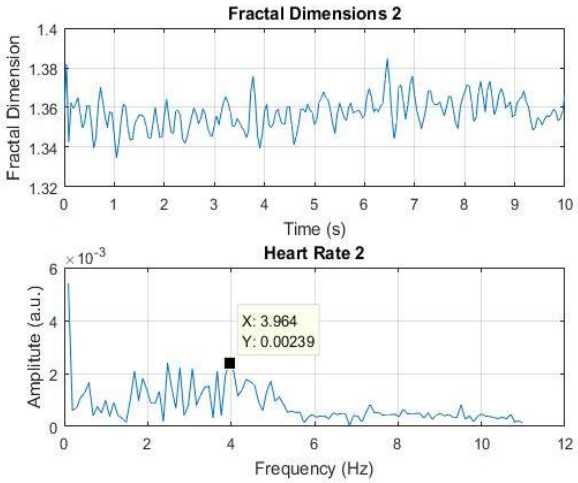

Figure 10. Fractal dimensions and the heart rate of the 10 day chicken embryo.

Table 2. The comparison of spectral contrast and fractal analysis in-vivo results.

Day of embryo	Results from speckle contrast analysis		Results from fractal analysis		Error(%)
	Frequency (Hz)	Heart Rate (bpm)	Frequency (Hz)	Heart Rate (bpm)	
8	2.531	151.86	2.389	143.34	5.6 %
10	4.031	241.86	3.964	237.84	1.7 %
18	3.656	219.36	3.584	215.04	2 %

Values of the fractal dimensions and the heart rate (in Hz) of 18 day chicken embryo can be seen in Figure 11. It can be said that the heart rate of 18 day chicken embryo is '215.04 bpm'. However, according to the contrast analysis method, the heart rate of 18 day chicken embryo is '219.36 bpm' and the error is 2%.

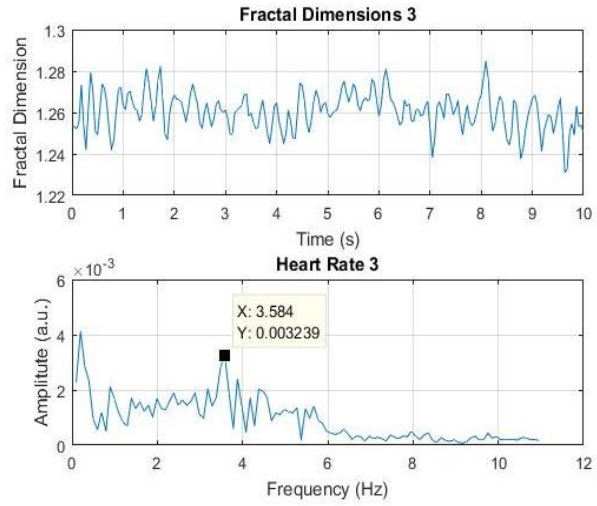

Figure 11. Fractal dimensions and the heart rate of the 18 day chicken embryo.

All the results, comparisons and the errors for the in-vivo study can be seen in Table 2. When the table values are examined, it is observed that daily age of embryos affect error rates. Heart rate in the early period (8 days and before) embryos is not rhythmic because heart rate is not completed yet.

4. Conclusion

In this study, it was investigated the fractal dimension change of in-vitro and in-vivo speckle images to obtain the heart rates and compared it to the model results, which were measured by laser speckle contrast analysis method. At the end, the errors between the results were calculated.

When in-vitro results are examined, it is seen that the results are sufficiently accurate. Therefore, it can be said that if the proposed system is made industrial prototype (like reference system), it can be used in the monitoring of embryo viability in poultry sector.

Author's Contributions

Ayla Burçin Şişli: Drafted and wrote the manuscript, performed the result analysis.

Arman Jalali Pahnvar: Performed the experiment.

Mehmet Engin: Supervised the experiment's progress and edited the manuscript.

Erkan Zeki Engin: Supervised the result analysis.and helped in manuscript preparation.

Ethics

There are no ethical issues after the publication of this manuscript.

References

1. Cohn A.E. 1925. Physiological Ontogeny: A chicken embryos. V. on the rate of the heart beat during the development of chicken embryos, *J. Exp. Med.*, 42(3): 291–297.

2. Writing Group Members, et al. 2006. Heart disease and stroke statistics—2006 update: a report from the American Heart Association Statistics Committee and Stroke Statistics Subcommittee, *Circulation*, 113.6, e85-e151.

3. Malik, Marek, et al. 1996. Heart rate variability: Standards of measurement, physiological interpretation, and clinical use, *European Heart Journal*, 17(3): 354-381.

4. Pahnvar, A.J. 2016. Estimation of near subcutaneous blood microcirculation related blood flow using laser speckle contrast imaging, Ege University Graduate School of Natural and Applied Sciences Department of Electrical and Electronics Engineering.

5. Laguna, P., et al. 1990. New algorithm for QT interval analysis in 24-hour Holter ECG: performance and applications, *Medical and Biological Engineering and Computing*, 28(1): 67-73.

6. Gottdiener, John S., et al. 2004. American Society of Echocardiography recommendations for use of echocardiography in clinical trials: A report from the American society of echocardiography's guidelines and standards committee and the task force on echocardiography in clinical trials, *Journal of the American Society of Echocardiography*, 17(10): 1086-1119.

7. Boas, David A., and Dunn, A.K. 2010. Laser speckle contrast imaging in biomedical optics, *Journal of Biomedical Optics*, 15(1): 011109.

8. Dainty, J. Christopher, ed. 2013. Laser speckle and related phenomena, *Springer Science & Business Media*, 9.

9. Nemati, M., et al. 2016. Fractality of pulsatile flow in speckle images, *Journal of Applied Physics*, 119(17): 174902.

10. Zhang, X., et. al., A low-cost and smartphone-based laser speckle contrast imager for blood flow, *BIBE 2018; International Conference on Biological Information and Biomedical Engineering*, Shanghai, China, 2018.

11. Escobar, C.P.V., New laser speckle methods for in vivo blood flow imaging and monitoring, Universitat Politecnica de Catalunya ICFO, 2014.

12. Briers, J. D. 2001. Laser Doppler, speckle and related techniques for blood perfusion mapping and imaging, *Physiological Measurement*, 22(4): 35-66.

13. Boeing, G. 2016. Visual analysis of nonlinear dynamical systems: Chaos, fractals, self-similarity and the limits of prediction, Systems, 4(4), 37.

14. Falconer, K., Fractal geometry: mathematical foundations and applications, Wiley, 2013.

15. Tamas, V., Fractal growth phenomena, World Scientific, 1992.

16. Tan, C.O., et al. 2009. Fractal properties of human heart period variability: physiological and methodological implications, *The Journal of Physiology*, 2009, 587.15, 3929-3941.

17. AC03515164, A., ed., Fractals: complex geometry, patterns, and scaling in nature and society, World Scientific, 1997.

18. Gültepe, M.D., and Tek, Z. 2018. Investigation of phase transitions in nematic liquid crystals by fractional calculation, *Celal Bayar University Journal of Science*, 14(4): 373-377.

19. Lopes, R., and Nacim B. 2009. Fractal and multifractal analysis: a review, *Medical Image Analysis*, 13(4): 634-649.

20. Mandelbrot, B.B., The fractal geometry of nature, New York: WH Freeman, 1983, Vol. 173.

21. Iannaccone, P. M., and Khokha, M., Fractal geometry in biological systems: an analytical approach, CRC Press, 1996.

22. Li, J., Qian, D., and Caixin, S. 2009. An improved box-counting method for image fractal dimension estimation, *Pattern Recognition*, 42(11): 2460-2469.

23. So, G.K., Hye-Rim, S., and Gang-Gyoo, J. 2017. Enhancement of the box-counting algorithm for fractal dimension estimation, *Pattern Recognition Letters*, 98: 53-58.

Celal Bayar University Journal of Science

Cytotoxic Effects of Probiotic Bacteria *Lactobacillus acidophilus* and *Lactobacillus rhamnosus* Grown in the Presence of Oleuropein on Human Prostate Cancer Cells

Hasan Ufuk CELEBIOGLU[1*], Busenur CELEBI[1], Yavuz ERDEN[2], Emre EVİN[3], Orhan ADALI[3]

[1] Bartın University, Faculty of Science, Department of Biotechnology, Bartın-Turkey.
[2] Bartın University, Faculty of Science, Department of Molecular Biology and Genetics, Bartın-Turkey.
[3] Middle East Technical University, Faculty of Science and Arts, Department of Biological Sciences, Ankara-Turkey.
* hcelebioglu@bartin.edu.tr

Received: 16 October 2019
Accepted: 17 March 2020
DOI: 10.18466/cbayarfbe.633237

Abstract

Functional foods are groups of foods that have potentially positive effects on health beyond basic nutrition. Probiotics are beneficial microorganisms, being as a group of functional foods, and when ingested in adequate amounts, they possess positive health effects to host organisms including having anti-carcinogenic functions, yet their exact mechanisms how they possess anti-carcinogenic activities are still under investigation. Another group of functional foods is plant-based phenolic compounds. They also have potential to possess anti-carcinogenic activities. Among them, oleuropein is very interesting and well-known phenolic compound naturally present in olive fruits and olive oil. As the phenolic compounds and probiotic bacteria can be present at the same time in human gastrointestinal tract, this study aims to investigate the *in vitro* cytotoxic effects of *Lactobacillus acidophilus* LA-5 (LA-5) and *Lactobacillus rhamnosus* GG (GG) grown in the presence of oleuropein on human prostate cancer cell line. For this, oleuropein was added to media of these bacteria and effects of cell-free supernatants of these combinations (phenolic+probiotic) on cytotoxicity of prostate cancer cell line PC-3 were investigated using MTT Method. Different concentrations of oleuropein were added to bacterial cultures and oleuropein added to the growth medium of LA-5 had additional effects on the cytotoxicity of cell-free supernatants of this bacterium. However, addition of oleuropein to the growth medium of GG did not show significant changes on the cytotoxicity of cell-free supernatants of this bacterium.
Thus, the results indicate that new combinations of functional foods have potential to formulate new nutraceuticals.

Keywords: Cytotoxicity, MTT Assay, Phenolic compounds, Probiotics, Prostate Cancer, Oleuropein.

1. Introduction

Functional foods are groups of foods having potentially positive effects on health beyond basic nutrition [1]. Probiotics, a group of functional foods, are microorganisms that have positive effects on human health when administered in sufficient amounts [2].

Lactic acid bacteria are the group of probiotic microorganisms investigated in detail for health benefits [3]. The best known probiotics are *Lactobacillus acidophilus* and *Lactobacillus rhamnosus*. One of the best studied beneficial bacteria is *Lactobacillus rhamnosus*, which is available as a dietary supplement and added to a variety of foods, such as dairy products. It belongs to the genus *Lactobacillus*, a type of bacteria that produces the lactase enzyme. This enzyme converts sugar lactose found in dairy products into lactic acid. *L. rhamnosus* can survive in acidic and alkaline conditions in the human body and has many potentials and uses for the digestive system and other health areas. *L. acidophilus* produces antimicrobial agents such as hydrogen peroxide (H_2O_2), diacetyl and bacteriocin as well as organic acids. These substances inhibit degrading organisms and foodborne pathogens. It has been found that *L. acidophilus* inhibits various bacterial strains by producing bacteriocin [4]. Probiotic bacteria are expected to adhere to the mucus layer, form colonies

and multiply. Adherence to the cell wall in the intestine is an important feature for colonization in the digestion [5]. *L. acidophilus* can be found in more parts of the intestine compared to other bacteria [6].

Another group of functional foods is plant-based phenolic compounds. Humans have been using extracts of olive leafs for medicinal purposes for centuries [7]. As a traditional 'Mediterranean Diet', olive and olive oil are the most famous and popular diet components [7]. Olive leaf extracts, olive fruits, and olive oil contain tocopherols, carotenoids, phospholipids, and phenolic compounds. Oleuropein is considered as main ingredient in olive tree and in all other constituent parts of the fruit (peel, pulp, and seed) [8]. It is one of the secoiridoids, a specific group of coumarin-like compounds [7]. It is a glycosylated compound, produced in secondary metabolisms of the plants (Figure 1) [9]. It reaches more than 140 mg/g in dried immature olives and reaches 60-90 mg per g of dried leaves [9]. It is a very intensively studied phytochemical for its health benefits and for its medicinal usage [7]. Although most of the studies related with oleuropein and its health effects have been performed *in vitro*, some human and animal trials used 'Mediterranean diet' to show its effects on the health. Anti-oxidant tests showed that oleuropein potentially inhibits oxidation of low-density lipoproteins induced by copper sulfate [10], to scavenge nitric oxide [11] and the free radical 1,1-diphenyl-2-picrylhy-drazyl (DPPH) [12]. Furthermore, oleuropein has a strong anti-microbial activities against different microorganisms, including Gram(+) and Gram(-) bacteria, and mycoplasma [13–15]. Using different cancer cell lines, oleuropein showed anti-carcinogenic activities. Oleuropein and its aglycone inhibited *in vitro* growth of glioblastoma, erythroleukemia, renal cell adenocarcinoma, malignant melanoma of the skin-lymph node metastasis,ductal carcinoma of the breast pleural effusion, colorectal adenocarcinoma, and breast cancer [16, 17].

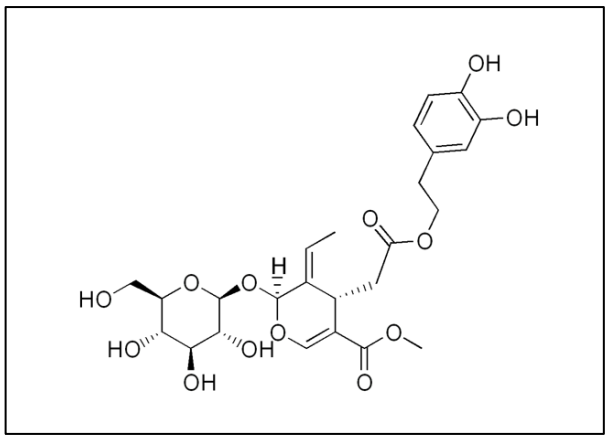

Figure 1. Chemical structure of oleuropein.

This study aimed to reveal the *in vitro* cytotoxic effects of probiotic-oleuropein combination on PC-3, a prostate cancer cell line. Thus, different concentrations of oleuropein were added to bacterial cultures and it was observed whether these concentrations showed any inhibition on *L. acidophilus* LA-5 (LA-5) or *L. rhamnosus* GG (GG). Then, cell-free supernatants of the probiotic bacteria grown on the presence of oleuropein were used to investigate its cytotoxic activity on PC-3 cell line.

2. Materials and Methods

2.1. Growth of probiotic bacteria in the presence of Oleuropein

Lactobacillus acidophilus LA-5 and *Lactobacillus rhamnosus* GG, which are kind gifts of Chr. Hansen, Turkey, were grown in Man, Rogosa and Sharpe (MRS) medium without shaking, at 37ºC [18]. The bacteria were divided into groups and treated with oleuropein. Oleuropein was not added to the control group (MRS only), and 50-250 µg/mL oleuropein was added to the treated groups in MRS medium. Bacteria were sub-cultured three times before the experiments.

2.2. Cell Culture

In the present study, androgen receptor negative human prostate cancer cell line PC-3 was used to investigate the effects of probiotics grown in the presence of oleuropein. Cells were grown in RPMI-1640 medium (containing %10 FBS, 0.1 mg/mL streptomycin, and 100 U/mL penicillin) in 75 cm^2 culture flasks in a humidified CO_2 incubator (%5 CO_2 + %95 O_2 at 37°C). 3-(4,5-dimetiltiazol–2-il)-diphenyl tetrazolium bromide assay (MTT Assay) was used to investigate the effects of cell-free supernatants of probiotics grown in the presence of oleuropein on prostate cancer cells [19].

2.3. MTT Method for Cytotoxic Investigation

PC-3 cells were seeded into 96-well plates ($15x10^3$ cells/well). The cells were treated with 10 times and 50 times diluted cell-free supernatants of probiotics grown with oleuropein (250 µg/mL) for 24 h at 37°C. 0.5 mg/mL MTT working solutions in sterile PBS, were added to each well, followed by incubation for 24 h (37°C). Then, excessive MTT was removed, washed with PBS, solubilized with DMSO, and OD at 550 nm was read with ELISA reader. Cell-free supernatants of probiotics grown without oleuropein were taken as control, while the absorbance of the cells treated with MRS medium without any growth diluted with RPMI-1640 was taken 100% cell viability [20]. The cell viabilities were determined by absorbance obtained from treated wells proportioned to the control absorbance values.

2.4. Statistical Analysis

Each experiment was conducted as at least three biological replicates and three technical replicates. All data were represented as mean ± S.D. Student's *t*-test was used to evaluate the significance in differences between treated and control groups. The significant differences were accepted when $p<0.05$.

3. Results and Discussion

Three different concentrations (50, 100, and 250 µg/mL) of oleuropein were used in the growth cultures of probiotic bacteria *L. acidophilus* LA-5 and *L. rhamnosus* GG and their effects on growth, surface hydrophobicity, and auto-aggregation properties of the bacteria were evaluated previously [21]. None of the oleuropein concentrations inhibited the growth of the bacteria. This indicates that even though oleuropein has significant inhibitory effects on pathogenic bacteria, it does not affect the probiotic growth, thus it has a potential to selectively inhibit the bacteria, making a good candidate for new formulations of functional foods, as well as to further study the interactions between oleuropein and probiotics [13, 14].

We previously showed that the surface hydrophobicity of LA-5 was significantly reduced ($p <0.05$) at 50 µg/mL concentration of oleuropein and increased at 100 µg/mL concentration [21]. In contrast, at only 100 µg/mL, it ($p <0.05$) decreased the surface hydrophobicity of GG bacteria compared to the control group. Bacterial surface hydrophobicity (*i.e.* adhesion to hydrophobic solvents) is an important feature for bacteria to retain in the gastrointestinal tract [22]. This is one of the factors providing better adhesion of probiotic bacteria to the mucosa. In the present study, it was found that oleuropein reduced or increased the surface hydrophobicity of LA-5 depending on the dose. Increased cell surface hydrophobicity at a concentration of 100 µg/mL may enable these bacteria to colonize the intestinal tract better to demonstrate their probiotic activity. Furthermore, although it is undesirable that the surface hydrophobicity of GG bacteria is reduced at the same concentration, other factors are important for the attachment of bacteria to the mucosa [23].

Auto-aggregation results showed there is statistically significant ($p <0.05$) decrease in aggregation of LA-5 bacteria at only 50 µg/mL concentration of oleuropein [21]. Bacterial aggregation is defined as the clustering of bacteria by adhering to each other [24]. The high amount of auto-aggregation may lead to better adhesion [25]. However, other factors that play a role in adhesion to the mucosa are proteins in the surface layer of bacteria, particularly S-layer proteins [26]. In this respect, the effects of oleuropein on mucosal adhesion of probiotic bacteria and also on surface proteins should be examined.

Prostate cancer is a leading health problem within the male individuals and has a high death rate [27]–[29]. Table 1 shows cell-free supernatants of probiotics possess *in vitro* cytotoxic activities against human prostate cell line PC-3.

When LA-5 grown without oleuropein, its cell free supernatant had no significant cytotoxic effects; however, when oleuropein added to the growth medium, the supernatant significantly ($p<0.05$) lowered the cell viability (Table 1). On the other hand, we wanted to show whether oleuropein itself has a cytotoxic effect, the results indicated that oleuropein does not possess any significant alteration on the cell viability. This indicates that LA-5 may metabolize oleuropein so that the metabolite can further lowered the cell viability. It is known that when oleuropein metabolized, hydroxytyrosol can be produced and hydroxytyrosol has anti-tumorigenic activities [30]. The metabolite of oleuropein, hydroxytyrosol, has been found to lower the viability PC-3 cells [31]. Once PC-3 cells were treated with hydroxytyrosol (80 µmol/L), it enhanced superoxide level and apoptotic cell death was induced [31]. It also showed a dose-dependent proliferation inhibition of prostate cancer cells (LNCaP and C4-2), by inducing G1/S cell cycle arrest, inhibiting cyclins cdk2/4 and D1/E, as well as inducing p21/p27 [32].
Cell-free supernatants of GG showed very high inhibition of PC-3 cell viability ($p<0.05$). There was no additional effect when oleuropein added to the growth medium.

Cytotoxicity results indicate that beneficial interactions between oleuropein and *L. acidophilus* LA-5 have been observed, thus when oleuropein is ingested through the diet, it is possible to be metabolized by *L. acidophilus* into more bioactive compounds. Or, new formulations including oleuropein and *L. acidophilus* can be more beneficial when compared to either bacteria or phenolic compound alone.

Natural compounds are of paramount importance as alternative drug investigations are gaining attention. Studies have showed that either plant extracts or pure compounds could be potential candidates for the development of novel therapeutic anticancer compounds [16, 17, 33-35]. Furthermore, lactic acid bacteria are known to be effective against cancer cells *in vitro* [20]. However, combination of two potential therapeutic agents (i.e. phenolics and probiotics) could be more effective as bacteria can modulate the bio-active compounds, as well bio-active compounds can modulate the probiotics, which has been shown in the present study.

Table 1. Cytotoxic effects of cell-free supernatants of probiotics grown with oleuropein (250 µg/mL) on prostate cancer PC-3 cells. The values are the mean of three biological replicates, given with standard deviation in parenthesis.

***L. acidophilus* LA-5**	**Relative Viability Percentage (S.D.)**
1/10 Diluted Medium Control	100 (9.06)
1/10 Diluted Control (without oleuropein)	87.32 (34.27)
1/10 Diluted Supernatant	57.14 (29.41) [a, b]
1/50 Diluted Medium Control	100 (8.99)
1/50 Diluted Control (without oleuropein)	93.80 (6.86)
1/50 Diluted Supernatant	86.66 (7.40) [a, b]
***L. rhamnosus* GG**	**Relative Viability Percentage (S.D.)**
1/10 Diluted Medium Control	100 (9.06)
1/10 Diluted Control (without oleuropein)	5.16 (0.92) [a]
1/10 Diluted Supernatant	5.54 (1.60) [a]
1/50 Diluted Medium Control	100 (8.99)
1/50 Diluted Control (without oleuropein)	83.96 (10.57) [a]
1/50 Diluted Supernatant	75.11 (18.65) [a]
Oleuropein (250 µg/mL)	**Relative Viability Percentage (S.D.)**
1/10 Diluted	96.88 (4.82)
1/50 Diluted	95.57 (3.11)

[a] Statistically significant ($p<0.05$) when compared to Medium Control.
[b] Statistically significant ($p<0.05$) when compared to Control (without oleuropein).

4. Conclusion

The present study aimed to gain insight into *in vitro* cytotoxic activities of combination of oleuropein and probiotic bacteria against prostate cancer cells. Oleuropein has dose-dependent effects on probiotic properties like auto-aggregation and surface hydrophobicity, as well the combination may show additional inhibitory activities against prostate cancer cells.

In conclusion, oleuropein and probiotic bacteria have the potential to increase the benefits of each other through a synbiotic interaction.

Acknowledgement
Chr. Hansen, Turkey is acknowledged for the probiotic strains.

Author's Contributions

Hasan Ufuk Celebioglu: Designed the study, drafted and wrote the manuscript, performed the experiment and result analysis.

Busenur Celebi: Performed the experiment, result interpretation and helped in manuscript preparation.

Yavuz Erden: Performed the experiment and result analysis, and helped in manuscript preparation.

Emre Evin: Performed the experiment, result interpretation and helped in manuscript preparation.

Orhan Adali: Assisted in analytical analysis on the structure, supervised the experiment's progress, result interpretation and helped in manuscript preparation.

Ethics
There are no ethical issues after the publication of this manuscript.

References

1. Roberfroid MB. 2000. A European Consensus of Scientific Concepts of Functional Foods, *Nutrition*, 16 (7-8): 689-144.
2. Hill C, Guarner F, Reid G, Gibson GR, Merenstein DJ, Pot B, Morelli L, Canani RB, Flint HJ, Salminen S, Calder PC, Sanders ME. 2014. Expert Consensus Document: The International Scientific Association for Probiotics and Prebiotics Consensus Statement on the Scope and Appropriate Use of the Term Probiotic, *Nature Reviews Gastroenterology and Hepatology*, 11 (Augst 2014): 9.
3. Uymaz B. 2010. Probiyotikler ve Kullanım Alanları, *Pamukkale Üniversitesi, Mühendislik Bilim Dergisi*, 16 (1): 2010, 95-104.
4. Gülgör G, Özçelik F. 2014. Bakteriyosin Üreten Laktik Asit Bakterilerinin Probiyotik Amaçlı Kullanımı, *Akademik Gıda*, 12 (1): 63-68.
5. Servin AL, Coconnier MH. 2003. Adhesion of Probiotic Strains to the Intestinal Mucosa and İnteraction with Pathogens, *Best Practice Research Clinical Gastroenterology*, 17 (5): 741-754.
6. Celebioglu HU, Svensson B. 2018. Dietary Nutrients, Proteomes, and Adhesion of Probiotic *Lactobacilli* to Mucin and Host Epithelial Cells, *Microorganisms*, 6 (3): 90.
7. Wichers HJ, Soler-Rivas C, Espin JC. 2000. Oleuropein and Related Compounds, *Journal of the Science of Food and Agriculture*, 80 (7): 1013-1023.
8. Servili M, Baldioli M, Selvaggini R, Macchioni A, Montedoro GF. 1999. Phenolic Compounds of Olive Fruit: One- and Two-Dimensional Nuclear Magnetic Resonance Characterization of Nuzhenide and its Distribution in the Constitutive Parts of Fruit, *Journal of Agricultural and Food Chemistry*, 47 (1): 12-18.
9. Omar SH. 2010. Oleuropein in Olive and its Pharmacological Effects, *Scientia Pharmaceutica*, 78 (2): 133-154.
10. Visioli F, Galli C, Galli G, Caruso D. 2002. Biological Activities and Metabolic Fate of Olive Oil Phenols, *European Journal of Lipid Science and Technology*, 104 (9-10): 677-684.

11. De la Puerta R, Domínguez MEM, Ruíz-Gutíerrez V, Flavill JA, Hoult JRS. 2001. Effects of Virgin Olive Oil Phenolics on Scavenging of Reactive Nitrogen Species and Upon Nitrergic Neurotransmission. *Life Sciences*, 69 (10): 1213-1222.

12. Saija A, Trombetta D, Tomaino A, Lo Cascio R, Princi P, Uccella N, Bonina F, Castelli F. 1998. *In-vitro* Evaluation of the Antioxidant Activity and Biomembrane Interaction of the Plant Phenols Oleuropein and Hydroxytyrosol, *International Journal of Pharmaceutics*, 166: 123-133.

13. Bisignano G, Tomaino A, Lo Cascio R, Crisafi G, Uccella N, Saija A. 1999. On the *In-vitro* Antimicrobial Activity of Oleuropein and Hydroxytyrosol, *Journal of Pharmacy and Pharmacology*, 51 (8): 971-4.

14. Fleming HP, Walter WM, Etchells JL. 1973. Antimicrobial Properties of Oleuropein and Products of its Hydrolysis From Green Olives, *Journal of Applied Microbiology*, 26 (5): 777-782.

15. Furneri PM, Marino A, Saija A, Uccella N, Bisignano G. 2002. *In vitro* Antimycoplasmal Activity of Oleuropein, *International Journal of Antimicrobial Agents*, 20 (4): 293-6.

16. Hamdi HK., Castellon R. 2005. Oleuropein, a Non-Toxic Olive Iridoid, is an Anti-Tumor Agent and Cytoskeleton Disruptor, *Biochemical and Biophysical Research Communications*, 334 (3): 769-78.

17. Menendez JA, Colomer R, Carrasco-Pancorbo A, Fernández-Gutiérrez A, Vazquez-Martin A, Brunet J, Villalba RG, Carretero AS. 2007. Olive Oil's Bitter Principle Reverses Acquired Autoresistance to Trastuzumab (HerceptinTM) in HER2-Overexpressing Breast Cancer Cells, *BMC Cancer*, 7 (1): 80.

18. Celebioglu HU, Delsoglio M, Brix S, Pessione E, Svensson B. 2018. Plant Polyphenols Stimulate Adhesion to Intestinal Mucosa and Induce Proteome Changes in the Probiotic *Lactobacillus acidophilus* NCFM, *Molecular Nutrition & Food Research*, 62 (4): 1-11.

19. Denizot F., Lang R.1986. Rapid Colorimetric Assay for Cell Growth and Survival. Modifications to the Tetrazolium Dye Procedure Giving Improved Sensitivity and Reliability, *Journal of Immunological Methods*, 89 (2): 271-7.

20. Thirabunyanon M, Boonprasom P, Niamsup P. 2009. Probiotic Potential of Lactic Acid Bacteria Isolated from Fermented Dairy Milks on Antiproliferation of Colon Cancer Cells, *Biotechnology Letters*, 31 (4): 571-6.

21. Celebioglu HU, Celebi B.. Zeytinyağı Fenoliklerinden Oleuropeinin Probiyotik *Lactobacillus acidophilus* ve *Lactobacillus rhamnosus* Bakterileri Üzerine Etkileri, Uluslararası Marmara Fen ve Sosyal Bilimler Kongresi, Fen Bilimleri Bildiriler Kitabı Cilt I, Kocaeli-Turkey, 2019, pp 429-436.

22. Krasowska A., Sigler K. 2014. How Microorganisms Use Hydrophobicity and What Does this Mean for Human Needs?, Frontiers in Cellular and Infection Microbiology, 4: 112.

23. Juge N. 2012. Microbial Adhesins to Gastrointestinal Mucus, *Trends in Microbiology*, 20 (1): 30-9.

24. Collado MC, Meriluoto J, Salminen S. 2007. Adhesion and Aggregation Properties of Probiotic and Pathogen Strains, *European Food Research and Technology*, 226 (5): 1065-1073.

25. An YH, Friedman RJ, An YH., Dickinson RB, Doyle RJ 2003. Mechanisms of Bacterial Adhesion and Pathogenesis of Implant and Tissue Infections. In: An YH and Friedman RJ Handbook of Bacterial Adhesion, Humana Press, Totowa, NJ, pp 1-27.

26. Ouwehand AC, Salminen S. 2003. *In vitro* Adhesion Assays for Probiotics and their İn vivo Relevance: a Review, *Microbial Ecology in Health and Disease*, 15 (4): 175-184.

27. Ferlay J., Steliarova-Foucher E., Lortet-Tieulent J., Rosso S., Coebergh J. W. W., Comber H., Forman D., Bray F. 2015. Reprint of: Cancer Incidence and Mortality Patterns in Europe: Estimates for 40 Countries in 2012, *European Journal of Cancer*, 51 (9): 1201-1202.

28. Siegel R., Ma J., Zou Z., Jemal A. 2014. Cancer Statistics, 2014, *CA: A Cancer Journal for Clinicians*, 64 (1): 9-29.

29. Cimino S, Sortino G., Favilla V., Castelli T., Madonia M., Sansalone S., Russo G., Morgio G. 2012. Polyphenols: Key Issues Involved in Chemoprevention of Prostate Cancer, *Oxidative Medicine and Cellular Longevity*, 2012: 632959.

30. Imran M., Nadeem M., Gilani S. A., Khan S., Sajid M. W., Amir R. M. 2018. Antitumor Perspectives of Oleuropein and Its Metabolite Hydroxytyrosol: Recent Updates, *Journal of Food Science*, 83 (7): 1781-1791.

31. Luo C., Li Y., Wang H., Cui Y., Feng Z., Li H., Li Y., Wang Y., Wurtz K., Weber P., Long J., Liu J. 2013. Hydroxytyrosol Promotes Superoxide Production and Defects in Autophagy Leading to Anti-proliferation and Apoptosis on Human Prostate Cancer Cells, *Current Cancer Drug Targets*, 13 (6): 625-39.

32. Zubair H., Bhardwaj A ., Ahmad A., Srivastava SK ., Khan M.A ., Patel GK ., Singh S . 2017. Hydroxytyrosol Induces Apoptosis and Cell Cycle Arrest and Suppresses Multiple Oncogenic Signaling Pathways in Prostate Cancer Cells, *Nutrition and Cancer*, 69 (6): 932-942.

33. Atmaca H., Çamlı Ç., Sert S. 2018. Ethanol Extract of Pinus nigra ssp. pallasiana var. şeneriana Inhibits Human Breast Cancer Cell Viability through Induction of Apoptosis, *Celal Bayar University Journal of Science*, 14 (1):35-40.

34. Atmaca H. 2017. Effects of Galium aparine Extract on the Angiogenic Cytokines and ERK1/2 Proteins in Human Breast Cancer Cells, *Celal Bayar University Journal of Science*, 13 (1):171-179.

35. Karakurt S., Adali O. 2016. Tannic Acid Inhibits Proliferation, Migration, Invasion of Prostate Cancer and Modulates Drug Metabolizing and Antioxidant Enzymes, *Anti-Cancer Agents in Medicinal Chemistry*, 16 (6):781-789.

Celal Bayar University Journal of Science

Synthesis and Characterization of Bisindandione Derivative Azo Dye, Experimental and Theoretical Investigation of Its Tautomeric Properties

Selin Kınalı-Demirci[1]*

[1] Department of Chemistry, Amasya University 05100 Amasya, TURKEY.
* selin.kdemirci@amasya.edu.tr

Received: 15 December 2019
Accepted: 17 March 2020
DOI: 10.18466/cbayarfbe.659611

Abstract

In this study, the synthesis, characterization, and tautomeric properties of 2,2'-bis(phenylazo)-5,5'-biindane-1,1',3,3'-tetrone, a new bisindandione derivative, were investigated. 2,2'-Bis(phenylazo)-5,5'-biindane-1,1',3,3'-tetrone was obtained after the diazo coupling reactions between [5,5'-biindane]-1,1',3,3'-tetrone and aniline, and characterized by Fourier Transform-Infrared, proton nuclear magnetic resonance, ultraviolet-visible and mass spectroscopy. The structural and spectroscopic analyses of azo dye were examined using Density Function Theory, and vibration frequencies calculated with the optimized structure were compared with experimental data. The obtained data showed that 2,2'-bis(phenylazo)-5,5'-biindane-1,1',3,3'-tetrone could be found in two tautomers, and the molar ratio of azo/hydrazo was found to be 0.86. The obtained data showed that the hydrazo form was dominant for 2,2'-bis(phenylazo)-5,5'-biindane-1,1',3,3'-tetrone.

Keywords: Azo dye, DFT, tautomer.

1. Introduction

Ninhydrin has proven itself as an important analytical tool in the fields of Chemistry, Biochemistry, and Forensic Sciences since its discovery in 1910 [1]. Ninhydrin is often used in the analysis of amino acids, peptides, and proteins. In 1954, it was found to be an important reagent for fingerprint identification on porous surfaces. Ninhydrin [2], discovered by Ruhemann by chance, reacts with amines and amino acids to form the colorful compound known by the specific name Ruhemann's purple [3,4]. Ninhydrin analogs are used to obtain a highly effective amino acid reagent in forensic and analytical applications. A large number of ninhydrin analogs have been synthesized through the extension of the conjugated system, insertion of various substituents, and improvements to have a fluorescence effect. These analogs usually involve oxidation of 1-indanone or 1,3-indandions [5]. 1,3-indandione and its derivatives used as the starting reagent for the synthesis of many important compounds is used in many fields of science and technology, such as drug synthesis [6], forensic chemistry for fingerprint detection [7], dyes and pigments [8-10], semi- and photo-conductors [11], and synthesis of non-linear optical materials [12]. Furthermore, the synthesis of different derivatives, the preparation of complexes, the examination of their theoretical properties, as well as, the investigation of their antimicrobial effects have taken place in the literature [13-18]. Although the [5,5'-Biindandion]-1,1',3,3'-tetron, a bisindandione compound, was first synthesized by Ozolina and Neilina in 1971, no another study on this compound has been encountered in the literature [19].

Azo dye is a large π conjugated molecular system. Azo dye molecules, electron-giving (D), and electron-accepting groups (A) are bound by a π conjugate binder (D-π-A molecular structure). Azo dyes with D-π-A chromosphere system have large π systems located along with the azo bonding between the receiver and donor units. Azo dyes are a class of colorants that are widely used in many areas, from textiles to non-textile applications [20,21]. Numerous studies have been reported that they are used in various fields such as dyeing textile fibres, coloring various materials, colored plastics and polymers, biological-medical studies and advanced applications in organic synthesis [22-28].

In this study, 3,3',4,4'-biphenyltetracarboxylic acid tetramethyl ester was synthesized by reacting with methanol and 3,3',4,4'-biphenyltetracarboxylic dianhydride in the acidic medium. This compound was reacted with freshly prepared sodium sand and ethyl acetate and a compound of [5,5'-biindane]-1,1',3,3'-tetrone was obtained. Subsequently, using aniline as a

diazonium component, a new disperse azo dye, 2,2'-bis(phenylazo)-5,5'-biindane-1,1',3,3'-tetrone compound was obtained via diazonium bonding reaction (Figure 1). The structure of the compound was illuminated by determining its characterization. Experimental findings were compared with theoretical results.

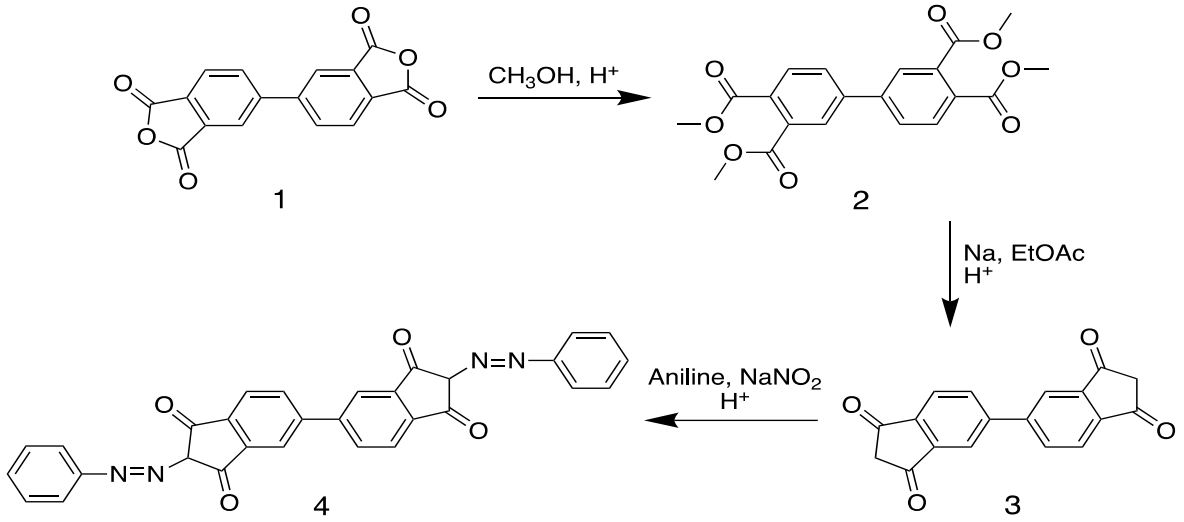

Figure 1. Synthesis of 2,2'-bis(phenylazo)-5,5'-biindane-1,1',3,3'-tetrone.

2. Experimental

2.1. Materials and Methods

3,3',4,4'-Biphenyltetracarboxylic dianhydride (**1**, 97%, Sigma-Aldrich), sodium (99.9%, Sigma-Aldrich), *p*-xylene (≥99%, Sigma-Aldrich), sodium nitrite (≥97%, Sigma-Aldrich), sodium hydroxide (≥98%, Sigma), methanol (≥99.9%, Sigma-Aldrich), ethyl acetate (99.8%, Sigma-Aldrich), aniline (≥99.5%, Sigma-Aldrich) and ethanol (≥99.8%, Sigma-Aldrich) were used as received without further purification. Infrared spectra were recorded using KBr in the Mattson 1000 Fourier Transform Infrared (FTIR) spectroscopy. Bruker Spectrospin Avance DTX 400 Ultra-Shield was used in DMSO-d_6 for proton nuclear magnetic resonance (^{1}H NMR) spectrometry, and Agilent 1100 MSD was used for mass spectrometry (MS). The ultraviolet-visible (UV-Vis) absorption spectra were measured on a Unicam UV2-100 spectrophotometer at the wavelength of maximum absorption in a range of solvents, including DMSO, DMF, methanol, acetonitrile, acetic acid and chloroform.

2.2. Synthesis

2.2.1. Synthesis of tetramethyl ester of 3,3',4,4'-biphenyltetracarboxyl acid (2)

3,3',4,4'-Biphenyltetracarboxylic dianhydride (**1**) (0.02 mol, 5.88 g) was taken into a 250 mL volumetric flask and heated under a condenser after 50 mL methanol added. At the end of 1 hour, the product, followed by thin-layer chromatography, was cooled at room temperature and 5 mL of the prepared with methanol was added with the help of separating funnel. The product was heated again for 4 hours under the condenser. At the end of the reaction, the product was cooled and poured into ice water. It was filtered and dried. It was purified by column chromatography using chloroform as eluent. Yield 80%, mp 95-97 °C.

2.2.2. Synthesis of [5,5'-biindane]-1,1',3,3'-tetron (3)

Sodium metal (1.22 g, 0.053 mol) was taken into a volumetric flask. It was heated under condenser in dry *p*-xylene. The sodium was melted and cooled. It was shaken to make sodium sand completely. Freshly prepared sodium sand was taken into a 250 mL volumetric flask. Then, **2** (0.013 mol, 5.12 g), 30 mL of ethyl acetate and 1 mL of methanol were added the flask. The red-colored mixture was heated under the condenser for 8 hours. Dark yellow precipitates were observed to form during the reaction. Then, 5 mL of ethanol was added on it, and the product was filtered. Obtained diethyl 1,1',3,3'-tetraoxo-[5,5'-biindan]-2.2'-dicarboxylate disodium salt was acidified with 10% H_2SO_4, cooled, filtered, and green-colored product was obtained. Yield 89%.

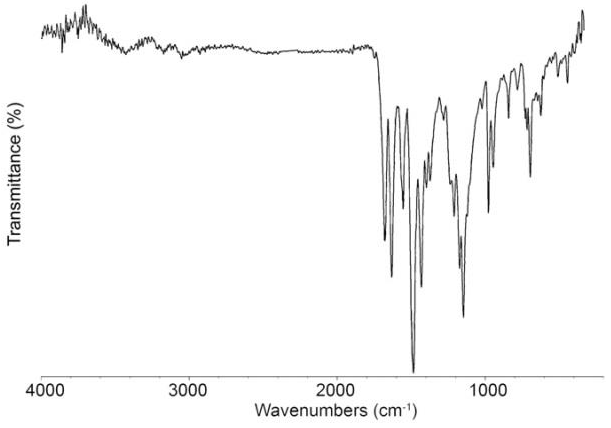

Figure 2. Experimental FTIR spectrum of the 2,2'-bis(phenylazo)-5,5'-biindane-1,1',3,3'-tetrone.

2.2.3. Synthesis of 2,2'-Bis(phenylazo)-5,5'-biindane-1,1',3,3'-tetrone (4)

Aniline (2 eq, 0.004 mol, 0.37 g) was dissolved in 5 mL of deionized water. Then, 4 mL of 36% HCl solution was added and cooled with ice bath. Sodium nitrite (2 eq, 0.004 mol, 0.28 g), which was dissolved in 5 mL of water, was added into the reaction mixture drop by drop. This prepared cold diazonium salt was added onto [5,5'-biindan]-1.1',3,3'-tetrone (**3**) (1 eq, 0.002 mol, 0.57 g), which is dissolved in dilute NaOH solution. Then pH was set to 8-9. It was mixed for 3 hours at room temperature, acidified, filtered, and crystallized with dimethyl sulfoxide. Yield 81%, mp: 243°C decomposition.

2.3. Theoretical Calculations

Density function theory calculations were performed using Gaussian 09W software [29], and molecular geometry was visualized with GaussView 5.0.9 [30]. The molecular structure of the 2,2'-bis(phenylazo)-5,5'-biindane-1,1',3,3'-tetrone compound was calculated using the DFT/B3LYP [31] method and the 6-31g(d) basis set. With the resulting optimized structure, vibration frequencies were calculated using DFT/B3LYP method.

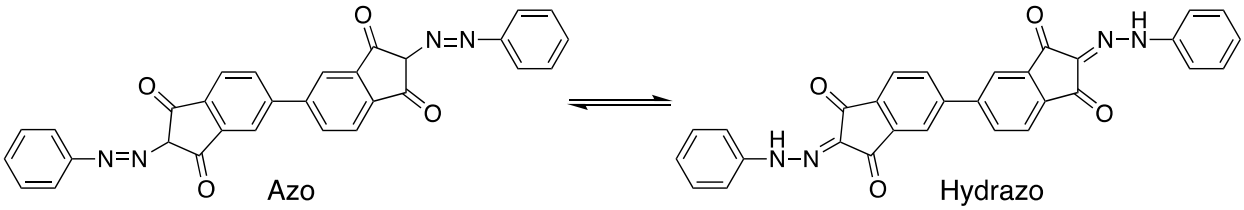

Figure 3. Tautomers of 2,2'-bis(phenylazo)-5,5'-biindane-1,1',3,3'-tetrone compound.

3. Results and Discussion

Synthesis of 2,2'-bis(phenylazo)-5,5'-biindane-1,1',3,3'-tetrone was performed in three steps, and the products obtained in each step were purified, and their yield were calculated. In the last step, 89% yield was obtained from 2,2'-bis(phenylazo)-5,5'-biindane-1,1',3,3'-tetrone as a result of diazonium coupling reaction between [5,5'-biindane]-1.1', 3,3'-tetrone and aniline. FTIR, ^{1}H NMR, UV-Vis and MS were used for the characterization of the resulting 2,2'-bis(phenylazo)-5,5'-biindane-1,1',3,3'-tetrone compound.

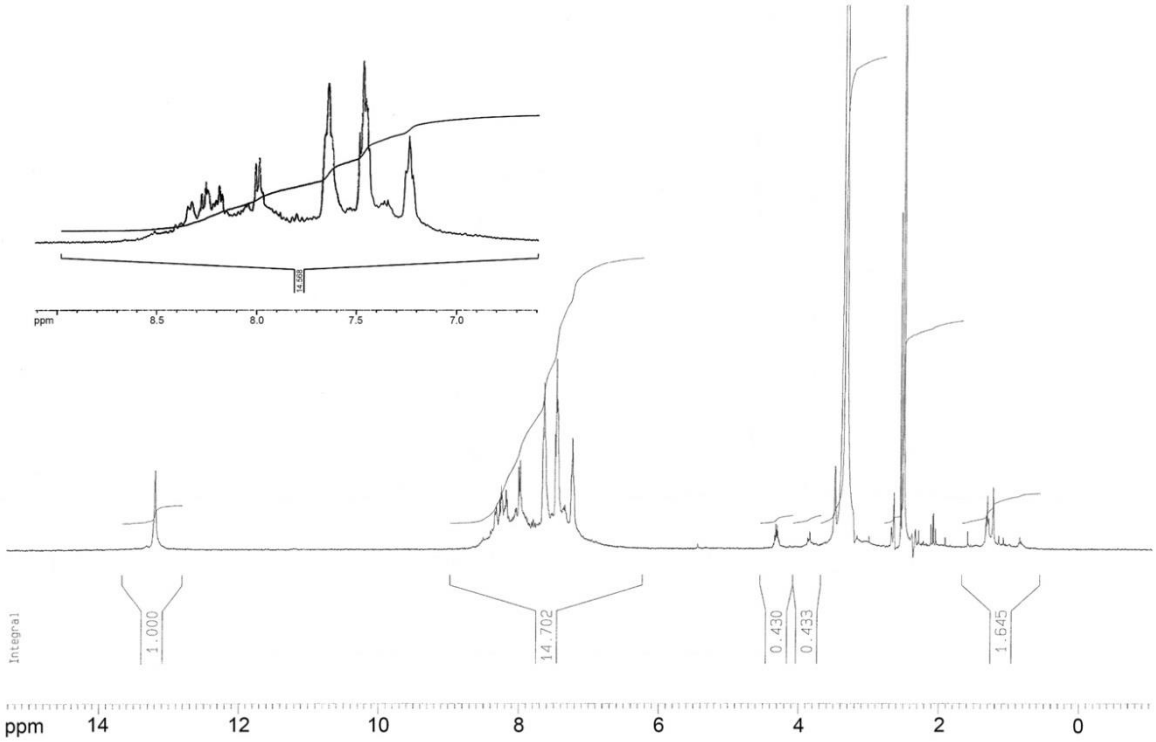

Figure 4. Experimental ^{1}H NMR spectrum of the 2,2'-bis(phenylazo)-5,5'-biindane-1,1',3,3'-tetrone.

Figure 2 shows the FTIR spectra of 2,2'-bis(phenylazo)-5,5'-biindane-1,1',3,3'-tetrone in the wavenumber region 4000-525 cm^{-1}. As seen, the absorption bands of azo dye appeared at around 3123, 1712 and 1660 cm^{-1} corresponding to the aromatic C-H, C=O and C=N stretching, respectively. The azo dye was characterized by the presence of the absorption band at 1560-1480 cm^{-1} assigned to N=N vibration [32]. At the same time, the presence of a weak band address to the N-H stretching at ~3200 cm^{-1} was determined. Azo dyes can be found in two possible tautomeric structures as azo and hydrazo (Figure 3). The bands of the N-H and C=N stretch observed at ~3200 and 1660 cm^{-1}, and the peaks of the N=N stretch indicate that the hydrazo and azo tautomers of the structure are together.

The ^{1}H-NMR spectrum of the 2,2'-bis(phenylazo)-5,5'-biindane-1,1',3,3'-tetrone in DMSO-d_6 is given in Figure 4. The aromatic protons were observed between 8.34 and 7.22 ppm. Two protons for azo form were observed at 4.31 and 3.89 ppm. However, hydrazo forms had two protons (N-H), and they were observed at 13.3 ppm. This result confirmed the FTIR results. The azo/hydrazo ratio was calculated by integrating the peak ratio of the characteristic chemical shifts (δ) corresponding to the azo and hydrazo by using the MestReNova v12.0.3. The integration of the characteristic peaks associated with azo (4.31-3.89 ppm) and hydrazo (13.3 ppm) were used to make the calculations. The molar ratio of azo/hydrazo was found to be 0.86. It was concluded that the hydrazo form is dominant for the 2,2'-bis(phenylazo)-5,5'-biindane-1,1',3,3'-tetrone. The mass of the 2,2'-bis(phenylazo)-5,5'-biindane-1,1',3,3'-tetrone compound ($C_{30}H_{18}N_4O_4$ m/z) was determined to be 498.40. The result is compatible with the theoretical (498.13) data.

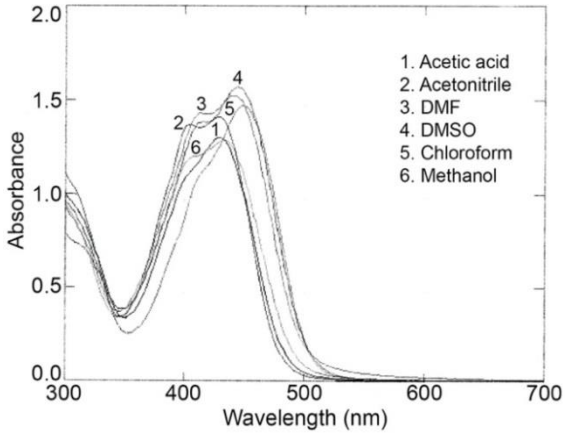

Figure 5. Absorption spectra of 2,2'-bis(phenylazo)-5,5'-biindane-1,1',3,3'-tetrone in various solvents.

The UV-Vis absorption spectra of the 2,2'-bis(phenylazo)-5,5'-biindane-1,1',3,3'-tetrone were recorded between 300-700 nm using a variety of solvents, and the results are shown in Figure 5. The absorption maxima of the dye were found to be independent of the solution phase and did not correlate with the dielectric constants of the solvents. 2,2'-Bis(phenylazo)-5,5'-biindane-1,1',3,3'-tetrone showed absorption maxima at 445 nm in DMSO, 441 nm in DMF, 433 nm in acetonitrile, 433 nm in methanol, 434 nm in acetic acid, and 445 nm in chloroform. There were no significant differences observed for absorption maxima. On the other hand, 2,2'-bis(phenylazo)-5,5'-biindane-1,1',3,3'-tetrone showed a maxima absorption peak with a shoulder in all solvents. It suggests that 2,2'-bis(phenylazo)-5,5'-biindane-1,1',3,3'-tetrone could be found in two tautomers. This result confirmed FTIR and ^{1}H-NMR results.

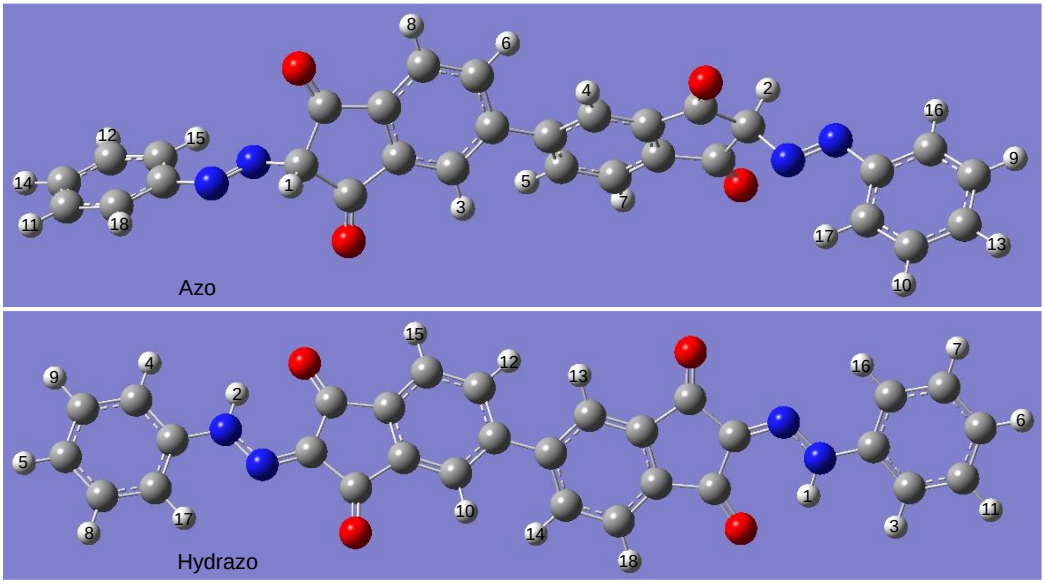

Figure 6. Optimized structures of azo and hydrazo forms of 2,2'-bis(phenylazo)-5,5'-biindane-1,1',3,3'-tetrone.

Table 1. The total energies calculated for the azo and hydrazo structures of the 2,2'-bis(phenylazo)-5,5'-biindane-1,1',3,3'-tetrone (E).

Tautomer	Total energy (a.u.)
Azo	-1673.84466610
Hydrazo	-1673.90499867

As mentioned above, azo dyes can be found in two possible tautomeric structures as azo and hydrazo. For both structures, the optimized structures obtained using the DFT/B3LYP method and the 6-31g(d) basis set are given in Figure 6. The total energies of azo and hydrazo structures were calculated using optimized structures and given in Table 1. When the calculated total energies were examined, it was determined that the hydrazo form for the compound 2,2'-bis(phenylazo)-5,5'-biindane-1,1',3,3'-tetrone was more stable. When the two tautomeric structures were examined, they were determined to be longer than the theoretical value (1.252 Å [33]) of diazene (HN=NH) bond length. The N=N bond length of azo form was determined to be 1.40 Å due to steric effects, while to be 1.2529 Å in the hydrazo structure.

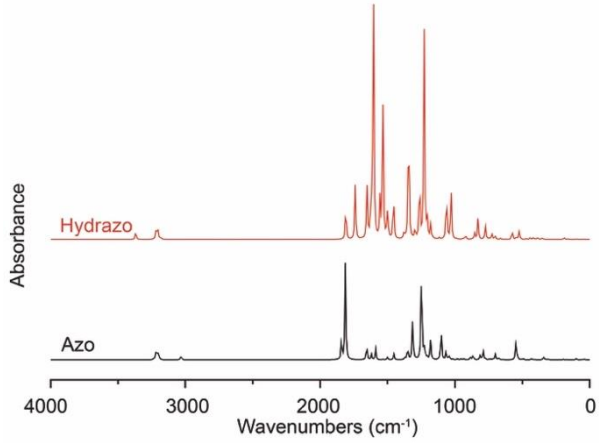

Figure 7. Theoretical FTIR spectra of 2,2'-bis(phenylazo)-5,5'-biindane-1,1',3,3'-tetrone compound.

The stable form of hydrazo was used in the calculation of the vibrational frequencies of the synthesized compound. Figure 7 contains the theoretical FTIR spectra for both tautomers of the 2,2'-bis(phenylazo)-5,5'-biindane-1,1',3,3'-tetrone compound. The wavenumbers calculated for the groups of -N-H and C=O were determined as 3368 cm^{-1} and 1810-1738 cm^{-1}, respectively. Compared to theoretical results, it shows that experimental results shift to a lower wavenumber of about 50-100 cm^{-1}. This lower shift makes it clear that strong hydrogen bonds are formed between the -N-H and C=O groups [22]. However, when the FTIR spectrum of azo form was examined, the characteristic band of N=N group was observed at 1588 cm^{-1}.

Table 2. Theoretical ^{1}H NMR data of azo and hydrazo forms of 2,2'-Bis(fenilazo)-5,5'-biindan-1,1',3,3'-tetrone.

Protons	Tautomer	
	Azo (ppm)	Hydrazo (ppm)
$H_{1Hydrazo}$	-	15.0059
$H_{2Hydrazo}$	-	14.9247
H_3	8.9224	8.2765
H_4	8.9106	8.2577
H_5	8.8158	8.2531
H_6	8.8050	8.2373
H_7	8.7376	8.1791
H_8	8.7333	8.1774
H_9	8.1367	8.0855
H_{10}	8.1311	8.0682
H_{11}	8.1023	8.0638
H_{12}	8.0570	8.0583
H_{13}	8.0432	8.0571
H_{14}	8.0158	8.0444
H_{15}	7.9681	8.0250
H_{16}	7.8655	8.0231
H_{17}	7.8583	8.0205
H_{18}	7.6393	8.0108
H_{1Azo}	5.9705	-
H_{2Azo}	5.5374	-

However, no bands were identified resulting from -N-H stretch. ^{1}H NMR spectra were obtained using the Gauge-including atomic orbital (GIAO) method given in Figure 6 for both optimized structures. Aromatic protons were observed between 8.3-7.0 ppm for both tautomers. Chemical shift values of protons in the ring to which carbonyl groups are attached in the azo

structure were calculated as 6.0-5.5 ppm. Protons belonging to hydrazo form (N-H) were observed in the range of 15.0-14.9 ppm, but no peak was observed in this region in the azo form. Theoretical ^{1}H NMR data for azo and hydrazo structures are given in Table 2.

4. Conclusion

In this study, synthesis and characterization of 2,2'-bis(phenylazo)-5,5'-biindane-1,1',3,3'-tetrone, a new bisindandione derivative, were performed. First, the compound **2** was obtained as a result of the reaction of the compound **1** with methanol in acidic medium, then, followed by the reaction with freshly prepared sodium sand and ethylacetate, compound **3** was obtained. At the last step, the synthesis of azo dye (**4**) was synthesized with 81% yield via a coupling reaction. The synthesized compound was characterized by FTIR, ^{1}H NMR, UV-Vis and MS. As a result of experimental and theoretical studies, it was determined that the hydrazo form of bisindandione derivatives was more stable than the azo form.

Acknowledgement

This work was supported in part by the Scientific Research Projects Coordination Unit of Amasya University (Project # FMB-BAP 14-089).

References

1. Joullié, MM, Thompson, TR, Nemeroff NH. 1991. Ninhydrin and ninhydrin analogs. Syntheses and applications. *Tetrahedron*; 47 (42): 8791-8830.

2. Ruhemann, S. 1996. CXXXII.-Cyclic di- and tri-ketones. *Journal of the Chemical Society Transactions*; 97: 1438-1449.

3. Khan, Z, Rafiquee, ZA, Khan, AA. 1996. Effect of Temperature, pH, Hydrindantin, Ascorbic Acid and Organic Solvents in the Colorimetric Estimation of a-Amino Acids with Ninhydrin. *Journal of the Indian Chemical Society*; 73 (6): 305-306.

4. Dietz, F, Rommel-Möhle, K, Schleitzer, A, Tyutyulkov, N. 1993. On the Chromophore of the Ninhydrin-Amino Acid Color Reaction. *Zeitschrift für Naturforschung B A Journal of Chemical Sciences*; 48 (8): 1133-1137.

5. Hark, RR, Hauze, DB, Petrovskais, O, Joullié, MM. 2001. Synthetic studies of novel ninhydrin analogs. *Canadian Journal of Chemistry*; 79:1632-1654.

6. Leblois, D, Piessard, S, Le Baut, G, Kumar, P, Brion, JD, Sparfel, L, Sanchez, RY, Juge, M, Petit, JY, Welin, L. 1987. Pyrophthalones VII. Synthesis and anti-inflammatory activity of 2-(4-pyridinyl)indane-1,3-diones diversely substituted on the benzene ring. *European Journal of Medicinal Chemistry*; 22 (3): 229-238.

7. Hansen, DB, Joullié, MM. 2005. The development of novel ninhydrin analogues. *Chemical Society Review*; 34: 408-417.

8. Bello, KA, Cheng, L, Griffiths, J. 1987. Perkin Transactions 2 Near-infrared absorbing methine dyes based on dicyanovinyl derivatives of indane-1,3-dione. *Journal of the Chemical Society*; 6: 815-818.

9. Li, X, Kim, SH, Son, YA. 2009. Optical properties of donor-π-(acceptor)$_n$ merocyanine dyes with dicyanovinylindane as acceptor group and triphenylamine as donor unit. *Dyes and Pigments*; 82: 293-298.

10. Hansen, DB, Joulie, MM. 2005. The development of novel ninhydrin analogues. *Chemical Society Reviews*; 34: 408-417.

11. Bryce, MR, Davies, SR, Hasan, M, Ashwell GJ, Szablewski, M, Drew, MGB, Short, R, Hursthouse, MB. 1989. Preparation and magnetic properties of a range of metal and organic cation salts of 2,3-dicyano-1,4-naphthoquinone (DCNQ). X-Ray crystal structure of (methyltriphenylphosphonium)$_1$(DCNQ)$_1$(H_2O)$_1$ and 2-dicyanomethylene-indan-1,3-dione (DCID). The rearrangement of DCID to DCNQ. *Journal of the Chemical Society, Perkin Transactions 2*; 9:1285-1292.

12. Seniutinas, G, Tomasiunas, R, Czaplicki, R, Sahraoui, B, Daskeviciene, M, Getautis, V, Balevicius, Z. 2012. Arylmethylene-1,3-indandione based molecular glasses: third order optical non-linearity. *Dyes and Pigments*; 95: 33-40.

13. Sarvesh, PK, Nizamuddin, K. 2008. Synthesis and Antimicrobial Study of Novel 1-Aryl-2-oxo- indano[3,2-d]pyrido/pyrimido[1,2-b]pyrimidines. *Archiv der Pharmazie - Chemistry in Life Sciences*; 341: 418-423.

14. Heravi, MM, Hosseini, T, Derikvand, F, Beheshtiha, SYS, Bamoharram, FF. 2010. $H_6P_2W_{18}O_{62}\cdot 18H_2O$-Catalyzed, Three-Component, One-Pot Synthesis of Indeno[1,2-b]quinoline-7-one Derivatives. *Synthetic Communications*; 40: 2402-2406.

15. Ahmedova, A, Atanasov, V, Marinova, P, Stoyanov, N, Mitewa, M. 2009. Synthesis, characterization and spectroscopic properties of some 2-substituted 1,3-indandiones and their metal complexes. *Central European Journal of Chemistry*; 7 (3): 429-438.

16. Ahmedova, A, Marinova, P, Ciattini, S, Stoyanov, N, Springborg, M, Mitewa, M. 2009. A combined experimental and theoretical approach for structural study on a new cinnamoyl derivative of 2-acetyl-1,3-indandione and its metal(II) complexes. *Journal of Structural Chemistry*; 20: 101-111.

17. Riahi, S, Ganjali, MR, Moghaddam, AB, Norouzi, P, Saied Saeed Hosseiny Davarani, SSH. 2008. Structural study of 2-(1-oxo-1 *H*-inden-3-yl)-2*H*-indene-1,3-dione by DFT calculations, NMR and IR spectroscopy. *Spectrochimica Acta Part A: Molecular and Biomolecular Spectroscopy*; 70: 94-98.

18. Gulbinas, V, Karpicz, R, Muzikante, I, Valkunas, L. 2010. Fluorescence quenching by trapped charge carriers in N,N-dimethylaminobenzylidene 1,3-indandione films. *Thin Solid Films*; 518: 3299–3304.

19. Ozalina, V, Neilands, O. 1971. Analogs of 2-methoxycarbonyl-1,3-indandione in the diphenyl and diphenyl oxide series. *Latvijas PSR Zinatnu Akademijas Vestis, Kimijas Serija*; 2: 235-240.

20. Çelik Erbaş, S, Gülle, S. 2018. Synthesis and photophysical behaviours of novel phenanthro[9,10-*d*] imidazole substituted azo dyes in solvent media. *Celal Bayar University Journal of Science;* 14: 285-289.

21. El-Shishtawy, RM, Borbone, F, Al-amshany, ZM, Tuzi, A, Barsella, A, Asiri, AM, Roviello, A. 2013. Thiazole azo dyes with lateral donor branch: Synthesis, structure and second order NLO properties. *Dyes and Pigments*; 96: 45-51.

22. Kinali, S, Demirci, S, Calisir, Z, Kurt, M, Atac, A. 2011. DFT, FT-IR, FT-Raman and NMR studies of 4-(substituted phenylazo)-3,5-diacetamido-1H-pyrazoles. *Journal of Molecular Structure*; 993(1-3): 254-258.

23. Kinali-Demirci, S, Demirci, S, Kurt, M. 2013. Synthesis, structure characterization and antimicrobial evaluation of 4-(substituted

phenylazo)-3,5-diacetamido-1H-pyrazoles. *Spectrachimica Acta-Part A: Molecular and Biomolecular Spectroscopy*; 106: 12-18.

24. Catino, SC, Farris, RE. Azo dyes. In: Grayson M (ed) Concise encyclopedia of chemical technology. John Wiley and Sons, New York, 1985, pp 142-144.

25. Zollinger, H. Color chemistry: Synthesis, properties and applications of organic dyes and pigments, 3rd, revised edition Wiley-VCH, 2003.

26. Kim, JP, Kim, JS, Park, JS, Jang, SS, Lee, JJ. 2016. Synthesis of temporarily solubilised azo disperse dyes containing a ß-sulphatoethylsulphonyl group and dispersant-free dyeing of polyethylene terephthalate fabric. *Coloration Technology*; 132: 368-375.

27. Mungmeechai, T, Jantip, S, Suwanruji, P. 2010. Study of the relationships between the chemical structures of azo disperse dyes and their dyeing properties on polyester. *Advanced Materials Research*; 93-94: 332-335.

28. Pazarbaşı, MB, Karaboz, İ, Koçyiğit, A, Özdemir, G, Yaşa, İ. 2011. The use of *Pleurotus ostreatus* MCC07 strain in decolorization of various dyes used in leather industry. *Celal Bayar University Journal of Science;* 7: 21-30.

29. Gaussian 09, Revision A.1, Frisch, MJ, Trucks, GW, Schlegel, HB, Scuseria, GE, Robb, MA, Cheeseman, JR, Scalmani, G, Barone, V, Mennucci, B, Petersson, GA, Nakatsuji, H, Caricato, M, Li, X, Hratchian, HP, Izmaylov, J. Bloino, AF, Zheng, G, Sonnenberg, JL, Hada, M, Ehara, M, Toyota, K, Fukuda, R, Hasegawa, J, Ishida, M, Nakajima, T, Honda, Y, Kitao, O, Nakai, H, Vreven, T, Montgomery Jr., JA, Peralta, JE, Ogliaro, F, Bearpark, M, Heyd, JJ, Brothers, E, Kudin, KN, Staroverov, VN, Kobayashi, R, Normand, J, Raghavachari, K, Rendell, A, Burant, JC, Iyengar, SS, Tomasi, J, Cossi, M, Rega, N, Millam, JM, Klene, M, Knox, JE, Cross, JB, Bakken, V, Adamo, C, Jaramillo, J, Gomperts, R, Stratmann, RE, Yazyev, O, Austin, AJ, Cammi, R, Pomelli, C, Ochterski, JW, Martin, RL, Morokuma, K, Zakrzewski, VG, Voth, GA, Salvador, P, Dannenberg, JJ, Dapprich, S, Daniels, AD, Farkas, O, Foresman, JB, Ortiz, JV, Cioslowski, J, Fox, DJ. Gaussian, Inc., Wallingford CT, 2009.

30. Dennington, R, Keith, T, Millam, J. GaussView, Version 5 Semichem Inc., Shawnee Mission KS, 2009.

31. Vural, H, İdil, Ö. 2019. Synthesis, spectroscopic investigation and biological activities of copper(II) complex of 2-(2,4-difluorophenyl)pyridine: A combined theoretical and experimental study. *Journal of Molecular Structure*; 1177: 242-248.

32. Ajaz, M, Rehman, A, Khan, Z, Nisar, MA, Hussain, S. 2019. Degradation of azo dyes by Alcaligenes aquatilis 3c and its potential use in the wastewater treatment. *AMB Express*; 9: 64.

33. Snehalatha, M, Ravikumar, C, Joe, IH, Sekar, N, Jayakumar, VS. 2009. Spectroscopic analysis and DFT calculations of a food additive Carmoisine. *Spectrachimica Acta-Part A: Molecular and Biomolecular Spectroscopy*; 72: 654-662.

Celal Bayar University Journal of Science

Iterative Perturbation Technique for Solving a Special Magnetohydrodynamics Problem

Sinan Deniz[1*]

Manisa Celal Bayar University, Department of Mathematics, Manisa/TURKEY
[*]sinan.deniz@cbu.edu.tr

Received: 8 October 2019
Accepted:17 March 2020
DOI: 10.18466/cbayarfbe.630780

Abstract

In this study, we use iterative perturbation technique for struggling MHD Jeffery-Hamel flow problem for some special values of Re and Ha numbers. This problem aroused from the classical work by Navier and Stokes and their equations. We exploit Maxwell's electromagnetism governing equations via reducing them to nonlinear differential equations to reform the main problem. After simplifying the well-known equation, we get a basic problem and we can readily investigate the emerged problem. In order to check the power of the technique, we prove that the results are well agreed with the numerical solutions. The present graphics prove that perturbation iteration technique has high accuracy for different α, Ha and Re numbers.

Keywords: Fluid mechanics, Jeffery-Hamel flows, perturbation iteration method.

1. Introduction

In many fields of engineering, it is very crucial to analyze an incompressible viscous fluid. These fluids generally have been occurred in nonparallel walls. Additionally, liquids through convergent-divergent channels are one of the most applicable cases in fluid mechanics. All these afore mentioned models have been criticized in civil, electronic and ocean engineering problems [1]. Besides all of that, one needs to model all these types of equations to handle the mathematical cases and correspondingly the real phenomena of the physical situations. The mathematical analysis of that problem was also extensively studied by two successful researchers Jeffery and Hamel (J-H) in 1916 [2,3]. On the other hand, the term of magnetohydrodynamic (MHD) was first used in 1970 [4]. Additionally, the aforementioned J-H flows are an exact similarity solution of the Navier and Stokes equations. Especially, these equations appear in the special case of two-dimensional (2-D) flow through a channel with inclined plane walls. These walls have been considered as meeting at a vertex with a source. Or it can be sink at the vertex [5]. Many researchers have studied to get approximate solutions to this flow problem. Most of them encounters with the highly difficult nonlinear terms and nonhomogeneous power terms. In order to get well-enough solutions, they use numerical techniques [1-4].

It is well known that there are many linear and nonlinear differential equations which are used in the study of several fields for example engineering, chemistry, physics, etc. The solutions of these equations can provide more information about the described process. However, because of the complexity of the nonlinear differential equations such as Jeffery-Hamel flows and other fluid problems, it is complicated to get the exact solutions. Therefore, a broad class of semi -analytical and analytical techniques have been proposed to solve these types of equations such as variational iteration method (VIM) [6], Adomian decomposition method (ADM) [7]. Besides these semi-analytical methods there are some semi-numerical techniques such as homotopy analysis method (HAM) [8], optimal homotopy asymptotic method [9]. Pandır has used generalized F expansion method for solving to Sine-Gordon equation [10]. Sezer et al. have implemented many kinds of collocation methods in their papers [11-12]. Inan has implemented exponential finite difference technique to nonlinear equations [13]. Lie symmetry is applied to handle ordinary differential equations [14]. In addition to these techniques, the well-known perturbation method has been recently used to construct the perturbation iteration method. This new effective technique has been used to solve some strongly nonlinear systems and yields better results than many other methods in literature [15-19]. Besides all these, stability analysis of these methods is very crucial concept to understand the qualitative idea behind the

methods. Therefore, many papers are devoted analyzing uniform continuity, convergence and stability analysis for all these types of techniques [20].

Geometrical analysis for many real word phenomena is also very important such as in fluid dynamics. For instance, null quaternionic rectifying curves and null quaternionic similar curves in special Minkowski space has been discussed by Kahraman in 2018 [21]. He also studied null quaternionic slant helices in Minkowski Spaces in 2019 [22]. In 2004, Hopkins et. al have investigated the effects of arterial geometry on aneurysm growth as three-dimensional computational fluid dynamics study [23]. Besides all that, approximate solutions for MHD squeezing fluid flow has been obtained by Akgül [24]. Reproducing kernel Hilbert space method based on reproducing kernel functions for investigating boundary layer flow of a Powell–Eyring non-Newtonian fluid has been also used by same author [25]. Solitary wave solutions of time–space nonlinear fractional Schrödinger's equation has been analyzed via two analytical approaches in [26]. Akgül has also published a paper about fluid equations including reproducing kernel Hilbert space method to solve MHD Jeffery-Hamel flows problem in nonparallel walls [26, 27].

2. Mathematical Formulation of Jeffery-Hamel Flow

In this part of the paper, we analyze the analytical plan with the help of fluid flow equation problems. They have been reviewed by many scientists in the literature [1-5]. We take the immovable and fixed two-dimensional (2-D) flow. Of course, these flows have been existed with incompressible conducting viscous fluid. These fluids arise from a source or sink. We also suppose that these phenomena occur at the intersection between two rigid plane walls. The angle between these walls are taken as 2α. The rigid walls are taken to be divergent if $\alpha > 0$. Reversely, convergent if $\alpha < 0$. We now imagine that the velocity is only along the radial direction and depends on r and θ so that $\mathbf{v} = (u(r;\theta); 0)$. Using continuity and the Navier-Stokes equations in polar coordinates,

$$\frac{\rho}{r}\frac{\partial}{\partial r}(ru(r,\theta)) = 0, \tag{2.1}$$

$$u(r,\theta)\frac{\partial u(r,\theta)}{\partial r} = -\frac{1}{p}\frac{\partial P}{\partial r} + \nu\left[\nabla^2 u(r,\theta) - \frac{u(r,\theta)}{r^2}\right] - \frac{\sigma B_0^2}{\rho r^2}u(r,\theta)$$

$$= -\frac{1}{p}\frac{\partial P}{\partial r} + \nu\left[\frac{\partial^2 u(r,\theta)}{\partial r^2} + \frac{1}{r}\frac{\partial u(r,\theta)}{\partial r} + \frac{1}{r^2}\frac{\partial^2 u(r,\theta)}{\partial \theta^2} - \frac{u(r,\theta)}{r^2}\right] - \frac{\sigma B_0^2}{\rho r^2}u(r,\theta), \tag{2.2}$$

$$0 = -\frac{1}{\rho r}\frac{\partial P}{\partial \theta} + \frac{2\nu}{r^2}\frac{\partial u(r,\theta)}{\partial \theta}. \tag{2.3}$$

Here P denotes the fluid pressure. The constant B_0 represents the electromagnetic induction and σ symbols the conductivity of the fluid. As in many papers, ρ denotes the fluid density. Finally, ν shows the coefficient of kinematic viscosity. The continuity Eq. (1) implies that

$$u(\theta,r) = \frac{f(\theta)}{r} \tag{2.4}$$

For simplification, we can use the following dimensionless parameters,

$$D(x) = \frac{f(\theta)}{f_{max}} \text{ where } x = \frac{\theta}{\alpha} \tag{2.5}$$

and eliminating P between Eqs. (2.2) and (2.3), we obtain an ordinary differential equation for the normalized function profile $D(x)$:

$$D'''(x) + 2\alpha^2\frac{f_{max}}{\nu}D(x)D'(x) + \left(4 - \sqrt{\sigma\frac{B_0^2}{\rho\nu}}\right)\alpha^2 D'(x) = 0 \tag{2.6}$$

or equivalently

$$D''' + 2\alpha ReDD' + (4 - Ha)\alpha^2 D' = 0 \tag{2.7}$$

Since one has a symmetric geometry here, we can take the boundary conditions as follows

$$D(0) = 1,\ D'(0) = 0,\ D(1) = 0. \tag{2.8}$$

3. A Short Description of the Perturbation Iteration Method

In this section, we give a short description of the perturbation iteration technique. For much more information, we refer to the papers [16-18]. This technique was firstly introduced by Pakdemirli et al. and applied to many types of nonlinear problems [28-30].

Celal Bayar University Journal of Science
Volume 16, Issue 1, 2020, p 69-74
Doi: 10.18466/cbayarfbe.630780

Many different kinds of ordinary and partial differential equations are solved by using perturbation iteration techniques and even fractional differential equations are also considered modified forms of this method [31-38].

Consider the following third order nonlinear differential equation:

$$F\left(D''', D', D, \varepsilon\right) = 0 \tag{3.1}$$

where $D = D(x)$. Here ε is the perturbation parameter. To obtain perturbation iteration algorithms (PIA), we will use only one correction term from classical perturbation expanding as

$$D_{n+1} = D_n + \varepsilon\left(D_c\right)_n \tag{3.2}$$

where $n \in \mathrm{N} \cup \{0\}$ and $\left(D_c\right)_n$ is the n th correction term of the iteration algorithm. Upon substitution of (3.2) into (3.1) then expanding it in a Taylor series with *n*th derivatives yields the PIA $-n$'s. With only first derivatives, we have PIA-1 as

$$\begin{aligned} &F + F_D(D_c)_n\varepsilon + F_{D'}(D_{c'})_n\varepsilon \\ &+F_{D''}(D_{c''})_n\varepsilon + F_\varepsilon\varepsilon = 0 \end{aligned} \tag{3.3}$$

where subscripts of *F* symbolize partial differentiation. Note here that all derivatives and functions are computed at $\varepsilon = 0$. We can now start to iterate. First of all, we require a trial function which is called D_0. This function can be chosen judiciously according to the given described conditions. After this step, $\left(D_c\right)_0$ is evaluated from the algorithms (3.3) with the help of D_0 and recommended condition(s). After this step, the first approximate PIM solution D_1 is obtained by using $\left(D_c\right)_0$ and so on.

4. Pim Solutions for Jeffery-Hamel Flow

Let us now apply OPIM to Jeffery-Hamel flow. Artificial perturbation parameter is inserted to Eq. (2.7) as follows:

$$\begin{aligned} &F\left(D''', D', D, \varepsilon\right) = D''' + 2\varepsilon\alpha ReDD' \\ &+\varepsilon(4 - Ha)\alpha^2 D' = 0. \end{aligned} \tag{4.1}$$

Using the Eqs. (3.2) and (3.3) and setting $\varepsilon = 1$ we get the following perturbation iteration algorithm:

$$\begin{aligned} &(D_c)_{n'''} = \\ &-\left(D_{n'''} + 2\alpha ReD_nD_{n'} + (4 - Ha)\alpha^2 D_{n'}\right). \end{aligned} \tag{4.2}$$

As a starting function we can use

$$D_0 = 1 - x^2 \tag{4.3}$$

which satisfies the boundary conditions (2.8). Substituting D_0 into Eq. (4.2) gives a first-order problem:

$$(D_c)_0''' = 2\alpha^2(4 - \mathrm{Ha})x + 4\alpha\mathrm{Re}x\left(1 - x^2\right). \tag{4.4}$$

By solving (4.4), first correction term is obtained as:

$$(D_c)_0 = \frac{1}{60}\begin{pmatrix} -5\alpha^2\mathrm{Ha}x^4 + 5\alpha^2\mathrm{Ha}x^2 \\ -2\alpha\mathrm{Re}x^6 + \\ 10\alpha\mathrm{Re}x^4 - 8\alpha\mathrm{Re}x^2 \\ +20\alpha^2x^4 - 20\alpha^2x^2 \end{pmatrix}. \tag{4.5}$$

Thus, the first approximate solution is

$$D_1 = 1 - x^2 + \frac{1}{60}\begin{pmatrix} -5\alpha^2\mathrm{Ha}x^4 + 5\alpha^2\mathrm{Ha}x^2 \\ -2\alpha\mathrm{Re}x^6 + 10\alpha\mathrm{Re}x^4 \\ -8\alpha\mathrm{Re}x^2 + 20\alpha^2x^4 \\ -20\alpha^2x^2 \end{pmatrix}. \tag{4.6}$$

Proceeding as mentioned in previous section, one can get second order solution and so on.

Higher order iterations can be reached in a similar manner. Manifestly, the more iterations, the more approximate solution becomes more sophisticated, which wants powerful computer programs. We use Mathematica 9.0 to handle the complex computations throughout this study.

In [5], optimal homotopy asymptotic method is used to get the second order approximate solution for $\alpha = \frac{\pi}{36}, Ha = 0$ and $Re = 50$.

In the following plots and tables, a comparison of the OHAM, PIM and the numerical results is shown. It is also clear from figure 4.1 and tables that PIM solutions are better than those of OHAM solutions. Figures 4.2 - 4.3 show the magnetic field effect on the velocity profiles for convergent and divergent channels for some fixed Reynolds, Hartmann numbers with angels α's.

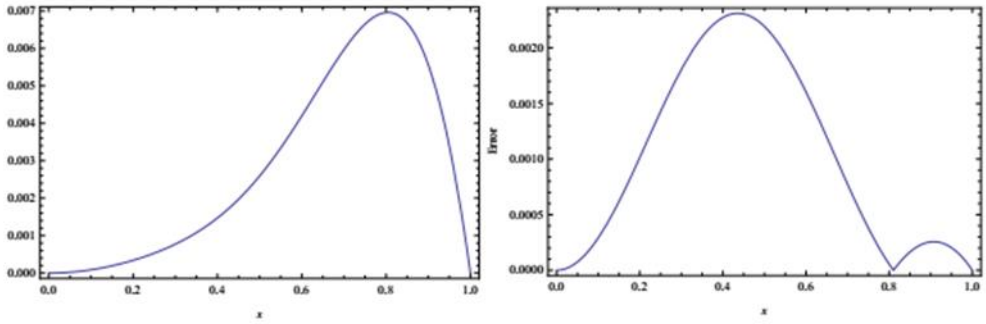

(a) Errors for OHAM (b) Errors for PIM

Figure 4.1: Comparison of the absolute erros obtained by second order OHAM and PIM approximate solutions

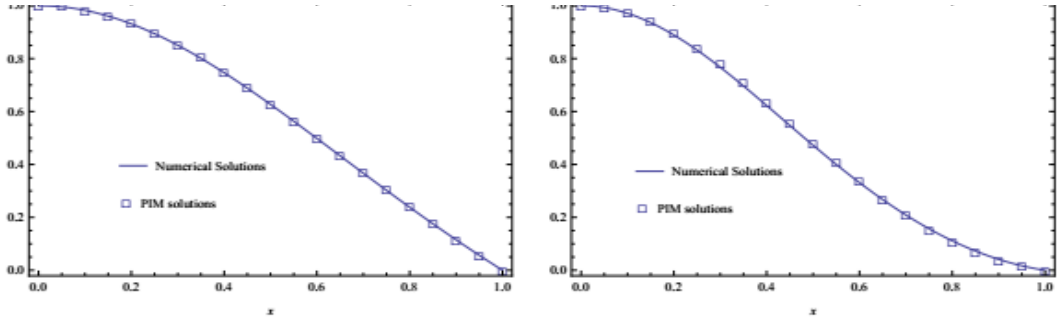

(a) $Re = 50$ (b) $Re = 100$

Figure 4.2: Comparison of the numerical results against the second order PIM approximation for the velocity profile using $\alpha = \dfrac{\pi}{36}$ and $Ha = 0$ for different Reynolds numbers

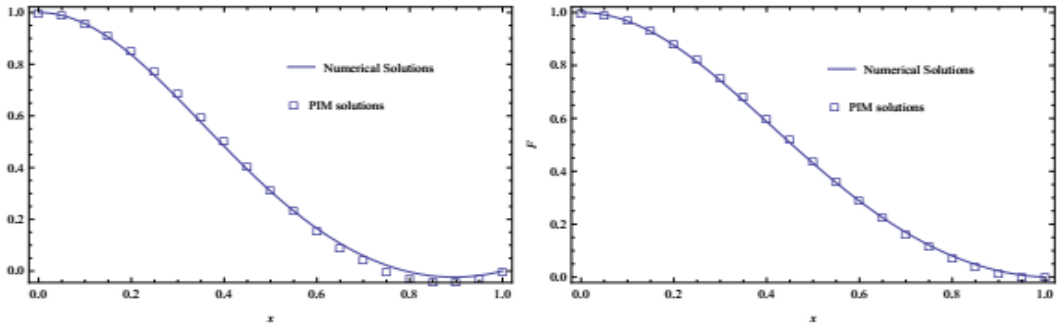

(a) $\alpha = \dfrac{\pi}{18}$ (b) $\alpha = \dfrac{\pi}{24}$

Figure 4.3: Comparison of the numerical results against the second order PIM approximation for the velocity profile using $Re = 75$ and $Ha = 0$ for different α

Table 1. Absolute errors for sixth order PIM solutions for different Reynolds and Hartmann numbers.

x	Re= 175, Ha=5	Re=200, Ha=5	Re=50, Ha= 10	Re=50, Ha=20
0.1	3.124×10^{-6}	4.632×10^{-7}	7.111×10^{-5}	2.044×10^{-5}
0.2	8.052×10^{-6}	1.057×10^{-7}	8.041×10^{-5}	6.034×10^{-5}
0.3	8.711×10^{-7}	1.086×10^{-7}	2.222×10^{-6}	4.706×10^{-6}
0.4	5.011×10^{-8}	2.997×10^{-7}	6.411×10^{-6}	7.055×10^{-6}
0.5	2.058×10^{-6}	5.088×10^{-7}	6.520×10^{-6}	3.524×10^{-6}
0.6	2.779×10^{-7}	2.410×10^{-6}	6.030×10^{-5}	4.001×10^{-5}
0.7	3.087×10^{-6}	5.085×10^{-6}	1.005×10^{-6}	3.041×10^{-5}
0.8	3.045×10^{-7}	6.047×10^{-6}	8.006×10^{-5}	7.770×10^{-5}
0.9	4.056×10^{-6}	8.047×10^{-6}	9.056×10^{-5}	9.055×10^{-5}

Table 2. Absolute errors for sixth order OHAM solutions for different Reynolds and Hartmann numbers.

x	Re= 175, Ha=5	Re=200, Ha=5	Re=50, Ha= 10	Re=50, Ha=20
0.1	5.004×10^{-5}	1.018×10^{-4}	5.032×10^{-4}	2.005×10^{-4}
0.2	2.067×10^{-4}	9.044×10^{-6}	4.502×10^{-4}	5.660×10^{-4}
0.3	8.046×10^{-6}	4.222×10^{-6}	5.177×10^{-5}	9.995×10^{-6}
0.4	1.110×10^{-6}	5.002×10^{-6}	9.025×10^{-5}	9.755×10^{-6}
0.5	8.096×10^{-6}	9.023×10^{-6}	5.023×10^{-5}	1.067×10^{-5}
0.6	1.009×10^{-6}	2.055×10^{-5}	5.023×10^{-6}	5.905×10^{-4}
0.7	9.066×10^{-5}	7.502×10^{-6}	6.024×10^{-3}	1.010×10^{-3}
0.8	4.068×10^{-6}	5.065×10^{-6}	2.014×10^{-4}	6.012×10^{-4}
0.9	9.098×10^{-7}	2.023×10^{-6}	5.014×10^{-4}	7.463×10^{-4}

5. Conclusion and Results

In this study, we implement perturbation iteration method to find the approximate solutions of nonlinear differential equation governing Jeffery-Hamel flow. Our results clearly demonstrate that PIM can solve nonlinear problems with successive rapidly convergent approximations without any restrictive assumptions or transformations causing changes in the physical definition of the considered problem. One of the fundamental advantages of this method is to be applicable directly to the nonlinear terms. Also, resulting equations can also be solved by using simple analytical methods. We also make a comparison with the OHAM solution and see that PIM is more useful because it reduces the size of calculations and also its iterations are direct and straightforward. The figures and tables also reveal that new solutions agree very well with the numerical solutions obtained from Mathematica 9.0. Finally, we can say that PIM can be safely used to handle fluid mechanics and other problems in engineering.

Ethics

There are no ethical issues after the publication of this manuscript.

References

1. Eagles, P. 1966. The stability of a family of Jeffery-Hamel solutions for divergent channel flow. *Journal of Fluid Mechanics;* 24(1): 191-207.

2. Jeffery, GB. 1915. The two-dimensional steady motion of a viscous fluid. *The London, Edinburgh, and Dublin Philosophical Magazine and Journal of Science*; 29(172): 455-465.

3. Hamel, G. 1917. Spiralförmige Bewegungen zäher Flüssigkeiten. *Jahresbericht der deutschen mathematiker-vereinigung*; 25: 34-60.

4. Alfvén, H, Arrhenius, G. 1970. Structure and evolutionary history of the solar system. *Astrophysics and Space Science*; 8(3): 338-421.

5. Esmaeilpour, M, Ganji, DD. 2010. Solution of the Jeffery-Hamel flow problem by optimal homotopy asymptotic method. *Computers & Mathematics with Applications;* 59(11): 3405-3411.

6. He, J. H. 1999. Variational iteration method–a kind of non-linear analytical technique: some examples. *International journal of non-*
7. El-Tawil, MA, Bahnasawi, AA, Abdel-Naby, A. 2004. Solving Riccati differential equation using Adomian's decomposition method. Applied Mathematics and Computation; 157(2): 503-514.

8. Liao, S. 2004. On the homotopy analysis method for nonlinear problems, Applied Mathematics and Computation; 147(2): 499-513.

9. Marinca, V, Herişanu, N. 2008. Application of optimal homotopy asymptotic method for solving nonlinear equations arising in heat transfer. International Communications in Heat and Mass Transfer; 35(6): 710-715.

10. Pandir, Y. 2018. A New Type of Generalized F-Expansion Method and its Application to Sine-Gordon Equation. Celal Bayar Üniversitesi Fen Bilimleri Dergisi; 13(3): 647-650.

11. Mollaoğlu, T, Sezer, M. 2017. A numerical approach with residual error estimation for evolution of high-order linear differential-difference equations by using Gegenbauer polynomials. Celal Bayar Üniversitesi Fen Bilimleri Dergisi; 13(1): 39-49.

12. Şahin, M., Sezer, M. 2018. Pell-Lucas Collocation Method for Solving High-Order Functional Differential Equations with Hybrid Delays. Celal Bayar Üniversitesi Fen Bilimleri Dergisi; 14(2): 141-149.

13. İnan, B. 2017. An Exponential Finite Difference Method Based on Padé Approximation. Celal Bayar Üniversitesi Fen Bilimleri Dergisi; 13(1): 71-80.

14. Açil, M., Konuralp, A., Bildik, N. 2017. Finding The Lie Symmetries of Some First-Order Odes Via Induced Characteristic. Celal Bayar Üniversitesi Fen Bilimleri Dergisi; 13(2): 275-278.

15. Bildik, N. 2017. General convergence analysis for the perturbation iteration technique. Turkish Journal of Mathematics and Computer Science; 6: 1-9.

16. Bildik, N, Deniz, S. 2017. A new efficient method for solving delay differential equations and a comparison with other methods. The European Physical Journal Plus; 132(1), 51.

17. Deniz, S. 2017. Optimal perturbation iteration method for solving nonlinear heat transfer equations. Journal of Heat Transfer; 139(7): 1-6.

18. Deniz, S, Bildik, N. 2017. A new analytical technique for solving Lane-Emden type equations arising in astrophysics. Bulletin of the Belgian Mathematical Society-Simon Stevin; 24(2): 305-320.

19. Bildik, N, Deniz, S. 2018. New analytic approximate solutions to the generalized regularized long wave equations. Bulletin of the Korean Mathematical Society; 55(3): 749-762.

20. Deniz, S, Bildik, N, Sezer, M. 2017. A note on stability analysis of Taylor collocation method. Celal Bayar University Journal of Science; 13(1): 149-153.

21. Kahraman, T. (2018). Some Null Quaternionic Curves in Minkowski spaces. Celal Bayar University Journal of Science; 14 (4) , 357-361.

22. Kahraman, T. (2019). Null Quaternionic Slant Helices in Minkowski Spaces. Mathematical Combinatorics; 1, 45-52.

23. Hoi, Y., Meng, H., Woodward, S. H., Bendok, B. R., Hanel, R. A., Guterman, L. R., & Hopkins, L. N. (2004). Effects of arterial *linear mechanics*; 34(4): 699-708.

geometry on aneurysm growth: three-dimensional computational fluid dynamics study. Journal of neurosurgery; 101(4), 676-681.

24. Akgül, A. (2014). Approximate solutions for MHD squeezing fluid flow by a novel method. Boundary Value Problems, 2014(1), 18.

25. Akgül, A. (2019). Reproducing kernel Hilbert space method based on reproducing kernel functions for investigating boundary layer flow of a Powell–Eyring non-Newtonian fluid. Journal of Taibah University for Science, 13(1), 858-863.

26. Hashemi, M. S., & Akgül, A. (2018). Solitary wave solutions of time–space nonlinear fractional Schrödinger's equation: two analytical approaches. Journal of Computational and Applied Mathematics, 339, 147-160.

27. Inc, M., Akgül, A., Kılıçman, A. (2013). A new application of the reproducing kernel Hilbert space method to solve MHD Jeffery-Hamel flows problem in nonparallel walls. Abstract and Applied Analysis (Vol. 2013). Hindawi.

28. Aksoy, Y., Pakdemirli, M. (2010). New perturbation–iteration solutions for Bratu-type equations. Computers & Mathematics with Applications, 59(8), 2802-2808.

29. Aksoy, Y., Pakdemirli, M., Abbasbandy, S., Boyacı, H. (2012). New perturbation-iteration solutions for nonlinear heat transfer equations. International journal of Numerical methods for Heat & fluid flow; 22(7), 814-828.

30. Şenol, M., Timuçin Dolapçı, İ., Aksoy, Y., Pakdemirli, M. (2013). Perturbation-iteration method for first-order differential equations and systems. Abstract and Applied Analysis; (Vol. 2013). Hindawi.

31. Deniz, S. (2020). Semi-analytical investigation of modified Boussinesq-Burger equations. Balıkesir Üniversitesi Fen Bilimleri Enstitüsü Dergisi, 22(1), 327-333.

32. Bildik, N., Deniz, S. (2020). New approximate solutions to the nonlinear Klein-Gordon equations using perturbation iteration techniques. Discrete & Continuous Dynamical Systems-S, 13(3), 503.

33. Bildik, N., Deniz, S. (2020). A comparative study on solving fractional cubic isothermal auto-catalytic chemical system via new efficient technique. Chaos, Solitons & Fractals, 132, 109555.

34. Agarwal, P., Deniz, S., Jain, S., Alderremy, A. A., Aly, S. (2020). A new analysis of a partial differential equation arising in biology and population genetics via semi analytical techniques. Physica A: Statistical Mechanics and its Applications, 542, 122769.

35. Bildik, N., Deniz, S. (2017). Modification of perturbation-iteration method to solve different types of nonlinear differential equations. AIP Conference Proceedings; 1798(1), 020027.

36. Deniz, S., & Bildik, N. (2017). Applications of optimal perturbation iteration method for solving nonlinear differential equations. AIP Conference Proceedings; 1798(1), 020046.

37. Bildik, N., Deniz, S. (2017). A practical method for analytical evaluation of approximate solutions of Fisher's equations. ITM Web of Conferences; 13, 01001.

38. Bildik, N., Deniz, S. (2018). Solving the burgers' and regularized long wave equations using the new perturbation iteration technique. Numerical Methods for Partial Differential Equations, 34(5), 1489-1501.

Celal Bayar University Journal of Science

Synthesis of Some Novel Alkoxysilyl-functionalized Ionic Liquids

Gülşah Türkmen[1*]

[1]Ege University, Aliağa Vocational School of Higher Education, 35800 Aliağa- Izmir, Turkey,
*gtrkmen@yahoo.com

Received: 20 November 2019
Accepted: 17 March 2020
DOI: 10.18466/cbayarfbe.649172

Abstract

The field of ionic liquid (IL) compounds has recently become one of the popular topics because of its green chemistry potential and superior properties. A series of some novel alkoxysilyl-functionalized ionic liquids that containing different hydrophobic chains have been synthesized and their structures were identified by an infrared spectrometer (FT-IR), nuclear magnetic resonance spectrometer (NMR). Thermal stabilities of synthesized ionic liquids were investigated. The new ionic liquid compounds are good candidates for different application areas due to their functional group which involves easy attachment of them on the surface of supporting materials.

Keywords: Alkoxysilyl-functionalized ionic liquid, dihydro imidazolium, ionic liquid.

1. Introduction

Ionic liquids (ILs) are salts which are created by combination of different type of cations, e.g., imidazolium, pyrrolidine pyridiniums, phosphonium, sulfonium, ammonium and anions e.g., halides (chloride, bromide, iodide), hexafluorophosphate, tetrafluoroborate, tosylated alkyl sulfates derivatives, thiocyanate, etc. They have good physical (melting point, boiling point, density, and viscosity…etc) and also chemical properties. ILs are thermally stable, non-volatile, non-flammable and have low toxicity solvents. Their melting points are generally below 100ºC. Their physical and chemical properties and behaviors can be changeable according to selected cation and anion and these flexible features make them most preferred materials for scientific and industrial fields [1-7].

ILs have wide application areas for different purposes. In geology, they have been used for extraction of some materials [8], In the textile industry, IL's have been preferable materials for some important textile processes and have been used successfully because of ecologically and industrial importance [9]. They are also important compounds for many fields of chemistry, such as biochemistry, electrochemistry, synthetic chemistry. The electrochemical deposition has been carried out successfully in IL's [10, 11]. They have been used in different types of batteries as electrolytes (solar cells, Li-Ion batteries, etc.) [12, 13], in biological systems for enzyme extractions and biocatalytic reactions as solvents [14]. In the other study, ILs have been used as an additive for the preparation of oxygen sensing solid matrix [15].

Ionic liquids have found attractive interest in the reactions as both solvent and also catalyst [16, 17, 18]. When IL's are used in reactions, the product isolation and setting up reactions are very easy and they take advantage in terms of recycling. They have perfect solubility for organic and inorganic materials. Laali's research group achieved great development by the use of ILs in synthetic chemistry. They used IL's as a solvent in different types of reactions (arylation, acylation, nitration, halogenation reactions …etc) and catalyst in metal-mediated bond-forming reactions. The progress was summarized in Laali's review study [19]. In the Welton's review study, it was also mentioned that ionic liquids were used for many synthesis and catalysis and green catalyst studies such as transition-Metal-Mediated Catalysis, substitution reactions, diels-alder, alkylation reactions, etc.) [20].

IL's are promising materials and synthesis of new derivatives and investigations on their properties is not enough yet. For this reason, synthesis and searching of properties of new IL's are crucial notably for their applications in different studies. In this study, some novel ionic liquids compounds (Figure1) containing alkoxysilyl functional group with different aliphatic and aromatic groups have been synthesized and their structures were determined by FTIR and ^{1}H and ^{13}C NMR techniques and also their thermal properties were investigated. We preferred to study the synthesis of

alkoxysilyl-functionalized ionic liquids because functionalized ionic liquids are important materials. IL compounds can be designed for specific purposes through functional groups. For example alkoxysilyl groups provide easy binding of ionic liquids to the supporting materials. There are some examples of analogous of synthesized compounds [21-24], but these ionic liquid compounds will be presented for the first time in the literature.

2. Materials and Methods

1,4-Bis(bromomethyl)-2,3,5,6-tetramethyl benzene and pentamethylbenzyl bromide were synthesized according to the presented procedure in the literature [25-26], N-3-(3-triethoxysilylpropyl)-4,5-dihydroimidazol was purchased from abcr. 1- Bromononane, diiodomethane, toluene were purchased from Sigma Aldrich.

^{1}H NMR and ^{13}C NMR spectra were recorded at room temperature on a Varian Mercury AS 400 instrument at 400 MHz (^{1}H) and 100.56 MHz (^{13}C) respectively. IR spectra were recorded on a Perkin Elmer-Spectrum 100 series spectrophotometer preparing KBr pellets. Thermal stability tests of compounds were performed by using Perkin Elmer Pyris 6 analyzer in the range 50-950 ºC under nitrogen (flow rate: 20 cm^3 / min) at a heating rate 20 ºC / min.

2.1. Synthesis of Ionic Liquid Compounds

2.1.1. Compound IL1

1-Nonyl-3-(3-triethoxysilylpropyl)-4,5-dihydro imidazolium bromide

Equal mole numbers of N-3-(3-triethoxysilylpropyl)-4,5-dihydroimidazol and 1-bromononane were stirred in toluene at room temperature overnight. After that solvent and volatiles were evaporated from the resulting mixture under reduced pressure. Compound **IL1** was purified by washing with hexane. The solid compound was recrystallized in ether and dichloromethane solution.

Pale yellow solid; yield: (98%). ^{1}H NMR (400 MHz, $CDCl_3$) δ (ppm) : 0.68 (m, 2H, CH_2-CH_2-Si), 0.82 (t, 3H, *J* = 6.8 Hz, -CH_2-C*H*$_3$,), 1.15-1.25 (m, 9H, C*H*$_3$-CH_2-O + 8H, 4C*H*$_2$), 1.60 (m, 2H, Si-CH_2-C*H*$_2$), 1.83 (m, 2H, C*H*$_2$), 2.22 (m, 2H, C*H*$_2$), 3.13 (m, 2H, C*H*$_2$), 3.50 (m, 4H, Si-CH_2-CH_2-C*H*$_2$-N, N-C*H*$_2$-CH_2-N-nonyl), 3.61 (q, 6H, *J* = 6.8 Hz, CH_3-C*H*$_2$-O,), 4.01 (m, 4H, N-C*H*$_2$-CH_2---CH_3, N-CH_2-C*H*$_2$--- CH_3), 8.95 (s, 1H, NC*H*-N). ^{13}C NMR (100 MHz, $CDCl_3$) δ (ppm): 10.5, 14.0, 18.4, 21.2, 22.6, 26.5, 27.5, 29.2, 29.4, 31.8, 48.4, 48.7, 50.2, 58.1, 157.6. FT-IR (KBr), (cm^{-1}): 3301, 2927, 2863, 1659, 1522, 1457, 1379, 1308, 1252, 1199, 1134, 1030, 914, 790, 589.

,

2.1.2. Compound IL2

1-(Pentamethybenzyl)-3-(triethoxysilylpropyl)-4,5-dihydroimidazolium bromide

Commercial N-3-(3-triethoxysilylpropyl)-4,5-dihydroimidazol and pentamethylbenzyl bromide compound, synthesized according to the presented procedure [25-26], were refluxed in toluene for six hours. At the end of the reaction, mixture was cooled and solvent and volatiles were evaporated under reduced pressure. Synthesized solid compound was purified by washing with ether and recrystallized in ether and dichloromethane solution.

White solid; yield: 99% ^{1}H NMR (400 MHz, $CDCl_3$) δ (ppm): 0.52 (t, 2H, *J* = 8.0 Hz, CH_2-C*H*$_2$-Si), 1.15 (m, 9H, *J* = 8.0 Hz, C*H*$_3$-CH_2-O), 1.70 (m, 2H, Si-CH_2-C*H*$_2$), 2.14-2.24 (6H, C*H*$_3$C$_6$H$_2$, 6H, m- C*H*$_3$C$_6$H$_2$, 3H, *p*-C*H*$_3$C$_6$H$_2$), 3.57 (t, 2H, *J* = 6.8 Hz, Si-CH_2-CH_2-C*H*$_2$-N), 3.73 (q, 6H, CH_3-C*H*$_2$-O), 3.93-3.97 (m, 4H N-C*H*$_2$-C*H*$_2$-N), 4.85 (s, 2H, C*H*$_2$C$_6$H$_2$Me$_3$), 8.84 (s, 1H, NC*H*-N). ^{13}C NMR (100 MHz, $CDCl_3$) δ (ppm) : 7.2, 17.0, 17.2, 17.3, 18.5, 18.6, 21.2, 47.7, 48.6, 48.8, 50.5, 58.8, 125.8, 133.6, 133.8, 136.8, 157.2. FT-IR (KBr), (cm-1) 3412, 2973, 2927, 2883, 1651, 1514, 1473, 1445, 1378, 1298, 1248, 1194, 1165, 1103, 1077, 1014, 958, 902, 870, 788, 686, 620, 493, 467.

2.1.3. Compound IL3

1,1'-(Methylene)bis{3-(3-triethoxysilylpropyl)-4,5-dihydroimidazolium iodide

N-3-(3-triethoxysilylpropyl)-4,5-dihydroimidazol (7.39 mmol) and diiodomethane (3.69 mmol) were stirred in toluene at reflux temperature for four hours. After cooling to room temperature solvent and volatiles were evaporated under reduced pressure. Further purification was done as mentioned before for **IL1** and **IL2**.

Yellow-orange solid; yield: 96% ^{1}H NMR (400 MHz, $CDCl_3$) δ (ppm): 0.65 (t, 4H, *J* = 8.8 Hz, CH_2-C*H*$_2$-Si), 1.23 (m, 18H, C*H*$_3$-CH_2-O), 1.86 (m, 4H, Si-CH_2-C*H*$_2$), 3.60 (t, 4H, *J* = 7.2 Hz, -C*H*$_2$), 3.83 (m, 12 H, CH_3-C*H*$_2$-O), 4.10 (t, 4H, *J* = 11.2 Hz, -C*H*$_2$) 4,45 (t, 4H, J = 9.6 Hz, C*H*$_2$), 5.90 (s, 2H, N-C*H*$_2$-N), 9.65 (s, 2H, N-C*H*-N). ^{13}C NMR (100 MHz, $CDCl_3$) δ (ppm): 7.8, 18.7, 21.2, 49.6, 49.8, 51.5, 58.8, 59.5, 96.4, 158.9. FT-IR (KBr), (cm-1) : 3520, 3440, 3308, 2937, 2882, 2054, 1651, 1526, 1449, 1378, 1304, 1249, 1195, 1102, 906, 636, 554, 453.

2.1.4. Compound IL4

1,1'-(2,3,5,6-Tetramethyl-1,4-phenylene) bis(methylene)bis{3-[3-(triethoxysilyl)propyl]-4,5-dihydroimidazolium bromide

Commercial N-3-(3-triethoxysilylpropyl)-4,5-dihydroimidazol and 1,4-Bis(bromomethyl)-2,3,5,6-tetramethylbenzene, synthesized according to published

Celal Bayar University Journal of Science
Volume 16, Issue 1, 2020, p 75-80
Doi: 10.18466/cbayarfbe.649172

procedure [25-26], were refluxed in toluene. Reaction mixture was cooled and solvent and volatiles were evaporated under reduced pressure. Synthesized yellow solid compound was purified by washing with ether and were recrystallized in ether and dichloromethane solution.

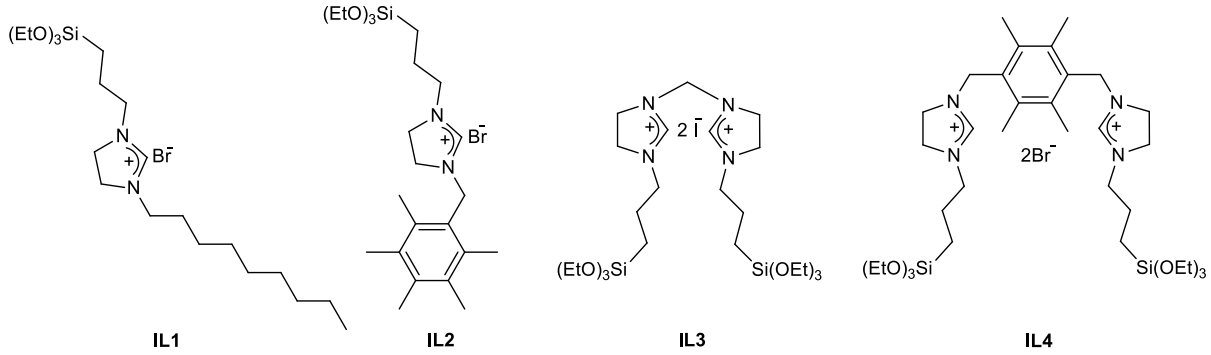

Figure 1. Structures of synthesized ionic liquid compounds.

(s, 4H, 2N-C*H*$_2$-Ph), 8.45 (s, 2H, N-C*H*-N). ^{13}C NMR (100 MHz, $CDCl_3$) δ (ppm): 7.2, 17.2, 18.4, 21.3, 47.9, 48.5, 50.3, 58.6, 129.7, 135.5, 157.2. FT-IR (KBr), (cm-1): 3579, 3440, 3180, 2936, 2881, 2055, 1652, 1627, 1449, 1377, 1305, 1250, 1195, 1100, 905, 693, 552, 461.

3. Results and Discussion

In this study, some novel ionic liquids by combining dihydroimidazol containing ethoxysilyl functional group with bromoalkyl(aryl) units were designed. The combinations of aryl and alkyl groups with dihydroimidazole rings were differentiated to give ionic liquid compounds of different styles. In compounds **IL1** and **IL2**, unilateral alkyl and benzyl groups are attached to the dihydroimidazole ring respectively. In compounds **IL3** and **IL4**, the alkyl and xylyl groups are bridged between the two dihydroimidazole rings. These alkoxysilyl-functionalized ionic liquids are flexible to design materials for specific purposes. Four ionic liquid compounds were successfully synthesized, easily purified and obtained in high yields (96-99 %).
Purifications were made with evaporation, washing with solvents and crystallization techniques. The structures of synthesized compounds were confirmed by FTIR and ^{1}H NMR, ^{13}C NMR techniques. ^{1}H NMR spectrum of **IL2** ionic liquid compound is presented in figure 2.

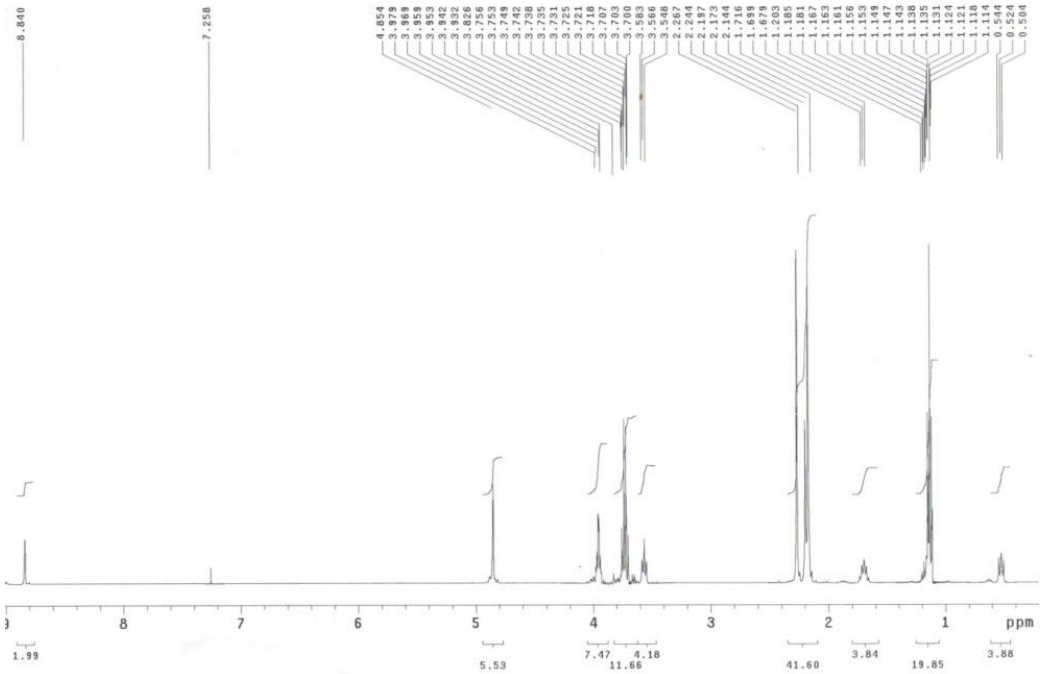

Figure 2. ^{1}H NMR spectrum of **IL2** ionic liquid compound.

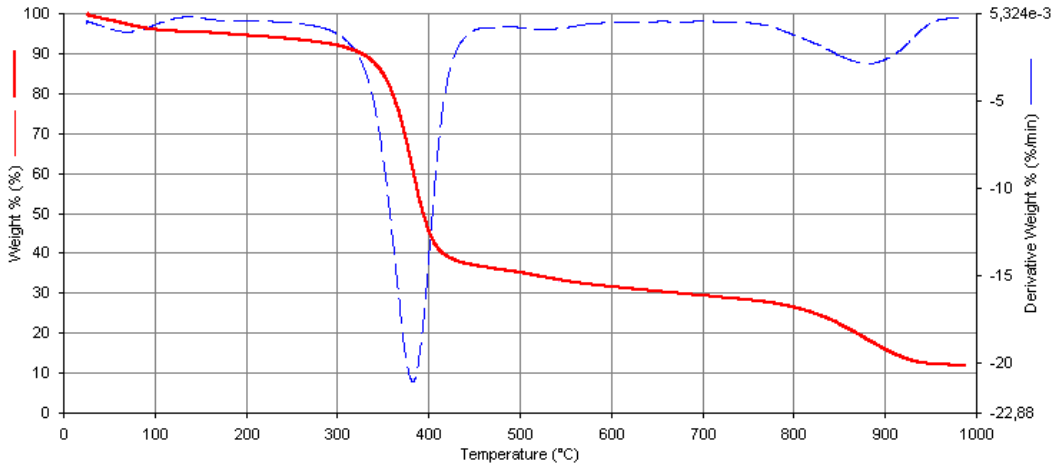

Figure 3. TGA curve of **IL1** compound.

Synthesized compounds are very valuable materials for applications. Ethoxysilyl functional groups allow them to bind some surfaces for different aims. Immobilization of catalysts or developing functionalized membrane systems can be provided easily [27-28]. They can be used as precursors of nanocomposites as well [29]. IL's are generally known to have high thermal stability in the literature [30-31]. In this study, thermal properties we investigated for IL1-4. Determination of thermal decomposition points are important for applications such as the use of substances as solvents or catalysts or etc. Thermal decomposition points of synthesized ionic liquids are shown in table 1 and TGA curve of **IL1** is also presented in figure 3.

When the TGA curves of the synthesized molecules are examined, mass loss before 100 ºC is thought to be caused by water. In other words, it is thought to be caused by the hygroscopic structure of ionic liquids. Hygroscopic behavior of IL's are known in the literature [32-33]. **IL1-4** are also thought to have hygroscopic properties. This can be specified that it can be understood from the OH peak in the IR spectrum and the loss of mass below 100 ºC in TGA measurement.

According to TGA curves, while **IL1** (figure 3) and **IL4** compounds were stable up to 380 ºC and 376 ºC respectively, disintegration of **IL2** and **IL3** compounds started at temperatures above 100 ºC and 20% mass losses were observed well before the onset of the main weight loss (main weight loss points: 358 ºC for **IL2**, 391 ºC for **IL3**), so Td values of **IL2** and **IL3** compounds were recorded at lower temperatures.

Table 1. Thermal decomposition points of IL's.

Ionic liquid	Td (ºC)	T (ºC) (for main weight loss)
IL1	**380**	**380**
IL2	**142**	**358**
IL3	**155**	**391**
IL4	**376**	**376**

Td: Degredation point **(**ºC**)**

4. Conclusion

In the study, triethoxy silyl attached ionic liquid compounds were synthesized successfully in different styles. The benzyl and alkyl groups were attached to a single imidazole (**IL1** and **IL2**) or used as the bridge between two imidazole rings (**IL3** and **IL4**). Their structures were verified by FTIR and ^{1}H NMR, ^{13}C NMR characterization techniques. It is important to identify the properties of the compounds to use the synthesized compounds in applications. In this sense, the thermal stability of the compounds was investigated in this study. The compounds **IL1** and **IL4** have also high thermal stability above 350 ºC and these ionic liquids suitable for use in high-temperature applications such as protection against high temperature corrosion of metals [34]. All new ionic liquids are very valuable for different applications because of ethoxysilyl functional group. Creating an immobilized catalyst systems with ILs can be one of the application area. Separation and

recycling of catalyst can become easier in catalytic reactions. They can be used in solid-phase microextraction (SPME) systems as coating materials as well.

Acknowledgment

I would like to express my gratitude to Ege University, Faculty of Science, Chemistry Department for using its laboratories and facilities.

Ethics

There are no ethical issues after the publication of this manuscript.

References

1. Bonhoˆte P, Dias AP, Papageorgiou N, Kalyanasundaram K, Gratzel M. 1996. Hydrophobic, Highly Conductive Ambient-Temperature Molten Salts, *Inorg. Chem*; 35: 1168-1178.

2. Huddleston JG, Visser AE, Reichert WM, Willauer HD, Broker GA, Rogers RD. 2001. Characterization and comparison of hydrophilic and hydrophobic room temperature ionic liquids incorporating the imidazolium cation, *Green Chemistry*; 3: 156–164.

3. Dzyuba SV, Bartsch RA. 2002. Influence of Structural Variations in 1-Alkyl(aralkyl)-3-MethylimidazoliumHexafluorophosphates and Bis(trifluoromethyl-sulfonyl)imides on Physical Propertiesof the Ionic Liquids, *ChemPhysChem*; 3: 161-166.

4. Wilkes JS. 2004. Properties of ionic liquid solvents for catalysis, *Journal of Molecular Catalysis A: Chemical*; 214: 11–17.

5. Seddon KR. 1997. Ionic Liquids for Clean Technology, *Journal of Chemical Technology & Biotechnology*; 68: 351-356.

6. Welton T. 1999. Room-Temperature Ionic Liquids. Solvents for Synthesis and Catalysis, *Chemical Review*; 99: 2071−2083.

7. Itoh T. 2017. Ionic Liquids as Tool to Improve Enzymatic Organic Synthesis, *Chemical Review*; 117: 10567−10607.

8. Hidayaha NN, Abidin SZ. 2017. The evolution of mineral processing in the extraction of rare earth elements using solid-liquid extraction over liquid-liquid extraction: A review *Minerals Engineering*; 112: 103–113.

9. Meksi N, Moussa A. 2017. A review of progress in the ecological application of ionic liquids in textile processes, *Journal of Cleaner Production*; 161: 105-126.

10. Shah NK, Pati RK, Ray A, Mukhopadhyay I. 2017. Electrodeposition of Si from an Ionic Liquid Bath at Room Temperature in the Presence of Water, *Langmuir;* 33: 1599−1604.

11. Pereira NM, Brincoveanu O, Pantazi AG, Pereira CM, Araújo JP, Silva AF, Enachescu M, Anicai L. 2017. Electrodeposition of Co and Co composites with carbon nanotubes using choline chloride-based ionic liquids, *Surface & Coatings Technology;* 324: 451–462.

12. Dupre N, Moreau P, Vito ED, Quazuguel L, Boniface M, Kren H, Bayle-Guillemaud P, Guyomard D. 2017. Carbonate and Ionic Liquid Mixes as Electrolytes To Modify Interphases and Improve Cell Safety in Silicon-Based Li-Ion Batteries, *Chemistry of Materials;* 29: 8132−8146.

13. Lennert A, Sternberg M, Meyer K, Costa RD, Guldi DM. 2017. Iodine-Pseudohalogen Ionic Liquid-Based Electrolytes for QuasiSolid-State Dye-Sensitized Solar Cells, *ACS Applied. Materials &. Interfaces*; 9: 33437−33445.

14. Nadar SS, Pawar RG, Rathod VK. 2017. Recent advances in enzyme extraction strategies: A comprehensive review. *International Journal of Biological Macromolecules*; 101: 931–957.

15. Ongun MZ. 2019. Development of Highly Sensitive Metal-Free TetraphenylporphyrinBased Optical Oxygen Sensing Materials along with ILs and AgNPs, *Celal Bayar University Journal of Science*; 15(1): 131-138

16. Saugar AI, Márquez-Alvarez C, Pérez-Pariente J. 2017. Direct synthesis of bulk AlPON basic catalysts in ionic liquids, *Journal of Catalysis*; 348: 177–188.

17. Elhamifar D, Eram A, Moshkelgosha R. 2017. Ionic liquid and ethyl-based bifunctional ordered nanoporous organosilica supported palladium: An efficient catalyst for homocoupling of phenylacetylenes, *Microporous and Mesoporous Materials*; 252: 173-178.

18. Sert E, Atalay FS. 2017. Application of Green Catalysts for the Esterification of Benzoic Acid with Different Alcohols, *Celal Bayar University Journal of Science*; 13(4): 907-912.

19. Laali KK. 2016. Ionic liquids as novel media for electrophilic/onium ion chemistry and metal-mediated reactions: a progress summary ARKIVOC (i) 150-171.

20. Welton T. 2004, Ionic liquids in catalysis, *Coordination Chemistry Reviews*; 248: 2459–2477.

21. Lee S-G. 2006. Functionalized imidazolium salts for task-specific ionic liquids and their applications, *Chemical Communications*; 10: 1049–1063.

22. Borja G, Pleixats R, Bied C, Moreaub JJE. 2008. Recoverable Palladium Catalysts for Suzuki–Miyaura CrossCoupling Reactions Based on Organic-Inorganic Hybrid Silica Materials Containing Imidazolium and Dihydroimidazolium Salts. *Advanced Synthesis & Catalysis*; 350: 2566 – 2574.

23. Trilla M, Pleixats R, Man MWC, Bied C. 2009. Organic-inorganic hybrid silica materials containing imidazolium and dihydroimidazolium salts as recyclable organocatalysts for Knoevenagel condensations, *Green Chem*istry; 11: 1815–1820.

24. Mehnert CP, Cook RA, Dispenziere NC, Afeworki M**.** 2002. Supported Ionic Liquid Catalysis - A New Concept for Homogeneous Hydroformylation Catalysis, *Journal of the American Chemical Society;* 120: 12932-12933.

25. Türkmen H, Ceyhan N, Karabay Yavasoglu, NÜ, Özdemir G, Çetinkaya B. 2011. Synthesis and antimicrobial activities of hexahydroimidazo[1,5-a]pyridinium bromides with varying benzyl substituents, *European Journal of Medicinal Chemistry;* 46: 2895-2900.

26. van der Made AW, van der Made RH. 1993. A Convenient Procedure for Bromomethylation of Aromatic Compounds. Selective Mono-, Bis-, or Trisbromomethylation, *The Journal of Organic Chemistry;* 58: 1262-1263.

27. Jia W, Wu Y, Huang J, An Q, Xu D, Wu Y, Lib F, Li G. 2010. Poly(ionic liquid) brush coated electrospun membrane: a useful platform for the development of functionalized membrane systems, *Journal of Materials Chemistry*; 20: 8617–8623.

28. Aksın O, Turkmen H, Artok L, Cetinkaya B, Ni C, Büyükgüngör O, Özkal E. 2006. Effect of immobilization on catalytic characteristics of saturated Pd-N-heterocyclic carbenes in

Mizoroki–Heck reactions, *Journal of Organometallic Chemistry* ;691 3027–3036

29. Stathatos E, Jovanovski V, Orel B, Jerman I, Lianos P. 2007. Dye-Sensitized Solar Cells Made by Using a Polysilsesquioxane Polymeric Ionic Fluid as Redox Electrolyte *The Journal of Physical Chemistry C*; 111: 6528-6532.

30. Grishina EP, Ramenskaya LM, Gruzdev MS, Kraeva OV. 2013. Water effect on physicochemical properties of 1-butyl-3-methylimidazolium based ionic liquids with inorganic anions, *Journal of Molecular Liquids*; 177: 267–272.

31. Ngo HL, LeCompte K, Hargens L, McEwen AB. 2000. Thermal properties of imidazolium ionic liquids, *Thermochimica Acta*, 357-358 : 97-102.

32. Billard I, Mekki S, Gaillard C, Hesemann P, Moutiers G, Mariet C, Labet A, Bünzli JCG. 2004. Eu III Luminescence in a Hygroscopic Ionic Liquid: Effect of Water and Evidence for a Complexation Process, *European Journal of Inorganic Chemistry*; 6: 1190-1197.

33. Anthony JL, Maginn EJ, Brennecke JF. 2001. Solution Thermodynamics of Imidazolium-Based Ionic Liquids and Water, *The Journal of Physical Chemistry B*; 105: 10942-10949

34. Perissi I, Bardi U, Caporali S, Lavacchi A, 2006. High temperature corrosion properties of ionic liquids. *Corrosion Science*; 48: 2349–2362.

Celal Bayar University Journal of Science
Volume 16, Issue 1, 2020, p 81-88
Doi: 10.18466/cbayarfbe.632176

Celal Bayar University Journal of Science

Ruled Surfaces Constructed by Planar Curves in Euclidean 3-Space with Density

Mustafa Altın[1]*, Ahmet Kazan[2], H.Bayram Karadağ[3]

[1] Technical Sciences Vocational School, Bingöl University, Bingöl, Turkey.
[2] Department of Computer Technologies, Doğanşehir Vahap Küçük Vocational School of Higher Education, Malatya Turgut Özal University, Malatya, Turkey.
[3] Department of Mathematics, Faculty of Arts and Sciences, İnönü University, Malatya, Turkey.
*maltin@bingol.edu.tr

Received: 11 October 2019
Accepted: 17 March 2020
DOI: 10.18466/cbayarfbe.632176

Abstract

In the present study, firstly we recall the parametric expressions of planar curves with zero φ-curvature in Euclidean 3-space with density e^{ax_1} and with the aid of the Frenet frame of these planar curves, we obtain the Smarandache curves of them. After that, we study on ruled surfaces which are constructed by the curves with zero φ-curvature in Euclidean 3-space with density e^{ax_1} and their Smarandache curves by giving the striction curves, distribution parameters, mean curvature and Gaussian curvature of these ruled surfaces. Also, we give some examples for these surfaces by plotting their graphs. We use *Mathematica* when we are plotting the graphs of examples.

Keywords: Ruled surfaces, Smarandache curves, Weighted curvature.

1. Introduction

The curves and surfaces are popular topics studied in classical differential geometry and the problem of acquiring mean and Gaussian curvature of a hypersurface in the Euclidean and other spaces is one of the most important problems for geometers. Nowadays, manifold with density (or weighted manifold) is a new topic in geometry and it has been studied in many areas of mathematics, physics and economics. On the other hand, a ruled surface is a surface that can be swept out by moving a line in space and they can be used on different areas such as architectural, CAD, electric discharge machining and etc [1-3].

Furthermore, weighted manifold is a Riemannian manifold with positive density function e^{φ}. In 2003, Gromow [4] has introduced weighted curvature (or φ-curvature) κ_{φ} of a curve and weighted mean curvature (or φ-mean curvature) H_{φ} of an n-dimensional hypersurface on a manifold with density e^{φ}. Also, the generalizations of weighted curvature of a curve, weighted mean curvature and weighted Gaussian curvature (or φ-Gaussian curvature) G_{φ} of a Riemannian manifold with density e^{φ} has been given in [5]. After these definitions, lots of studies about the different characterizations of the curves and surfaces in different spaces with density have been done, for instance, [6-23] and etc.

In the present paper, striction curves, distribution parameters, mean and Gaussian curvatures of the ruled surfaces constructed by curves with zero weighted curvature in Euclidean 3-space with density and the Smarandache curves of them are obtained and some characterizations are given for them.

2. Preliminaries

Let $\alpha(u)$ be a planar curve given by $\alpha(u) = (x_1(u), x_2(u), 0)$. Then the Frenet frame $\{T, N, B\}$ and curvature κ of it in the Euclidean 3-space are [24].

$$\begin{aligned} T(u) &= \frac{1}{\sqrt{x_1'(u)^2 + x_2'(u)^2}}(x_1'(u), x_2'(u), 0), \\ N(u) &= \frac{1}{\sqrt{x_1'(u)^2 + x_2'(u)^2}}(-x_2'(u), x_1'(u), 0), \\ B(u) &= (0,0,1), \\ \kappa(u) &= \frac{x_1'(u)x_2''(u) - x_1''(u)x_2'(u)}{(x_1'(u)^2 + x_2'(u)^2)^{\frac{3}{2}}}. \end{aligned} \quad \textbf{(2.1)}$$

Also, Smarandache curves which are introduced with the aid of Frenet frame of a curve is an important topic

Celal Bayar University Journal of Science
Volume 16, Issue 1, 2020, p 81-88
Doi: 10.18466/cbayarfbe.632176

for differential geometry of curves and if we denote TN-Smarandache curve as γ_{TN}, TB-Smarandache curve as γ_{TB}, NB-Smarandache curve as γ_{NB} and TNB–Smarandache curve as γ_{TNB} of $\alpha(u)$, then they are defined as follows

$$\gamma_{TN}(u)=\frac{T(u)+N(u)}{\|T(u)+N(u)\|},\ \gamma_{TB}(u)=\frac{T(u)+B(u)}{\|T(u)+B(u))\|}, \quad \textbf{(2.2)}$$

$$\gamma_{NB}(u)=\frac{N(u)+B(u)}{\|N(u)+N(u)\|} \text{ and } \gamma_{TNB}(u)=\frac{T(u)+N(u)+B(u)}{\|T(u)+N(u)+B(u)\|}.$$

The parametrization of

$$\varphi(u,v)=\alpha(u)+v.X(u),\ \ u,v\in I\subset\mathbb{R} \quad \textbf{(2.3)}$$

is called a *ruled surface*, where the curve $\alpha(u)$ is *base curve* and $X(u)$ is *ruling* of it. The *striction curve* and *distribution parameter* of a ruled surface are given by

$$\beta(u)=\alpha(u)-\frac{\langle\alpha'(u),X'(u)\rangle}{\|X'(u)\|^2}X(u) \quad \textbf{(2.4)}$$

and

$$\delta=\frac{det[\alpha'(u),X(u),X'(u)]}{\|X'(u)\|^2}, \quad \textbf{(2.5)}$$

respectively [25,26]. Also, the distribution parameter gives a characterization for ruled surface and it is known that, the ruled surface whose distribution parameter vanishes is *developable*.

If κ and N are the curvature and the normal vector of a curve, respectively, then the *φ-curvature* κ_φ of the curve on a manifold with density e^{φ} is defined by [5]

$$\kappa_\varphi=\kappa-\frac{d\varphi}{dN}. \quad \textbf{(2.6)}$$

3. Results and Discussion

3.1. Planar Curves with Zero φ-Curvature in E^3 with Density

In [27], authors have found that, the planar curves with zero φ-curvature in Euclidean space with density e^{ax_1}, $(a\neq 0)$ can be parameterized by

$$\alpha_1(u)=\left(x_1(u),c_2\mp\frac{arctan\left(\sqrt{c_1e^{2ax_1(u)}-1}\right)}{a},0\right)$$

or

$$\alpha_2(u)=\left(d_2-\frac{ln(cos(d_1+ax_2(u)))}{a},x_2(u),0\right),$$

where, $c_1>e^{-2ax_1(u)}$, $-\frac{\pi}{2}+2k\pi<d_1+ax_2(u)<\frac{\pi}{2}+2k\pi$ and $c_1,c_2,d_1,d_2\in\mathbb{R},\ k\in\mathbb{Z}$.

So, the TN-Smarandache curve $\gamma_{1_{TN}}$, TB-Smarandache curve $\gamma_{1_{TB}}$, NB-Smarandache curve $\gamma_{1_{NB}}$ and TNB-Smarandache curve $\gamma_{1_{TNB}}$ of the curve $\alpha_1(u)$ are written as

$$\gamma_{1_{TN}}(u)=\left(\frac{\sqrt{-1+c_1e^{2ax_1(u)}}-1}{\sqrt{2c_1e^{2ax_1(u)}}},\frac{\sqrt{-1+c_1e^{2ax_1(u)}}+1}{\sqrt{2c_1e^{2ax_1(u)}}},0\right),$$

$$\gamma_{1_{TB}}(u)=\left(\frac{\sqrt{-1+c_1e^{2ax_1(u)}}}{\sqrt{2c_1e^{2ax_1(u)}}},\frac{1}{\sqrt{2c_1e^{2ax_1(u)}}},\frac{1}{\sqrt{2}}\right), \quad \textbf{(3.1)}$$

$$\gamma_{1_{NB}}(u)=\left(\frac{-1}{\sqrt{2c_1e^{2ax_1(u)}}},\frac{\sqrt{-1+c_1e^{2ax_1(u)}}}{\sqrt{2c_1e^{2ax_1(u)}}},\frac{1}{\sqrt{2}}\right),$$

$$\gamma_{1_{TNB}}(u)=\left(\frac{\sqrt{-1+c_1e^{2ax_1(u)}}-1}{\sqrt{3c_1e^{2ax_1(u)}}},\frac{\sqrt{-1+c_1e^{2ax_1(u)}}+1}{\sqrt{3c_1e^{2ax_1(u)}}},\frac{1}{\sqrt{3}}\right),$$

respectively and the TN-Smarandache curve $\gamma_{2_{TN}}$, TB-Smarandache curve $\gamma_{2_{TB}}$, NB-Smarandache curve $\gamma_{2_{NB}}$ and TNB-Smarandache curve $\gamma_{2_{TNB}}$ of the curve $\alpha_2(u)$ are written as

$$\gamma_{2_{TN}}(u)=\frac{1}{\sqrt{2}}(sin(d_1+ax_2(u))-cos(d_1+ax_2(u)),\ cos(d_1+ax_2(u))+sin(d_1+ax_2(u)),0),$$

$$\gamma_{2_{TB}}(u)=\frac{1}{\sqrt{2}}(sin(d_1+ax_2(u)),cos(d_1+ax_2(u)),1), \quad \textbf{(3.2)}$$

$$\gamma_{2_{NB}}(u)=\frac{1}{\sqrt{2}}(-cos(d_1+ax_2(u)),sin(d_1+ax_2(u)),1),$$

$$\gamma_{2_{TNB}}(u)=\frac{1}{\sqrt{3}}(sin(d_1+ax_2(u))-cos(d_1+ax_2(u)),\ sin(d_1+ax_2(u))+cos(d_1+ax_2(u)),1),$$

respectively.

Furthermore, the results of the planar curves with zero φ-curvature in Euclidean space with density e^{bx_2} can be obtained with similar procedure to the planar curve with zero φ-curvature in Euclidean space with density e^{ax_1}.

3.2. Ruled Surfaces Constructed by Planar Curves in Euclidean 3-Space with Density

3.2.1. Ruled Surfaces Constructed by the curve $\alpha_1(u)$ and its Smarandache Curves

In this subsection, firstly we construct the ruled surfaces with the help of the curve $\alpha_1(u)$ and its Smarandache curves. Also, we obtain the mean curvatures, Gaussian curvatures, distribution parameters and striction curves for each of these ruled surfaces and give some characterizations for them.

Throughout this subsection, the base curves of ruled surfaces will be taken as the curve $\alpha_1(u)$.

Celal Bayar University Journal of Science
Volume 16, Issue 1, 2020, p 81-88
Doi: 10.18466/cbayarfbe.632176

If the ruling of the ruled surface is the TN-Smarandache curve $\gamma_{1_{TN}}(u)$ of the curve $\alpha_1(u)$, then from (2.3) and (3.1), the ruled surface $\varphi_{1_{TN}}(u,v)$ can be given by

$$\varphi_{1_{TN}}(u,v) = \alpha_1(u) + v\gamma_{1_{TN}}(u)$$
$$= (x_1(u) + v\left(\frac{\sqrt{-1+c_1e^{2ax_1(u)}}-1}{\sqrt{2c_1e^{2ax_1(u)}}}\right),$$
$$c_2 + \frac{\arctan\left(\sqrt{c_1e^{2ax_1(u)}-1}\right)}{a}$$
$$+ v\left(\frac{\sqrt{-1+c_1e^{2ax_1(u)}}+1}{\sqrt{2c_1e^{2ax_1(u)}}}\right), 0).$$

Since the ruled surface $\varphi_{1_{TN}}$ is a parameterization of a plane, it is obvious that, the Gaussian and mean curvatures are zero and from (2.5), also the distribution parameter is zero and the surface is developable.

Also,
Theorem 3.2.1.1. *The base curve and the striction curve of $\varphi_{1_{TN}}$ never intersect.*

Proof. From (2.4), the striction curve $\beta_{1_{TN}}$ of $\varphi_{1_{TN}}$ is

$$\beta_{1_{TN}}(u) = \alpha_1(u) - \frac{\sqrt{c_1e^{2ax_1(u)}}}{\sqrt{2}a}\gamma_{1_{TN}}(u)$$

and this completes the proof.

Example. If we take $a = 1$, $x_1(u) = \sin(u)$, $c_1 = 3$ and $c_2 = 5$ in the ruled surface $\varphi_{1_{TN}}$, we obtain that

$$\varphi_{1_{TN}}(u,v) = (sin(u) + v\left(\frac{\sqrt{-1+3e^{2sin(u)}}-1}{\sqrt{6e^{2sin(u)}}}\right),$$

$$arctan\left(\sqrt{3e^{2sin(u)}-1}\right) + v\left(\frac{\sqrt{-1+3e^{2sin(u)}}+1}{\sqrt{6e^{2sin(u)}}}\right)$$
$$+ 5, 0).$$

In the following figure, one see this ruled surface for $(u,v) \in \left(0, \frac{\pi}{2}\right) \times (-5,5)$.

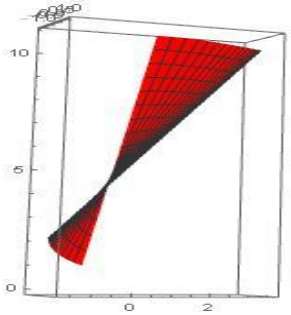

Figure 1. The ruled surface $\varphi_{1_{TN}}$.

If the ruling of the ruled surface is the TB-Smarandache curve $\gamma_{1_{TB}}(u)$ of the curve $\alpha_1(u)$, then from (2.3) and (3.1), the ruled surface $\varphi_{1_{TB}}(u,v)$ is parametrized by

$$\varphi_{1_{TB}}(u,v) = \alpha_1(u) + v\gamma_{1_{TB}}(u)$$
$$= (x_1(u) + v\left(\frac{\sqrt{-1+c_1e^{2ax_1(u)}}}{\sqrt{2c_1e^{2ax_1(u)}}}\right),$$
$$c_2 + \frac{arctan\left(\sqrt{c_1e^{2ax_1(u)}-1}\right)}{a}$$
$$+ v\left(\frac{1}{\sqrt{2c_1e^{2ax_1(u)}}}\right), \frac{v}{\sqrt{2}}).$$

The Gaussian curvature and mean curvature of $\varphi_{1_{TB}}$ are

$$G = -\frac{a^2c_1e^{2ax_1}}{(c_1e^{2ax_1}+a^2v^2)^2}$$

and

$$H = \frac{a^2v\left(av\sqrt{c_1e^{2ax_1(u)}} - c_1\sqrt{2c_1e^{2ax_1(u)}-2}\right)}{\sqrt{2}\sqrt{c_1e^{2ax_1(u)}}(c_1e^{2ax_1(u)}+a^2v^2)^{3/2}},$$

respectively.

Also,
Theorem 3.2.1.2. ***i)*** *The ruled surface $\varphi_{1_{TB}}$ is not developable.*

ii) *The base curve and the striction curve of $\varphi_{1_{TB}}$ coincide.*

Proof. From (2.5), the distribution parameter of $\varphi_{1_{TB}}$ is

$$\delta_{1_{TB}} = \frac{\sqrt{c_1e^{2ax_1(u)}}}{a}.$$

Since $\delta_{1_{TB}}$ cannot be zero, $\varphi_{1_{TB}}$ is not developable. Also, from (2.4) the striction curve is

$$\beta_{1_{TB}}(u) = \alpha_1(u).$$

So, the proof completes.

Example. If we take $a = 1$, $x_1(u) = \ln(u)$, $c_1 = 3$ and $c_2 = 5$ in the ruled surface $\varphi_{1_{TB}}$, we obtain that

$$\varphi_{1_{TB}}(u,v) = (ln(u) + v\left(\frac{\sqrt{-1+3e^{2ln(u)}}}{\sqrt{6e^{2ln(u)}}}\right),$$
$$arctan\left(\sqrt{3e^{2ln(u)}-1}\right) + v\left(\frac{1}{\sqrt{6e^{2ln(u)}}}\right) + 5, \frac{v}{\sqrt{2}}).$$

The following figure shows the graphic of this ruled surface for $(u,v) \in \left(\frac{1}{\sqrt{3}}, 8\right) \times (-14,14)$.

Celal Bayar University Journal of Science
Volume 16, Issue 1, 2020, p 81-88
Doi: 10.18466/cbayarfbe.632176

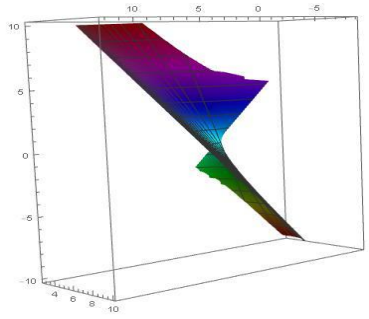

Figure 2. The ruled surface $\varphi_{1_{TB}}$.

Let the ruling curve of the ruled surface be the NB-Smarandache curve $\gamma_{1_{NB}}(u)$ of $\alpha_1(u)$. Thus from (2.3) and (3.1), the ruled surface $\varphi_{1_{NB}}(u,v)$ can be parametrized by

$$\begin{aligned}\varphi_{1_{NB}}(u,v) &= \alpha_1(u) + v\gamma_{1_{NB}}(u)\\ &= \left(x_1(u) + v\left(\frac{-1}{\sqrt{2c_1e^{2ax_1(u)}}}\right),\right.\\ &\quad c_2 + \frac{arctan\left(\sqrt{c_1e^{2ax_1(u)}-1}\right)}{a}\\ &\quad \left. + v\left(\frac{\sqrt{-1+c_1e^{2ax_1(u)}}}{\sqrt{2c_1e^{2ax_1(u)}}}\right), \frac{v}{\sqrt{2}}\right).\end{aligned}$$

The Gaussian curvature and mean curvature of $\varphi_{1_{NB}}$ are

$$G = 0$$

and

$$H = \frac{a\left(a^2\sqrt{c_1e^{2ax_1(u)}}v^2 + 2c_1e^{2ax_1(u)}\left(\sqrt{c_1e^{2ax_1(u)}} + \sqrt{2}av\right)\right)}{2\sqrt{c_1e^{2ax_1(u)}}\left(2c_1e^{2ax_1(u)} + av\left(2\sqrt{2}\sqrt{c_1e^{2ax_1(u)}} + av\right)\right)},$$

respectively.

Also,

Theorem 3.2.1.3. ***i)*** *The ruled surface $\varphi_{1_{NB}}$ is developable.*

ii) *The base curve and the striction curve of $\varphi_{1_{NB}}$ never intersect.*

Proof. From (2.5), the distribution parameter of $\varphi_{1_{NB}}$ is

$$\delta_{1_{NB}} = 0$$

and so, $\varphi_{1_{NB}}$ is developable. Also, from (2.4) the striction curve $\beta_{1_{NB}}(u)$ on $\varphi_{1_{NB}}$ is

$$\beta_{1_{NB}}(u) = \alpha_1(u) - \frac{\sqrt{2}\sqrt{c_1e^{2ax_1(u)}}}{a}\gamma_{1_{NB}}(u)$$

and this completes the proof.

Example. Taking $a = 1$, $x_1(u) = \frac{1}{u}$, $c_1 = 3$ and $c_2 = 5$ in the ruled surface $\varphi_{1_{NB}}$, we get

$$\begin{aligned}\varphi_{1_{NB}}(u,v) &= \left(1/u + v\left(\frac{-1}{\sqrt{6e^{2/u}}}\right),\right.\\ &\quad \left. arctan\left(\sqrt{3e^{2/u}-1}\right) + v\left(\frac{\sqrt{3e^{2/u}-1}}{\sqrt{6e^{2/u}}}\right) + 5, \frac{v}{\sqrt{2}}\right).\end{aligned}$$

Figure 3 shows the graphic of this ruled surface for $(u,v) \in (0.01,100) \times (-50,50)$.

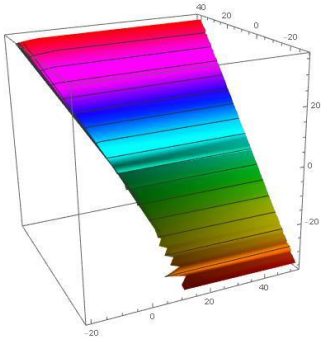

Figure 3. The ruled surface $\varphi_{1_{NB}}$.

Finally, let the ruling curve of the ruled surface be the TNB-Smarandache curve $\gamma_{1_{TNB}}(u)$ of the curve $\alpha_1(u)$. Thus from (2.3) and (3.1), the ruled surface $\varphi_{1_{TNB}}$ can be given by

$$\begin{aligned}\varphi_{1_{TNB}}(u,v) &= \alpha_1(u) + v\gamma_{1_{TNB}}(u)\\ &= \left(x_1(u) + v\left(\frac{\sqrt{-1+c_1e^{2ax_1(u)}}-1}{\sqrt{3c_1e^{2ax_1(u)}}}\right)\right.\\ &\quad c_2 + \frac{arctan\left(\sqrt{c_1e^{2ax_1(u)}-1}\right)}{a}\\ &\quad \left. + v\left(\frac{\sqrt{-1+c_1e^{2ax_1(u)}}+1}{\sqrt{3c_1e^{2ax_1(u)}}}\right), \frac{v}{\sqrt{3}}\right).\end{aligned}$$

The Gaussian curvature and mean curvature of $\varphi_{1_{TNB}}$ are

$$G = -\frac{a^2c_1e^{2ax_1(u)}}{4\left(c_1e^{2ax_1(u)} + av\left(\sqrt{3}\sqrt{c_1e^{2ax_1(u)}} + av\right)\right)^2}$$

and

$$H = \frac{a\left(\begin{array}{c}2a^2\sqrt{c_1e^{2ax_1(u)}}v^2 +\\ c_1e^{2ax_1(u)}\left(\sqrt{c_1e^{2ax_1(u)}} - \sqrt{3}a\left(-2+\sqrt{-1+c_1e^{2ax_1(u)}}\right)v\right)\end{array}\right)}{4\sqrt{2}\sqrt{c_1e^{2ax_1(u)}}\left(c_1e^{2ax_1(u)} + av\left(\sqrt{3}\sqrt{c_1e^{2ax_1(u)}} + av\right)\right)^{3/2}},$$

respectively.

Also,

Celal Bayar University Journal of Science
Volume 16, Issue 1, 2020, p 81-88
Doi: 10.18466/cbayarfbe.632176

Theorem 3.2.1.4. ***i)*** *The ruled surface* $\varphi_{1_{TNB}}$ *is not developable.*

ii) *The base curve and the striction curve of* $\varphi_{1_{TNB}}$ *never intersect.*

Proof. From (2.5), the distribution parameter of $\varphi_{1_{TNB}}$ is

$$\delta_{1_{TNB}} = \frac{\sqrt{c_1 e^{2ax_1(u)}}}{2a}$$

and from (2.4), the striction curve $\beta_{1_{TNB}}(u)$ on $\varphi_{1_{TNB}}$ is

$$\beta_{1_{TNB}}(u) = \alpha_1(u) - \frac{\sqrt{3}\sqrt{c_1 e^{2ax_1(u)}}}{2a}\gamma_{1_{TNB}}(u).$$

So, (i) and (ii) are obvious.

Example. If we take $a = 1$, $x_1(u) = \ln(\tan(u))$, $c_1 = 3$ and $c_2 = 5$ in this ruled surface, then we obtain

$$\begin{aligned}\varphi_{1_{TNB}}(u,v) = (&ln(tan(u)) \\ &+ v\left(\frac{\sqrt{-1+3e^{2\,ln(tan(u))}}-1}{\sqrt{9e^{2\,ln(tan(u))}}}\right), \\ &5 + arctan\left(\sqrt{3e^{2ln(tan(u))}-1}\right) \\ &+ v\left(\frac{\sqrt{-1+3e^{2ln(tan(u))}}+1}{\sqrt{9e^{2ln(tan(u))}}}\right), \frac{v}{\sqrt{3}}).\end{aligned}$$

Figure 4 shows this ruled surface for $(u,v) \in \left(\frac{7\pi}{6}, \frac{8\pi}{6}\right) \times (-1,1)$.

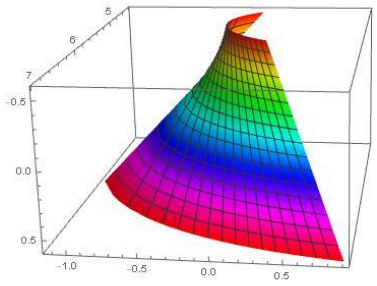

Figure 4. The ruled surface $\varphi_{1_{TNB}}$.

3.2.2. Ruled Surfaces Constructed by the curve $\alpha_2(u)$ and its Smarandache Curves

In this subsection, firstly we construct the ruled surfaces with the help of the curve $\alpha_2(u)$ and its Smarandache curves. Also, we obtain the mean curvatures, Gaussian curvatures, distribution parameters and striction curves for each of these ruled surfaces and give some characterizations for them.

Throughout this subsection, the base curves of ruled surfaces will be taken as the curve $\alpha_2(u)$.

If the ruling curve of the ruled surface is the TN-Smarandache curve $\gamma_{2_{TN}}(u)$ of the curve $\alpha_2(u)$, then from (2.3) and (3.2), the ruled surface $\varphi_{2_{TN}}(u,v)$ can be given by

$$\begin{aligned}\varphi_{2_{TN}}(u,v) &= \alpha_2(u) + v\gamma_{2_{TN}}(u) \\ &= (d_2 - \frac{\ln(\cos(d_1+ax_2(u)))}{a} + \\ &\quad v\left(\frac{sin(d_1+ax_2(u))-cos(d_1+ax_2(u))}{\sqrt{2}}\right), \\ &\quad x_2(u) + v\left(\frac{cos(d_1+ax_2(u))+sin(d_1+ax_2(u))}{\sqrt{2}}\right), 0).\end{aligned}$$

Since the ruled surface $\varphi_{2_{TN}}$ is a parametrization of a plane, it is obvious that, the Gaussian curvature and mean curvature are zero and from (2.5), the distribution parameter $\delta_{2_{TN}}$ of it is zero and so it is developable.

Also,

Theorem 3.2.2.1. *The base curve and the striction curve of* $\varphi_{2_{TN}}$ *never intersect.*

Proof. From (2.4), the striction curve $\beta_{2_{TN}}(u)$ on $\varphi_{2_{TN}}$ is

$$\beta_{2_{TN}}(u) = \alpha_2(u) - \frac{sec(d_1 + ax_2(u))}{\sqrt{2}a}\gamma_{2_{TN}}(u),$$

which completes the proof.

Example. Taking $a = -1$, $x_2(u) = u^2$, $d_1 = 3$ and $d_2 = 5$ in the ruled surface $\varphi_{2_{TN}}$, we get

$$\begin{aligned}&\varphi_{2_{TN}}(u,v) = (5 + ln(cos(3-u^2)) + \\ &v\left(\frac{sin(3-u^2)-cos(3-u^2)}{\sqrt{2}}\right), \\ &u^2 + v\left(\frac{cos(3-u^2)+sin(3-u^2)}{\sqrt{2}}\right), 0).\end{aligned}$$

Figure 5 shows the graphic of this ruled surface for $(u,v) \in \left(\sqrt{3-\frac{\pi}{2}}, \sqrt{3+\frac{\pi}{2}}\right) \times (-1,1)$.

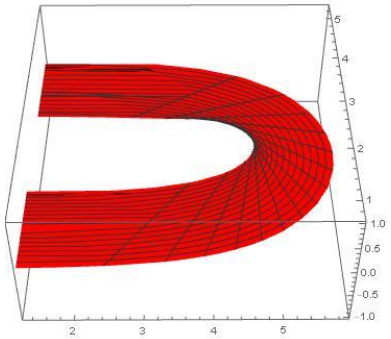

Figure 5. The ruled surface $\varphi_{2_{TN}}$

Celal Bayar University Journal of Science
Volume 16, Issue 1, 2020, p 81-88
Doi: 10.18466/cbayarfbe.632176

If the ruling of the ruled surface is the TB-Smarandache curve $\gamma_{2_{TB}}(u)$ of $\alpha_2(u)$, then from (2.3) and (3.2), the ruled surface $\varphi_{2_{TB}}(u,v)$ can be given by

$$\varphi_{2_{TB}}(u,v) = \alpha_2(u) + v\gamma_{2_{TB}}(u)$$
$$= (d_2 - \frac{ln(cos(d_1+ax_2(u)))}{a} + v\left(\frac{sin(d_1+ax_2(u))}{\sqrt{2}}\right),$$
$$x_2(u) + v\left(\frac{cos(d_1+ax_2(u))}{\sqrt{2}}\right), \frac{v}{\sqrt{2}}).$$

The Gaussian curvature and mean curvature of the ruled surface $\varphi_{2_{TB}}$ are

$$G = -\frac{4a^2\cos(d_1+ax_2(u))}{(2+a^2v^2+a^2v^2\cos(2(d_1+ax_2(u))))^2}$$

and

$$H = \frac{a^2v(av+av\cos(2(d_1+ax_2))-2\sqrt{2}\sin(d_1+ax_2))}{\sqrt{2}\sec(d_1+ax_2)(2+a^2v^2+a^2v^2\cos(2(d_1+ax_2)))^{3/2}},$$

respectively.

Also,
Theorem 3.2.2.2. ***i)*** *The ruled surface $\varphi_{2_{TB}}$ is not developable.*

ii) *The base curve and the striction curve of $\varphi_{2_{TB}}$ coincide.*

Proof. From (2.5), the distribution parameter of $\varphi_{2_{TB}}$ is

$$\delta_{2_{TB}} = \frac{sec(d_1+ax_2(u))}{2a}$$

and from (2.4), the striction curve $\beta_{2_{TB}}(u)$ on $\varphi_{2_{TB}}$ is

$$\beta_{2_{TB}}(u) = \alpha_2(u).$$

So, we have (i) and (ii).

Example. If we take $a = 1$, $x_2(u) = u$, $d_1 = 3$ and $d_2 = 5$ in the ruled surface $\varphi_{2_{TB}}$, we obtain that

$$\varphi_{2_{TB}}(u,v) = (5 - ln(cos(u+3)) + v\left(\frac{sin(u+3)}{\sqrt{2}}\right),$$
$$u + v\left(\frac{cos(u+3)}{\sqrt{2}}\right), \frac{v}{\sqrt{2}}).$$

In figure 6, one see this ruled surface for $(u,v) \in \left(-3-\frac{\pi}{2}, -3+\frac{\pi}{2}\right) \times (-15,15)$.

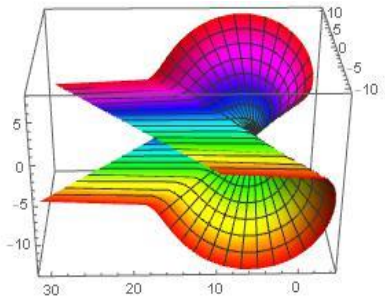

Figure 6. The ruled surface $\varphi_{2_{TB}}$

If the ruling of the ruled surface is the NB-Smarandache curve $\gamma_{2_{NB}}(u)$ of the curve $\alpha_2(u)$, then from (2.3) and (3.2), the ruled surface $\varphi_{2_{NB}}(u,v)$ can be given by

$$\varphi_{2_{NB}}(u,v) = \alpha_2(u) + v\gamma_{2_{NB}}(u)$$
$$= (d_2 - \frac{ln(cos(d_1+ax_2(u)))}{a} - v\left(\frac{cos(d_1+ax_2(u))}{\sqrt{2}}\right),$$
$$x_2(u) + v\left(\frac{\sin(d_1+ax_2(u))}{\sqrt{2}}\right), \frac{v}{\sqrt{2}}).$$

The Gaussian curvature and mean curvature of the ruled surface $\varphi_{2_{NB}}$ are

$$G = 0$$

and

$$H = \frac{a(4+a^2v^2+4\sqrt{2}av\cos(d_1+ax_2(u))+a^2v^2\cos(2(d_1+ax_2(u))))}{4(2+2\sqrt{2}av\cos(d_1+ax_2(u))+a^2v^2\cos^2(2(d_1+ax_2(u))))^{3/2}},$$

respectively.

Also,
Theorem 3.2.2.3. ***i)*** *The ruled surface $\varphi_{2_{NB}}$ is developable.*

ii) *The base curve and the striction curve of $\varphi_{2_{NB}}$ never intersect.*

Proof. From (2.5), the distribution parameter of $\varphi_{2_{NB}}$ is

$$\delta_{2_{NB}} = 0.$$

So, $\varphi_{2_{NB}}$ is developable. Also, from (2.4) the striction curve $\beta_{2_{NB}}(u)$ on $\varphi_{2_{NB}}$ is

$$\beta_{2_{NB}}(u) = \alpha_2(u) - \frac{\sqrt{2}sec(d_1+ax_2(u))}{a}\gamma_{2_{NB}}(u)$$

and this completes the proof.

Example. Taking $a = 1$, $x_2(u) = \ln(u)$, $d_1 = 3$ and $d_2 = 5$ in the ruled surface $\varphi_{2_{NB}}$, we get

$$\varphi_{2_{NB}}(u,v) = (5 - ln(cos(ln(u)+3)) -$$
$$v\left(\frac{cos(ln(u)+3)}{\sqrt{2}}\right), ln(u) + v\left(\frac{sin(ln(u)+3)}{\sqrt{2}}\right), \frac{v}{\sqrt{2}}).$$

Celal Bayar University Journal of Science
Volume 16, Issue 1, 2020, p 81-88
Doi: 10.18466/cbayarfbe.632176

In the following figure, one see this ruled surface for $(u,v) \in \left(e^{-3-\frac{\pi}{2}}, e^{-3+\frac{\pi}{2}}\right) \times (-5,5)$.

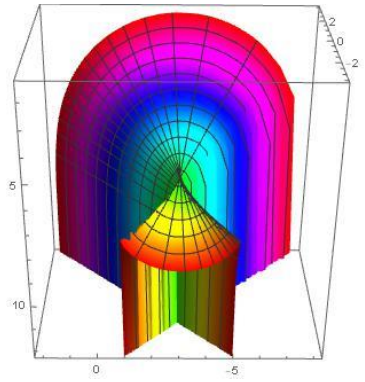

Figure 7. The ruled surface $\varphi_{2_{NB}}$

Finally, if the ruling of the ruled surface is the TNB-Smarandache curve $\gamma_{2_{TNB}}(u)$ of the curve $\alpha_2(u)$, then from (2.3) and (3.2), the ruled surface $\varphi_{2_{TNB}}(u,v)$ can be given by

$$\varphi_{2_{TNB}}(u,v) = \alpha_2(u) + v\gamma_{2_{TNB}}(u)$$
$$= (d_2 - \frac{\ln(\cos(d_1+ax_2(u)))}{a} + v\left(\frac{\sin(d_1+ax_2(u))-\cos(d_1+ax_2(u))}{\sqrt{3}}\right),$$
$$x_2(u) + v\left(\frac{\cos(d_1+ax_2(u))+\sin(d_1+ax_2(u))}{\sqrt{3}}\right), \frac{v}{\sqrt{3}}).$$

The Gaussian and mean curvatures of the ruled surface $\varphi_{2_{TNB}}$ are

$$G = -\frac{a^2\cos(d_1+ax_2(u))}{\left(2+a^2v^2+2\sqrt{3}av\cos(d_1+ax_2(u))+a^2v^2\cos(2(d_1+ax_2(u)))\right)^2}$$

and

$$H = \frac{a\left(1+2\sqrt{3}av\cos(d_1+ax_2(u))+a^2v^2\cos\left(2(d_1+ax_2(u))\right)-\sqrt{3}av\sin(d_1+ax_2(u))\right)}{2\left(2+a^2v^2+2\sqrt{3}av\cos(d_1+ax_2(u))+a^2v^2\cos\left(2(d_1+ax_2(u))\right)\right)^{3/2}},$$

respectively.

Also,

Theorem 3.2.2.4. ***i)*** *The ruled surface $\varphi_{2_{TNB}}$ is not developable.*

ii) *The base curve and the striction curve of $\varphi_{2_{TNB}}$ never intersect.*

Proof. From (2.5), the distribution parameter of $\varphi_{2_{TNB}}$ is

$$\delta_{2_{TNB}} = \frac{\sqrt{3}sec(d_1+ax_2(u))}{2a}$$

and from (2.4), the striction curve $\beta_{2_{TNB}}$ on the ruled surface $\varphi_{2_{TNB}}$ is

$$\beta_{2_{TNB}} = \alpha_2(u) - \frac{\sqrt{3}\sec(d_1+ax_2(u))}{2a}\gamma_{2_{TNB}}(u).$$

Thus, these equations prove (i) and (ii).

Example. If we take $a = 1$, $x_2(u) = u$, $d_1 = 3$ and $d_2 = 5$ in the ruled surface $\varphi_{2_{TNB}}$, we obtain that

$$\varphi_{2_{TNB}}(u,v) = (5 - ln(cos(u+3)) + v\left(\frac{sin(u+3)-cos(u+3)}{\sqrt{3}}\right),$$
$$u + v\left(\frac{cos(u+3)+sin(u+3)}{\sqrt{3}}\right), \frac{v}{\sqrt{3}}).$$

In figure 8, one see this ruled surface for $(u,v) \in \left(-3-\frac{\pi}{2}, -3+\frac{\pi}{2}\right) \times (-1.5,1.5)$.

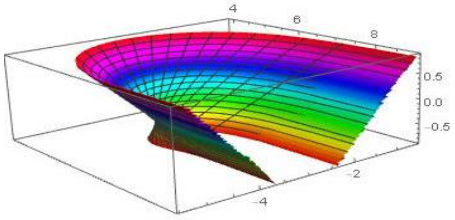

Figure 8. The ruled surface $\varphi_{2_{TNB}}$.

4. Conclusion

In the present study, we give some important results for ruled surfaces constructed by curves with zero φ-curvature in Euclidean 3-space with density. We hope that, this study will help to engineers and geometers who are dealing with surfaces in Euclidean space with density and in near future, this study can be tackled in Minkowski space, Galilean space and etc.

Acknowledgement

1. This paper has been supported by Scientific Research Projects (BAP) unit of İnönü University (Malatya/TURKEY) with the Project number FDK-2018-1349.

2. The authors gratefully thank to the Referees for the constructive comments and recommendations which definitely help to improve the readability and quality of the paper.

Ethics

There are no ethical issues after the publication of this manuscript.

Authors' Contributions

All authors contributed equally to this manuscript and all authors reviewed the final manuscript.

References

1. Brauner H. and Kickinger W. Baugeometrie 1. Bauverlag, 1977.

2. Hanbay K., Alpaslan N., Talu M.F. and Hanbay D. 2016. Principal curvatures based rotation invariant algorithms for efficient texture classification. *Neurocomputing*; 199: 77–89.

3. Ravani B. and Wang J.W. 1991. Computer Aided Geometric Design of Line Constructs. *ASME Journal of Mechanical Design*; 113(4): 363-371.

4. Gromov M. 2003. Isoperimetry of Waists and Concentration of Maps. *Geometric and Functional Analysis*; 13: 178–215.

5. Corwin I., Hoffman N., Hurder S., Sesum Vojislav and Xu Y. 2006. Differential Geometry of Manifolds with Density. *Rose-Hulman Und. Math. J.*; 1–15.

6. Alarcón A., Ferrer L. and Martín F. 2008. Density theorems for complete minimal surfaces in R^3. *Geometric and Functional Analysis*; 18(1): 1–49.

7. Belarbi L. and Belkhelfa M. 2015. Some Results in Riemannian Manifolds with Density. *Analele Universitatii Oradea Fasc. Matematica*; XXII(2): 81–86.

8. Engelstein M., Marcuccio A, Quinn M.. and Pritchard T. 2009. Isoperimetric problems on the sphere and on surfaces with density. *New York Journal of Mathematics*; 15: 97–123.

9. Hieu D.T. and Nam T. Le. 2008. On the four vertex theorem in planes with radial density $e^{\phi(r)}$. *Colloquium Mathematicum*; 113(1): 119–149.

10. Hieu D.T. and Nam T. Le. 2009. The classification of constant weighted curvature curves in the plane with a log-linear density. *Communications on Pure and Applied Analysis*; 243(2): 277–285.

11. Hieu D.T. and Hoang N.M. 2009. Ruled minimal surfaces in R^3 with density e^z. *Pacific Journal of Mathematics*; 243(2): 277–285.

12. Belarbi L. and Belkhelfa M. 2012. Surfaces in R^3 with density. *I-Manager's Journal on Mathematics*; 1(1): 34–48.

13. Morgan F., Hutchings M. and Howards H. 2000. The isoperimetric problem on surfaces of revolution of decreasing Gauss curvature. *Transactions of the American Mathematical Society*; 352(11): 4889–4909.

14. Morgan F. 2005. Manifolds with Density. *Notices Amer Math Soc*; 52(8): 853–858.

15. Morgan F. 2009. Manifolds with Density and Perelman's Proof of the Poincaré Conjecture. *The American Mathematical Monthly*; 116(2): 134–142.

16. Rosales C., Cañete A., Bayle V. and Morgan F. 2008. On the isoperimetric problem in Euclidean space with density. *Calculus of Variations and Partial Differential Equations*; 31(1): 27–46.

17. Yıldız Ö. 2018. Constructions of Helicoidal Surfaces in a 3-Dimensional Complete Manifold with Density. *Mathematics*; 7(27): 1–10.

18. Yıldız Ö.G., Hızal S. and Akyiğit M. 2018. Type I^+ helicoidal surfaces with prescribed weighted mean or Gaussian curvature in Minkowski space with density. *Analele Stiintifice Ale Universitatii Ovidius Constanta, Seria Matematica*; 26(3): 99–108.

19. Yoon D.W. 2017. Weighted minimal translation surfaces in the Galilean space with density. *Open Mathematics*; 15(1): 459–466.

20. Yoon D.W., Kim D.-S., Kim H. Y. and Lee, J. W. 2017. Constructions of Helicoidal Surfaces in Euclidean Space with Density. *Symmetry*; 9(173): 1–9.

21. Yoon D.W. and Yuzbasi Z.K. 2018. Weighted Minimal Translation Surfaces in Euclidean Space with Density. *International Journal of Geometric Methods in Modern Physics*; 15(11).

22. Altın M., Kazan A. and Karadağ, H.B. 2019. Ruled Surfaces in E^3 with Density. *Honam Mathematical Journal;* 41(4): 683-695.

23. Altın M., Kazan A. and Karadağ, H.B. 2020. Monge Hypersurfaces in Euclidean 4-Space with Density. *Journal of Polytechnic;* 23(1): 207-214.

24. Rutter J.W. Geometry of Curves (1st), New York: Chapman and Hall/CRC, 2000.

25. Hacısalihoğlu H.H. Differensiyel Geometri, Ankara: Gazi Üniversitesi Basın Yayın Yüksekokulu Basımevi, 1983.

26. O'Neill B. Elementary Differential Geometry, Academic Press Inc, 1966.

27. Altın M., Kazan A. and Karadağ, H.B. 2019. Rotational Surfaces Generated by Planar Curves in E^3 with Density. *Int. J. of Anal. and Appl.*; 17(3): 311-328.

Celal Bayar University Journal of Science

Some New Results on Absolute Summability Factors

G. Canan HAZAR GÜLEÇ[1]*

[1]Department of Mathematics, Pamukkale University, 20070, Denizli.
*gchazar@pau.edu.tr

Received: 13 September 2019
Accepted: 17 March 2020
DOI: 10.18466/cbayarfbe.619883

Abstract

In this paper, we establish the general summability factor theorems related to generalized absolute Cesàro summability $|C,\alpha,\beta|_k$ and absolute factorable matrix summability $\left|A_f,\varphi_n\right|_k$ methods for $k \geq 1$, $\alpha+\beta>-1$, where (φ_n) is arbitrary sequence of positive real constants and $A_f=(a_{nv})$ is a factorable matrix such that $a_{nv}=\hat{a}_n a_v$ for $0 \leq v \leq n$, $a_{nv}=0$ for $v>n$, $(\hat{a}_n)$ and (a_n) are any sequences of real numbers. Also, absolute factorable summability method includes all absolute Riesz summability and absolute weighted summability methods in the special cases. Therefore, not only some well known results but also several new results for absolute Cesàro and weighted means are obtained as corollaries.

Keywords: Absolute Cesàro summability, Factorable matrix, Matrix methods, Sequence spaces, Summability factors.

1. Introduction

Let $\sum x_n$ be a given infinite series with sequence of partial sums (s_n) and $A=(a_{nv})$ be an infinite matrix of complex numbers. By $A(s)=\left(A_n(s)\right)$, we denote the A-transform of the sequence $s=(s_n)$, i.e.,

$$A_n(s)=\sum_{v=0}^{\infty} a_{nv}s_v$$

which converges for $n \geq 0$.
The nth $(\bar{N},p_n)$ weighted mean of the sequence (s_n) is given by

$$T_n=\frac{1}{P_n}\sum_{v=0}^{n} p_v s_v,$$

where (p_n) is a sequence of positive real constants such that $P_n=\sum_{v=0}^{n} p_v \to \infty$ as $n \to \infty$ $(P_{-1}=p_{-1}=0)$. Let (φ_n) be any sequence of positive real constants. Then the series $\sum x_n$ is said to be summable $|\bar{N},p_n,\varphi_n|_k$, $k \geq 1$, if (see [1])

$$\sum_{n=1}^{\infty}(\varphi_n)^{k-1}|T_n-T_{n-1}|^k<\infty. \qquad (1.1)$$

Note that $|\bar{N},p_n,P_n/p_n|_k=|\bar{N},p_n|_k$ and $|\bar{N},p_n,n|_k=|R,p_n|_k$, which are defined by Bor and Sarıgöl in [2,3].

Taking account of

$$T_n-T_{n-1}=\frac{p_n}{P_nP_{n-1}}\sum_{v=1}^{n} P_{v-1}x_v$$

the relation (1.1) can be stated as

$$\sum_{n=1}^{\infty}(\varphi_n)^{k-1}\left|\frac{p_n}{P_nP_{n-1}}\sum_{v=1}^{n} P_{v-1}x_v\right|^k<\infty. \qquad (1.2)$$

An appropriate extension of (1.2) to a factorable matrix would be as follows [4]. Let $A_f=(a_{nv})$ denote the factorable matrix defined by

$$a_{nv}=\begin{cases}\hat{a}_n a_v, & 0 \leq v \leq n,\\ 0, & v>n,\end{cases}$$

where $(\hat{a}_n)$ and (a_n) are any sequences of real numbers. Then the series $\sum x_n$ is said to be summable $\left|A_f,\varphi_n\right|_k$, $k \geq 1$, if (see [4])

$$\sum_{n=1}^{\infty}(\varphi_n)^{k-1}\left|\hat{a}_n\sum_{v=1}^{n} a_v x_v\right|^k<\infty.$$

If we take $\hat{a}_n=\frac{p_n}{P_nP_{n-1}}$ and $a_v=P_{v-1}$, then $\left|A_f,\varphi_n\right|_k$ summability is equivalent to $|\bar{N},p_n,\varphi_n|_k$ summability.

Celal Bayar University Journal of Science
Volume 16, Issue 1, 2020, p 89-93
Doi: 10.18466/cbayarfbe.619883

Borwein [5] has introduced the nth generalized Cesàro mean (C,α,β) of order (α,β) with $\alpha+\beta>-1$, of the sequence (s_n) by

$$\sigma_n^{\alpha,\beta}=\frac{1}{A_n^{\alpha+\beta}}\sum_{v=1}^{n}A_{n-v}^{\alpha-1}A_v^{\beta}s_v,$$

where $A_n^{\alpha+\beta}=O\left(n^{\alpha+\beta}\right)$, $\alpha+\beta>-1$, $A_0^{\alpha+\beta}=1$, $A_n^{\alpha}=\frac{(\alpha+1)(\alpha+2)\ldots(\alpha+n)}{n!}$ and $A_{-n}^{\alpha+\beta}=0, n\geq 1$.

Obviously, $(C,\alpha,0)$ is the same as (C,α) whereas $(C,0,\beta)$ is $(C,0)$.

We write $\tau_n^{\alpha,\beta}$ as the (C,α,β) transform of the sequence (nx_n), i.e.,

$$\tau_n^{\alpha,\beta}=\frac{1}{A_n^{\alpha+\beta}}\sum_{v=1}^{n}A_{n-v}^{\alpha-1}A_v^{\beta}vx_v.$$

Then, the series $\sum x_n$ is said to be summable $|C,\alpha,\beta|_k$, $k\geq 1$, for $\alpha+\beta>-1$, if (see [6])

$$\sum_{n=1}^{\infty}\frac{1}{n}\left|\tau_n^{\alpha,\beta}\right|^k<\infty.$$

The summability $|C,\alpha,\beta|_k$ includes all Cesàro methods in the special cases. For example, if we take $\beta=0$, $\alpha=0$ and $\alpha=1$, then the summability $|C,\alpha,\beta|_k$ reduces to $|C,\alpha|_k$ defined by Flett in [7], to $|C,0|_k$ and the absolute Riesz summability $|R,p_n|_k$ with $p_n=A_n^{\beta}$ for $\beta\geq 0$ [3].

Throughout this paper, k^* denotes the conjugate of $k>1$, i.e., $1/k+1/k^*=1$, and $1/k^*=0$ for $k=1$.
Let X and Y be two summability methods. If $\sum\varepsilon_n x_n$ is summable by the method Y whenever $\sum x_n$ is summable by the method X, then we say that the sequence $\varepsilon=(\varepsilon_n)$ is a summability factor of type (X,Y) and we write $\varepsilon\in(X,Y)$. Also, note that if $\varepsilon=1$, then $1\in(X,Y)$ means the comparisons of these methods, where $1=(1,1,\ldots)$, i.e., $X\subset Y$.

Absolute summability factors and comparison of the methods related to $|\bar{N},p_n|_k$ and $|C,\alpha|_k$ were widely studied by many authors [8-12]. We refer the reader to [11-13] for the most recent work in this topic. Also the Cesàro series spaces have been defined as the set of all series summable by absolute Cesàro summability methods in [14-16].

2. Results and Discussion

The aim of this paper is to characterize the sets $(|C,\alpha,\beta|,|A_f,\varphi_n|_k)$, $k\geq 1$ and $(|A_f,\varphi_n|_k,|C,\alpha,\beta|)$, $k>1$ for $\alpha+\beta>-1$. As a direct consequence of these results, we also obtain various new results as corollaries.

We use the following lemmas to prove our results.
Lemma 2.1. Let $1<k<\infty$. Then, $A(x)\in\ell$ whenever $x\in\ell_k$ if and only if

$$\sum_{v=0}^{\infty}\left(\sum_{n=0}^{\infty}|a_{nv}|\right)^{k^*}<\infty$$

where $\ell_k=\{x=(x_v):\sum_v|x_v|^k<\infty\}$, $\ell_1=\ell$, [17].
Lemma 2.2. Let $1\leq k<\infty$. Then, $A(x)\in\ell_k$ whenever $x\in\ell$ if and only if

$$\sup_v\sum_{n=0}^{\infty}|a_{nv}|^k<\infty,$$

[18].

Lemma 2.3. Let $\mu>-1$, $1\leq k<\infty$ and $\lambda<\mu$. Then, for $k=1$,

$$E_v=\begin{cases}O(v^{-\mu-1}), & \lambda\leq-1\\ O\left(v^{-\mu+\lambda}\right), & \lambda>-1\end{cases}$$

and

$$E_v=\begin{cases}O(v^{-k\mu-1}), & \lambda<-1/k\\ O(v^{-k\mu-1}logv), & \lambda=-1/k\\ O\left(v^{-k\mu+k\lambda}\right), & \lambda>-1/k\end{cases}$$

for $1<k<\infty$, where $E_v=\sum_{n=v}^{\infty}\frac{\left|A_{n-v}^{\lambda}\right|^k}{n\left(A_n^{\mu}\right)^k}$ for $v\geq 1$, [9].

Now, we are ready to prove the main theorems.

Theorem 2.4. Let $k\geq 1$ and $\alpha+\beta>-1$. Then the necessary and sufficient condition for $\varepsilon\in(|C,\alpha,\beta|,|A_f,\varphi_n|_k)$ is that

$$\sup_r\left\{\sum_{n=r}^{\infty}\left|\varphi_n^{1/k^*}\hat{a}_n rA_r^{\alpha+\beta}\sum_{v=r}^{n}\frac{a_v\varepsilon_v A_{v-r}^{-\alpha-1}}{vA_v^{\beta}}\right|^k\right\}<\infty. \quad (2.1)$$

Proof. Let $\tau_n^{\alpha,\beta}$ be the nth (C,α,β) mean of the sequence (nx_n) and define the sequence (y_n) by

$$y_n=\frac{\tau_n^{\alpha,\beta}}{n}=\frac{1}{nA_n^{\alpha+\beta}}\sum_{v=1}^{n}A_{n-v}^{\alpha-1}A_v^{\beta}vx_v,$$
$$n\geq 1 \quad and \quad y_0=x_0. \quad (2.2)$$

So, $\sum x_n$ is summable $|C,\alpha,\beta|$ iff $y=(y_n)\in\ell$. Also, by inversion of (2.2), we have for $n\geq 1$

$$x_n=\frac{1}{nA_n^{\beta}}\sum_{v=1}^{n}A_{n-v}^{-\alpha-1}vA_v^{\alpha+\beta}y_v. \quad (2.3)$$

Celal Bayar University Journal of Science
Volume 16, Issue 1, 2020, p 89-93
Doi: 10.18466/cbayarfbe.619883

Using definition of factorable matrix A_f, we define the sequence $(\tilde{y}_n)$ by

$$\tilde{y}_n = \varphi_n^{1/k^*}\hat{a}_n \sum_{v=1}^{n} a_v x_v \varepsilon_v \ , \qquad \tilde{y}_0 = \varepsilon_0 x_0.$$

This gives us that $\sum \varepsilon_n x_n$ is summable $|A_f, \varphi_n|_k$ iff $\tilde{y} = (\tilde{y}_n) \in \ell_k$.

Hence, in view of (2.3), we get for $n \geq 1$,

$$\begin{aligned}\tilde{y}_n &= \varphi_n^{1/k^*}\hat{a}_n \sum_{v=1}^{n} a_v \varepsilon_v \, x_v \\ &= \varphi_n^{1/k^*}\hat{a}_n \sum_{v=1}^{n} a_v \varepsilon_v \frac{1}{vA_v^{\beta}} \sum_{r=1}^{v} A_{v-r}^{-\alpha-1} r A_r^{\alpha+\beta} y_r \\ &= \varphi_n^{1/k^*}\hat{a}_n \sum_{r=1}^{n} \left(r A_r^{\alpha+\beta} \sum_{v=r}^{n} \frac{a_v \varepsilon_v A_{v-r}^{-\alpha-1}}{vA_v^{\beta}} \right) y_r \\ &= \sum_{r=1}^{n} d_{nr}\, y_r\end{aligned}$$

where

$$d_{nr} = \begin{cases} \varphi_n^{1/k^*}\hat{a}_n r A_r^{\alpha+\beta} \sum_{v=r}^{n} \frac{a_v \varepsilon_v A_{v-r}^{-\alpha-1}}{vA_v^{\beta}} \ , 1 \leq r \leq n \\ 0, r > n. \end{cases}$$

Then, $\sum \varepsilon_n x_n$ is summable $|A_f, \varphi_n|_k$ whenever $\sum x_n$ is summable $|C, \alpha, \beta|$ if and only if $\tilde{y} \in \ell_k$ whenever $y \in \ell$. Hence using Lemma 2.2, we obtain that $\varepsilon \in (|C, \alpha, \beta|, |A_f, \varphi_n|_k)$ if and only if

$$\sup_r \left\{ \sum_{n=r}^{\infty} \left| \varphi_n^{1/k^*}\hat{a}_n r A_r^{\alpha+\beta} \sum_{v=r}^{n} \frac{a_v \varepsilon_v A_{v-r}^{-\alpha-1}}{vA_v^{\beta}} \right|^k \right\} < \infty$$

which completes the proof.

Theorem 2.5. Let $k > 1$, $\alpha + \beta > -1$ and $\beta > -1$. Then the necessary and sufficient condition for $\varepsilon \in (|A_f, \varphi_n|_k, |C, \alpha, \beta|)$ is that

$$\sum_{v=1}^{\infty} \left(\sum_{n=v}^{\infty} \left| \frac{1}{nA_n^{\alpha+\beta} \varphi_v^{1/k^*}\hat{a}_v} \Omega_{nv} \right| \right)^{k^*} < \infty, \qquad (2.4)$$

where $\Omega = (\Omega_{nv})$ is defined by

$$\Omega_{nv} = \begin{cases} \frac{A_{n-v}^{\alpha-1} A_v^{\beta} v\varepsilon_v}{a_v} - \frac{A_{n-v-1}^{\alpha-1} A_{v+1}^{\beta}(v+1)\varepsilon_{v+1}}{a_{v+1}}, 1 \leq v \leq n, \\ 0, v > n. \end{cases}$$

Proof. Let $(\tilde{y}_n)$ denote the sequence defined by

$$\tilde{y}_n = \varphi_n^{1/k^*}\hat{a}_n \sum_{v=1}^{n} a_v x_v \, , n \geq 1, and \ \tilde{y}_0 = x_0. \ (2.5)$$

So, we can write that $\sum x_n$ is summable $|A_f, \varphi_n|_k$ iff $\tilde{y} = (\tilde{y}_n) \in \ell_k$. By inversion of (2.5), we obtain for $n \geq 1$,

$$x_n = \frac{1}{a_n} \left(\frac{\tilde{y}_n}{\varphi_n^{1/k^*}\hat{a}_n} - \frac{\tilde{y}_{n-1}}{\varphi_{n-1}^{1/k^*}\hat{a}_{n-1}} \right). \qquad (2.6)$$

Also let $(u_n^{\alpha,\beta})$ be the nth (C, α, β) mean of the sequence $(nx_n\varepsilon_n)$, i.e.,

$$u_n^{\alpha,\beta} = \frac{1}{A_n^{\alpha+\beta}} \sum_{v=1}^{n} A_{n-v}^{\alpha-1} A_v^{\beta} v\varepsilon_v x_v.$$

If we define $y = (y_n)$ by

$$y_n = \frac{u_n^{\alpha,\beta}}{n} = \frac{1}{nA_n^{\alpha+\beta}} \sum_{v=1}^{n} A_{n-v}^{\alpha-1} A_v^{\beta} v\varepsilon_v x_v,$$

then, we say that $\sum \varepsilon_n x_n$ is summable $|C, \alpha, \beta|$ iff $y = (y_n) \in \ell$. Hence, by virtue of the (2.6), we get for $n \geq 1$,

$$\begin{aligned} y_n &= \frac{1}{nA_n^{\alpha+\beta}} \sum_{v=1}^{n} A_{n-v}^{\alpha-1} A_v^{\beta} v\varepsilon_v x_v \\ &= \frac{1}{nA_n^{\alpha+\beta}} \sum_{v=1}^{n} A_{n-v}^{\alpha-1} A_v^{\beta} v\varepsilon_v \frac{1}{a_v} \left(\frac{\tilde{y}_v}{\varphi_v^{1/k^*}\hat{a}_v} - \frac{\tilde{y}_{v-1}}{\varphi_{v-1}^{1/k^*}\hat{a}_{v-1}} \right) \\ &= \frac{1}{nA_n^{\alpha+\beta}} \left(\sum_{v=1}^{n} \frac{A_{n-v}^{\alpha-1} A_v^{\beta} v\varepsilon_v \tilde{y}_v}{a_v \varphi_v^{1/k^*}\hat{a}_v} \right. \\ &\quad \left. - \sum_{v=0}^{n-1} \frac{A_{n-v-1}^{\alpha-1} A_{v+1}^{\beta}(v+1)\varepsilon_{v+1}\tilde{y}_v}{a_{v+1}\varphi_v^{1/k^*}\hat{a}_v} \right) \\ &= -\frac{A_{n-1}^{\alpha-1} A_1^{\beta} \varepsilon_1 \tilde{y}_0}{nA_n^{\alpha+\beta} a_1 \varphi_0^{1/k^*}\hat{a}_0} \\ &\quad + \frac{1}{nA_n^{\alpha+\beta}} \sum_{v=1}^{n} \left(\frac{A_{n-v}^{\alpha-1} A_v^{\beta} v\varepsilon_v}{a_v} \right. \\ &\quad \left. - \frac{A_{n-v-1}^{\alpha-1} A_{v+1}^{\beta}(v+1)\varepsilon_{v+1}}{a_{v+1}} \right) \frac{\tilde{y}_v}{\varphi_v^{1/k^*}\hat{a}_v} = \sum_{v=0}^{n} d_{nv}\tilde{y}_v \end{aligned}$$

where $D = (d_{nv})$ is defined by

$$d_{nv} = \begin{cases} -\frac{A_{n-1}^{\alpha-1} A_1^{\beta} \varepsilon_1}{nA_n^{\alpha+\beta} a_1 \varphi_0^{1/k^*}\hat{a}_0}, & v = 0, n \geq 1, \\ \frac{1}{nA_n^{\alpha+\beta} \varphi_v^{1/k^*}\hat{a}_v} \Omega_{nv} \, , 1 \leq v \leq n \\ 0, & v > n, \end{cases}$$

and $\Omega = (\Omega_{nv})$ is as in Theorem 2.5.

Celal Bayar University Journal of Science
Volume 16, Issue 1, 2020, p 89-93
Doi: 10.18466/cbayarfbe.619883

Then, $\sum \varepsilon_n x_n$ is summable $|C,\alpha,\beta|$ whenever $\sum x_n$ is summable $|A_f,\varphi_n|_k$ if and only if $y \in \ell$ whenever $\tilde{y} \in \ell_k$. Hence in view of Lemma 2.1, we obtain that $\varepsilon \in (|A_f,\varphi_n|_k, |C,\alpha,\beta|)$ if and only if

$$\sum_{v=0}^{\infty}\left(\sum_{n=v}^{\infty}|d_{nv}|\right)^{k^*} < \infty$$

which gives that

$$\left(\sum_{n=1}^{\infty}|d_{n0}|\right)^{k^*} + \sum_{v=1}^{\infty}\left(\sum_{n=v}^{\infty}|d_{nv}|\right)^{k^*} = \left(\sum_{n=1}^{\infty}\left|\frac{A_{n-1}^{\alpha-1}A_1^{\beta}\varepsilon_1}{nA_n^{\alpha+\beta}a_1\varphi_0^{1/k^*}\hat{a}_0}\right|\right)^{k^*}$$

$$+\sum_{v=1}^{\infty}\left(\sum_{n=v}^{\infty}\left|\frac{1}{nA_n^{\alpha+\beta}\varphi_v^{1/k^*}\hat{a}_v}\left(\frac{A_{n-v}^{\alpha-1}A_v^{\beta}v\varepsilon_v}{a_v} - \frac{A_{n-v-1}^{\alpha-1}A_{v+1}^{\beta}(v+1)\varepsilon_{v+1}}{a_{v+1}}\right)\right|\right)^{k^*} < \infty.$$

Since $\sum_{n=1}^{\infty}\left|\frac{A_{n-1}^{\alpha-1}}{nA_n^{\alpha+\beta}}\right| < \infty$ from Lemma 2.3 , we get that (2.4) holds, which completes the proof.

3. Conclusion

Our results have several consequences depending on $\alpha,\beta,(\hat{a}_n)$ and (a_n) .

If we consider the special case $\varepsilon = 1$ in the Theorem 2.4 and Theorem 2.5, we have following results dealing with comparison of summability fields of methods $|C,\alpha,\beta|$ and $|A_f,\varphi_n|_k$.

Corollary 3.1. Let $k \geq 1$ and $\alpha+\beta > -1$. Then, $|C,\alpha,\beta| \subset |A_f,\varphi_n|_k$ if and only if

$$\sup_r\left\{\sum_{n=r}^{\infty}\left|\varphi_n^{1/k^*}\hat{a}_n r A_r^{\alpha+\beta}\sum_{v=r}^{n}\frac{a_v A_{v-r}^{-\alpha-1}}{vA_v^{\beta}}\right|^k\right\} < \infty.$$

Corollary 3.2. Let $k > 1$, $\alpha+\beta > -1$ and $\beta > -1$. Then $|A_f,\varphi_n|_k \subset |C,\alpha,\beta|$ if and only if

$$\sum_{v=1}^{\infty}\left(\sum_{n=v}^{\infty}\left|\frac{1}{nA_n^{\alpha+\beta}\varphi_v^{1/k^*}\hat{a}_v}\left(\frac{A_{n-v}^{\alpha-1}A_v^{\beta}v}{a_v} - \frac{A_{n-v-1}^{\alpha-1}A_{v+1}^{\beta}(v+1)}{a_{v+1}}\right)\right|\right)^{k^*} < \infty.$$

Taking $\hat{a}_n = \frac{p_n}{P_nP_{n-1}}$, $a_v = P_{v-1}$ in the Theorem 2.4 and Theorem 2.5, we get the following results, respectively.

Corollary 3.3. Let $k \geq 1$ and $\alpha+\beta > -1$. Then the necessary and sufficient condition for $\varepsilon \in (|C,\alpha,\beta|, |\bar{N},p_n,\varphi_n|_k)$ is that

$$\sup_r\left\{\sum_{n=r}^{\infty}\left|\varphi_n^{1/k^*}\frac{p_n}{P_nP_{n-1}}rA_r^{\alpha+\beta}\sum_{v=r}^{n}\frac{P_{v-1}\varepsilon_v A_{v-r}^{-\alpha-1}}{vA_v^{\beta}}\right|^k\right\} < \infty.$$

Corollary 3.4. Let $k > 1$, $\alpha+\beta > -1$ and $\beta > -1$. Then the necessary and sufficient condition for $\varepsilon \in (|\bar{N},p_n,\varphi_n|_k, |C,\alpha,\beta|)$ is that

$$\sum_{v=1}^{\infty}\left(\sum_{n=v}^{\infty}\left|\frac{P_vP_{v-1}}{nA_n^{\alpha+\beta}\varphi_v^{1/k^*}p_v}\left(\frac{A_{n-v}^{\alpha-1}A_v^{\beta}v\varepsilon_v}{P_{v-1}} - \frac{A_{n-v-1}^{\alpha-1}A_{v+1}^{\beta}(v+1)\varepsilon_{v+1}}{P_v}\right)\right|\right)^{k^*} < \infty.$$

If we take $\beta = 0$, Theorem 2.4 and Theorem 2.5 reduce to the next results, respectively.

Corollary 3.5. Let $k \geq 1$ and $\alpha > -1$. Then the necessary and sufficient condition for $\varepsilon \in (|C,\alpha|, |A_f,\varphi_n|_k)$ is that

$$\sup_r\left\{\sum_{n=r}^{\infty}\left|\varphi_n^{1/k^*}\hat{a}_n rA_r^{\alpha}\sum_{v=r}^{n}\frac{a_v\varepsilon_v A_{v-r}^{-\alpha-1}}{v}\right|^k\right\} < \infty.$$

Corollary 3.6. Let $k > 1$ and $\alpha > -1$. Then the necessary and sufficient condition for $\varepsilon \in (|A_f,\varphi_n|_k, |C,\alpha|)$ is that

$$\sum_{v=1}^{\infty}\left(\sum_{n=v}^{\infty}\left|\frac{1}{nA_n^{\alpha}\varphi_v^{1/k^*}\hat{a}_v}\left(\frac{A_{n-v}^{\alpha-1}v\varepsilon_v}{a_v} - \frac{A_{n-v-1}^{\alpha-1}(v+1)\varepsilon_{v+1}}{a_{v+1}}\right)\right|\right)^{k^*} < \infty.$$

Also, taking $\hat{a}_n = \frac{p_n}{P_nP_{n-1}}$, $a_v = P_{v-1}$ in the Corollary 3.5. and Corollary 3.6, we have:

Corollary 3.7. Let $k \geq 1$ and $\alpha > -1$. Then the necessary and sufficient condition for $\varepsilon \in (|C,\alpha|, |\bar{N}, p_n, \varphi_n|_k)$ is that

$$\sup_r \left\{ \sum_{n=r}^{\infty} \left| \varphi_n^{1/k^*} \frac{p_n}{P_n P_{n-1}} r A_r^{\alpha} \sum_{v=r}^{n} \frac{P_{v-1} \varepsilon_v A_{v-r}^{-\alpha-1}}{v} \right|^k \right\} < \infty.$$

Corollary 3.8. Let $k > 1$ and $\alpha > -1$. Then the necessary and sufficient condition for $\varepsilon \in (|\bar{N}, p_n, \varphi_n|_k, |C,\alpha|)$ is that

$$\sum_{v=1}^{\infty} \left(\sum_{n=v}^{\infty} \left| \frac{P_v P_{v-1}}{n A_n^{\alpha} \varphi_v^{1/k^*} p_v} \left(\frac{A_{n-v}^{\alpha-1} v \varepsilon_v}{P_{v-1}} - \frac{A_{n-v-1}^{\alpha-1} (v+1) \varepsilon_{v+1}}{P_v} \right) \right| \right)^{k^*} < \infty.$$

Acknowledgement

Authors may acknowledge technical assistance, the source of special materials, financial support and the auspices under which work was done. The names of funding organizations should be written in full.

Ethics

There are no ethical issues after the publication of this manuscript.

References

1. Sulaiman, W.T., "On some summability factors of infinite series", Proc. Amer. Math. Soc., 115: 313-317, (1992).
2. Bor, H., "On two summability methods", Math. Proc. Cambridge Philos Soc., 97: 147-149, (1985).
3. Sarıgöl, M.A., "On two absolute Riesz summability factors of infinite series" Proc. Amer. Math. Soc.,118: 485-488, (1993).
4. Sarıgöl, M. A., " On absolute factorable matrix summability methods" , Bull. Math. Anal. Appl., 8: 1-5, (2016).
5. Borwein, D., "Theorems on some methods of summability", Quart. J. Math. Oxford Ser. (2), 9: 310-314, (1958).
6. Das, G., "A Tauberian theorem for absolute summability", Proc. Camb. Phil. Soc., 67: 321-326, (1970).
7. Flett, T.M., "On an extension of absolute summability and some theorems of Littlewood and Paley", Proc. London Math. Soc., 7: 113-141, (1957).
8. Mazhar, S.M. "On the absolute summability factors of infinite series", Tohoku Math. J., 23: 433-451, (1971).
9. Mehdi, M.R., "Summability factors for generalized absolute summability I", Proc. London Math. Soc., 10(3): 180-199, (1960).
10. Mohapatra, R.N., "On absolute Riesz summability factors", J. Indian Math. Soc., 32: 113-129, (1968).
11. Bor, H., "Some equivalence theorems on absolute summability methods", Acta Math. Hung., 149: 208-214, (2016).
12. Hazar Güleç, G.C., Sarıgöl, M.A., "On factor relations between weighted and Nörlund means", Tamkang J. Math., 50(1): 61-69, (2019).
13. Sulaiman, W.T., "On some absolute summability factors of Infinite Series", Gen. Math. Notes, 2, 2: 7-13, (2011).
14. Hazar, G.C., Sarıgöl, M.A., "Absolute Cesàro series spaces and matrix operators", Acta App. Math., 154: 153-165, (2018).
15. Hazar Güleç, G.C., Sarıgöl, M.A., "Compact and Matrix Operators on the Space $|C,-1|_k$", J. Comput. Anal. Appl., 25(6): 1014-1024, (2018).
16. Sarıgöl, M.A., "Spaces of series summable by absolute Cesàro and matrix operators", Commun. Math. Appl., 7(1): 11-22, (2016).
17. Sarıgöl, M.A., "Extension of Mazhar's theorem on summability factors", Kuwait J. Sci.,42(3): 28-35, (2015).
18. Maddox, I.J., "Elements of Functional Analysis", Cambridge University Press, London, New York, (1970).

Celal Bayar University Journal of Science

pH-Dependent Behavior and Stability of Protein-Based Particles in Aqueous Media

Alev Emine İnce Coşkun[1*], Özgül Özdestan Ocak[1], Buğra Ocak[2], Semih Ötleş[1]

[1]Department of Food Engineering, Ege University, Bornova, İzmir.
[2]Department of Leather Engineering, Ege University, Bornova, İzmir.
*alevince@gmail.com

Received: 25 September 2019
Accepted: 17 March 2020
DOI: 10.18466/cbayarfbe.624428

Abstract

This review focused on the characteristics of protein particles from different sources, namely whey proteins, sodium caseinate and gelatin, their structural stability and the stability of dispersions at different pH values. To create particles, controlled aggregation and gelation were used in several methods. Different chemical structures of the proteins provide different gelation properties. Whey proteins undergo thermal denaturation above 68°C, therefore heat-set gelatin was often used for particle preparation. When whey protein particles were prepared at the iso-electric point (IEP) of proteins, they became dense and small; whereas at other pH values, particles were soft and spherical due to increased repulsive forces between proteins. Such particles could swell when the pH of the aqueous phase was away from the IEP. Sodium caseinate is more heat stable compared to whey proteins; however, it is pH-sensitive. When sodium caseinate particles were prepared through acidification, particles were stable against disintegration only around the IEP of proteins. More stable caseinate particles could be produced using enzymatic crosslinking. On the other hand, gelatin particles, which were prepared via cold-set gelation, were stable over a wide pH range; however, as they were thermo-sensitive, particles disintegrated above 30°C. This review explained the chemical differences of proteins, preparation of particles using different methods, and stability of particles and their dispersions at different conditions. Such differences in protein particles should be carefully investigated before they are used in food products, which could have complex matrix.

Keywords: Aggregation, gelatin, microstructure, sodium caseinate, whey protein

1. Introduction

Stability of proteins refers to a wide range of area, such as stability against aggregation, against sedimentation or against structural integrity. Native proteins, due to the presence of ionic groups in their structure, are affected by the electrostatic interactions. In this review, we focused on the structure and stability of different proteins (namely whey proteins, caseins and gelatin) in dispersions particularly considering the electrostatic interactions through pH change. These proteins are widely used in food industry and their micro- and nano-particulate forms could give several properties to food products. Therefore, their behaviour at different pH values in aqueous media is important to know. The chosen proteins are from different sources, have different chemical structures, and thereby having all different properties from each other.

Whey proteins are the by-product in cheese production and constitute almost 0.6% (w/v) of the proteins in milk. Of the total protein, nearly 20% (w/w) is whey proteins and 80% (w/w) is caseins. Whey proteins include β-lactoglobulin (BLG), α-lactalbumin (ALAC), bovine serum albumin and immunoglobulin, and therefore it is highly complex [1]. In whey proteins, secondary and tertiary structures, including α-helix and β-sheets, are present [2]. BLG and ALAC have disulfide bonds, which could change the hydrophobicity and thereby the solubility of the protein. Therefore, solubility of whey proteins is also affected by the chemical structure besides physical conditions, such as acidification or heating [3]. Such treatments often cause aggregation of whey proteins that result in increased turbidity or viscosity in aqueous solutions. In addition, heating of whey protein solution with a high concentration could result in gel formation. These changes in liquid food

products including whey proteins are not desired as the product acceptability decreases.

Caseins, another protein from milk source, has a complex structure with little amount of secondary or tertiary structure [4]. Caseins show amphiphilic characteristics and therefore they are highly used in emulsion or foaming systems [5]. Caseins could also give texture and increase the water binding capacity of food products. The main function of casein in bovine milk is thought to be nutritional [6], however there are many techno-functional properties in food products. α_{S1}, α_{S2}-, β-, and κ-casein are the different types and they found in the ratio 4:1:4:1.3 [7]. In the native form, κ-caseins forms a hairy layer around the micelles and these hairs becomes inactive upon acidification at or around the iso-electric point (IEP) of casein (pH 4.6) and thereby forming aggregates through formation of salt bridges [8]. On the other hand, stability of casein against aggregation upon heating is quite high compared to whey proteins. Heat coagulation of casein could happen above 120°C [9]. Therefore, gelation or aggregation of caseins is often achieved by acidification or enzymatic crosslinking [10].

Caseins are often found in micelle form in milk, however in food products salt derived forms, which are caseinates, are more commonly used. At the IEP of caseins, washing is done to obtain pure precipitate of caseins and then it is neutralized. When NaOH is used for neutralization process, sodium caseinate (NaCas) is obtained [11]. In food systems, NaCas has several techno-functional properties such as texturizer, thickening or gelling agent, or more commonly as emulsifier due to its amphiphilic property [12].

Another protein from animal source is gelatin, which is obtained through hydrolysis of collagen [13]. Molecular structure of gelatin includes single or multiple strands of polypeptides in a helix conformation [14]. The most commonly known characteristic of gelatin is being a thermo-reversible gel. Below the melting point, gelatin has a triple-helix structure; whereas above the melting point, hydrogen bonds between helical structures are broken and the molecular structure turns into a random-coil state [15].

Gelatin could be obtained from different sources such as pork, bovine or fish, each of which has different properties. Gelling and melting temperatures of gelatin changes with respect to the species. For instance, cold water fish gelatin can melt at 4°C and gel below at 17°C, whereas warm water fish gelatin can melt at 18°C and gel at 24°C. On the other hand, melting temperature of pork or bovine gelatin can be above 30°C [13]. Depending on the pretreatment during the extraction process, either alkaline or acid conditions, two main types of gelatin are obtained, which are namely type-A and type-B. The IEP of type-A gelatin is around at pH 8-9, whereas that of type-B is around at pH 4-5 [13]. Another classification of gelatin can be made based on the gel strength, which is often expressed using Bloom number. Bloom number is mainly a function of source of gelatin and its processing conditions [16]. Source of gelatin determines the amino acid composition and processing conditions could change the molecular weight distribution, both of which affect the bloom number. Bloom number affects the physical properties of gelatin, and thereby determining its use area.

Whey proteins, NaCas and gelatin are all from different sources and have different physical and chemical properties, thereby having different functional properties. Their gelation conditions are also different from each other. Their potential use areas vary from solid state food materials, such as dough, to fluids, such as emulsion and foam systems. Therefore, in this review we focus on the particle formation through controlled gelation of these proteins and their behavior against changing pH in an aqueous medium.

2. Preparation Methods of Protein Particles

Preparation of functional foods and functional components are important [17]. One possible way to give extra functionality is to create particles through gelation of proteins. Particles produced using different biomaterials were studied previously [18, 19, 20]. Presence of proteins in these studies supply many functional and structural properties, such as biocatalysis, bioactivity, thickening, drug delivery or possible applications in tissue engineering.

Protein aggregation or gelation under certain conditions can be turned into an advantage for further stability of proteins. To make protein particles with a better control over the physicochemical properties, several methods were described in literature, such as heat-set or cold-set gelation [21, 22]. In aggregation or gelation of proteins, peptide chains interact through hydrophobic interactions, hydrogen bonding, electrostatic interactions, disulfide bridges or van der Waals interactions, and therefore rearrangement of proteins occurs [23]. Once the aggregation or gelation is done in a controlled way, protein particles with different properties could be obtained.

Heat-set gelation of proteins is a commonly used method to make particles from globular proteins, especially from the whey proteins [21, 22, 24, 25]. Whey protein solutions were heated above their denaturation temperature (68°C), which allows the reactive groups of amino acids to be free, and subsequently aggregates were formed via hydrophobic interactions, hydrogen bonding, and disulfide bonding [24]. Heat-set gelation is irreversible; therefore, stable forms of aggregates can be obtained. The size of

aggregates, which depended on the heating time and temperature, has ranged between a few hundred nm to a few microns [24, 26]. Larger aggregate formation was reported at higher temperatures during the gelation process and longer heating times through nucleation and growth process. Heat application can also be used as a pre-application in particle formation, as many proteins are susceptible to heating.

Cold-set gelation is another method to prepare protein particles. In cold-set gelation, often acidification [27, 28, 29], salt addition [26, 30], or enzymatic crosslinking [31, 32, 33] methods were used. A heating step either before or after the cold process can be used to create aggregates or to stabilize the aggregates [22, 34].

To create protein particles, acidification can be done using either acid solutions [27, 28] or acidifying agents, such as glucono-δ-lactone (GDL) [35, 36]. This method uses the principle of decreasing or totally inhibiting the net charge of the proteins and as a result, aggregates are formed. For many proteins, acidification is done until IEP is reached as the net charge is zero at the point. Salt addition also has a similar effect on the net charge of proteins; however the mechanism is different from pH-induced aggregation. Salt ions screen the charges of proteins, which are responsible for the repulsive forces. Monovalent salt (e.g. NaCl) ions can only screen the charges, whereas multivalent salt (e.g. $MgCl_2$, $AlCl_3$) ions can have additional effects, such as salt bridge formation or specific ion adsorption, besides screening [25, 37].

Enzymatic cross-linking of proteins is an alternative method for the production of particles [31, 32]. In this method, protein solutions with or without a pretreatment, such as heating or pH adjustment, were mixed with an enzyme. As enzyme functions, protein cross-linking has been achieved, and therefore particles have been formed as separate stable entities.

A recent method to produce protein particles is the emulsification method [32, 38]. In this method, a protein solution has been emulsified in an oil solution to create droplets. Then, the gelation of these droplets has been induced using one of the methods explained above. After gelation of the protein in droplets, particles have been separated from the water-in-oil emulsion using a centrifuge. This method was used for several proteins using different gelation techniques and was shown to be flexible to change the size, source, concentration, and pH of the protein particles [39, 40]. Changing these properties allow changing the internal and surface structure of particles, influencing the functional properties and thus the use area of them.

3. Effect of pH on Whey Protein Particles and Their Dispersions

Whey proteins have an IEP of around pH 5.1 and native whey proteins in their neutral aqueous solution are negatively charged. At different pH values, overall charge of whey proteins varies. The net charge of proteins at pH values away from the IEP prevents the aggregation due to the presence of repulsive forces. The pH of the aqueous phase influences the stability against aggregation of proteins, which could limit the acceptability of beverages. Such stability problems could be solved to some extent by using controlled aggregation and thereby creating protein particles or changing the surface properties of protein particles [41].

Protein particles behave like colloidal particles and they can be stabilized against coagulation by changing their surface properties. For instance, increasing the electrostatic or steric repulsive forces through changing pH, adding salt, or coating the particles with different polymers prevents the particles from approaching to each other, thereby preventing the coagulation [42].

In a study, soft and hard whey protein isolate (WPI) particles were prepared using a two-step emulsification method [43]. Sağlam and co-workers [43] prepared soft WPI particles, which were at pH 6.8, and hard WPI particles, which were at pH 5.5. These particles had different physical properties from each other [44]. For instance, soft WPI particles, which were spherical, had lower internal protein concentration, more open microstructure and smoother surface structure than the hard WPI particles [44]. On the other hand, hard WPI particles had a denser network inside particle than soft ones and a cauliflower-like shape. These properties affect the stability and colloidal behavior of particles. For example, the maximum volume fraction of the particles for a stable dispersion in the case of soft ones was found to be lower than that in the case of corresponding rigid particles. The theoretical approach for this difference explained the reason as the smaller energy barrier for two interacting colloids, which includes the electrical energy and van der Waals energy, for the soft particles than for the rigid ones [45]. Practically, the porous structure and swelling ability of the soft particles, as a result of the interaction with the co-solvents, allow a lower volume fraction of particles for a stable dispersion. At the same protein concentrations (in terms of weight) and the same size of particles, soft WPI particles had a volume fraction of 0.35, whereas hard WPI particles had a volume fraction of 0.15 [46]. This finding suggests that the volume fraction of soft particles increase faster due to the flexible network inside particles, which disrupts the colloidal stability, than that of hard particles.

Other than the colloidal stability, the stability of particle integrity is also highly dependent on the electrostatic interactions. Both soft and hard WPI particles were found to be sensitive to changes in pH of the dispersion [47]. When pH of the dispersion was changed from neutral to alkaline values, the protein network inside the particle was disrupted with the increasing repulsive force. Depending on the strength of this repulsive force, particles either swelled or at the extremes they disintegrated. When the pH of the dispersion was lowered, until the IEP was reached, WPI particles were reported to shrink, and below the IEP, due to the increased repulsive forces, particles again showed swelling. Soft WPI particles had relatively an open structure compared to the hard particles, and therefore the sensitive characteristics of soft particles to any changes in the medium, like pH or salt concentration, is expected. In the case of hard WPI particles, due to their dense and compact structure, the sensitivity to pH or salt may be less expected. However, they showed the similar vulnerability to changes in electrostatic forces [47]. At highly alkaline pH, the protein leakage from the hard particles was even more than the soft ones. The reason of the situation could be that during preparation of the hard particles, dominant contribution of electrostatic forces to the aggregation of proteins besides covalent interactions, such as disulfide bonds, which can stabilize the network as in the case of heat-set gelation [23, 34].

Disintegration of soft WPI particles could have been observed from the appearance of dispersions [47]. Particularly at pH 2 and pH 9.5, dispersions became translucent, most probably due to the disintegration of the particles. On the other hand, at other pH values in between pH 2 and pH 9.5, dispersions seemed more homogeneous and opaque, which means particle integrity was not largely disrupted. At or around the IEP of proteins, at pH 5, dispersions showed phase separation with a clear upper phase. In the same study, a flow-cell set-up for CLSM indicated that increasing pH of the continuous phase up to 10.5 resulted in swelling of particles and decreasing pH till 5.5 resulted in shrinking of particles. These results indicate that soft WPI particles were reversible pH-responsive micro-gels, as they kept their integrity upon consecutive increase and decrease of pH of the continuous phase. Such pH-responsive micro-gels could be promising in controlled delivery systems, particularly in pharmaceutical applications.

4. Effect of pH on Sodium Caseinate (NaCas) Particles and Their Dispersions

NaCas particles were produced using two-step emulsification method and using acidification in the gelation step [40]. In this case, emulsification was followed by acidification using GDL, which hydrolyses slowly in the aqueous phase, and thereby lowering the pH of NaCas droplets in the emulsion till its IEP. At this point, electrostatic repulsion between proteins decreased and therefore aggregation occurred. NaCas particles were a few hundred microns, highly porous and had irregular shapes. In that study, there was whey protein as co-solvent in the aqueous phase, and therefore pH-dependent phase separation was observed at pH 5 due to reduced electrostatic repulsion. NaCas dispersions were stable and opaque at pH values between 3 and 4. At lower and higher pH values than these, appearances of dispersions were less opaque and translucent, indicating disintegration of protein particles. SEM images of NaCas particles at pH 2, pH 3.5, and pH 6 also proved the pH-dependent disintegration away from the IEP of proteins. Above pH 6, translucent appearance was more pronounced and few particles could have been observed under CLSM, indicating that the particle integrity was not kept due to strong electrostatic repulsion [40]. In the same study, rheological behavior of dispersions at different pH values was also investigated to determine the effect of swelling of particles. Before disintegration of particles due to strong repulsion, there were pH values at which particles still kept their integrity, however depending on the strength of repulsion size of particles could have increased and microstructure of particles have changed. Viscosity measurements in rheological tests showed that at pH 2, the viscosity of dispersions increased, indicating the swelling of particles; whereas at pH 6, viscosity of dispersions decreased, indicating the disintegration of particles.

In another study, NaCas was used as a stabilizer for zein colloidal particles [48]. Zein particles were prepared using a controlled precipitation method, and NaCas was then added to cover the zein particles. Zein particles with negative surface charge density attracted the NaCas electrostatically, and the IEP of the new system became in between those of native proteins. As the pH of the system shifted from the IEP of zein, where zein aggregated, particles became stable against aggregation. In the same study, zein dispersion system was found to be stable in the presence of different NaCl concentrations, which means screening of charges did not affect the stability of colloidal particles and there was still enough repulsion. Stability of dispersion in the presence of NaCas was attributed to both electrostatic and steric interactions. Repulsive forces kept particles from approaching to each other and full surface coverage of particles by NaCas supplied steric stabilization. Thus, the concentration of NaCas could determine the strength of steric and electrostatic interactions; at higher concentrations complete surface coverage could have been reached and therefore dispersions became more stable against aggregation or precipitation [48].

A more recent and similar study was done with zein particles including NaCas for encapsulation and

controlled release systems [49]. An aromatic organic chemical, coumarin, was encapsulated using zein/NaCas-mix particles and also using NaCas coated zein particles. They have investigated the effect of several parameters during fabrication of particles, such as mixing ratio, concentration of protein, and temperature; and thus they obtained either nano- or micro-particles with optimized concentration and temperature for high stability against aggregation. In addition, the mechanisms of particle formation in both cases (either mix particles or NaCas coated particles) were explained and resulting particles were found to be similar. In the case of zein/NaCas mix particle formation, they proposed adsorption driven particle formation and coacervate formation during mixing. Both adsorption and coacervation could have occurred in short time during the course of mixing, therefore particles probably included both proteins inside their structure, changing the microstructure of particles. On the other hand, the size distribution and zeta potential values of particles showed that NaCas most probably sat on the surface of zein particles. Similar to this structure, already-formed zein particles with a NaCas coating on their surface had a core and shell structure. However, for the coated particles, FTIR results showed a shift to lower peak values, indicating the bonding interactions were different from zein/NaCas mix particles [49].

In another study, effect of pH on the accumulation of NaCas on alginate micro-gels was studied [50]. In that study, interaction between NaCas and alginate micro-gels was determined at different pH values. Alginate gels were always negatively charged at pH values between 3 and 7, whereas as NaCas has an IEP around pH 4.1, at pH 3, it is positively charged and at and above pH 5 it is negatively charged. Therefore, at these pH values, interaction was shaped by the electrostatic forces. Alginate particles could have been coated with NaCas at pH 3 as a result of attractive forces, whereas at and above pH 5 they repel each other. Interestingly, authors showed an accumulation of NaCas around alginate particles at pH 4, where no electrostatic attraction was expected. They reported the reason of this behavior as the presence of positively charged patches on the surface of NaCas protein at the IEP, as the point was actually indicated a narrow range of pH values. The IEP being a range rather than a single value is due to the presence of NaCas from different sources. Different sources of caseins provided a different distribution of carboxyl and amine groups, and this distribution resulted in a range of IEP of protein instead of specifying an exact single pH value [51].

5. Effect of pH on Gelatin Particles and Their Dispersions

As gelatin is a thermo-reversible protein, its particles are highly sensitive to temperature changes [40]. Gelatin micro-particles were prepared via two-step emulsification method with cold-set gelation. Physical properties of these particles were investigated in a broad pH range, from pH 2 to pH 12. SEM pictures showed homogeneous and spherical structures for all tested pH values between 2 and 12, indicating that gelatin micro-gels were stable against disintegration upon pH changes. Alternatively, dispersions of gelatin particles in whey protein solution showed stability against sedimentation for all pH values except pH 6. At pH 6, a phase separation was observed probably due to the electrostatic attraction between gelatin and whey proteins, which occurred as a result of charge neutralization [40].

Gelatin gels have triple-helix structure and flexible, therefore changes in the strength of repulsive forces affect the strength of gels [52]. Gelatin micro-gels were able to swell; they had an average diameter of 4 μm at neural pH of the medium and at other pH values their sizes were found to increase [40]. Viscosity measurements of dispersions also indicated the swelling of particles at pH values away from pH 6, at which the overall charge of particles was close to zero. Strength of repulsive forces increased at pH values away from pH 6 and thereby increasing the effective size of particles, which increased the volume fraction of particles in the dispersion. Dispersions showed higher viscosities at acidic pH values than the alkaline pH values, indicating that acidic pH values had stronger repulsive effect on gelatin micro-gels.

Other than emulsification method, gelatin nano-particles were produced using desolvation method [53, 54]. With this method under controlled conditions, homogeneous and monodisperse gelatin particles could have been obtained. Such particles, due to their flexible network structure and thermo-sensitive properties, were used in controlled release systems. In controlled release systems, size of particles and their internal network density were found to be important [54]. Microstructure of nano-particles was shown to depend on the changing pH of gelatin. Adjusted pH values of gelatin solutions altered the hydration characteristics, and thereby changing the electrostatic interactions [29]. As a result of changing electrostatic forces; different shapes of gelatin particles such as spherical, needle-like or irregular-shaped were obtained. Such morphological differences were found to be dependent also on the concentration of gelatin through hydrophobic interactions, hydrogen bonding, or van der Waals forces. Particularly, at the IEP of gelatin, as there was no net charge on the protein, these weak non-covalent interactions were more favored [53]. On the other hand, Ahsan and Rao [54] explained that at lower pH values than the IEP of proteins could have increased the number of hydrogen bonds via increasing available hydrophilic sections of gelatin with water. As a result of

increasing water retention, gelatin network became denser. Particle size increase at pH values away from the IEP was mainly a result of increased electrostatic repulsion. When gelatin concentration was high, the reason of particle size increase at pH values lower than the IEP was further explained with the macromolecular crowding, which could induce swelling of particles or deposition of biomaterials on the surface of particles. It was also reported that even under strong electrostatic repulsion, it was still possible to produce nano-particles using desolvation method and the particles could keep their integrity well at different pH values.

6. Conclusion

In this review, we considered three different types of protein in micro- or nano-sized particles and their stability against disintegration or swelling at different pH values. We have explained the chemical and physical properties of whey proteins, caseins and gelatin. As a globular protein, whey proteins aggregate above denaturation temperature and therefore most of the time heat-set gelation was used with different techniques. Whey proteins have a net charge except their IEP, so pH of the medium affected the integrity and stability of the particles. Whey protein particles could have swollen depending on the strength of the electrostatic forces. On the other hand, sodium caseinate particles were heat stable but highly sensitive to pH changes. As they were often formed via acidification to the IEP of casein, they kept their integrity only around that pH. Alternatively, gelatin particles were highly stable against pH changes; they could keep their integrity well at different pH values. As gelatin also has a net charge in aqueous environment, flexible micro-particles can swell or shrink depending on the strength of the electrostatic repulsion, which was similar to the case of whey protein particles. These particles have a high potential use in food and pharmaceutical industries, as texturizer and/or in controlled delivery systems. Therefore, it is important to know the physicochemical properties of these particles in aqueous media. To gain more insight on the behaviour of the protein particles, further research should focus on the interaction of these particles with other biopolymers in the matrix.

Author's Contributions

Alev Emine İnce Coşkun: Structured and wrote the manuscript.

Özgül Özdestan Ocak: Helped in preparing the manuscript and explaining the chemistry of the materials.

Buğra Ocak: Helped and designed the 5th part, which is about gelatin particles.

Semih Ötleş: Decided the main topic and narrowed down the subtitles.

Ethics

There are no ethical issues after the publication of this manuscript.

References

1. Haug, A, Hostmark, AT, Harstad, OM. 2007. Bovine milk in human nutrition – a review. *Lipids in Health and Disease;* 6: 25-40.

2. Hammann, F, Schmid, M. 2014. Determination and quantification of molecular interactions in protein films: A review. *Materials*; 7: 7975-7996.

3. Pelegrine, DHG, Gasparetto, CA. 2005. Whey protein solubility as function of temperature and pH. *LWT-Food Science and Technology;* 38(1): 77-80.

4. Horne, DS. 2006. Casein micelle structure: Models and muddles. *Current Opinion in Colloid and Interface Science;* 11: 148-153.

5. Broyard, C, Gaucheron, F. 2015. Modifications of structures and functions of caseins: a scientific and technological challenge. *Dairy Science and Technology;* 95: 831-862.

6. Thorn, DC, Meehan, S, Sunde, M, Rekas, A, Gras, SL, MacPhee, CE, Dobson, CM, Wilson MR, Carver JA. 2005. Amyloid fibril formation by bovine milk kappa-casein and its inhibition by the molecular chaperones alphaS- and beta-casein. *Biochemistry;* 44(51): 17027-36.

7. Braga, ALM, Menossi, M, Cunha, RL. 2006. The effect of the glucono-δ-lactone/caseinate ratio on sodium caseinate gelation. *International Dairy Journal;* 16: 389-398.

8. Chu, B, Zhou, Z, Wu, G, Farrell Jr, HM. 1995. Laser light scattering of model casein solutions: Effects of high temperature. *Journal of Colloid and Interface Science*; 170(1): 102-112.

9. Guo, MR, Fox, PF, Flynn, PF, Kindstedt, PS. 1996. Heat-induced modifications of the functional properties of sodium caseinate. *International Dairy Journal;* 6(5): 473-483.

10. Stanic, D, Monogioudi, E, Dilek, E, Radosavljevic, J, Atanaskovic-Markovic, M, Vuckovic, O, Raija, L, Mattinen, L, Buchert, J, Cirkovic Velickovic, T. 2010. Digestibility and allergenicity assessment of enzymatically crosslinked β-casein. *Molecular Nutrition and Food Research;* 54: 1273–1284.

11. O'Kennedy, BT, Mounsey, JS, Murphy, F, Duggan, E, Kelly, PM. 2006. Factors affecting the acid gelation of sodium caseinate. *International Dairy Journal;* 16(10): 1132-1141.

12. Dickinson, E, Golding, M. 1997. Rheology of sodium caseinate stabilized oil-in-water emulsions. *Journal of Colloid and Interface Science;* 191(1): 166-176.

13. Gomez-Guillen, MC, Gimenez, B, Lopez-Caballero, ME, Montero, MP. 2011. Functional and bioactive properties of collagen and gelatin from alternative sources: A review. *Food Hydrocolloids;* 25: 1813-1827.

14. Nikoo, M, Benjakul, S, Ocen, D, Yang, N, Xu, B, Zhang, L, Xu, X. 2013. Physical and chemical properties of gelatin from the skin of cultured Amur sturgeon (*Acipenser schrenckii*). *Journal of Applied Ichthyology;* 29: 943-950.

15. Gornall, JL, Terentjev, EM. 2008. Helix-coil transition of gelatin: helical morphology and stability. *Soft Matter;* 4: 544-549.

16. Gomez-Guillen, MC, Turnay, J, Fernandez-Diaz, MD, Ulmo, N, Lizarbe, MA, Montero P. 2002. Structural and physical properties of gelatin extracted from different marine species: a comparative study. *Food Hydrocolloids;* 16(1): 25-34.

17. Seçkin, AK, Baladura, E. 2011. Süt ve süt ürünlerinin fonksiyonel özellikleri. *Celal Bayar University Journal of Science;* 7.1:27-38.

18. Güy, N. 2018. Papain immobilization on $NiFe_2O_4$ magnetic nanoparticles functionalized with gallic acid and microwave assisted digestion of bovine serum albumin. *Celal Bayar University Journal of Science;* 14(4): 449-454.

19. Kapusuz, D, Ercan, B. 2019. Calcium phosphate mineralization on calcium carbonate particle incorporated silk-fibroin composites. *Celal Bayar University Journal of Science;* 15(3): 301-306.

20. Büyüköz, M, Alsoy Altınkaya, S. 2015. Jelatin doku iskelesinin mekanik özellikleri üzerine gözenek oluşturucu ajanın boyutu ve bağlantı süresinin etkileri. *Celal Bayar University Journal of Science;* 11(2): 167-173.

21. Mehalebi, S, Nicolai, T, Durand, D. 2008. Light scattering study of heat- denatured globular protein aggregates. *International Journal of Biological Macromolecules;* 43: 129-135.

22. Schmitt, C, Bovay, C, Vuilliomenet, AM, Rouvet, M, Bovetto, L. 2011. Influence of protein and mineral composition on the formation of whey protein heat-induced microgels. *Food Hydrocolloids;* 25: 558-567.

23. Dill, KA. 1990. Dominant forces in protein folding. *Biochemistry;* 29: 7133-7155.

24. Moitzi, C, Donato, L, Schmitt, C, Bovetto, L, Gillies, G, Stradner, A. 2011. Structure of β-lactoglobulin microgels formed during heating as revealed by small-angle X-ray scattering and light scattering. *Food Hydrocolloids;* 25: 1766-1774.

25. Nicolai, T, Durand, D. 2013. Controlled food protein aggregation for new functionality. *Current Opinion in Colloid and Interface Science;* 18: 249-256.

26. Phan-Xuan, T, Durand, D, Nicolai, T. 2013. Tuning the structure of protein particles and gels with calcium or sodium ions. *Biomacromolecules;* 14: 1980-1989.

27. Ruis, HGM, Venema, P, van der Linden, E. 2007. Relation between pH-induced stickiness and gelation behaviour of sodium caseinate aggregates as determined by light scattering and rheology. *Food Hydrocolloids;* 21: 545-554.

28. Lee, WJ, Lucey, JA. 2010. Formation and physical properties of yogurt. *Asian-Australian Journal of Animal Science;* 23: 1127-1136.

29. Xu, J, Li, T, Tao, F, Cui, Y, Xia, Y. 2013. Structure evolution of gelatin particles induced by pH and ionic strength. *Microscopy Research and Technique;* 76: 272-281.

30. Dumetz, AC, Snellinger-O'brien, AM, Kaler, EW, Lenhoff, AM. 2007. Patterns of protein protein interactions in salt solutions and implications for protein crystallization. *Protein Science;* 16: 1867-1877.

31. Lorenzen, PC. 2007. Effects of varying time/temperature-conditions of pre-heating and enzymatic cross-linking on techno-functional properties of reconstituted dairy ingredients. *Food Research International;* 40: 700-708.

32. Zhang, W, Zhong, Q. 2009. Microemulsions as nanoreactors to produce whey protein nanoparticles with enhanced heat stability by sequential enzymatic cross-linking and thermal pretreatment. *Journal of Agricultural and Food Chemistry;* 57: 9181-9189.

33. Nivala, O, Mäkinen, OE, Kruus, K, Nordlund, E, Ercili-Cura, D. 2017. Structuring colloidal oat and faba bean protein particles via enzymatic modification. *Food Chemistry;* 231: 87-95.

34. Alting, AC, de Jongh, HHJ, Visschers, RW, Simons, JWFA. 2002. Physical and chemical interactions in cold gelation of food proteins. *Journal of Agricultural and Food Chemistry;* 50: 4682-4689.

35. Lucey, JA, van Vliet, T, Grolle, K, Geurts, T, Walstra, P. 1997. Properties of acid casein gels made by acidification with glucono-δ-lactone. 1. Rheological properties. *International Dairy Journal;* 7: 381-388.

36. Andoyo, R, Guyomarc'h, F, Cauty, C, Famelart, MH. 2014. Model mixtures evidence the respective roles of whey protein particles and casein micelles during acid gelation. *Food Hydrocolloids;* 37: 203-212.

37. Guldbrand, L, Jönsson, B, Wennerström, H, Linse, P. 1984. Electrical double layer forces. A Monte Carlo study. *The Journal of Chemical Physics;* 80: 2221-2228.

38. Zhang, W, Zhong, Q. 2010. Microemulsions as nanoreactors to produce whey protein nanoparticles with enhanced heat stability by thermal pretreatment. *Food Chemistry;* 119: 1318-1325.

39. Sağlam, D, Venema, P, de Vries, R, Sagis, LMC, van der Linden, E. 2011. Preparation of high protein micro-particles using two-step emulsification. *Food Hydrocolloids;* 25: 1139-1148.

40. Ince Coskun, AE, Sağlam, D, Venema, P, van der Linden, E, Scholten, E. 2015. Preparation, structure and stability of sodium caseinate and gelatin micro-particles. *Food Hydrocolloids;* 45: 291-300.

41. Purwanti, N, Peters, JPC, van der Goot, AJ. 2013. Protein micro-structuring as a tool to texturize protein foods. *Food and Function;* 4: 277-282.

42. Wagoner, T, Vardhanabhuti, B, Foegeding, EA. 2016. Designing whey protein-polysaccharide particles for colloidal stability. *Annual Review of Food Science and Technology;* 7: 93-116.

43. Sağlam, D, Venema, P, de Vries, R, Shi, J, van der Linden, E. 2013. Concentrated whey protein particle dispersions: Heat stability and rheological properties. *Food Hydrocolloids;* 30: 100-109.

44. Sağlam, D, Venema, P, de Vries, R, van Aelst, A, van der Linden, E. 2012. Relation between gelation conditions and the physical properties of whey protein particles. *Langmuir;* 28: 6551-6560.

45. Liu, BT, Hsu, JP. 2009. Stability of soft colloidal particles in a salt-free medium. *Langmuir;* 25: 9045-9050.

46. Sağlam, D, Venema, P, de Vries, R, van der Linden, E. 2014. Exceptional heat stability of high protein content dispersions containing whey protein particles. *Food Hydrocolloids;* 34: 68-77.

47. Sağlam, D, Venema, P, de Vries, R, van der Linden, E. 2013. The influence of pH and ionic strength on the swelling of dense protein particles. *Soft Matter;* 9: 4598-4606.

48. Patel, AR, Bouwens, ECM, Velikov, KP. 2010. Sodium caseinate stabilized zein colloidal particles. *Journal of Agricultural and Food Chemistry;* 58: 12497-12503.

49. Li, F, Chen, Y, Liu, S, Qi, J, Wang, W, Wang, C, Zhong, R, Chen, Z, Li, X, Guan, Y, Kong, W, Zhang, Y. 2017. Size-controlled fabrication of zein nano/microparticles by modified anti-solvent precipitation with/without sodium caseinate. *International Journal of Nanomedicine;* 12: 8197-8209.

50. Ching, SH, Bhandari, B, Webb, R, Bansal, N. 2015. Visualizing the interaction between sodium caseinate and calcium alginate microgel particles. *Food Hydrocolloids;* 43: 165-171.

51. Ma, H, Forssell, P, Partanen, R, Seppanen, R, Buchert, J, Boer, H. 2009. Sodium caseinates with an altered isoelectric point as emulsifiers in oil/water systems. *Journal of Agricultural and Food Chemistry;* 57: 3800-3807.

52. Van der Linden, E, Parker, A. 2005. Elasticity due to semiflexible protein assemblies near the critical gel concentration and beyond. Langmuir; 21(21):9792-9794.

53. Farrugia, CA, Groves, MJ. 1999. Gelatin behaviour in dilute aqueous solution: Designing a nanoparticulate formulation. *Journal of Pharmacy and Pharmacology;* 51: 643-649.

54. Ahsan, SM, Rao, CM. 2017. The role of surface charge in the desolvation process of gelatin: implications in nanoparticle synthesis and modulation of drug release. *International Journal of Nanomedicine;* 12: 795-808.

Celal Bayar University Journal of Science

A Comprehensive Analysis to Determine the Phytochemical Characteristics of *Fraxinus americana* and *Fraxinus excelsior* Leaves Extracts: Influence of the Extraction Method

Buse Aydoğan[1], Mustafa Cittan[1]*, Ali Çelik[1], Kenan Dost[1]

[1] Department of Chemistry, Faculty of Science and Letters, Manisa Celal Bayar University, 45140, Manisa, Turkey
*mustafa.cittan@cbu.edu.tr

Received: 28 August 2019
Accepted: 17 March 2020
DOI: 10.18466/cbayarfbe.612481

Abstract

A comprehensive investigation was carried out to determine the phytochemical properties of *Fraxinus americana* and *Fraxinus excelsior* leaves extracts. In addition, infusion extraction method using only water as the extraction solvent and ultrasound-assisted extraction technique were followed comparatively to extract the phenolic compounds from the leaves to estimate the efficacy of the traditional hot water infusion method. Initially, total antioxidant capacities, total phenolic contents, and radical scavenging activities of the extracts were determined. Afterwards, 34 potential phenolic compounds were analyzed by LC-ESI-MS/MS technique. The paper gives a comprehensive insight to the literature about the phytochemical properties of *Fraxinus americana* and *Fraxinus excelsior* leaves extracts.

Keywords: *Oleaceae*; Genus *Fraxinus*; Traditional preparation; Hot water infusion technique; LC-ESI-MS/MS

1. Introduction

Genus Fraxinus (family Oleaceae) contain significant amounts of phytochemicals aimed at scavenging the reactive oxygen species (ROS) causing important damage to cellular structures. This valuable content has led to intensive research in phenolic compounds in the leaves of Oleaceae family.

Natural products from plants have proven their worth as main sources of chemical compounds having medicinal properties. To this end, several studies were carried out to determine the phytochemical profiles of different plant materials [1,2].

People traditionally prefer the hot water infusion, which is the easiest way to extract the pharmaceutical properties of plants. On the other hand, more complicated extraction methods, such as microwave-assisted extraction (MAE) [3,4], ultrasound-assisted extraction (UAE) [5–7], supercritical fluid extraction (SFE) [8,9], accelerated solvent extraction (ASE) [10,11], soxhlet [12,13] and heat reflux extraction (HRE) [13] were all followed to extract the bioactive compounds (especially phenolic compounds) with a higher yield before analytical determination of the phenolic contents of plants. However, these extraction techniques were usually carried out using a mixture comprising methanol which is not suitable for human consumption to enhance the extraction efficiency.

In this study, infusion extraction (IE) and UAE techniques were followed to determine the antioxidant capacities, radical scavenging activities and phenolic profiles of leaves extracts of two different species of fraxinus (*Fraxinus excelsior* and *Fraxinus americana*). UAE was carried out using methanol/water mixture (70/30, v/v) which is an efficient aid to extract the bioactive compounds from different plant parts. Then the phytochemical contents of the leaves were determined by using the extracts obtained by UAE. Otherwise, IE was performed using only water. Therefore, the efficacy of the IE method was compared to the efficient UAE technique. For this purpose, leaves extracts of both species obtained by UAE and IE methods were firstly screened for their total antioxidant capacities (TACs), total phenolic contents (TPCs) and radical scavenging activities (RSAs) via CUPRAC, Folin-Ciocalteu and DPPH methods, respectively. Afterwards, liquid chromatography-electrospray tandem mass spectrometry (LC-ESI-MS/MS) technique was used for scanning 34 individual phenolics in the extracts.

Present work is quite original in its nature since it provides information on the efficacy of the simple hot

water infusion method that is traditionally applied at homes compared to UAE method, which has proven to be effective extracting phenolic compounds from plant matrices. On the other hand, this is the first comprehensive report in terms of number of individual phenolics determined in two species of genus Fraxinus. It gives a comprehensive insight to the literature about the phytochemical properties of *Fraxinus excelsior* and *Fraxinus americana* leaves extracts.

2. Materials and Methods

2.1. Apparatus

A Jasco V-530 UV/Vis Spectrophotometer was used for the spectrophotometric measurements. Agilent 1260 LC system hyphenated to an Agilent 6420 Triple Quadrupole MS system was used to determine the individual phenolics.

2.2. Reagents

All commercial phenolic standards were purchased from Sigma-Aldrich (St. Louis, MO, USA), Fluka (St. Louis, MO, USA) and HWI Analytik (Ruelzheim, Germany). Trolox, neocuproine, methanol and 2,2-diphenyl-1-picrylhydrazyl (DPPH) were obtained from Sigma-Aldrich (St. Louis, MO, USA). Sodium carbonate, copper (II) chloride, Folin-Ciocalteu reagent and formic acid were purchased from Merck (Darmstadt, Germany).

2.3. Plants

Fraxinus excelsior and Fraxinus americana leaves (Figure 1) were washed with distilled water, and dried in the dark. Dried plant leaves were kept at +4 °C. Dried plant material was powdered and sieved before the extraction.

Figure 1. The leaves (a) *Fraxinus excelsior*, (b) *Fraxinus Americana*

2.4. Extraction procedures

For UAE, sample powder (0.2 g) was extracted initially with 20 mL of methanol/water mixture (70/30, v/v) in ultrasonic bath for 60 min. Then, the procedure was repeated twice in a row using 20 and 10 mL of the same mixture for 45 and 15 min respectively to enhance the extraction efficiency. For IE, 50 mL of ultrapure water was added on 0.2 g sample powder and brewed for 1 hour at 95 °C.

2.5. LC-ESI-MS/MS technique

Two different chromatographic techniques were followed to determine 34 phenolic compounds in the leaves extracts. 31 of these compounds were scanned following the procedure described in our previous work [14]. On the other hand, oleuropein (a secoiridoid) and phenyl ethyl alcohols (hydroxytyrosol and tyrosol), which are specific groups of Oleaceae family, was determined by a separate method given below. The chromatographic column was Poroshell 120 EC-C18 (100 mm x 4.6 mm I.D., 2.7 µm). The mobile phase was made up from solvent A (5mM ammonium acetate solution) and solvent B (methanol). The gradient profile was set as follows: 0.00 min 5% solvent B, 2.00 min 25% solvent B, 4.00 min 50% solvent B, 6.00 min 95% solvent B, 8.00 min 95% solvent B, and 9.00 min 5% solvent B. The injection volume was 5.0 µL. The column temperature was 25 °C and the flow rate was 0.4 mL/min.

All the method details and LC-ESI-MS/MS chromatograms for the 31 phenolic compounds were provided in the previous work [14]. MS/MS parameters and retention times of each compounds determined by the second method proposed were provided in Table 1 and a representative LC-ESI-MS/MS chromatogram of the phenolics were represented in Figure 2.

2.6. Total phenolic content, cupric reducing antioxidant capacity, and DPPH radical scavenging activity assays

The Folin–Ciocalteu method [15] was followed to determine the TPCs of the extracts. Total antioxidant capacities (TACs) of the extracts were determined following the method, which is CUPRAC of Apak et al. [16]. The scavenging of 2,2-diphenyl-1-picrylhydrazyl (DPPH) radicals was used to determine the RSAs of the leaves extracts [17].

Table 1. MS/MS parameters for target compounds and retention times.

Compounds	R_t (min)	Precursor ion	MRM1 (CE, V)	MRM2 (CE, V)	Linear range (µg/L)	R^2
Hydroxytyrosol	5.667	153.0 $[M-H]^-$	123.0 (10)	94.9 (18)	25-500	0.9986
Tyrosol	6.263	137.0 $[M-H]^-$	119.1 (12)	105.8 (12)	25-500	0.9965
Oleuropein	6.941	539.2 $[M-H]^-$	377.1 (10)	275.1 (16)	25-500	0.9975

R_t, retention time; MRM, multiple reaction monitoring; CE, collision energy.

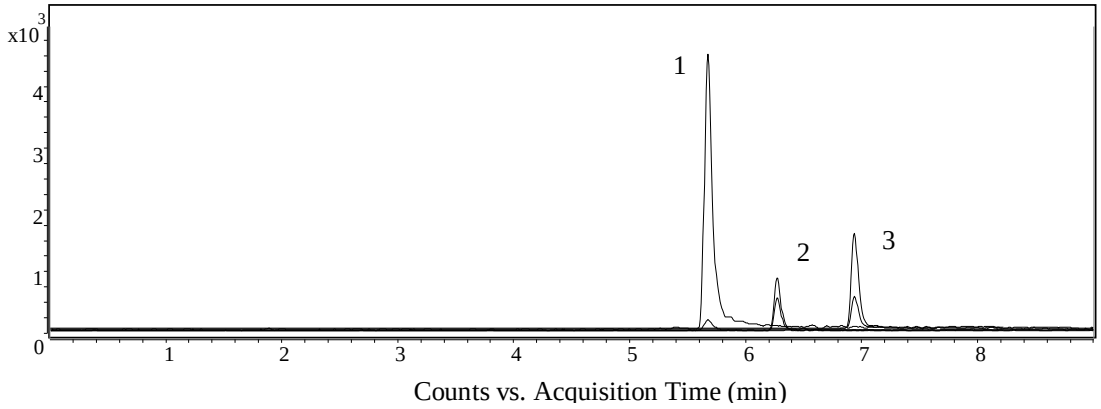

Figure 2. LC-ESI-MS/MS MRM chromatogram of the standard phenolic compounds. 1-3 represent the chromatograms of hydroxytyrosol, tyrosol and oleuropein, respectively.

3. Results and Discussion

TPCs, TACs and RSAs of the leaves extracts of both species were provided in Table 2. In all cases, the leaves extracts obtained by UAE showed higher antioxidant capacity and were found to be richer in terms of the phenolic compounds when compared to extracts obtained by IE. In addition, especially the results of the leaves extracts obtained by UAE technique which is more effective to extract phytochemicals from plant matrices showed that *Fraxinus americana* contains higher amount of phenolic compounds and has higher antioxidant capacity. In contrast, there was no significant difference in the RSAs of the leaves extracts of the species obtained by both extraction techniques.
LC-ESI-MS/MS method was used to determine the some potential phenolic compounds in both leaves extracts of the species. The phenolic compounds contents of the extracts were provided in Table 3. Among phenolics, 22 compounds were quantitatively determined with oleuropein as the dominant one. It is well known that secoiridoids are the most common compounds in Oleaceae [18]. However, their concentrations and those of their derivatives are also dependent on the season [19].

While the TPCs and TACs of the ultrasound-assisted extracts of the leaves of *Fraxinus excelsior* was lower (see Table 2), it was clear from Table 3 that the amount of oleuropein was determined higher in both leaves extracts of *Fraxinus excelsior*. This result reveals that *Fraxinus americana* leaves are richer in some other phenolic compounds (except for the 34 phenolic compounds involved in the study) showing antioxidant properties compared to *Fraxinus excelsior* leaves. The other dominant compounds in the extracts were verbascoside and hesperidin.

In concluding, oleuropein, tyrosol, hydroxytyrosol, protocatechuic acid, chlorogenic acid, 2,5-dihydroxybenzoic acid, 4-hydroxybenzoic acid, vanillic acid, caffeic acid, verbascoside, *p*-coumaric acid, ferulic acid, luteolin 7-glucoside, hesperidin, hyperoside, apigenin 7-glucoside and pinoresinol were determined in both leaves extracts of the species. In some cases, the IE technique provided a more efficient phenolic compound extraction from the leaves of the species compared to UAE. Especially, hydroxytyrosol and tyrosol (the phenyl ethyl alcohols) concentrations were higher in the both leaves extracts obtained via IE technique using only water as extractant. The results indicated that the hot water infusion technique is more efficient in extracting phenyl ethyl alcohols, which are more polar and relatively small phenolic compounds. Also, gallic acid and 3,4–dihydroxyphenylacetic acid were determined only in aqueous extract obtained by using IE technique. In contrast, quercetin was found only in methanolic extract obtained via UAE method. Finally, (+)-catechin, pyrocatechol, (−)-epicatechin, syringic acid, vanillin, taxifolin, rosmarinic acid, 3-hydroxybenzoic acid, 2-hydroxycinnamic acid, sinapic acid, eriodictyol and kaempferol were not detected in both extracts.

Table 2. TPCs, TACs and RSAs of *Fraxinus americana and Fraxinus excelsior* leaves extracts (n=3).

Species	Extraction technique	TPCs (mg GAE/g dry sample)	TACs (mg TE/g dry sample)	RSAs (mg TE/g dry sample)
Fraxinus americana	UAE	110.92±4.75	238.38±6.74	2.21±0.01
	IE	45.06±5.16	76.74±3.31	2.08±0.07
Fraxinus excelsior	UAE	70.21±3.64	138.45±5.07	2.19±0.04
	IE	46.45±4.49	91.42±2.66	2.08±0.07

Table 3. Quantitative results of phenolic compounds in *Fraxinus americana* and *Fraxinus excelsior* leaves extracts obtained by ultrasound-assisted extraction and infusion extraction techniques (n=3).

Compound	*Fraxinus americana*		*Fraxinus excelsior*	
	UAE (µg/g dry sample)	IE (µg/g dry sample)	UAE (µg/g dry sample)	IE (µg/g dry sample)
Oleuropein	27085±1896	17299±1211	55192±3863	29443±2061
Tyrosol	119±16	363±25	154±12	406±27
Hydroxtyrosol	161±19	496±27	118±15	392±26
Gallic acid	nd	1.0±0.1	nd	2.3±0.5
Protocatechuic acid	54.4±1.0	12.8±1.0	3.9±0.2	61.3±4.4
3,4 -Dihydroxyphenylacetic acid	nd	0.4±0.1	nd	1.6±0.1
(+)-Catechin	nd	nd	nd	nd
Pyrocatechol	nd	nd	nd	nd
Chlorogenic acid	265±16	963±52	1765±25	153±18
2,5-Dihydroxybenzoic acid	5.3±0.1	1.6±0.2	2.3±0.1	4.9±0.3
4-Hydroxybenzoic acid	1.7±0.1	3.5±0.1	3.0±0.1	2.3±0.1
(−)-Epicatechin	nd	nd	nd	nd
Vanillic acid	3.6±0.7	4.6±1.0	4.0±0.3	3.1±0.6
Caffeic acid	2.9±0.2	33.0±1.3	6.9±0.6	23.0±0.7
Syringic acid	nd	nd	nd	nd
3-Hydroxybenzoic acid	nd	nd	nd	nd
Vanillin	nd	nd	nd	nd
Verbascoside	18585±265	846±134	2809±79	6850±968
Taxifolin	nd	nd	nd	nd
Sinapic acid	nd	nd	nd	nd
p-Coumaric acid	5.3±0.3	10.9±0.3	4.9±0.3	9.5±0.6
Ferulic acid	2.9±0.1	11.4±0.8	9.0±0.4	4.5±0.3
Luteolin 7-glucoside	984±31	0.6±0.1	0.8±0.1	304±12
Hesperidin	14369±238	11086±1131	23691±1147	7092±306
Hyperoside	793±7.8	317±16	805±53	329±25
Rosmarinic acid	nd	nd	nd	nd
Apigenin 7-glucoside	372±51	0.8±0.1	1.0±0.1	156±18
2-Hydroxycinnamic acid	nd	nd	nd	nd
Pinoresinol	5.1±0.3	56.6±2.5	58.8±7.4	7.5±1.6
Eriodictyol	nd	nd	nd	nd
Quercetin	0.8±0.1	nd	0.9±0.1	nd
Luteolin	17.0±1.3	nd	nd	3.1±0.2
Kaempferol	nd	nd	nd	nd
Apigenin	7.8±0.5	nd	nd	1.6±0.2

4. Conclusion

Present work addressed two important issues. The first one was a detailed investigation in terms of number of

individual phenolic compounds in two species of genus Fraxinus. Twenty two compounds were identified and quantified in the extracts with oleuropein as the dominant one. The other important issue was the demonstration of the efficacy of the simple hot water infusion technique which can easily be applied at home. It was clear from the results that both extraction solvent and extraction technique play important roles in the extraction efficacy of the phenolics from different plant leaves. Although, higher amounts of oleuropein (approximately 2-fold) were extracted in all cases from the leaves of genus Fraxinus by using UAE method with methanol as the extractant, it was considered that the hot water infusion technique was also effective enough to extract phenolic compounds from the leaves. In addition, some relatively polar compounds (especially phenyl ethyl alcohols) were only determined in the extracts obtained by IE method using only water as the extraction solvent.

Author's Contributions

Buse Aydoğan: Performed the experiment and result analysis.

Mustafa Cittan: Drafted and wrote the manuscript, performed the experiment and result analysis.

Ali Çelik: Supervised the experiment's progress, result interpretation and helped in manuscript preparation.

Kenan Dost: Assisted in analytical analysis on the structure.

Ethics

There are no ethical issues after the publication of this manuscript.

References

1. Ayvaz, MÇ. 2019. Phenolic profile and cholinesterase, tyrosinase, urease and lipid peroxidation inhibition potentials of *Artemisia argyi* from Ordu, Turkey. *Celal Bayar University Journal of Science*; 15(1): 29–33.

2. Uygun, M, Kilimci, N, Kaya, SK, Yavaş, İ. 2017. Investigation of some chemical and biochemical properties of locally grown *Lavandula stoechas*. *Celal Bayar University Journal of Science*; 13(1): 63–69.

3. Cittan, M, Koçak, S, Çelik, A, Dost, K. 2016. Determination of oleuropein using multiwalled carbon nanotube modified glassy carbon electrode by adsorptive stripping square wave voltammetry. Talanta; 159: 148–154.

4. Radojković, M, Moreira, MM, Soares, C, Fátima Barroso, M, Cvetanović, A, Švarc-Gajić, J. et al. 2018. Microwave-assisted extraction of phenolic compounds from Morus nigra leaves: optimization and characterization of the antioxidant activity and phenolic composition. Journal of Chemical Technology & Biotechnology; 93(6): 1684–1693.

5. Goltz, C, Ávila, S, Barbieri, JB, Igarashi-Mafra, L, Mafra, MR. 2018. Ultrasound-assisted extraction of phenolic compounds from Macela (Achyrolcine satureioides) extracts. Industrial Crops and Products; 115: 227–234.

6. Luo, X, Cui, J, Zhang, H, Duan, Y, Zhang, D, Cai, M. et al. 2018. Ultrasound assisted extraction of polyphenolic compounds from red sorghum (Sorghum bicolor L.) bran and their biological activities and polyphenolic compositions. Industrial Crops and Products; 112: 296–304.

7. Nipornram, S, Tochampa, W, Rattanatraiwong, P, Singanusong, R. 2018. Optimization of low power ultrasound-assisted extraction of phenolic compounds from mandarin (Citrus reticulata Blanco cv. Sainampueng) peel. Food Chemistry; 241: 338–345.

8. Giannuzzo, AN, Boggetti, HJ, Nazareno, MA, Mishima, HT. 2003. Supercritical fluid extraction of naringin from the peel of Citrus paradisi. Phytochemical Analysis; 14(4): 221–223.

9. Alvarez, MV, Cabred, S, Ramirez, CL, Fanovich, MA. 2019. Valorization of an agroindustrial soybean residue by supercritical fluid extraction of phytochemical compounds. The Journal of Supercritical Fluids; 143: 90–96.

10. Luthria, DL. 2008. Influence of experimental conditions on the extraction of phenolic compounds from parsley (Petroselinum crispum) flakes using a pressurized liquid extractor. Food Chemistry; 107(2): 745–752.

11. Toubane, A, Rezzoug, SA, Besombes, C, Daoud, K. 2017. Optimization of Accelerated Solvent Extraction of Carthamus Caeruleus L. Evaluation of antioxidant and anti-inflammatory activity of extracts. Industrial Crops and Products; 97: 620–631.

12. Nile, SH, Nile, AS, Keum, YS. 2017. Total phenolics, antioxidant, antitumor, and enzyme inhibitory activity of Indian medicinal and aromatic plants extracted with different extraction methods. 3 Biotech; 7(1): 76.

13. Jun, X, Deji, S, Ye, L, Rui, Z. 2011. Comparison of in vitro antioxidant activities and bioactive components of green tea extracts by different extraction methods. International Journal of Pharmaceutics; 408(1–2): 97–101.

14. Cittan, M, Çelik, A. 2018. Development and Validation of an Analytical Methodology Based on Liquid Chromatography–Electrospray Tandem Mass Spectrometry for the Simultaneous Determination of Phenolic Compounds in Olive Leaf Extract. Journal of Chromatographic Science; 56(4): 336–343.

15. Singleton, VL, Orthofer, R, Lamuela-Raventós, RM. 1999. Analysis of total phenols and other oxidation substrates and antioxidants by means of folin-ciocalteu reagent. Methods in Enzymology; 299: 152–178.

16. Apak, R, Güçlü, K, Özyürek, M, Karademir, SE. 2004. Novel Total Antioxidant Capacity Index for Dietary Polyphenols and Vitamins C and E, Using Their Cupric Ion Reducing Capability in the Presence of Neocuproine: CUPRAC Method. Journal of Agricultural and Food Chemistry; 52(26): 7970–7981.

17. Molyneux, P. 2004. The use of the stable free radical diphenylpicryl-hydrazyl (DPPH) for estimating antioxidant activity. Songklanakarin Journal of Science and Technology; 26: 211–219.

18. Soler-Rivas, C, Espin, JC, Wichers, HJ. 2000. Oleuropein and related compounds. Journal of the Science of Food and Agriculture; 80(7): 1013–1023.

19. Sugiyama, M, Machida, K, Matsuda, N, Kikuchi, M. 1993. A secoiridoid glycoside from Osmanthus asiaticus. Phytochemistry; 34(4): 1169–1170.